

Fluctuations and Synchronization in Complex Physiological Systems

Dissertation zur Erlangung des akademischen Grades
Dr. rer. nat.

eingereicht von

Dipl. Physiker Aicko Yves Schumann

an der
Naturwissenschaftlichen Fakultät II - Chemie und Physik
der Martin-Luther-Universität Halle-Wittenberg

am 17. Januar 2010

Tag der öffentlichen Disputation: Montag, der 17. Mai 2010

Gutachter: JProf. PD Dr. Jan W. Kantelhardt (Uni Halle)
Prof. Dr. Philipp Maaß (Uni Osnabrück)
Prof. Dr. Steffen Trimper (Uni Halle)

Contents

Preface	iv
1. Basic Concepts of Time Series and Stochastic Modeling	1
1.1. Terminology	1
1.2. Short- and Long-Range Dependence	6
1.2.1. Linear Time Space Approach	7
1.2.2. Spectral Approach	8
1.2.3. Nonlinear Approach – Fluctuations	8
1.3. Real Time-Frequency Decomposition – Wavelet Analysis	9
1.4. Fractality	10
1.5. Stochastic Modeling of Time Series	12
1.5.1. Generation of Short-Range Correlated Data	12
1.5.2. Generation of Long-Range Correlated Data	13
2. Introduction to Human Physiology	15
2.1. The Autonomous Nervous System	15
2.2. The Cardiorespiratory System – Heartbeat and Respiration	16
2.2.1. Heartbeat	17
2.2.2. Respiration and Respiratory Sinus Arrhythmia	19
2.3. Sleep - Polysomnographic Recordings	20
2.3.1. Brain Waves - The Human Electroencephalogram	22
2.3.2. Sleep Stages	22
2.3.3. Sleep Apnea – a Sleep Related Disorder	23
2.3.4. Parkinson’s Disease	24
2.4. Databases Used in This Thesis	24
2.4.1. ISAR-I Database	24
2.4.2. SIESTA Database	24
2.4.3. DAPHNET Database	26
3. Studying Fluctuations	27
3.1. Monofractal Fluctuation Analysis Methods	27
3.1.1. Hurst Rescaled-Range Analysis	28
3.1.2. Fluctuation Analysis (FA)	28
3.1.3. Detrended Fluctuation Analysis (DFA)	30
3.1.4. Centered Moving Average Analysis (CMA) – And Other Monofractal Fluctuation Analysis Methods	33
3.2. Fluctuations During Nocturnal Sleep	35
3.2.1. Impact of Undetected Heartbeats and Extrasystoles on DFA	35
3.2.2. Fluctuations in Heartbeat and Respiration	37
3.2.3. Fluctuations in Patients	43
3.3. Multifractal Fluctuation Analysis Methods	44
3.3.1. Multifractal Detrended Fluctuation Analysis (MF-DFA)	45
3.3.2. Multifractal Centered Moving Average (MF-CMA) Analysis	46
3.3.3. Standard Multifractality Properties	46
3.3.4. Generalized Binomial Multi-Fractal Model (GB-MFM)	48
3.3.5. Analysis of Data from the GB-MFM	51
3.3.6. Surrogate Data Generation by Block Shuffling	53

3.4.	Spurious Multifractality in Monofractals	54
3.4.1.	Spurious Multifractality in Block Shuffled Data	54
3.4.2.	Spurious Multifractality Due to Finite-Size Effects and Nonstationary Correlations	56
3.4.3.	Spurious Multifractality Due to Patchy Correlation Behavior	58
3.4.4.	Spurious Multifractality in Data With Trends	60
3.4.5.	Spurious Multifractality in Data With Periodicities	62
4.	Investigating Quasiperiodicities	63
4.1.	Univariate Phase Rectified Signal Averaging (PRSA)	64
4.1.1.	PRSA Algorithm With Variants	65
4.1.2.	Interpretation of PRSA Curves	69
4.1.3.	PRSA Curves of Cardiac Data	70
4.1.4.	Wavelet Analysis of PRSA Results	71
4.1.5.	Definition of Deceleration Capacity (DC)	72
4.1.6.	Age Dependence in Post-Infarction DC	74
4.1.7.	Circadian Rhythm in PRSA Results	75
4.1.8.	Quasioscillations Across Sleep Stages	77
4.1.9.	Quasioscillations in Patients	79
4.1.10.	Aging Effects on DC Across Sleep Stages	81
4.2.	Bivariate PRSA (BPRSA) and Multivariate PRSA (MPRSA)	82
4.2.1.	BPRSA Algorithm	83
4.2.2.	Limitations of Cross-Correlation Analysis	84
4.2.3.	Interpretation of BPRSA Curves	85
4.2.4.	Comparison of Cross-Correlation Analysis and BPRSA	86
4.2.5.	Example I: Event Modulated Oscillations	88
4.2.6.	Example II: White Noises with Linear Relation	89
4.2.7.	Example III: Nonlinear Relation	90
4.2.8.	Example IV: Influence of Trends in the Signal	90
4.2.9.	Towards a Multivariate Analysis	91
5.	Quantifying Interrelation by Synchronization Analysis Methods	93
5.1.	Introduction to Synchronization Analysis	93
5.1.1.	Concepts of Characterizing and Detecting Synchronization	93
5.1.2.	Defining Instantaneous Amplitudes, Phases, and Frequencies	95
5.1.3.	Quantifying Mutual Synchronization	98
5.2.	Automated Synchrogram Analysis	102
5.2.1.	Reconstruction of Respiration from Heartbeat	102
5.2.2.	Assessing Reconstruction Quality	103
5.2.3.	Description of an Automated Synchrogram Approach	105
5.2.4.	Optimizing Synchrogram Evaluation Parameters	107
5.2.5.	Phase Synchronization with Reconstructed Breathing	107
5.2.6.	Higher Order Cardiorespiratory Synchronization and Age Dependence	108
5.3.	Cross-Modulation Analysis	112
5.3.1.	Cross-Modulation Analysis Algorithm	113
5.3.2.	A Matrix Representation of Results	116
5.3.3.	Cross-Modulated Amplitudes and Frequencies During Disease-Free Sleep	116
5.3.4.	Surrogate Testing	119
5.3.5.	Cross-modulation in Parkinson's Disease	120
6.	Summary	124
A.	Wiener-Khinchin Theorem	126

B. Auto Correlation in AR(1) Time Series	127
C. Tile Patterns formed by Pentagons	129
D. Statistical Tests	130
D.1. Student's t-Test	130
D.2. Wilcoxon Rank Order Test and Mann-Whitney U Test	131
D.3. P-Value	132
D.4. Receiver Operating Characteristics (ROC) Plots and Bootstrapping	132
E. Further fluctuation analysis methods	136
E.1. Wavelet Based (Multifractal) Fluctuation Analysis	136
E.2. Equivalence of DFA n and WLn	138
E.3. Multifractal Box Counting (MF-Box)	140
E.4. Wavelet Transform Modulus Maxima (WTMM)	140
F. Additional cross-modulation results	142
F.1. Cross-Modulation in Individuals	142
F.2. Cross-Modulation in Random Subgroups	143
F.3. Cross-Modulation Matrices for Parkinson Patients and Age-Matched Disease-Free Controls	144
F.4. Cross-Modulation Matrices for Sleep Apnea Patients and Age-Matched Disease- Free Controls	146
Bibliography	148
G. Publications / Veröffentlichungen	161
H. Danksagung	163

Preface

In the daily language use the term *complex system* is often considered to be synonymous to the term *complicated system*. However, in nonlinear dynamics both attributes of a system are well distinguished. While we might not be able to completely understand both types of systems and their dynamics in general, a complicated system can be fully characterized by knowing its microscopic components. The interactions and dynamics of these components can be well described by a set of possibly difficult and *complicatedly* coupled equations. Although understanding a complicated system might require great effort, it is in principle possible since complicated systems are deterministic by definition. If we understand the microscopic components and their interaction we are able to predict the outcome. Complicated systems are further characterized by a limited number of degrees of freedom and a limited number of components. These numbers, however, might be very large depending on the system. Technical systems are at a macroscopic level by definition deterministic. For example, while we might not know why our car does not start in the morning there are trained mechanics who will likely identify the faulting components. Another important property of a complicated system is that it can be subdivided into subsystems which interact with other subsystems via a limited (or just a few) control chains. Thus, the dynamics of the whole system can be researched by studying its sub-systems. Its future state can be fully predicted when knowing all components, interactions, and hence the whole dynamics.

In contrast a *complex system* is non-deterministic and stochastic. In general we do not possess models to describe each component. Indeed, we do not even know the correct number of interacting components which is in general infinite resulting in an infinite number of degrees of freedom. A complex system cannot be subdivided into subsystems without affecting its behaviour due to an infinite number of nonlinear control loops and an in general chaotically interwoven interrelation structure between the microscopic components. When a complex system is subdivided the dynamics of the subsystems changes in an unpredictable fashion compared with the whole system. Hence, the typical approach to study the dynamics of an unknown system, i. e., the attempt to identify and isolate the essential components responsible for its dynamics, is not at all applicable to a complex system. For instance compare the above example of the car with the human brain. When our brain is not performing as desired we cannot consult a mechanic who isolates faulty components in order to replace them with spare parts.

However, complex systems can be investigated by studying emergent properties that are characteristic of the 'many-particle' system, i. e., the system of many different complex interacting components. For the brain this means that although an assessment of all single neurons and their firing scheme is impossible we can study their mean-field. From the dynamics of the group, in particular from its changes upon stimulation, we can obtain (at least) some average information about underlying mechanisms that generate observed properties. In brain research prominent mean-field properties are brain waves which can be non-invasively recorded from different locations at the skull. Despite a complete understanding of all mechanisms in such system is impossible by definition, researching its unknown dynamics appeals to scientists.

Among the most prominent examples for natural complex systems are the climate system and the weather system in geophysics, the release of hormones or gene expression in biology, electrons in solids in solid state physics, stock exchange in financing, social networks, life in ant colonies, or the ecosystem. In physiology the cardiorespiratory complex system and the complex brain system, which are additionally linked with each other via the autonomous nervous system, are of special interest. In my thesis I will focus on both systems and study their characteristics.

In spite of their non-deterministic and stochastic behaviour, natural complex systems often exhibit oscillations on a wide range of frequencies which emerge from their many linearly and nonlinearly interacting sub-components. Due to these complex interactions they are in addition characterized

by nonstationarities and fluctuations. The coupled components possess regulation loops and control chains that operate on a variety of frequencies. Moreover, scaling laws which are a special type of order in fluctuations are observed in many complex systems and were exploited to characterize the dynamics of the system.

Therefore, fluctuations and oscillations as well as the linear and nonlinear interactions can be studied by time series analysis. The ultimate goal of time series analysis is to obtain mathematical models that describe the mean-field properties, i. e., the typical dynamics of the system.

In a simple additive model an observable (time series) measured from a complex system can be interpreted as an additive superposition of fluctuations and oscillations (mean-field properties), and a component describing the dynamics of the underlying process (the actual signal component). Hence, a time series analysis should aim at a separate characterization of fluctuations, oscillations, and the interrelation between signals obtained from different observables of the complex system (e. g., from different spacial locations or from different complex 'sub-systems' such as respiration and heartbeat). My thesis will be divided into three main parts each dealing exclusively with one of the characteristics.

Firstly I will explore fluctuations in Chapt. 3 and study characteristic time scales. In general, fluctuation analysis tries to attenuate the systematic dynamics of the system, i.e., to remove trends and oscillatory components. It aims at studying the signal's 'background' noise. Such stochastic noise is generally not purely 'random' but often exhibits a correlated structure. For instance long-term correlation which can be imagined by larger values in a signal being more likely followed by larger values and smaller values being more likely followed by smaller values. Two prominent examples are temperature records or human heartbeat during rapid-eye-movement (REM) sleep. In the first case one finds that warm days are rather followed by warm days and cold days are rather followed by cold days. In the second example long-term persistence means that short beat-to-beat intervals more likely follow short beat-to-beat intervals and long intervals rather succeed long intervals.

In contrast, fluctuations are disturbing an exploration of oscillatory components which provide information about characteristic frequencies and delay times in the system. This yields the completely opposite aim of removing fluctuations from the recording by simultaneously enhancing the effects of oscillations. Hence, this topic to which Chapt. 4 is devoted is strongly related to noise reduction. Moreover, the framework introduced in Chapt. 4 allows for studying interrelations of oscillatory components from different signals which might or might not be originated from the same source. In this context the question of quantifying time delays between oscillatory components found in different signals can also be addressed. I will exploit quasi-oscillatory components to quantify total mortality risk in post-infarction patients.

The third topic presented in Chapt. 5 deals with mutual interactions between systems components, and which are sometimes acting in synchrony. The most prominent example in human physiology is the cardio-respiratory coupling which everybody can easily experience by controlled breathing. When we breath slowly as in a meditative state our heart rate decreases (beat-to-beat intervals increase) compared to an approaching tachycardia (accelerated heart) when we hyperventilate. Synchronization effects might be situated somewhere in between. While oscillatory components are mandatory to define properties such as instantaneous phases, amplitudes, and frequencies synchronization effects are much more robust and noise is far less disturbing, and moreover, even capable to induce synchronization when a common noise effects (forces) different oscillators and thus introducing a coupling.

The thesis is organized as follows: First I establish proper quantities and the notation of time series that will be employed throughout the document in Chapt. 1. Chapter 2 is exclusively dedicated to human physiology to provide a basic overview of the signals and the regulatory mechanisms that I study. In particular heartbeat and brain wave recordings will be explained. Most of my studies are based on polysomnographic (sleep) recordings. I will throughout all chapters distinguish between different sleep stages and for that reason I give a short introduction to the phenomenon sleep and discuss how sleep is scored. If the reader is not interested in this phenomenological part of my thesis she/he might skip Chapt. 2.

The main part of this thesis begins in Chapt. 3 where I focus on fluctuations in heartbeat and respiration during sleep and develop methods to conveniently study and generate multifractal data of (almost) arbitrary multifractality strength and tuned correlations. I further explore how reliable results obtained from a multifractal analysis are and which type of data yields spurious multifractality. Readers whose research interest include fluctuation are especially pointed to Appendix E.1 and E.2 where I discuss an analysis method that provides the same detrending capabilities as the standard method but requires less computational power.

Chapter 4 is devoted to studying quasioscillations in noisy nonstationary data. I will review the phase-rectified signal averaging method that is capable of studying oscillations in such data and employ it to investigate for the first time oscillations across sleep stages in a large database comprising both healthy and diseased subjects. In the second part I will generalize the methodology of PRSA to study the interrelation between two or more signals.

In Chapter 5 I will concentrate on mutual synchronization between signals and suggest an automated method to inspect phase synchrograms which until now are mostly studied by eye. The automated synchrogram algorithm will be applied to study aging effects on phase synchronization across all sleep stages. The last part of Chapt. 5 describes a new method to study modulations between amplitudes and frequencies of signals. This method will be illustrated for brain wave recordings.

Note that I cannot provide details for every subject and patient in the framework of this thesis since combining all databases I present here yields multivariate datasets of more than 2000 individuals. However, I did not blindly apply methods to the data from these databases but indeed visually inspected results from each subject and for each signal separately.

Halle/Saale, January 17th 2010

Aicko Yves Schumann

1. Basic Concepts of Time Series and Stochastic Modeling

Before I address in detail questions concerning fluctuations and oscillations in physiological data and discuss the mutual coupling between multivariate recordings basic concepts of time series analysis and required terminology will be introduced in the following. Among others, this chapter discusses the concepts of *stationarity*, *dependence*, and classical approaches to study oscillations by means of the *Fourier power spectrum* and the *wavelet power spectrum*, as well as tools to investigate interrelations between different signals such as the *cross-correlation function* or *cross-coherence function*.

1.1. Terminology

Random Variables and Stochastic Processes

For a probability space (Ω, Σ, P) and a measurable space (Ω', Σ') a (general) random variable X can be defined as a ($[\Sigma\Sigma']$ -measurable) mapping $X : \Omega \rightarrow \Omega'$ where the sample space Ω contains all elementary events (outcomes of X), the σ -algebra Σ over Ω is a collection of all events (not necessarily elementary events itself but a collection of sets containing elementary events), and P is a probability measure ($P : \Sigma \rightarrow [0, 1]$). Analogously, Σ' is the σ -algebra over Ω'

As an example consider the experiment of throwing a die twice. The sample space Ω then contains 36 elementary events, $\Omega = \{(1, 1), (1, 2), \dots, (6, 6)\}$ and the corresponding σ -algebra Σ is the power set¹ of Ω , $\Sigma = \mathcal{P}(\Omega)$, e. g., containing the event $A =$ “both throws show an odd number” = $\{(1, 1), (1, 3), \dots, (5, 5)\}$ ($A \in \Sigma$ is only one element of many more). Assuming a ‘fair’ die the probability measure is defined by $P(\omega) = 1/36$ where $\omega \in \Omega$ is an elementary event; the full $P(\Sigma)$ is obtained by combining probabilities of corresponding elementary events, e. g., $P(A) = P(\omega_1 = (1, 1)) + P(\omega_2 = (1, 3)) + \dots$. After having defined the probability space $(\Omega, \Sigma = \mathcal{P}(\Omega), P(\Sigma))$, consider the random variable X which describes the “sum of pips”, i. e., the mapping from $\omega \in \Omega$ to the (measurable) real² space $\Omega' = \mathbb{R}$. A suitable σ -algebra Σ' is then the (canonical) Borel σ -algebra of \mathbb{R} which contains all open intervals (a, b) and closed intervals $[a, b]$ of \mathbb{R} with a, b being rational numbers.

In the application such as time series analysis one does in general not describe both spaces (Ω, Σ, P) and (Ω', Σ') in detail, since for discrete probability spaces, i. e., probability spaces with a limited and/or countable number of elements $\omega \in \Omega$, and setting $\Sigma = \mathcal{P}(\Omega)$ it can be shown that the mapping

$$X : \Omega \rightarrow \mathbb{R} \quad (1.1a)$$

is always measurable with a measurability condition

$$\forall x \in \mathbb{R} : \{\omega | X(\omega) \leq x\} \in \Sigma. \quad (1.1b)$$

Equation 1.1b means that for each x there exists an element in Σ which is a set of all elementary events $\omega \in \Omega$ whose mapping $X(\omega)$ is equal or smaller as x . A mapping according to Eqs. (1.1) is referred to as *real random variable*. In order to define a time series I will in the following exclusively consider real random variables.

¹Please avoid confusion of the probability measure P being a mapping of a set to $[0, 1]$ and the power set \mathcal{P} (calligraphic letter P) being a set of subsets.

²The space $\Omega' = \{2, 3, \dots, 12\}$ would be sufficient in this example but one often defines a larger more intuitive and/or better describable space.

An indexed set of random variables $\{X_t\}_{t \in \mathbb{I}}$ where the index set \mathbb{I} is either discrete ($t \in \mathbb{I} = \mathbb{N}$) or continuous ($t \in \mathbb{I} = \mathbb{R}$) is referred to as a *stochastic process*. However, the continuous case is generally difficult to access due to an unlimited number of random variables.

As a simple example for a discrete real random variable consider a 'randomly' beating heart whose beat-to-beat time intervals³ are monitored at 1000Hz (to the split millisecond). Then the probability P of an event "the beat-to-beat interval is smaller than 965ms" is denoted by $P(\{\omega | X(\omega) \leq 965\}) = P(X \leq 965)$ where the notation of the argument is usually simplified (right side), although $P : \Sigma \rightarrow [0, 1]$ and $X(\omega) \in \mathbb{R}$. In general the probability P of an event $X \leq x$ can be expressed by the *cumulative probability density function*

$$F_X(x) = P(X \leq x) = \int_{-\infty}^x p_X(x) dx \quad (1.2)$$

where the *probability density function* $p_X(x)$ satisfies $p_X(x) \geq 0$ and $\int_{\mathbb{R}} p_X(x) dx = 1$.

Dependence

Dependence and independence of N random variables X_j with $j = 1, 2, \dots, N$ is studied by means of the *joint probability distribution function*, i.e., the probability that X_1, X_2, \dots, X_N are jointly less or equal than the real constants x_1, \dots, x_n ,

$$F_{X_1, X_2, \dots, X_N}(x_1, x_2, \dots, x_n) = P(X_1 \leq x_1, X_2 \leq x_2, \dots, X_N \leq x_N). \quad (1.3)$$

Such a set of N random variables is called *independent* when the joint probability in Eq. (1.3) splits into the product of the individual cumulative distribution functions' marginals

$$F_{X_1, X_2, \dots, X_N}(x_1, x_2, \dots, x_N) = \prod_{j=1}^N P(X_j \leq x_j) \quad (1.4)$$

and it is called *dependent* otherwise. Note that independence also implies the *conditional probability* $P(X_j \leq x_j | X_i \leq x_i) = P(X_j \leq x_j)$ for each pair of random variables $X_i, X_j : i \neq j$.

For instance, $P(X_j \leq x_j) = (2\pi)^{-1/2} \int_{-\infty}^{x_j} \exp\{-z^2/2\} dz$ for standard normal distributed random variables. If they exist, the one-dimensional *distribution functions* $F_{X_j}(x) = P(X_j \leq x)$ and their derivatives, the *density functions* $p_{X_j}(x) = \partial F_{X_j}(x) / \partial x$ [Eq. (1.2)], yield the *mean value functions* $\mu_{X_j} = E[X_j] = \langle X_j \rangle = \int_{-\infty}^{\infty} x p_{X_j}(x) dx$. In general the n th moment is defined by

$$\mu_{X_j}^{(n)} = E[X_j^n] = \langle X_j^n \rangle = \int_{-\infty}^{\infty} x^n p_{X_j}(x) dx \quad , \quad n = 1, 2, 3, \dots \quad (1.5)$$

where $n = 1$ retrieves the mean value function for which the index n will be dropped.

Measuring Dependence

The most common time-domain approach for measuring linear interdependence between two random variables X_i and X_j ($1 \leq i, j \leq N$) is the *covariance function*⁴

$$\text{Cov}(X_i, X_j) = E[(X_i - E[X_i])(X_j - E[X_j])] \quad (1.6a)$$

or, more importantly, its normalized version, the *correlation function*

$$\text{Cor}(X_i, X_j) = \frac{\text{Cov}(X_i, X_j)}{\sqrt{\text{Var}(X_i)\text{Var}(X_j)}} \quad (1.6b)$$

³The exact definition what a 'beat' and a 'beat-to-beat' interval mean will be discussed in Sect. 2.2.

⁴Note that in this representation I consider the general case where dependence of two different random variables is characterized in an abstract way. The indexes do not refer to time but index the set of random variables. For the moment the expectation value of a random variable is, except from its definition by the mean value function, not further specified, e. g., it could refer to a time average when X_j describes measurements of some quantity in time or to a spacial average when X_j describes a sequence of values associated with a position. The well known 'time-lag' covariance and correlation requires stationarity and is discussed later.

where $E[X_j]$ denotes the expectation value (first moment, $n = 1$) of the j th random variable according to Eq. (1.5), and $\text{Var}(X_j) = \text{Cov}(X_j, X_j)$ denotes the *variance* (*auto-covariance*). Note that due to the normalization in Eq. (1.6b) $-1 \leq \text{Cor}(X_i, X_j) \leq 1$. If the linear dependence between all combinations of the N random variables is studied one constructs a *covariance matrix*⁵ \mathbf{Cov} (or, alternatively a *correlation matrix* \mathbf{Cor}) where the matrix element $\text{Cov}_{i,j} = \text{Cov}(X_i, X_j)$ (or $\text{Cor}_{i,j} = \text{Cor}(X_i, X_j)$). When $\text{Cor}(X_i, X_j) = 1$ both variables are perfectly correlated and they are anti-correlated for $\text{Cor}(X_i, X_j) = -1$. In these cases X_i can be expressed by a linear function of X_j and vice versa. While the absolute value of the correlation function is a measure of the strength of the linear interrelation its sign indicates the direction of dependence in the sense that “+” implies values of the same signs in magnitude coincide with each other, i. e., small values (or large values) in X_i correspond to small values (or large values) in X_j , and a “-” sign indicates opposite signs in both variables’ magnitude. However, it is not possible to determine whether variable X_i is influencing X_j , or vice versa. In the case of uncorrelated random variables $\text{Cor}(X_i, X_j) = 0$. Since the correlation function only quantifies the linear part of a possibly complex dependence structure, a vanishing correlation not necessarily implies the absence of dependence where, on the other hand, a correlation different from zero indicates dependence.

Time Series

An ordered sequence $\{x_k\}_{k=1,\dots,N}$ of measurements obtained from an observable X at successive times $t = t_k$ is called a time series. The time intervals (sampling) between subsequent measurements are not required to be of equal size. Equally sampled time series ($\forall k : t_{k+1} - t_k = \Delta t$) and unequally sampled time series ($\exists j, k : t_{j+1} - t_j \neq t_{k+1} - t_k$) are distinguished.

There are two alternative conceptions of what time series can be thought of. One might interpret the instances of a time series $\{x_k\}_{k=1,\dots,N}$ (i) as a set of N realizations of a single random variable X at distinct times t_k , or (ii) as a set momentary realizations (at a fixed time t^*) of a set of N different random variables X_k .

In this thesis I will consider a time series according to the first concept, however, allow a physiological complex system such as the cardiorespiratory system which basically consists of the heart, the blood vessels, and the lungs to be described by different random variables X_j and its realizations $\{x_{j,k}\}$, e.g., time series of beat-to-beat intervals⁶ or oronasal airflow. The index j which here indicates different random variables (further denoted as signals) will be dropped in the following since I will generally focus on either single signals X or the mutual coupling between two signals X and Y .

The primary objectives of time series analysis are: (i) understanding underlying mechanisms that generated the single signal, (ii) the exploration of control mechanisms and interactions between different components each captured by a time series, or (iii) obtaining information about their (possibly combined) dynamics. The ultimate goal is to understand the dynamics of the much larger complex system from which the recordings were obtained, and finally, to develop mathematical models that *hopefully* describe both the sampled data and the complete system.

Stationarity and Nonstationarity

Stationarity of a time series $\{x_k\}_{k=1,\dots,N}$ is a special type of regularity over time. *Strict stationarity* is fulfilled when the joint probability distribution corresponding to Eq. (1.3) is identical to the one of any admissible τ -shifted set ($\tau \in \mathbb{Z}$)

$$P\left(\underbrace{X_n \leq x_n, \dots, X_{n+m} < x_{n+m}}_{\substack{m\text{-element subset } \{x_n, \dots, x_{n+m}\} \text{ of} \\ \text{subsequent elements of the time series } \{x_k\} \\ 1 \leq n \leq N-m}} \right) \equiv P\left(\underbrace{X_{n+\tau} \leq x_n, \dots, X_{n+m+\tau} \leq x_{n+m}}_{\substack{\tau\text{-shifted } m\text{-element subset from } \{x_k\} \\ \text{compared with values from the unshifted subset} \\ 1-n \leq \tau \leq N-n-m}} \right) \quad (1.7)$$

for any valid subset of $\{x_k\}$ and $m \in \mathbb{N}$. Note that I switched to the concept of a time series being the realizations in time of a *single* random variable X ; the subscripts now index the realizations

⁵Often simply denoted by the symbol Σ .

⁶The time interval between two successive heart beats, see Sect. 2.2.

of X in time. This concept will be used from now on. In real world applications the definition in Eq. (1.7) is generally too strong. One considers *weak stationarity* when the first two moments, i.e., the mean value [Eq. (1.5) with $n = 1$] and the variance [Eq. (1.5) with $n = 2$], are constant in time. Similarly, one defines *n th-order stationarity* when the first n moments are constant [Eq. (1.5)].

Covariance and Correlation of Weakly Stationary Time Series

For a weakly stationary time series the first moment and the second moment are constant by definition and can be estimated by

$$\mu_x = \langle x \rangle = \frac{1}{N} \sum_{k=1}^N x_k \quad \text{and} \quad \sigma_x^2 = \langle (x - \mu_x)^2 \rangle = \frac{1}{N} \sum_{k=1}^N x_k^2 - \left(\frac{1}{N} \sum_{k=1}^N x_k \right)^2 \quad (1.8)$$

Then the *cross-covariance function* and the *cross-correlation function* measuring the linear dependence of two time series $\{x_k\}$ and $\{y_k\}$ ($k = 1, \dots, N$) only dependent on the time lag $s = k - j$ between two instances x_k and y_j . Rewriting Eqs. (1.6) according to the concept of time series and using the properties in Eq. (1.8) one obtains for the cross-covariance function

$$\begin{aligned} \text{Cov}_{xy}(s) &= \langle (x_k - \mu_x)(y_{k+s} - \mu_y) \rangle \\ &= \begin{cases} \frac{1}{N} \sum_{k=1}^{N-s} (x_k - \mu_x)(y_{k+s} - \mu_y) & : s = 0, 1, 2, \dots \\ \frac{1}{N} \sum_{k=1-s}^N (x_k - \mu_x)(y_{k+s} - \mu_y) & : s = -1, -2, \dots \end{cases} \end{aligned} \quad (1.9a)$$

and for the cross-correlation function

$$\begin{aligned} \text{Cor}_{xy}(s) &= \frac{\langle (x_k - \mu_x)(y_{k+s} - \mu_y) \rangle}{\sigma_x \sigma_y} \\ &= \begin{cases} \frac{1}{\sigma_x \sigma_y N} \sum_{k=1}^{N-s} (x_k - \mu_x)(y_{k+s} - \mu_y) & : s = 0, 1, 2, \dots \\ \frac{1}{\sigma_x \sigma_y N} \sum_{k=1-s}^N (x_k - \mu_x)(y_{k+s} - \mu_y) & : s = -1, -2, \dots \end{cases} \end{aligned} \quad (1.9b)$$

Note that in the estimators in Eqs. (1.9) are biased due to the normalization by N rather than by the 'correct' number of summands, $N - s$. This substitution has the advantage that the cross-covariance matrix and the cross-correlation matrix are non-negative definite [BROCKWELL AND DAVIS 2003]. It further facilitates the use of fast Fourier transform to quickly calculate both covariance and correlation⁷. I will come back to the issue of normalization in cross-correlation function in Sect. 4.2.4.

When the signal X is identical to the signal Y , i. e. $\{x_k\} = \{y_k\}$, Eqs. (1.9) yield the *auto-covariance function* ($\text{Cov}_{xx} = \text{Cov}$, subscripts are dropped where applicable) and the *auto-correlation function* (*ACF*). I will denote the latter in the following by $C(s)$ for simplification,

$$\text{Cov}(s) = \langle (x_k - \mu_x)(x_{k+s} - \mu_x) \rangle = \frac{1}{N} \sum_{k=1}^{N-s} (x_k - \mu_x)(x_{k+s} - \mu_x) \quad (1.10a)$$

$$C(s) = \frac{\langle (x_k - \mu_x)(x_{k+s} - \mu_x) \rangle}{\sigma_x \sigma_x} = \frac{1}{\sigma_x^2 N} \sum_{k=1}^{N-s} (x_k - \mu_x)(x_{k+s} - \mu_x) \quad (1.10b)$$

⁷Equations (1.9) can be rewritten as a convolution and derived as the inverse Fourier transform of the product of the individual Fourier transforms obtained from both time series according to the convolution theorem.

for $s \geq 0$ and expressions for $s < 0$ are defined analogously to Eqs. (1.9). The auto-correlation function measures the linear dependence between two points of the same time series at different times. For an uncorrelated time series the auto-covariance function, and thus, the auto-correlation function is zero for all non-zero time lags s . All other properties discussed below Eq. (1.6b) remain valid: $-1 \leq C(s) \leq 1$; the absolute value of $C(s)$ measures the strength of linear dependence; a negative (positive) sign indicates large values at positions $k + s$ correspond to small (large) values at positions k and vice versa. In the weak stationary case Eqs. (1.9) exhibit *time reversal symmetry*, i. e.,

$$\text{Cov}_{xy}(s) = \text{Cov}_{xy}(-s) \quad \text{and} \quad \text{Cor}_{xy}(s) = \text{Cor}_{xy}(-s). \quad (1.11)$$

Such time series are sometimes referred to as *jointly stationary*. Correspondingly, time series not fulfilling above properties are generally called *nonstationary*. Among other reasons, nonstationarities are typically introduced by changes in the local mean, trends (linear or higher order polynomials) or periodicities.

Cross Spectrum, Power Spectrum, and Coherence

Spectral analysis originates from communication engineering where most signals obey oscillations of many different frequencies around certain stable states. These oscillatory components might be present for an intermediate time interval or during the complete observational period. In order to separate and study such superimposed oscillations with respect to their frequency the signal is expanded in periodic functions (Fourier expansion). The discrete *spectral amplitude* is the Fourier transform⁸ of the signal $\{x_k\}_{k=1,\dots,N}$,

$$\mathcal{F}(\{x_k\}) = \hat{x}_f = \frac{1}{N} \sum_{k=1}^N x_k e^{-2\pi i k f} \quad , \quad f \in (-1/2, 1/2]. \quad (1.12)$$

The normalization by N ensures $\hat{x}_0 = \mu_x$. Note that $f = m/(N\Delta t)$ where Δt denotes the sampling interval of the signal and $m = -N/2 + 1, \dots, -2, -1, 0, 1, 2, \dots, N/2$ is a typical set of grid points in a fast Fourier transform algorithm for an even N . Without loss in generality I set $\Delta t = 1$ in the following for simplification. On the other hand, the *cross spectrum* is defined as the Fourier transform of the covariance function in Eqs. (1.9a)

$$P_{xy}(f) = \frac{1}{N} \sum_{s=1-N}^{N-1} \text{Cov}_{xy}(s) e^{-2\pi i s f} \quad , \quad f \in (-1/2, 1/2] \quad (1.13)$$

Note that due the definition in Eq. (1.9a), the cross spectrum in Eq. (1.13) is only valid for weakly stationary signals. When setting $y = x$, the covariance reduces to the auto covariance and the conventional *power spectrum* of a (single) time series is retrieved,

$$P(f) = P_{xx}(f) = \frac{1}{N} \sum_{s=1-N}^{N-1} \text{Cov}_{xx}(s) e^{-2\pi i s f} \quad , \quad f \in (-1/2, 1/2] \quad (1.14)$$

In practice the power spectrum $P(f)$ can be derived directly from Eq. (1.12)

$$P(f) = |\hat{x}_f|^2 = \hat{x}_f \hat{x}_f^* = \frac{1}{N^2} \sum_{k,l=1}^N x_k x_l e^{-2\pi i k f} e^{+2\pi i l f} \quad , \quad (1.15)$$

where $*$ denotes the complex conjugate. However, there is no consensus on the normalization of the power spectrum. I use N^2 here since it descends from Eq. (1.12). Note that the power spectrum in Eq. (1.15) is symmetric for real valued time series, and hence, I will only show frequencies in the range $f \in [0, 1/2]$ throughout this thesis. The equivalence of Eqs. (1.14) and (1.15) is formulated

⁸Throughout this thesis denoted by \mathcal{F} .

in the discrete Wiener-Khinchin theorem [see Appendix A and HONERKAMP 1994; RANGARAJAN AND DING 2000].

Since the cross spectrum is in general a complex function one can obtain an amplitude function and a phase function:

$$A_{P_{xy}}(f) = [\Re(P_{xy}(f))^2 + \Im(P_{xy}(f))^2]^{1/2}, \quad \Phi_{xy}(f) = \arctan\left(\frac{\Im(P_{xy}(f))}{\Re(P_{xy}(f))}\right). \quad (1.16)$$

Analogously to the definition of the correlation function as the quotient of the covariance and the product of the roots of individual auto covariances (variances) one can then obtain a *coherence spectrum*⁹ as the quotient of the cross spectrum and the product of the individual auto-cross spectra according to

$$\text{Coh}_{xy}(f) = \frac{A_{P_{xy}}(f)}{\sqrt{P_{xx}(f)}\sqrt{P_{yy}(f)}}. \quad (1.17)$$

While cross-correlation function studies linear dependences between two different signals $X = \{x_k\}$ and $Y = \{y_k\}$ in the time domain there might be a similar type of linear interrelation in the frequency domain. E. g., one might want to study *coherence*, i. e., correlation indexed by frequency. To elucidate the meaning of such interrelation consider two signals that can be modeled as the superposition of a high frequency component (HF) and a low frequency component (LF), $x_k = x_k^{HF} + x_k^{LF}$ and $y_k = y_k^{HF} + y_k^{LF}$ with $k = 1, \dots, N$. The coherence spectrum in Eq. (1.17) then measures whether LF components vary simultaneously (large LF coherence) or HF components vary simultaneously (large HF coherence). In the full coherence spectrum such inferences can be drawn for any frequency component. However, I will in the following not further employ Eq. (1.17). An alternative approach for studying simultaneous variations of oscillations at different frequency will be presented in Sect. 5.3.

White Noise and Random Walks

A sequence of random numbers is generally denoted as noise because of the absence of determinism. Time series that are constructed of independently distributed random numbers are termed white noises since the corresponding power spectrum $P(f)$ [Eq. (1.15)] is flat, i.e., all frequencies are statistically equally distributed. For convenience one chooses uniformly or normally distributed random numbers, however, the term white noise is used for all sequences obeying a flat $P(f)$.

When a noise time series $\{\varepsilon_k\}_{k=1,\dots,N}$ is integrated, the time series $Y_j = \sum_{k=1}^j \varepsilon_k$ describes a one-dimensional *random walk*. Y_j is the position of the random walker after j steps where ε_j is the displacement. The concept of many fluctuation analysis methods (presented in Chapt. 3) are based on the concept of random walks.

1.2. Short- and Long-Range Dependence

Long-range dependence is associated with the term *persistence*, i.e., the tendency of a random variable to exhibit similar values in the next time steps. In a persistent dataset large values are more likely followed by large values and small values are more likely followed by small values. For instance, the timing of the heart exhibits long-range persistence during rapid-eye-movement (REM) sleep as we will see in Chapt. 3. Sleep and sleep stages are introduced in Sect. 2.3.

Since long-range persistence is strongly linked with correlation and scaling behaviour, or 'memory' the terms *long-range persistence*, *long-range correlation*, *long-range scaling*, or *long-range memory* are often used synonymously and *long-range* is usually equivalent with *long-term*.

There are three equivalent definitions for distinguishing short-range correlations from long-range correlations.

⁹The similarity to cross correlation is seen when one recalls that spectra are squared properties.

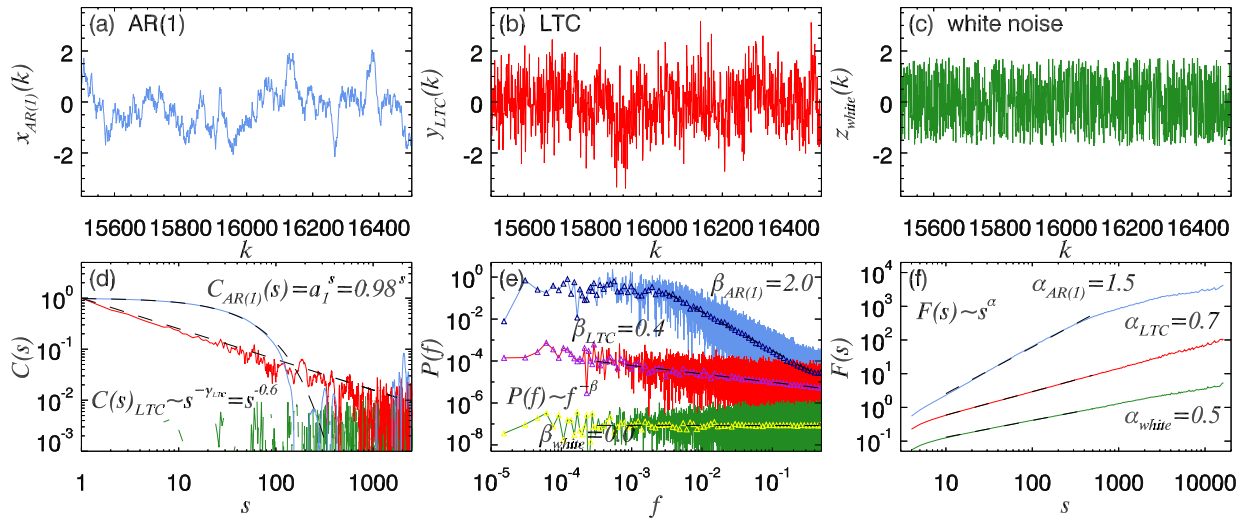


Figure 1.1.: Concurrent approaches to short-range and long-range dependence for three example time series [$N = 65536$]; fragments are shown for (a) a short-term correlated AR(1) process [$a_0 = 0, a_1 = 0.98$; light blue], (b) a long-term correlated signal generated by Fourier filtering [$\alpha = 0.7$; red], and (c) an uncorrelated Gaussian noise process [green]. (d-f) Corresponding correlation functions $C(s)$ [(d)], power spectra $P(f)$ [(e)], and fluctuation functions $F(s)$ obtained by DFA2 [(f); see Sect. 3.1.3 for DFA methodology] in the same color coding. Black dashed curves represent intermediate behavior [fit: $10 \leq s \leq 500$] used to calculate annotated scaling exponents. In (d) the black dashed curve corresponding to the AR(1) realization describes the theoretical $C(s)$; for white noise the theoretical $C(s)$ vanishes $\forall s \neq 0$. Power spectra $P(f)$ in (e) have been logarithmically binned [colored triangles] before fitting. $F(s)$ for the AR(1) signal [light blue in (f)] exhibits random walk long-term behavior [$\alpha_{AR(1)} = 1.5$] for short scales. A correct value of $\alpha_{AR(1)} = 0.5$ is found on larger scales.

1.2.1. Linear Time Space Approach

When the *auto-correlation function*, see Eq. (1.10b), of the time series decays exponentially and is thus integrable, a characteristic time scale exists

$$s_x = \int_0^{\infty} C(s) ds \quad \text{or} \quad s_x = \sum_{s=0}^{\infty} C(s) \quad (1.18)$$

and the time series exhibits *short-term correlations (STC)*. On the other hand, it exhibits *long-term correlations (LTC)* if Eq. (1.18) is diverging and the decay in $C(s)$ follows a power law with a correlation exponent γ describing the correlation strength for large scales $s \gg 1$.

$$C_{LTC}(s) \sim s^{-\gamma} \quad \text{where} \quad 0 < \gamma < 1 \quad (1.19)$$

Figure 1.1(a) illustrates the correlation function $C(s)$ for three types of signals. A *short-term correlated auto-regressive process (AR(1))* following $X_t = 0.98X_{t-1} + \varepsilon_t$ [light blue in Fig. 1.1], where the *stochastic component* or *innovation term* ε_t is drawn from a white-noise process, exhibits a sharply decaying $C(s)$ for scales $s > 50$ [see also Sect. 1.5.1]. Note, the theoretical behavior $C(s) = 0.98^s$ can be derived by modeling the AR(1) process in terms of a *moving average process (MA)* [see Appendix B] yielding a characteristic decay time $\tau = -1/\ln(0.98) \approx 50$ with $C(\tau) = 1/e$. For long-term correlated signals [modeled by Fourier filtering according to Sect. 1.5.2 with $\gamma = 0.6$; red in Fig. 1.1] $C(s)$ decays according to a power law expressed by a linear function in the double-logarithmic plot. For pure white noise [green in Fig. 1.1] the theoretical correlation function $C(s)$ vanishes for all $s \neq 0$. However, in practice values of $C(s) = 0$ are not achieved due to edge effects and a limited series length resulting in a lack of statistics. The small values fluctuating around zero for large scales (in the asymptotic regime) are a serious problem for obtaining reliable results based on $C(s)$ or s_x .

1.2.2. Spectral Approach

Due to the equivalence of Eq. (1.14) and (1.15) as established by the Wiener-Khinchin theorem, long-term correlations can alternatively be defined by a power law decay with a *spectral exponent* β in the power spectrum of a signal,

$$P_{xx}(f) = P(f) \sim f^{-\beta}. \quad (1.20)$$

The auto-correlation function $C(s)$ for a weakly stationary time series is just a normalized version of the auto-covariance function. When considering only the positive half of the symmetric power spectrum it follows for the scaling exponent in the power spectrum [RANGARAJAN AND DING 2000]

$$P(f) \sim \int_0^\infty C(s)e^{-2\pi ifs} ds \sim \int_0^\infty s^{-\gamma} e^{-2\pi ifs} ds = \frac{-2 \sin(\pi\gamma/2)\Gamma(-\gamma+1)}{(2\pi f)^{-\gamma+1}} \sim f^{-(1-\gamma)} \quad (1.21)$$

where $\Gamma(\xi) = \int_0^\infty x^{\xi-1} e^{-x} dx$ is the Gamma function which converges for $\xi > 0$, i. e., for $\gamma < 1$. The latter is fulfilled since $0 < \gamma < 1$ in the case of long-range correlations. Comparing Eqs. (1.20) and (1.21) yields [RANGARAJAN AND DING 2000]

$$\beta = 1 - \gamma. \quad (1.22)$$

Note that Eq. (1.22) is only valid for $0 < \beta < 1$ which is violated in the case of nonstationary data where $\beta > 1$ or in the case of anti correlations where $\beta < 0$. The power spectra corresponding to the same examples as described in Sect. 1.2.1 are depicted in Fig. 1.1(e).

The main advantage of the spectral approach compared with studying the correlation function is avoiding values close to zero in the asymptotic area and the computationally fast Fourier transform algorithm. Nevertheless, as can be seen in Fig. 1.1(e) fluctuations in the power spectrum do also severely increase for large frequencies (Nyquist frequency = $1/2 \cdot f_{\text{sampling}}$). This hampers a correct determination of β , and an additional *logarithmic binning* has to take place. Logarithmic binning means typical averages of $\log(P(f))$ are taken within windows of frequencies systematically increased by a *binfactor* yielding equally distributed data points in the double-logarithmic plot.

1.2.3. Nonlinear Approach – Fluctuations

In this approach one focuses on stochastic fluctuations in the time series and derives a fluctuation function $F(s)$ employing one of various methods designed to study fluctuations in time series, e. g., *fluctuation analysis (FA)*, *detrended fluctuation analysis (DFA)* or *centered moving average analysis (CMA)* to be discussed in detail in Chapt. 3. For a simple scenario consider a cumulated random walk $Y_j = \sum_{k=1}^j x_k$. The root of its mean square displacement in non-overlapping windows $\nu = 0, \dots, [N/s] - 1$ of width s then represents the FA-fluctuation function $F_{\text{FA}}(s)$ that scales according to a power law in the presence of long-term correlations, see Sect. 3.1.2,

$$F_{\text{FA}}(s) = \sqrt{\langle (Y_{(\nu+1)s} - Y_{\nu s})^2 \rangle} \sim s^{\alpha_{\text{FA}}}. \quad (1.23)$$

Note that the square brackets in $[N/s]$ denote the integer division, $[N/s] = \text{int}(N/s)$. I will employ this notation throughout my thesis. However, FA is not capable to deal with nonstationarities (trends) in the signal which are commonly present in time series recorded from complex systems, e. g., in heartbeat or in respiration. Other methods as DFA [Sect. 3.1.3] and CMA [Sect. 3.1.4] were developed to handle data with nonstationarities such as trends. The fluctuation functions (here of DFA2, see Sect. 3.1.3) corresponding to the same examples as described in Sect. 1.2.1 are shown in Fig. 1.1(f).

While I have already shown the relationship between the spectral exponent β and the correlation exponent γ in the derivation of Eq. (1.22), the fluctuation exponent α can also be related to the correlation exponent γ . One obtains [see also Sect. 3.1.2]

$$1 - \beta \stackrel{(1.22)}{=} \gamma \stackrel{(3.15)}{=} 2 - 2\alpha. \quad (1.24)$$

1.3. Real Time-Frequency Decomposition – Wavelet Analysis

Although, Fourier transform (FT) and the FT based power spectrum are well established linear tools to study periodicities in time series they have the disadvantage that time information associated with identified oscillations is by definition inaccessible. For instance consider heartbeat that is monitored in a sportsman during training time where his physiological state changes between rest and exercise. Clearly, during resting times his heart will beat slower compared with times where he is for example fast riding a bike. A spectrum analysis of the complete signal without separating times that correspond to rest and exercise will clearly identify both fast (exercise) and slow (rest) oscillations but from the spectrum alone an association of frequency components with actual time is not possible. The reason is the well defined frequency location of the Fourier basis (sine and/or cosine functions have a fixed frequency) but a complete delocalization in sample (time) space. A short-time Fourier transform in a sliding window, mathematically being the Fourier transform of the convolution of the signal one wants to study and a window function w of compact support¹⁰, only partially overcomes this problem. The *windowed Fourier transform (WFT)* follows for the continuous and the discrete case, respectively,

$$\text{WFT} \left(x(t) \right) (\omega, \tau) = \mathcal{F} \left(x(t) * w(t) \right) (\omega, \tau) = \int_{\mathbb{R}} x(t) w(t - \tau) e^{-i\omega t} dt \quad (1.25a)$$

$$\text{WFT} \left(\{x_k\} \right) (\omega, k') = \mathcal{F} \left(\{x_k\} * \{w_k\} \right) (\omega, k') = \frac{1}{N} \sum_{k=1}^N x_k w_{k-k'} e^{-i\omega k} \quad (1.25b)$$

where $*$ denotes the convolution, \mathcal{F} indicates the Fourier transform, and w is the window function that is translated over the signal. If the window function is a Gaussian the windowed Fourier transform is often referred to as Gabor transform [GABOR 1946]. Note that the windowed Fourier transform is for example used to support medical technicians of sleep laboratories in scoring sleep stages based on brain wave recordings [see Sect. 2.3]. However, the windows w in the WFT are of a fixed width; let this width be h . If the part of the signal that is currently covered by the window w only contained a few periods of a fast oscillatory component with $\omega \gg 1/h$, its location in time could not successfully be retrieved by WFT. On the other hand, very slow oscillations with $\omega \ll 1/h$ cannot be captured because the window is much smaller than a single period.

The solution of this problem are frequency-adaptive window functions which are today known by the name *wavelets* but date back to the year 1910 and Alfred Haar who principally invented the most simple 'wavelet', the Haar wavelet [HAAR 1910]. However, the term wavelet is a coinage blended from the English word 'wave' and the French word 'ondelette' that was established 75 years after Haar by Pierre Goupillaud, Alex Grossman, and Jean Morlet [GOUPILLAUD *et al.* 1984]. For the wavelet transform Eqs. (1.25) are slightly changed:

$$\text{WT}_{\Psi} \left(x(t) \right) (s, \tau) = \frac{1}{\sqrt{s}} \int_{\mathbb{R}} x(t) \overline{\Psi} \left(\frac{t - \tau}{s} \right) dt \quad (1.26a)$$

$$\text{WT}_{\Psi} \left(\{x_k\} \right) (s, k') = \frac{1}{\sqrt{s}} \sum_{k=1}^N x_k \overline{\Psi} \left(\frac{k - k'}{s} \right) \quad (1.26b)$$

where $\overline{\Psi}(t)$ denotes the complex conjugate of the mother-wavelet function $\Psi(t)$. Note that there is no consensus on the normalization of the wavelet transform. I here use $1/\sqrt{s}$ as a normalization instead of $1/s$ because this ensures unit energy, i. e., the L^2 norm of the wavelet is independent of the parameters s and τ satisfying $(\int_{\mathbb{C}} |\Psi((t - \tau)/s)|^2 dt)^{1/2} = (\int_{\mathbb{C}} |\Psi(t)|^2 dt)^{1/2}$. Sometimes one finds an additional normalization term, $1/\sqrt{c_{\Psi}}$, which descends from the admissibility condition $c_{\Psi} = 2\pi \int_{\mathbb{R}} |\mathcal{F}(\Psi(t))(\omega)|/|\omega| d\omega < \infty$, see [GOUPILLAUD *et al.* 1984; FARGE 1992]. Here I set $c_{\Psi} = 1$. Note that the wavelet $\Psi(t)$ is required to be absolutely integrable ($\int_{\mathbb{R}} \Psi(t) dt < \infty$) and quadrate integrable ($\int_{\mathbb{R}} \Psi^2(t) dt < \infty$); the admissibility condition further implies $\mathcal{F}(\Psi(t))(0) = 0$,

¹⁰Alternatively, w must be a fast decaying function (Schwartz function) as for example a Gaussian.

i. e., a zero mean of $\Psi(t)$. Among the most popular mother wavelets are the Haar wavelet [Eq. (1.27a)], derivatives of a Gaussian (DOG) [Eq. (1.27b)], and the Morlet wavelet [Eq. (1.27c)]:

$$\Psi_{\text{Haar}}(t) = \begin{cases} -\frac{1}{2} & : -1 \leq t < 0 \\ \frac{1}{2} & : 0 \leq t < 1 \\ 0 & : \text{otherwise} \end{cases} \quad (1.27a)$$

$$\Psi_{\text{DOG}n}(t) = \frac{(-1)^{n+1}}{\Gamma(m + \frac{1}{2})} \frac{d^m}{dt^m} e^{-t^2/2} \quad (1.27b)$$

$$\Psi_{\text{Morlet}}(t) = \pi^{-1/4} s^{-1/2} e^{i\omega_0 t} e^{-t^2/2} \quad (1.27c)$$

where $\Gamma(z) = \int_0^\infty t^{z-1} e^{-t} dt$ denotes the Gamma function. Although the parameter ω_0 in Eq. (1.27c) is a frequency that in principle can take any real value, it is generally defined as an integer¹¹ ($\omega_0 \geq 3$) and considered to be the 'order' of the Morlet wavelet due to its similar role in adjusting the wavelet's shape compared with the order parameter n in $\Psi_{\text{DOG}n}$ [Eq. (1.27b)]. Note that the Haar wavelet is rather suited to detect steps in the signal than oscillations. Hence, I will employ in Chapt. 4 explicitly only the Gaussian wavelet and the Morlet wavelet.

Since the wavelet function is complex in general, so is the wavelet transform in Eqs. (1.26). From its real and imaginary parts one can define a wavelet amplitude, a wavelet phase, and a wavelet power:

$$|WT(x)| = \sqrt{\Re^2\{WT_\Psi(x)\} + \Im^2\{WT_\Psi(x)\}} \quad , \quad (1.28)$$

$$\varphi_{WT_\Psi}(x) = \arctan \frac{\Im\{WT_\Psi(x)\}}{\Re\{WT_\Psi(x)\}} \quad , \quad \text{and} \quad (1.29)$$

$$|WT_\Psi(x)|^2 = \Re^2\{WT_\Psi(x)\} + \Im^2\{WT_\Psi(x)\} \quad . \quad (1.30)$$

1.4. Fractality

Heuristics - A Geometrical Approach

“Clouds are not spheres, mountains are not cones, coastlines are not circles, and bark is not smooth, nor does lightning travel in a straight line.”

“I coined fractal from the Latin adjective fractus. The corresponding Latin verb frangere means 'to break' to create irregular fragments. It is therefore sensible - and how appropriate for our need! - that, in addition to 'fragmented' (as in fraction or refraction), fractus should also mean 'irregular', both meanings being preserved in fragment.”

BENOÎT B. MANDELBROT [MANDELBROT 1975]

The approach to studying fluctuations which will be an integral part of this thesis in Chapt. 3 is strongly linked with the term fractality. What are fractals and what is fractality? In mathematics fractals are geometric objects that lack a certain characteristic length scale. Their associated scale-invariant 'complicated' structures are characterized by a non-integer (at least in most cases) fractal dimension larger than the topological dimension. While entities which we today refer to as fractals are already as old as the *“Tile Patterns formed by Pentagons”* an artwork by Albrecht Dürer (1471–1528) [DÜRER 1525, Appendix C] or Gottfried Wilhelm Leibniz (1646–1716) who studied *recursive self-similarity*, it aroused large interest during the last century in the context of

¹¹The restriction $\omega_0 \geq 3$ is today implemented in most software tools such as ITT IDL or Matlab and originates from a simplification that took place to obtain Eq. (1.27c) from the mathematically correct Morlet-wavelet function [GOUPIILLAUD *et al.* 1984, and discussion on parameter b therein]. In the latter an additional exponential term can be neglected for a 'sufficiently large' ω_0 . In this thesis I will set $\omega_0 = 6$ which is more than ample. Because of this simplification Eq. (1.27c) is sometimes referred to as *abbreviated Morlet wavelet*.

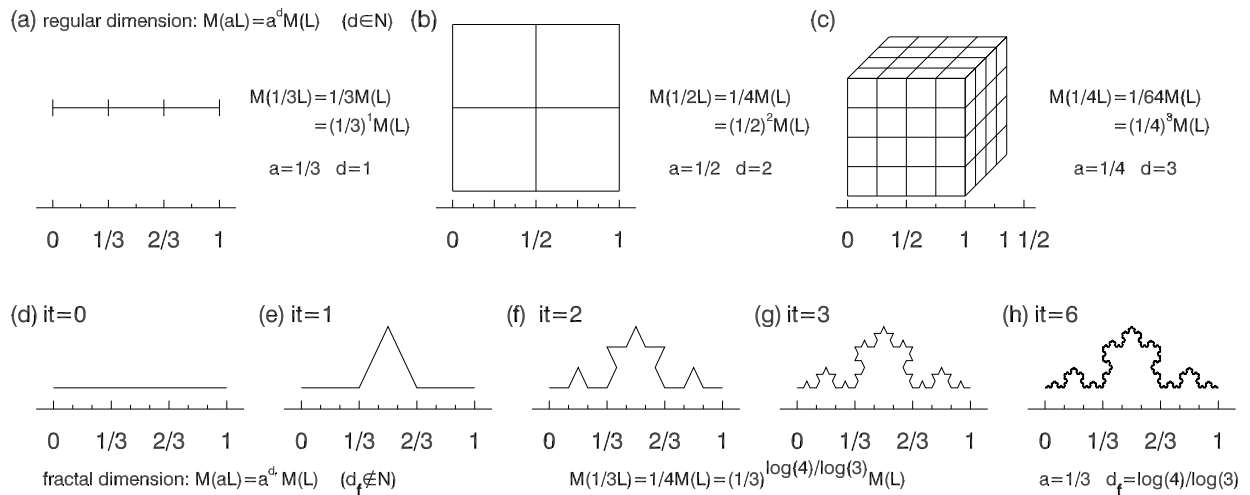


Figure 1.2.: Illustration of systems exhibiting regular dimensionality: (a) a linear wire, (b) a thin plate, (c) a cube; and fractal dimensionality: (d-h) different iterations [it=0,1,2,3,4] of the Koch curve. Homogeneous mass distribution is assumed everywhere.

continuous and non-differential functions in mathematics. The term *fractal* is strongly linked to properties like *self-affine*, *self-similar*, and *scale-invariant* which will be explained shortly. In the sixties Mandelbrot started investigation of self-similarity and published the famous paper *How Long Is the Coast of Britain? Statistical Self-Similarity and Fractional Dimension* [MANDELBROT 1967]. Since then intriguing studies found fractal structures in many other natural systems as clouds, lightning strikes, plant leaves, particle deposition during growth processes (diffusion-limited aggregation (DLA)), fracture cracks and many more [BUNDE AND HAVLIN 1996]. But what is a non-integer dimension? Regular dimensions can easily be obtained for Euklidian objects such as a wire of length L , a thin plate, or a solid cubicle by assuming homogeneous density distribution and considering how the mass $M(L)$ changes with system size L . This is illustrated in Figs. 1.2(a-c). Clearly, one finds for an arbitrary rescaling $L' = aL$, $a \in \mathbb{R}$ that $M(L') = M(aL) = a^d M(L)$ where L is the (length) scale, M the mass, and d the dimension of the system. Non-fractal objects always yield an integer dimension d . Now consider the Koch curve [VON KOCH 1904] where in each iteration step the center third of the previous scale is substituted by an equilateral triangle, see Figs. 1.2(d-h). A rescaling by $a = 1/3$ leads to a reduction of mass by a factor of $1/4$. Thus, the above definition $M(1/3L) = (1/3)^d M(L) \stackrel{!}{=} 1/4 M(L)$ can only be satisfied by a non-integer dimension $d = d_f = \log 4 / \log 3$ where d_f denotes the *fractal dimension*. Systems exhibiting a non-integer dimension d_f are denoted as fractal systems, where the term *fractal* was coined by Mandelbrot [MANDELBROT 1975]. However, there are fractals that are characterized by an integer fractal dimension, i. e., a non-integer fractal dimension is sufficient but not necessary for a fractal. Among the fractals with an integer fractal dimension are the Sierpiński tetrahedron, the Julia set, or a random walk in higher dimensions. Fractality is further linked to the phenomenon of *self-similarity*, i.e., a part of a fractal object is exactly or statistically similar to the whole object. Exact similarity is equal to *scale-invariance*, i.e., when applying a certain scale factor to the system the shape is not changing. The Koch curve is scale-invariant for a scaling $s = 1/a = 3$, i.e., magnification by a factor 3 does not change the appearance of the Koch curve. In self-similar multi-dimensional objects the same scaling factor has to be applied to each dimension in order to achieve similarity (isotropic transformation). When different scaling factors (anisotropic transformation) are required, the system is called *self-affine*, thus, being a more generalized type of similarity. After this rather phenomenological approach I will put this concept into a more mathematical framework and motivate how it can be used to study time series and fluctuations, see also Chapt. 3.

Scaling Laws

Scale-invariance (here in general self-affinity) of a function $f(x)$ can be described in a mathematical fashion by the property

$$f(ax) = bf(x) = a^H f(x) \iff f(x) = a^{-H} f(ax) = ba^{-H} f(x) \quad (1.31)$$

where a is the scaling of the abscissa x and b the scaling of the ordinate $y = f(x)$. Equation (1.31) is satisfied by a *power law*

$$f(x) = Cx^H \quad (1.32)$$

which will reappear in the context of fluctuations within Chapt. 3. The scaling exponent H is denoted as Hurst exponent in honor of the geologist E. H. Hurst who became famous due to his early fluctuation studies of Nile river runoffs [HURST 1951]. *Hurst rescaled-range analysis* will briefly be introduced in Sect. 3.1.1. Note, that power laws exhibit linear behavior (scaling) with slope H in a double-logarithmic plot, $\log f(x) = H \log x$.

Relation to Time Series

It is easy to imagine that a noisy time series with its seemingly irregular structure of edges and vertices has much resemblance with the geometrical object of a fractal. Hence, it makes sense to transfer successfully employed methodology to characterize the topological properties of (geometrical) fractal objects to time series which itself can be imagined as a special type of such fractal object that is extended in one dimension.

Multifractality

Multifractality can be thought of as a generalization of fractality. Recall, in a fractal system scale invariance is described by a single scaling law and, thus, a single scaling exponent. Now, there are systems which are rather composed of many interwoven subsets obeying different scaling laws. Hence, the complete system, its characteristics, and dynamics, captured by time series, can not be properly described by a single scaling exponent (monofractal), but rather requires a set of many different scaling exponents, see Sect. 3.3.

1.5. Stochastic Modeling of Time Series

For testing and validating time series analysis methods as well as for a comparison of results obtained from applying such methods to real datasets in order to test hypotheses, model data exhibiting well defined properties are often required. In all chapters dealing with fluctuations, oscillations, or synchronization properties I will need surrogate long-term correlated datasets, see Chapt. 3, 4, and 5. In Appendix E.2 I will discuss how short-term correlation might be misinterpreted by fluctuation analysis methods and therefore also require surrogate short-term correlated data. There are different approaches available to generate both types of correlations. I will focus and employ just one for each type here.

1.5.1. Generation of Short-Range Correlated Data

The standard models for short-term memory are *autoregressive (AR) processes of the order p* (see, e.g., in [BOX *et al.* 1994]):

$$x_k = a_0 + \sum_{j=1}^p a_j x_{k-j} + \varepsilon_k, \quad (1.33)$$

where $\{x_k\}_{k=1, \dots, N}$ denotes the generated $AR(p)$ time series, a_j with $j = 0, \dots, p$ are the model parameters (often one sets $a_0 = 0$), and $\{\varepsilon_k\}$ is some input sequence; usually it is chosen as independent and normally distributed white noise with zero mean and unit variance. In the simplest case, $p = 1$, the autocorrelation function decays with a *decay time* τ (time constant), see Appendix B for a derivation:

$$C(s) = a_1^{|s|}, \quad C(\tau) = a_1^\tau = 1/e \implies \tau = -1/\ln(a_1). \quad (1.34)$$

An example AR(1) signal is depicted in Fig. 1.1(a). In the same figure the correlation function [Fig. 1.1(d)], the power spectrum [Fig. 1.1(e)], and the DFA2-fluctuation function [Fig. 1.1(f), see Sect. 3.1.3] corresponding to the example are illustrated. Higher-order $AR(p)$ processes or additive combinations of different $AR(1)$ with differing parameters a result in a superposition of short-term dependencies with different time constants τ_j , $j = 1, \dots, p$. When some τ_j are large such process might spuriously appear long-term correlated when fluctuation functions are studied for scales smaller than the largest τ_j . A superposition of three AR(1) processes is discussed in Appendix E.2.

1.5.2. Generation of Long-Range Correlated Data

Fourier Filtering

For the null hypothesis of an underlying Gaussian linear stochastic process one needs to ensure that first and second order quantities follow a certain law. A randomized sample can thus be generated by ensuring the same first and second order moments, but with otherwise random quantities. Note, that automatically weak stationarity is preserved, see Sect. 1.1.

According to the definition in Sect. 1.2.2 long-range correlated data is characterized by a power-law decay in the power spectrum. Hence, such data can be generated by adjusting the flat ($\beta = 0$) power spectrum of an uncorrelated white noise time series to a desired target scaling, $P(f) \sim f^{-\beta_{\text{target}}}$. Note that this method is related but not identical to the amplitude adjusted Fourier transform (AAFT) method which includes a phase randomization rather than an adjustment in the power spectrum to a desired spectral exponent and purely aims at generating surrogate data of similar properties for a given dataset [THEILER *et al.* 1992].

The *Fourier filtering technique* comprises three simple steps:

Step 1 – Fourier Transform of Gaussian White Noise:

One starts with a white noise signal $\{\varepsilon_k\}_{k=1, \dots, N}$ which I consider throughout this thesis to be generated by independent, normally distributed random numbers with mean zero and unit variance, i. e., $\langle \varepsilon_k \varepsilon_{k'} \rangle = \delta_{kk'}$, $\langle \varepsilon_k \rangle = \mu_\varepsilon = 0$, and $\langle \varepsilon_k^2 \rangle - \langle \varepsilon_k \rangle^2 = \sigma_\varepsilon^2 = 1$. Then $\{\varepsilon_k\}$ is Fourier transformed into frequency space employing Eq. (1.12). Note that it is not necessary to calculate the actual power spectrum because of the Wiener-Khinchin theorem and Eq. (1.15) stating the equivalence of the squared Fourier amplitude of the signal and the power spectrum. Since the latter decays for long-term correlated data according to a power law with spectral exponent β , the Fourier coefficients $\{\hat{\varepsilon}_f\}$ [Eq. (1.12)] must decay with an exponent of $\beta/2$.

Step 2 – Adjusting the Power Spectrum:

The power spectrum of the white noise signal $\{\varepsilon_k\}$ is flat with $\beta = 0$, i. e., all frequencies have an equivalent weight. In order to adjust the power spectrum to a power law the Fourier coefficients $\{\hat{\varepsilon}_f\}$ are multiplied with the factor $f^{-\beta/2}$ yielding the coefficients $\{\hat{x}_f\}$.

Step 3 – Inverse FT:

Finally, the spectrum adjusted signal $\{\hat{x}_f\}$ is transformed back to time domain employing the inverse Fourier transform

$$\{x_k\} = \mathcal{F}^{-1}(\{\hat{x}_f\}) = \sum_{m=-N/2+1}^{N/2} \hat{x}_f e^{2\pi i k m / N} \quad , \quad f = m/N \quad (1.35)$$

yielding a long-term correlated time series $\{x_k\}$ for an even N . Note that in this definition there is no prefactor of $1/N$ compared with Eq. (1.12).

Although I started with a Gaussian white noise in *Step 1*, it is possible to begin with any other signal. In Sect. 3.3.4 I will suggest an algorithm that employs the Fourier filtering technique to tune long-term correlations in a multifractal model.

Iterative Fourier Filtering – Schreiber-Schmitz Method

In general the Fourier filtering does preserve the distribution of the input signal (e. g. white noise) only on average [SCHREIBER AND SCHMITZ 1996]. This property depends on the length of the

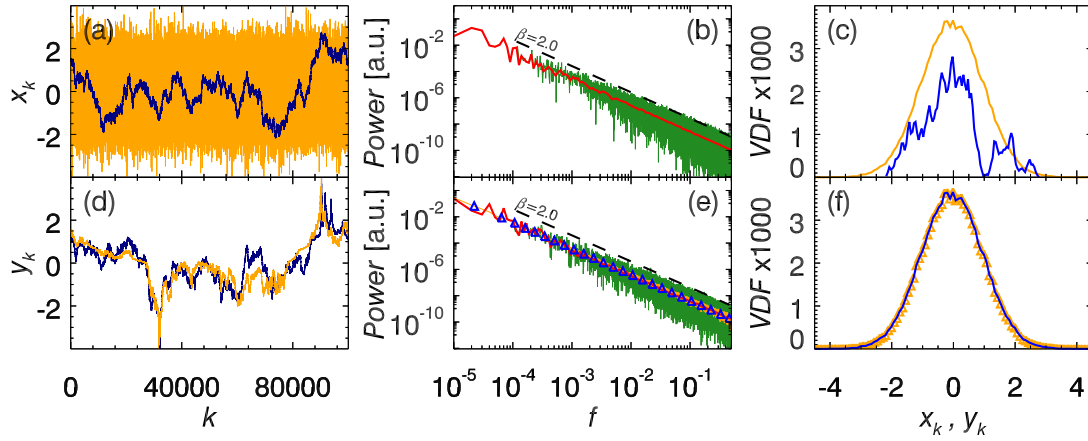


Figure 1.3.: Illustration of the Schreiber-Schmitz algorithm for generating surrogate data: (a) Gaussian white noise time series $\mu_x = 0$, $\sigma = 1$ [yellow] and a long-term correlated time series with $\beta = 2.0$ and $\alpha = 1.5$ [blue]; (b) corresponding power spectrum [green] and logarithmically binned spectrum [red], the white noise power spectrum is flat with $\beta = 0$ [not shown]; (c) corresponding value distribution functions [VDF] in the same colors as in (a). The difference from a normal distribution is obvious for the long-term correlated signal which was generated by Fourier filtering. In the lower panels results for employing Schreiber-Schmitz' algorithm [10 iterations] starting with the same white noise as in (a) are shown: (d) Time series after adjusting (i) the slope of the spectrum to a power law [blue], and (ii) each frequency component in the power spectrum separately to fit a perfect power law [yellow]. (e) corresponding power spectra [(i) green, binned version in red, (ii) yellow, binned version marked by blue triangles]. (f) corresponding value distributions in the same colors as in (d).

modeled dataset. Schreiber and Schmitz proposed an iterative algorithm. When the described algorithm of Fourier filtering is applied to an input signal in order to adjust its power spectrum in most cases the value distribution of the input signal is changed after the inverse Fourier transform. However, the value distribution can be adjusted in time domain by rank wise exchanging the values of the output signal obtained from *Step 3*, $\{x_k\}$, with the input signal $\{\varepsilon_k\}$. In this step, on the other hand, long-term correlations and hence the scaling of the power spectrum are again modified. Employing Fourier filtering followed by an adjustment of the value distribution in an iterative way finally yields a time series exhibiting the desired long-term correlations and value distribution. From my own experience generation of long-term correlated data with $\beta_{\text{target}} < 1.2$ does not notably alter the distribution compared with the input Gaussian. However, differences in the distribution after Fourier Filtering become relevant when $\beta_{\text{target}} > 1.25$. In my experiments there was neither an indication that this effect was induced by edge effects, i. e., N not being a power of two, nor any noticeable dependence on the series length N as speculated by Schreiber and Schmitz [SCHREIBER AND SCHMITZ 1996].

The capabilities of the Schreiber-Schmitz algorithm are illustrated in Fig. 1.3. In the top row results from employing the standard Fourier filtering method are shown. For a Gaussian white noise of zero mean and unit variance [yellow in Figs. 1.3(a,c)] the power spectrum [$\beta = 0$, not shown] is adjusted to satisfy $\beta = 2$ [Fig. 1.3(b); green, and red after logarithmic binning]. As can be observed in Fig. 1.3(c) the value distribution of the output signal [blue] does not well fit the original Gaussian. In the lower panels in Fig. 1.3 the same white noise was used in a Schreiber-Schmitz iteration (10 iterations) which successfully adjusts long-term persistence and preserves the original distribution [blue curves in Figs. 1.3(d-f)]. Note that the yellow signal in Fig. 1.3(d) was obtained by a perfect adjustment to a power law in *Step 2* of the Fourier filtering technique, meaning for each frequency f the correct multiplier to fit the power law was derived separately.

Note that long-term correlated time series can also be derived from a *fractional autoregressive integrated moving average process* – (FARIMA) [SCHLITTGEN AND STREITBERG 1999] or generated by the *random midpoint displacement method* [FEDER 1988]. A technique to generate multifractal time series of arbitrary multifractality strength and simultaneously tuned long-term correlations will be presented in Sect. 3.3.4 and can be found in [SCHUMANN AND KANTELHARDT 2010b].

2. Introduction to Human Physiology

This chapter does not report achievements in pure physics but is rather intended to inform the reader about the very basic mechanisms of human physiology. It gives a short overview about the autonomous nervous system that is responsible for controlling the cardiorespiratory system and can be studied by analysing time series from heartbeat and breathing. While respiration signals are rather intuitive the mechanisms behind heartbeat data require some knowledge about the physiology of the heart. After introducing the cardiorespiratory system I will discuss brain wave recordings and the structure of sleep since most of the analyses I will present in the main part of this thesis [Chapts. 3, 4, and 5] are based on sleep recordings. Data from three databases are described in Sect. 2.4. Since, this chapter has a rather medical and phenomenological background theoretical physicists might want to continue with Chapt. 3.

2.1. The Autonomous Nervous System

The *autonomous nervous system (ANS)* is a part of the peripheral nervous system that controls and regulates homeostasis of the human body, i. e., it maintains certain controllable physiological variables such as blood pressure or heart rate in a sustained condition and within a tolerable limit. Each control circuit forms a closed loop where a controller (brain, nervous system) continuously obtains the actual value of the variable to control, e. g., mechanoreceptors¹ (baroreceptors) in the blood vessels monitor the blood pressure level, and adjusts this value according to the required target value. However, due to disturbances and the interaction with other variables the target value is likely not achieved. Its current state is reported back to the controller by the sensor via a negative feedback loop. The controller can then readjust the variable's value according to the (possibly also changed) target value. Properties that are regulated by the ANS comprise the content of gasses, ions, and nutrients in tissue; salivation², perspiration³, the diameter of pupils, micturition⁴, or erection; and most importantly digestive, cardiovascular, and respiratory functions. In this thesis I will exclusively consider the latter two.

The ANS is further subdivided into the three parts: (i) the sympathetic nervous system (SNS), (ii) the parasympathetic nervous system (PNS), and (iii) the enteric⁵ nervous system (ENS). For the cardiorespiratory system [basically comprising the heart, the lungs, and blood vessels, see Sect. 2.2 for details] that I study in this thesis only *sympathetic* and *parasympathetic (vagal)*⁶ control is of importance. Both components are active on a basal level (sympathetic tone and parasympathetic tone) and acting complementary. Their ratio, the *sympathovagal balance*⁷, determines the control direction. Activation of the parasympathetic branch results in the release of the neurotransmitter acetylcholin by the vagus nerve which is detected by muscarinic acetylcholin receptors at the heart that increase the K^+ conductance in the cell membranes of the heart and finally trigger the deceleration of the heart. In contrast, an acceleration of the heart is induced by sympathetic activation due to the release of epinephrine and norepinephrine which docks to adrenergic receptors.

¹Stretch sensors that 'measure' the deformation of the blood vessels due to high blood pressure.

²Flow of spittle

³Respiration through the skin

⁴Discharge of urine

⁵Bowel control

⁶Since parasympathetic nerves partially originate from the vagus nerve – indeed parasympathetic innervation of the heart is mediated by the vagus nerve – both terms, parasympathetic and vagal, are often used synonymously.

⁷It is for instance measured by the ratio of total power in the LF band and total power in the HF band. Both bands are explained in Fig. 2.4. See also [GOLDBERGER 1999] for a different measure.

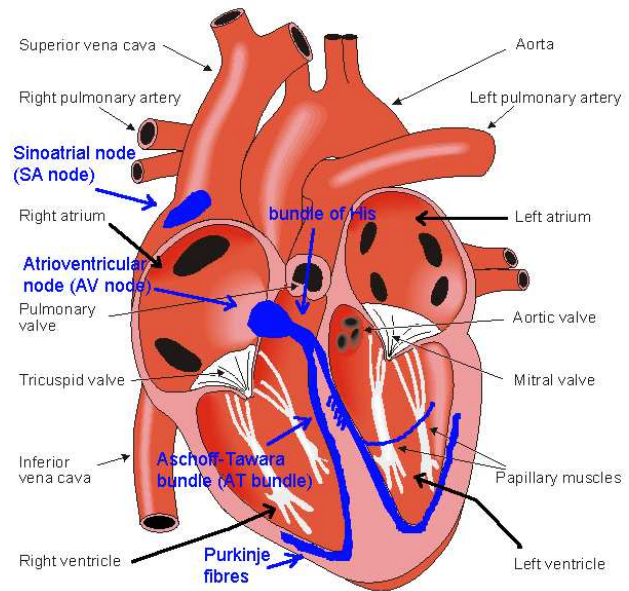
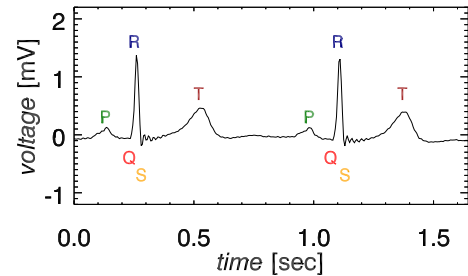


Figure 2.1.: Schematic picture of the heart with pacemaker system [blue]. Note that the SA node [intrinsic frequency approx. 60min^{-1}] is only the primary pacemaker (healthy), the secondary pacemaker [AV node; intrinsic frequency approx. 40min^{-1}] and the tertiary pacemaker [His bundle, AT bundle, and Purkinje system; intrinsic frequency approx. 25min^{-1}] can be interpreted as "Nature's backup systems" in case the SA node fails. Note the order of right and left. Improved version of a figure borrowed from [MALMIVUO AND PLONSEY 1995].

Figure 2.2.: Nomenclature of time points in electrocardiograms (ECG) after Einthoven. The ECG curve records potential differences [in mV] and corresponds to cardiac excitation [see text]: (i) depolarization of the atria [positive P-wave], (ii) repolarization of the atria [isoelectric episode], (iii) depolarization of ventricles [QRS complex; R positive, and Q and S negative], (iv) completely depolarized state [isoelectric ST episode], and (v) repolarization of ventricles [extended T-wave].



Studies have associated parasympathetic activation with the high frequency components (0.15Hz to 0.4Hz) of heartbeat while sympathetic activation influences low frequency components (0.04Hz to 0.15Hz) [see Sect. 2.2 for details on heartbeat recordings]. However, the latter issue was discussed controversially since some studies support the statement that the LF band is additionally influenced by the parasympathetic nervous system, see [HRV TASK FORCE 1996, and references therein].

Note that parasympathetic activation is rather fast due to a high concentration of acetylcholinesterase in the sinoatrial node (SA) which triggers the contraction of the heart [see Sect. 2.2] and quickly hydrolyses the parasympathetic neurotransmitter acetylcholine compared with sympathetic activation. However, we find sympathetic predominance in situations where a quick response is required, e. g., when quickly getting up from supine position or when getting frightened. In contrast responses to parasympathetic activation seem to be much slower. For instance think about the time that is required to return to a resting state after exercise. The reason for this apparent contradiction is originated in the omnipresence of both sympathetic and vagal components. Sympathetic activation can be triggered by a reduction in parasympathetic tone which appears rather fast. Nevertheless, the regulation mechanisms of the autonomous nervous system mediated by the sympathetic and vagal interaction is not fully understood and ongoing research.

2.2. The Cardiorespiratory System – Heartbeat and Respiration

The cardiorespiratory system consisting of the heart, the blood vessels as well as the lungs is besides the central nervous system one of the most important complex subsystems in human physiology. Therefore, it has been studied extensively during the last decades. Most approaches covered monivariate analysis of either heartbeat or breathing signals, e. g., employing spectral methods to investigate heart rate variability (HRV) [AKSELROD *et al.* 1981; KOBAYASHI AND MURASHI 1982; GOLDBERGER *et al.* 1990; KESELBRENER AND AKSELROD 1996; HRV TASK FORCE 1996] or exploring correlation behavior and fluctuations by applying detrended fluctuation anal-

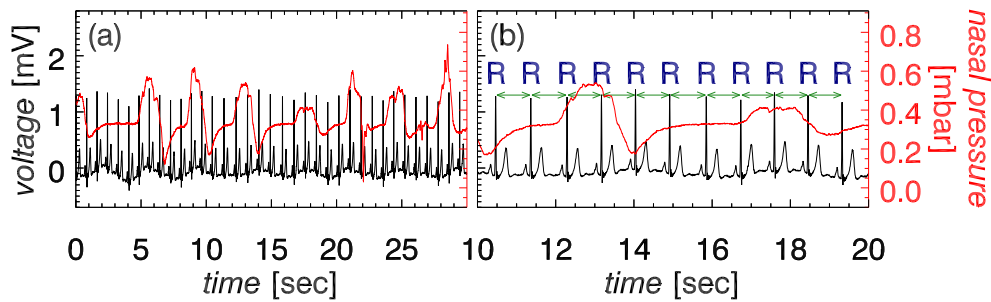


Figure 2.3.: Illustration on the extraction of beat-to-beat interval time series from an electrocardiogram (ECG). (a) Shown are an ECG fragment of 30s duration [black left axis] and a corresponding nasal pressure signal [red right axis] recorded from a healthy subject [DAPHNET database]. Note that the amplitudes of the R peaks recover the respiratory cycle in this fragment. (b) Enlarged part from (a) with detected R peaks. The beat-to-beat interval [RRI] time series is constructed of the time intervals between consecutive R peaks [marked by green arrows].

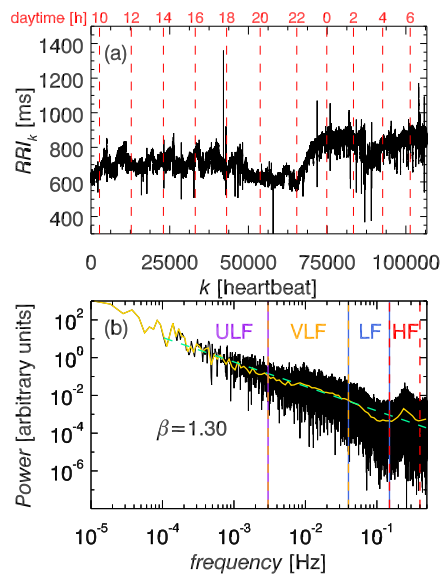


Figure 2.4.: (a) Example of heartbeat interval time series recorded from a post-infarction patient [ISAR-I database]. Red dashed lines mark the daytime. The transition to sleep associated with a deceleration of the heart is clearly observed in this patient after 22:00 o'clock. Note that the irregular spacing of the lines is originated in the X-axis being heartbeat number and not time. (b) Corresponding power spectrum. The yellow curve is obtained from logarithmic binning. The dashed yellow-green line indicates power-law scaling with a spectral exponent $\beta = 1.30$. Important physiological frequency ranges are marked by vertical lines [from left to right]: ultra low frequency band (ULF) [$f \leq 0.003\text{Hz}$], very low frequency band (VLF) [$0.003\text{Hz} < f \leq 0.04\text{Hz}$], low frequency band (LF) [$0.04\text{Hz} < f \leq 0.15\text{Hz}$], and high frequency band (HF) [$0.15\text{Hz} < f \leq 0.4\text{Hz}$]. The pronounced peak in the HF band is caused by respiration.

ysis [PENG *et al.* 1995; BUNDE *et al.* 2000; KANTELHARDT *et al.* 2003a; ROSTIG *et al.* 2005] or recently phase rectified signal averaging (PRSA) [BAUER *et al.* 2006a]. Cross-modulations and cross-interactions between the components of the cardiorespiratory system have been studied by means of cross-correlation analysis, transfer function analysis, or (phase) synchronization analysis [SCHÄFER *et al.* 1998; STEFANOVSKA *et al.* 2000; LOTRIC AND STEFANOVSKA 2000; TOLEDO *et al.* 2002; BARTSCH *et al.* 2007].

2.2.1. Heartbeat

Information about the heart, its condition, and its dynamics can be obtained from studying electrocardiograms (ECGs) which non-invasively measure potential differences induced by cardiac excitation. ECG recordings were established in physiology by Willem Einthoven who received for his work on ECG recordings the Nobel Prize in 1924. In order to understand the emergence of the healthy ECG curve as is shown for two consecutive heartbeats in Fig. 2.2 knowledge about the electro-physiological heart cycle is needed.

Depolarization and repolarization mechanisms of the heart form the typical shape of an ECG curve, consult in the following Fig. 2.2 for the P, Q, R, S, T nomenclature invented by Einthoven and Fig. 2.1 for anatomical orientation. In resting state the heart cells are in an equilibrium of positive charges on the outside of the cell membrane and negative charges on the inside yielding a polarization. A contraction of the healthy heart is then stimulated by the sinoatrial node (SA node) which is only of the size of a few square millimeters and embedded on top of the right atrium⁸ next

⁸Note that 'right' and 'left' are ordered according to one's own body and heart.

to the superior vena cava, see Fig. 2.1. Although the SA is connected to the autonomous nervous system, and thus its pulse repetition rate can be modulated by parasympathetic and sympathetic activation, its function as a pacemaker is generally autonomous due to self-excitabile cells and a natural discharge occurs at rate of $60 - 100\text{min}^{-1}$ [DESPOPOULOS AND SILBERNAGL 2003]. The SA triggers the depolarization in the right atrium (approx. 50ms after impulse generation) which evolves to the left atrium (85ms) and down towards the atrioventricular node (AV node). This depolarization of the atria manifests in the ECG P-wave [Fig. 2.2] while its repolarization cannot be observed (isoelectric region before QRS-complex). When the pulse arrives at the AV node it is delayed and relayed to the His bundle (PQ-segment; arrival: 50ms, relay: 125ms) from where it is conducted further to the Purkinje fibres. Depolarization of the ventricles manifests in the QRS-complex (inner myocardium⁹: right 175ms, left 190ms; outer myocardium: right 205ms, left 225ms) where the R peak is associated with the largest action current approximately in direction of the cardiac apex ('tip' of the heart). Repolarization of the heart tissue finally generates the T-wave and a new cardiac cycle can start.

Although, a *heartbeat* is a rather complex interplay between depolarization and repolarization (a single cycle from P-wave towards T-wave) the R peak is the most prominent feature in ECG recordings. In the following I will denote the *R peak* as *beat* and the time interval between the R peaks of two consecutive heart beats as *RR interval (RRI)* for simplification. The time series which is constructed from all recorded RR intervals will also be denoted by RRI, see Fig. 2.3. Further note that the discussed mechanism only applies for a healthy *normal (N)* beat. The ECG curve is deformed if the depolarization is triggered by the AV node. This occurs when (i) the intrinsic frequency of the SA node falls below the one of the AV node (e. g. observed in sportsmen or at 'sinus arrest'), or (ii) the self-excitation frequency of the AV node is increased due to pathologies. Note that other pathologies that affect polarization and depolarization properties of heart tissue locally also change the ECG signal.

The most important type of ectopic beats that can disturb the analysis that I present in this thesis are *super ventricular extrasystoles (SVES)* and *ventricular extrasystoles (VES)*. They are distinguished according to the location of the impulse triggering the additional or earlier depolarization. Both types are characterized by premature beats triggered, in the first case, by the AV node or above ('normal' QRS-complex), and in the latter case by a tertiary pacemaker (His bundle, AT bundle, Purkinje system; QRS deformation) [OHLY 2008].

QRS detection, in particular the detection of the R peaks, is an especially challenging and time consuming part of any heartbeat analysis due to many different patterns in the ECG curve and various artifacts due to movements, changes in body exposition, or recording devices. Today, there is no fully automatic peak detector available. A software guided detection process always requires visual inspection of identified beats, and more importantly missed beats and artifacts¹⁰. For principles on QRS detection see the review [KOHLER *et al.* 2002] while an overview on artifacts in electro-physiological signals in general is given in [WEHRLI AND LOOSLI-HERMES 2003].

Heartbeat Related Observables

In order to gain knowledge about heartbeat dynamics and to design scores for cardiac risk assessment, i. e., identifying cardiovascular diseases and patients at cardiovascular risk or forecasting of dangerous cardiac events such as *Sudden Cardiac Deaths (SCD)*, different quantities of ECG recordings have been studied. The medically most popular properties that are obtained from RRI time series (or its inverse the heart rate) can be divided into time domain variables and spectral variables. Among the first group of observables are: (i) the standard deviation of Normal-R-to-Normal-R (NN) intervals which is calculated for a predefined time such as 10 min or 24 hours (SDNN), (ii) the standard deviation of the average NN intervals calculated over short periods, e. g., 5 minutes (SDANN), (iii) the square root of the mean squared difference of successive NN intervals (RMSSD), (iv) the number of pairs of successive NN intervals differing by more than 50ms (NN50), and (v) NN50 divided by the total number of NN intervals (pNN50). The second group of

⁹Myocardial muscle = 'muscle of the heart'

¹⁰To give the reader an impression, the time that is to my experience required to classify a single whole night ECG recording of approximately 8 hours duration is on average 2 hours.

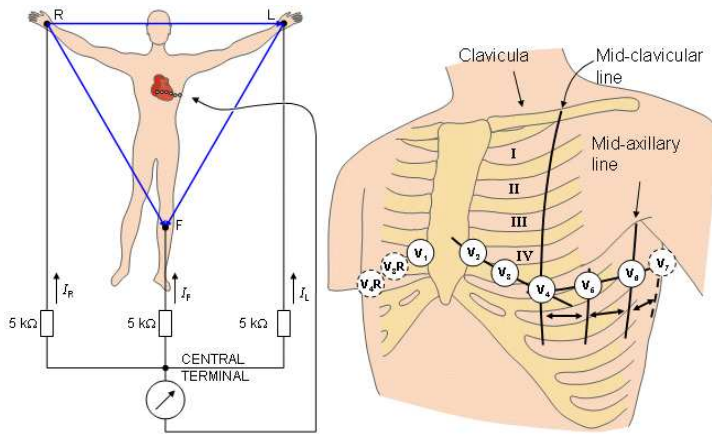


Figure 2.5.: Illustration of ECG leads after Wilson. (left panel) The negative reference electrode is defined by combining leads attached to the left leg [LL], left arm [LA], and the right arm [RA; in the US additionally right leg RL]. (right panel) Positioning and notation of unipolar ECG breast leads. Figures borrowed with permission from [MALMIVUO AND PLONSEY 1995].

spectral variables comprises the total power in certain frequency ranges¹¹ [see Fig. 2.3]: (i) power in the high frequency band (HF: $f \in (0.15\text{Hz}, 0.4\text{Hz})$), (ii) power in the low frequency band (LF: $f \in (0.04\text{Hz}, 0.15\text{Hz})$), (iii) power in the very low frequency band (VLF: $f \in (0.0033\text{Hz}, 0.04\text{Hz})$), (iv) power in the ultra low frequency (ULF: $f \leq 0.0033\text{Hz}$) that can only be reliably assessed in 24 hours recordings, and (v) the quotient of total power in the LF band and total power in the HF band which was proposed as an index of sympathetic to parasympathetic balance¹². For a more detailed overview I point to the standard on HRV parameters [HRV TASK FORCE 1996].

Heart Failure – Sudden Cardiac Death (SCD)

The origin of a myocardial infarction is the closure of a coronary artery which results in a delay of the depolarization of the heart that can be observed in the ECG by an elevation of the ST episode [Fig. 2.2]. When the closure is not resolved for a longer period the myocardial tissue becomes necrotic and loses its capability to polarize and depolarize (reduction in R-peak magnitude). Finally, an initial myocardial infarction can yield a sudden cardiac death (SCD). However, SCDs might be prevented by the implantation of a cardioverter defibrillator (CVD) device. Since this device is rather expensive and an implantation is chancy for the patient, a reliable risk assessment is required to identify patients at high cardiac risk.

Measurement of Heartbeat

Heartbeat is generally monitored by measuring electrical potentials (mV) between electrodes attached to predefined locations at body. Although there exist a few different approaches, the most prominent electrode placement technique after Wilson defines a negative indifferent reference electrode of high resistance ($5\text{k}\Omega$) as the interconnection of three limb leads (left leg, left arm, and right arm) and attaches the positive electrode¹³ to fixed locations on the breast [WILSON *et al.* 1931a,b,c, 1934]. For positioning and notation of breast leads see Fig. 2.5.

2.2.2. Respiration and Respiratory Sinus Arrhythmia

Respiratory signals that I consider in Chapt. 3 and 5 do not have a complicated structure compared with heartbeat and I will not go into details here, see Sect. 2.3.3 for a description of sleep apnea – a respiratory disorder. For more details on the physiology of respiration I point the reader to, e. g. [DESPOPOULOS AND SILBERNAGL 2003]. Recordings from respiration ideally oscillate sinusoidal where the extrema and the intervals between them are associated with certain respiratory phases (inspiration and expiration). Respiration can be measured by either one of the following

¹¹While the frequency ranges are well defined and standardized there is no general agreement on a standardized length of the heartbeat recording or on a standardized width of frequency bins in the fast Fourier transform. Unless normalized by quantities as total power, reported values as 'power in the HF band' are meaningless without a proper description of used frequency bins. This complicates comparison among different studies.

¹²The meaning of the sympatho-vagal ratio is still under discussion since in particular the mechanisms for generating power in the LF band are not completely understood.

¹³Since the negative reference electrode is a composite pole, other leads are referred to as *unipolar* in contrast to *bipolar* leads which possess one negative and one positive pole.

rather uncomfortable and encumbering and/or invasive and thus ambulatory ill suited methods: (i) by using stretch sensors embedded in a belt and attached to the chest and/or abdomen surveying excursions and motions of the body surface, (ii) by means of a thermistor and/or a spirometer (flow meter) incorporated in a mouthpiece, a nose-clamp or a breathing-mask covering the whole nose-mouth area, (iii) by expensive inductive plethysmographs or respiratory magnetometers, or (iv) by impedance pneumography based on impedance cardiographic signals [ERNST *et al.* 1999; HOUTVEEN *et al.* 2006]. A major aim of the study I present in Sect. 5.2.1 was to investigate the possibility of reproducing cardiorespiratory-synchronization properties from heartbeat alone. That could allow to reduce the number of disturbing respiratory measurements during sleep where currently three different breathing proxies are typically recorded [see Sect. 2.3].

In this thesis I will focus on data obtained by temperature measurements (method (ii) utilizing a thermistor) from oronasal airflow recordings. While the continuous oronasal airflow signal will be employed in section following Sect. 5.2.1, I study the scaling of inter-breath intervals (IBI) in Sect. 3.2.2. IBIs can be defined in a similar way as RRIs by considering the time interval between points of the same respiratory phase. For simplification I assume inspiration (cold air is inhaled) to be completed at minima of oronasal airflow and analogously expiration to be terminated at temperature maxima (exhaled air is warm).

Respiratory Sinus Arrhythmia

The nonlinear coupling between heartbeat and respiration across different physiological states during sleep will be investigated in Chapt. 5 by means of *phase-synchronization analysis* which will then be introduced. However, the effect of *respiratory sinus arrhythmia (RSA)* is worth mentioning. RSA describes the modulation of heartbeat due to respiration [ECKBERG 2003; YASUMA AND HAYANO 2004]. In vertebrates the heart beats faster during inspiration while it beats slower during expiration. Indeed this effect can in principle be controlled by deliberately breathing at a higher or lower frequency. In humans a RSA was associated with cardiac vagal function and thus with cardiac risk since cardiovascular diseases are often associated with a reduction in vagal responsiveness. Note that the RSA effect most probably is caused by two interacting coupling mechanisms (i) a mechanical coupling between the heart and the lungs – the heart is deformed upon inflation and deflation of the lung, and (ii) an autonomic coupling due to the sympathovagal balance which influences both heartbeat and respiration but also affects blood pressure and other components of the complex cardiorespiratory system.

2.3. Sleep - Polysomnographic Recordings

Humans spend about one third of their life sleeping. Sleep and wake stages are found among almost all vertebrates¹⁴. Sleep is essential for our body's recreation while a disturbed sleep negatively affects our daily physical and mental fitness. During wakefulness the cardiorespiratory system [Sect. 2.2] is continuously influenced by its environment. For instance, we respond to external stimuli such as sonic or visual input and are sensitive to mental stress. In contrast, the cardiorespiratory system is self-sustained during sleep reflecting the intrinsic characteristics of the autonomous nervous system [Sect. 2.1] and the subjects' physiology.

More than ten percent of the human population in the industrialized world¹⁵ suffer from sleep related disorders or sleep-wake dysfunctions. Investigating human physiology during sleep is of high interest not only for identifying sleep related disorders, but also for detecting and understanding changes in sleep patterns related to non-sleep-related disorders such as, e.g., Alzheimer's or Parkinson's disease.

The standard procedure in a hospitals' sleep laboratory includes full night polysomnography (PSG) – multi-channel sleep recording – where many sensors and electrodes are attached to the patient's body in order to measure variables such as heartbeat, respiration, muscle activity, brain

¹⁴Sleep among certain migratory birds that do not sleep for days while flying or certain fish cannot be classified in the way that is discussed in the following. However, it appears that they still have phases of reduced behavioral responsiveness which might be interpreted as another type of sleep.

¹⁵Others were not systematically studied.

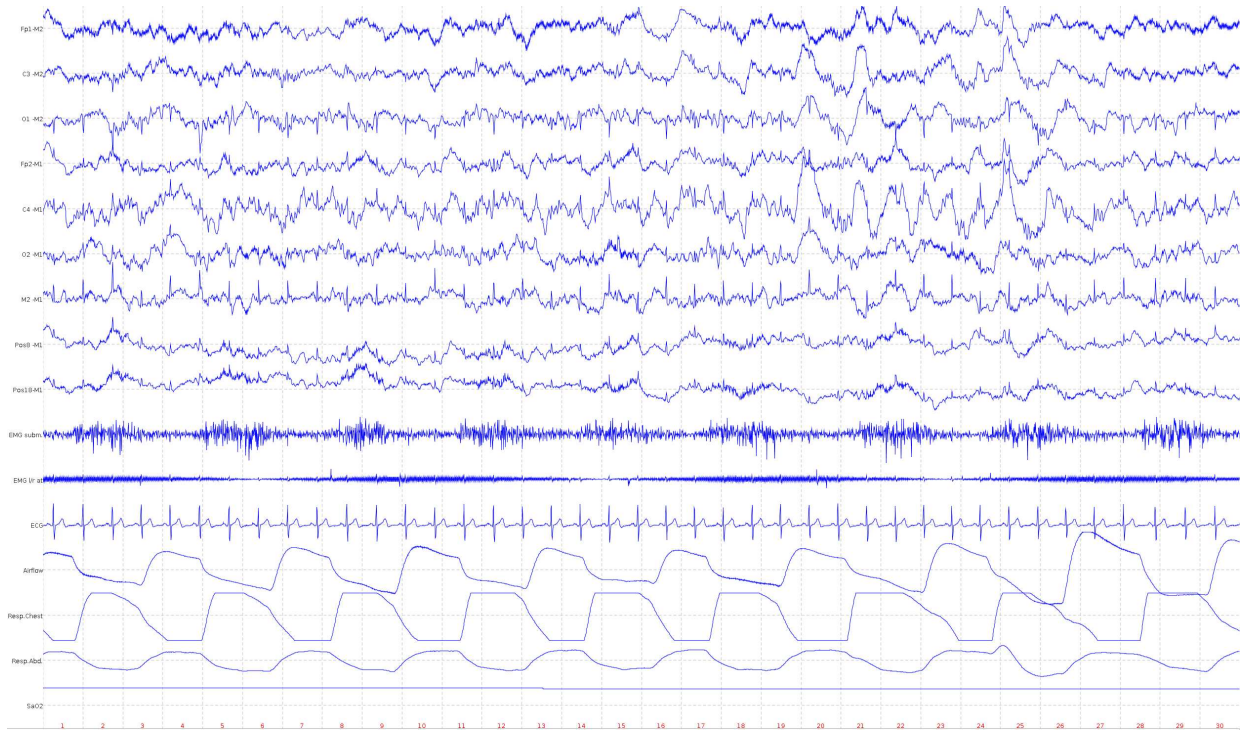


Figure 2.6.: Randomly chosen 30s fragment of a whole night polysomnographic recording from the SIESTA database, channels are from top to bottom: 6 leads electroencephalogram (EEG) [Fp1-M2, C3-M2, O1-M2, Fp2-M1, C4-M1, O2-M1, M2-M1], 2 leads electrooculogram (EOG) [Pos8-M1, Pos18-M1], 2 leads electromyogram (EMG) [EMG subm., EMG l/r at], electrocardiogram (ECG), 3 channels describing respiration [oro-nasal airflow, chest movement, abdomen movement], oxygen saturation (SaO2).

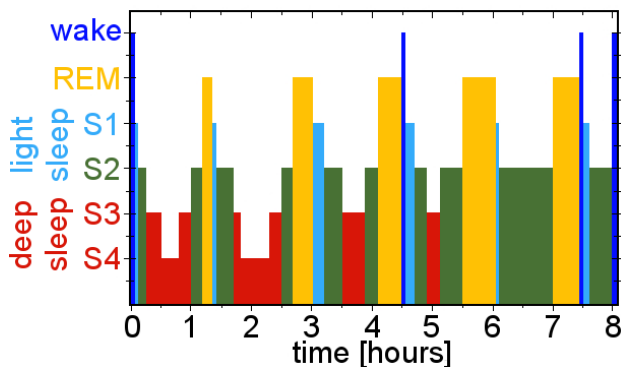
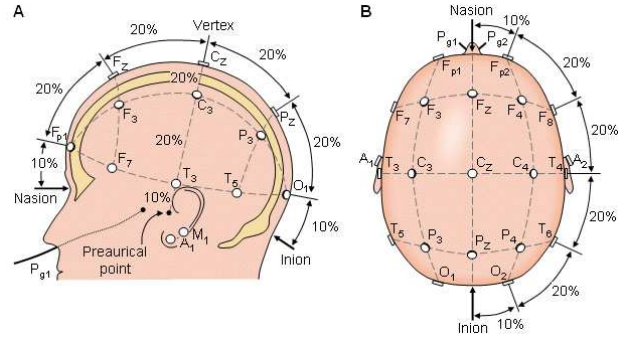


Figure 2.7.: Idealized sleep stages during healthy nocturnal sleep [shown are hours after sleep onset]. Sleep depth increases from top to bottom. Approximately 5 sleep cycles of about 90 min duration are observed. Each cycle typically progresses from wake via light sleep towards deep sleep and finally towards REM sleep via an intermediate short light sleep episode. Intra-sleep arousals might occur. In sleep research this type of plot is referred to as a hypnogram.

waves and eye movements [MEMBERS OF SIESTA EU PROJECT 1998]. A 30s fragment of a PSG recording taken from the SIESTA database [Sect. 2.4] is depicted in Fig. 2.6. Although the major aim of these measurements is to monitor natural sleeping behavior, sleep is often disturbed by the unfamiliar environment and the distemping measuring devices. For that reason PSGs are obtained from two different nights – an *adaptation night* where the subject should get used to the procedure and a *recording night* where the medical relevant data is recorded. Since I found differences in scaling behaviour and cardiorespiratory coupling not significantly different during both nights I will later combine the data from both nights to increase statistics.

It is well known that healthy sleep consists of approximately five cycles of roughly 1-2 hours duration; for a *hypnogram* showing the structure of sleep in healthy subjects see Fig. 2.7. Each cycle usually evolves from non-REM sleep (non-rapid-eye-movement sleep), i. e., from light sleep stages 1 and 2 followed by the deep sleep stages 3 and 4, to REM sleep (rapid eye movement sleep). Sleep stages are scored based on the frequency content of brain wave recordings, muscle tone, and eye movements according to the rules in [RECHTSCHAFFEN AND KALES 1968] or nowadays sometimes following the suggestions in [IBER *et al.* 2007]. I will introduce and differentiate all above mentioned sleep stages in Sect. 2.3.2 after having explained brain wave recordings.

Figure 2.8.: Illustration of the 10-20 system to place EEG electrodes ensuring standardized brain wave recordings. Panel A shows the left hemisphere and panel B the skull from above. Symbolics derive from Pg - nasopharyngeal, Fp - frontal pole, F - frontal, C - central, P - parietal, O - occipital (back), A - auricular (ear lobe), and M - mastoid. Odd (even) subscripts denote electrodes in the left (right) hemisphere, T - temporal. Figure adapted from [MALMIVUO AND PLONSEY 1995] under general public license.



band	freq. (Hz)	band	freq. (Hz)	band	freq. (Hz)
δ	0.5 – 3.99	α	7 – 11.49	β	16 – 22
θ	4 – 6.99	σ	11.5 – 15.99	γ	> 30

Table 2.1.: Frequency bands used for EEG analysis.

2.3.1. Brain Waves - The Human Electroencephalogram

The most prominent recording in full night PSG is the electroencephalogram (EEG) measuring electrical potentials at the cortex by attaching electrodes to the skull. This is in principle similar to ECG electrodes attached to breast and limbs. However, the generation of EEG signals cannot be elucidated as easily as for the ECG since the EEG can be thought of a 'mean field' approach summarizing the activity of thousands of superimposed neurons firing at individual rates. It is not possible to access the dynamics of single neurons based on EEG recordings. The oscillations we observe in the EEG are believed to originate in the thalamus which is characterized by excitable neurons producing (upon stimulation) single spikes (depolarization) or 'slow spikes' (hyperpolarization) [BUZSAKI 2006].

In order to relate brain wave recordings obtained from different subjects with each other a standardized system for electrode positioning, the still employed *10-20 system*, was developed by Jasper [Jasper *et al.* 1958]. Based on the length of the vertex mid-line between nasion and inion EEG electrodes are positioned in anterior-posterior (front-back) direction by subdividing the mid-line in 6 segments 10% – 20% – 20% – 20% – 20% – 10%. The same 10-20 arrangement is then repeated for the mid-line connecting the preauricular points of both hemispheres passing through the central point Cz resulting in T3, C3, C4, and T4 [for symbols consult Fig. 2.8]. Finally, by again applying 10-20 division one defines all other points except for the references at the ear (A1, A2, M1, M2) at the lines through previously marked points, see Fig. 2.8 for details.

Note, often electrodes placed at auricular position (A - 'ear lobe') and at the mastoid process (M - 'behind the ear') are considered comparable.

2.3.2. Sleep Stages

Oscillations in the human EEG are classified according to their frequency content. Typically, six different frequency ranges with increasing frequency labeled by δ , θ , α , σ , β , and γ are defined¹⁶, consult Tab. 2.1.

Based on the frequency content in EEG signals, muscle tone measured by electromyography (EMG), and monitored eye movements by electrooculography (EOG), sleep is subdivided into five different physiological stages and nocturnal wakefulness¹⁷ within predefined time windows¹⁸

¹⁶In Sect. 5.3.1 I study (cross-)modulations in EEG data. Then the frequency bands will be slightly modified, i. e., the δ band will be divided into two parts and the γ band will be disregarded due to frequency band-pass filters (0.16Hz-35Hz) that were already employed in the sleep laboratories.

¹⁷Note that I remove all wake episodes before sleep onset in the evening and after awakening in the morning preceding any analysis presented in this thesis. Thus, wake always refers to intra-sleep wake and arousals (short wake occurring after an apnea event, Sect. 2.3.3).

¹⁸A time window of 30s descends from the time when EEGs could not be saved to a hard disk but where plotted

of 30s [RECHTSCHAFFEN AND KALES 1968]:

Wakefulness: β waves that typically appear during task solving and α waves which are usually associated with a relaxed stage, beginning drowsiness, or the closed eyes condition dominate more than 50% of the epoch. Muscle tone is at the highest level; rapid eye movements occur.

Light Sleep Stage 1 (S1): Transition state between wake and sleep. α waves reduce their frequency and merge into the θ band. Muscle tone reduces, however, sudden twitches or hypnic jerks might occur. Eye movements are slow and conscious awareness mostly disappears.

Light Sleep Stage 2 (S2): Prevalence of θ waves over other components; sleep spindles (σ band) occur as do K-complexes (increases of large amplitude followed by a similar decreases). Muscle tone is low and no eye movements are observed.

Deep Sleep Stage 3 (S3): θ and δ waves dominate more than 20% but less than 80% of the epoch. Muscle tone is much lower than during light sleep S2.

Deep Sleep Stage 4 (S4): θ and δ waves dominate more than 50% of the epoch. Muscle tone is very low and no eye movements are recorded¹⁹.

Rapid-Eye-Movement (REM) Sleep: Rapid low-voltage EEG; muscle tone at the lowest or completely absent; rapid phasic eye movements are observed.

According to the suggestions in [IBER *et al.* 2007] I will in the following consider deep sleep S3 and deep sleep S4 as a combined deep sleep stage. Note that the γ frequency band ($> 30\text{Hz}$) which was related to cognitive properties such as memory consolidation is not considered for sleep scoring. While the specific functions of the different sleep stages are still not well understood, it is believed that deep sleep is essential for physical recreation, while REM sleep is important for mental recreation.

2.3.3. Sleep Apnea – a Sleep Related Disorder

Sleep disorders often manifest in a disrupted hypnogram characterized by many transitions between sleep stages and wakefulness and a reduced depth of sleep (less deep sleep). The complaint about 'bad sleep' correlates with the number of intra-sleep wake periods [PENZEL *et al.* 2005]. According to the International Classification of Sleep Disorders (ICSD) manual there are currently 88 different sleep disorders defined [BUYSSE 2001]. A particularly relevant sleep disorder is *sleep apnea*. Sleep apnea is a breathing disorder characterized by a temporary reduction in airflow. It is categorized according to its cause in *central sleep apnea* due to a dysfunction of the central nervous system and *obstructive sleep apnea* due to a mechanical blockade of the upper airways. In addition, apneas and hypopneas are distinguished considering the airflow magnitude. An *apnea* event is defined as the reduction of airflow baseline by more than 70% for a period of at least 10s, while for *hypopneas* airflow must only be reduced by 30% for at least 10s [KRYGER *et al.* 2005]. The *apnea-hypopnea index* being the sum of all apnea and hypopnea events that occur per hour quantifies the severeness of the sleep apnea disease. Although sleep apneas can in principle emerge during all sleep stages, they predominantly occur during deep sleep and light sleep. While sleep is often disrupted by an arousal induced by an apnea event, an apnea appearing during deep sleep might only yield a transition to light sleep. In severe sleep apnea patients apneas might prevent deep sleep and thus a proper physical recreation. Disturbed sleep manifests in symptoms such as daytime sleepiness, afternoon drowsiness, forgetfulness, or impaired concentration, and attention. For further reading on sleep medicine I recommend the book edited by Kryger, Roth, and Dement [KRYGER *et al.* 2005].

on endless paper; a DIN A4 page covered a duration of 30s and a sleep stage was associated with each page for convenience. Today, shorter periods are sometimes scored for researching the dynamics of shorter events such as arousals or sleep spindles.

¹⁹This is indeed consistent with deep sleep S3. While S4 cannot possess less than 50% θ and δ waves per episode, the main difference to S3 is an even more reduced muscle tone.

2.3.4. Parkinson's Disease

Parkinson's disease (PD) is not a sleep related disorder, however, the PD data that I investigate in the following are exclusively polysomnographic recordings which were obtained within the EU project SIESTA, and thus, related to sleep.

PD, first described and named after the English physician James Parkinson in 1817 [PARKINSON 1817; GOWERS 1893], is among the most prominent movement disorders (motor system disorders). It is caused by a severe loss in dopamine production and distribution in the brain. PD is typically accompanied and characterized by tremor (4-6Hz), trembling in extremities, muscle stiffness and rigidity, a slowing of physical movement (bradykinesia), and sometimes even a loss of physical movement (akinesia), cognitive dysfunction and language problems, all together leading to an impaired balance and coordination.

For example, patients with PD have reduced coordination in generating the anti-phase left-right stepping pattern while walking [PLOTNIK *et al.* 2007], and of rhythmic hand movements [PLOTNIK *et al.* 2009; NIEUWBOER *et al.* 2009]. Interestingly, the serenity of these deficits were not correlated with the level of the asymmetry in the classical motor symptoms of PD [YOGEV *et al.* 2007; PLOTNIK *et al.* 2005, 2008]. Numerous studies reported about the electro-encephalography (EEG) activity recorded in patients with PD (for review see [BERENDSE AND STAM 2007]), but none, to the best of my knowledge, addressed the issue of left-right hemispheric synchronization, and studied amplitude-amplitude, frequency-frequency auto-modulation properties as well as amplitude-frequency cross modulations [see Sect. 5.3.5].

2.4. Databases Used in This Thesis

2.4.1. ISAR-I Database

The ISAR-I database comprises 24-hour ECG recordings recorded from 1455 post-infarction patients one or two weeks after the infarction²⁰. Data were obtained at Klinikum Rechts der Isar, Munich and at the German Heart Center, Munich [BARTHEL *et al.* 2003; BAUER *et al.* 2006a]. 70 patients died during a follow-up of two years. Inclusion criteria were diagnosis of acute infarction, age of 75 years or younger, and the presence of sinus rhythm. The median of the subjects' age was 59 years with a quartile range from 51 to 67 years. 300 of all subjects (21%) were women, 242 (17%) suffered from diabetes mellitus (in addition to the myocardial infarction), and 209 (14%) had a history of myocardial infarctions. The mean left ventricular ejection fraction (LVEF) value, the gold standard indicator for cardiac risk, was 56%. All patients received up-to-date treatment including beta-blockers (93%), angiotensin converting enzyme inhibitors (90%), and Aspirin (99%), and most of them underwent a percutaneous coronary intervention (90%).

24-h Holter ECG tachograms were digitally recorded at 128 Hz and automatically processed with an Oxford Excel Holter system (Oxford Instruments, Abingdon, UK). Our partners visually verified and manually checked QRS classifications (normal, ventricular ectopic, and artifact) and corrected them if necessary. LVEF was assessed by left ventriculography in 1274 patients and by single-plane echocardiography in 181 patients.

2.4.2. SIESTA Database

Full-night polysomnographic data was obtained within the EU project SIESTA²¹ at seven sleep laboratories located in five European countries [Dorffner *et al.* 1998; DANKER-HOPFE *et al.* 2005]. The recordings consist of at least 6-lead electro-encephalogram (EEG), 2-lead electro-oculogram (EOG), at least 2-lead electro-myogram (EMG, chin and leg), oronasal airflow, respiratory body movements (belts around chest and abdomen), snoring (microphone), oxygen saturation and

²⁰The myocardial infarction event that occurred directly before the study is referred to as *index myocardial infarction*.

²¹Full project title: *Development of a System for Integrating polysomnographic recordings for dEscribing Sleep archiTecture and its vAlidation on sleep disturbances (SIESTA)*.

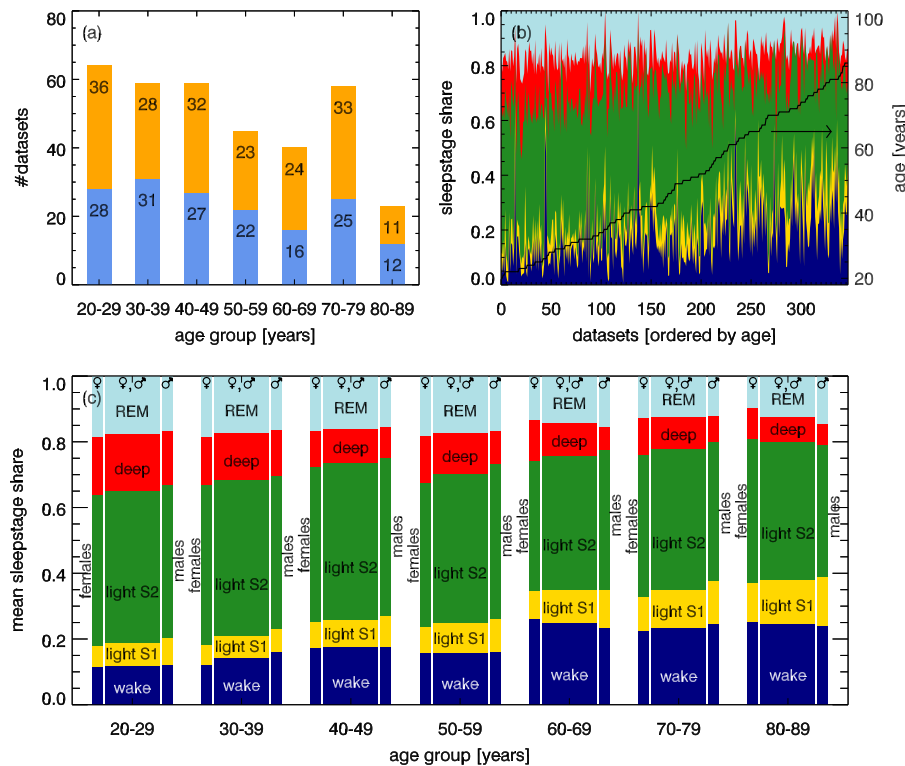


Figure 2.9.: (a) Age and gender characteristics of the considered study cohort of disease-free humans [males blue, females orange]. The total numbers of data sets [two nights] are shown for each age group. (b) Proportion of sleep stages on total time in bed for all subjects sorted by age [from left to right]. The colors indicate the states, from bottom to top: wake state - dark blue, light sleep S1 - yellow, light sleep S2 - green, deep sleep S3&S4 combined - red, and REM sleep - light blue. (c) Sleep stage distribution averaged over 10 years for all subjects [large bars in the center], and separately for females [left] and males [right]; colors and order as in (b).

single-channel electro-cardiogram (ECG). Sleep stages were identified according to the sleep scoring system of Rechtschaffen and Kales [RECHTSCHAFFEN AND KALES 1968] by three trained technicians (two independent scorers and one adjudicator) familiar with polysomnographic data. Here I focus on studying recordings from ECG, oronasal airflow, and EEG. The sampling of ECG and EEG data was 100Hz, 200Hz, or 256Hz, in contrast to oronasal-airflow recordings at 16Hz, 20Hz, 100Hz, or 200Hz depending on the laboratory and the equipment. The detailed experimental setup was reported elsewhere [Dorffner *et al.* 1998].

The database contains recordings from 190 healthy²² subjects²³. Cardiorespiratory data from 180 healthy subjects (85 males and 95 females) at ages from 20 to 89 years qualified for investigating the scaling behaviour [Chapt. 3], oscillations [Chapt. 4] of heartbeat and respiration, and cardiorespiratory phase synchronization [Chapt. 5] across sleep stages. All 190 healthy subjects are regarded in EEG cross-modulation analysis [Chapt. 5]. Sleep-stage distributions and age-group distributions are summarized in Fig. 2.9.

In addition to disease-free subjects the SIESTA database contains reliable recordings from patients suffering from (i) sleep apnea ($N = 51$, age 51.4 ± 9.7 years), (ii) anxiety ($N = 18$, age 43.3 ± 12.7), (iii) Parkinson’s disease (PD; $N = 15$, age 64.2 ± 5.7), (iv) depression ($N = 9$, age 46.4 ± 12.1), and (v) periodic leg movement syndrome (PLM; $N = 6$, age 55.2 ± 13.6).

All subjects gave informed consent, and the study was approved by the local ethics committees of all involved sleep laboratories. General exclusion criteria were a history of drug abuse or habitation (including alcohol), psychoactive medication or other drugs, e. g. beta-blockers, and night-shift work. All healthy (disease-free) subjects reported no symptoms of neurological, mental, medical or cardiovascular disorders. Additional exclusion criteria for healthy subjects comprised: (i) significant medical disorders, (ii) a mini mental state examination (MMSE) score < 25 [FOLSTEIN *et al.* 1975], (iii) a Pittsburgh sleep quality index (PSQI) global score > 5 [BUYSSE *et al.* 1988], (iv) a usual bedtime before 10pm or after 12am, (v) a self-rating anxiety scale (SAS) raw score ≥ 33 [ZUNG 1971], and (vi) a self-rating depression scale (SDS) raw score ≥ 35 [ZUNG *et al.* 1965].

²²Since it is physiologically not well defined what the term *healthy* means, I consider subjects that were classified ‘healthy’ according to the SIESTA study protocol as healthy or *disease-free* [MEMBERS OF SIESTA EU PROJECT 1998]. Note that the condition healthy has in practice a different meaning in young and in elderly.

²³The terms *subject* and *patient* are well distinguished in medicine: While a subject is always healthy or disease-free, a patient is always diseased.

During the study the consumption of coffee, alcohol, and cigarettes was limited to the subjects' habitual rate [Dorffner *et al.* 1998].

2.4.3. DAPHNET Database

The DAPHNET database contains polysomnographic recordings from 44 healthy subjects and 50 sleep apnea subjects in the same age range obtained within the European Union project DAPHNET²⁴. This project was not specifically designed for pure sleep research, and hence, only one sleep laboratory (Charité Berlin) was among the project partners. Polysomnographic data from the DAPHNET database comprises 3 different EEG channels, 2-lead electro-oculogram (EOG), and 2-lead electro-myogram (EMG, chin and leg). Respiration was measured by nasal-air pressure and respiratory body movements (belt around abdomen), and obtained from pletysmograms. In addition to monitored snoring (microphone), oxygen saturation, and single-channel electrocardiogram (ECG) blood pressure was recorded by Portapress²⁵ and a pletysmogram. Sleep stages were identified following the same rules as discussed above [Sect. 2.3.2 RECHTSCHAFFEN AND KALES 1968; IBER *et al.* 2007]. Since I will exclusively focus on EEG recordings from the DAPHNET database and obtained results are only presented in Appendix F.4, I will not go into detail here.

²⁴Project title: *Dynamical Analysis of PHysiological NETworks* (DAPHNET).

²⁵Blood pressure is non-invasively measured at the finger.

3. Studying Fluctuations

In this chapter I study the scaling behaviour of fluctuations in complex systems. A particular aim is the development of mathematical models that describe the essential dynamics. They shall help to understand the way the components of the system interact. In principle any attempt to capture all components of a complex system, extract, and model the complete dynamics of the system is likely about to fail due to the enormous number of different nonlinearly interacting components. Even if we were able to capture all components of the system and understand their isolated dynamics it is impossible that the behaviour of the whole system can be modeled because of their complicated, i.e., *complex*, structure. From a certain point of view fluctuations represent the superposition of many unaccessible¹ and complicatedly coupled variables.

In the most simple additive model an observable (time series) $\{x_k\}_{k=1,\dots,N}$ can be thought of as a superposition of a periodic component $\{y_k\}$, a trend component $\{t_k\}$, and a noise component (fluctuations) $\{\xi_k\}$ [BROCKWELL AND DAVIS 2003].

$$x_k = y_k + t_k + \xi_k, \quad k = 1, \dots, N \quad (3.1)$$

This chapter is dedicated to investigate the noise component $\{\xi_k\}$ in Eq. (3.1) on the basis of a measurement $\{x_k\}$, and hence, aims towards a removal of both oscillatory components and trends on different time scales. As will be seen shortly, detrending algorithms yield information about the structure of trends and/or oscillations. The later component will be studied in more detail in Chapt. 4 where I will suggest methods to remove fluctuations from Eq. (3.1).

When fluctuations are inspected more precisely, it is apparent that they are not completely random for most systems but exhibit a certain structure and follow statistical rules. For instance during REM sleep it is observed in heartbeat interval data that large values are rather followed by large values and small values are rather followed by small values. Such persistence is often referred to as long-term correlation; recall the exact definition of long-term correlations in Sect. 1.2. Analogously, in anti-correlated time series increases in magnitude are more likely followed by decreases in magnitude and vice versa. A prominent anti-correlated example is the series of increments of heartbeat intervals. For a review on fractal structure in physiology see for example [GOLDBERGER *et al.* 2002].

3.1. Monofractal Fluctuation Analysis Methods

In the working hypothesis² of monofractal fluctuations one focusses on identifying power-law correlations that are characterized by a single scaling exponent in the asymptotic regime, i.e., at large time scales. However, deviations from a power law can be observed, for instance, in the presence of (i) unattended trends, (ii) periodicities, (iii) different scaling on small- and large time scales [see Fig. 3.2 and related discussion], and (iv) artifacts [see Fig. 3.3 and corresponding text]. As will be illustrated in the following, cases (i) and (ii) can often be handled by detrending methods, while (iii) allows for the definition of two (or more) separate power-law scaling regimes, and (iv) is generally avoided by a proper data preparation before an analysis.

¹The reader might find this term rather superficial since in principle any component could be captured assuming it is known what, where, and how to measure it. Unfortunately, in a complicated and/or complex system profound knowledge is in general not available.

²For an unknown dataset one usually does not know which type of scaling the noise obeys. When employing a monofractal analysis method as described in the following, one either assumes only monofractal structure to be present, or one wittingly ignores other types of order such as multifractality.

3.1.1. Hurst Rescaled-Range Analysis

More than 20 years before the word fractality was coined by Mandelbrot [MANDELBROT 1975]³ the geologist H. E. Hurst invented a *rescaled adjusted range statistics*, also known as *Hurst-R/S analysis*. He was interested in the statistics of runoff time series recorded from the Nile river in order to understand the impact of the Assuan dam [HURST 1951]. Let $\{x_k\}_{k=1,\dots,N}$ denote a time series, e.g., heartbeat intervals where k might be the beat number. Then, the R/S method is based on the first two moments derived locally within windows $\nu = 0, \dots, [N/s] - 1$ of width s (*range width*). The *local mean* $\langle x \rangle_{\nu,s}$ and the *local standard deviation* $S_{\nu,s} = [\text{Var}(\{x_k\}_{k \in [\nu s+1, (\nu+1)s]})]^{1/2}$ in the window ν are defined as

$$\langle x \rangle_{\nu,s} = \frac{1}{s} \sum_{i=1}^s x_{\nu s+i} \quad \text{and} \quad S_{\nu,s} = \left[\frac{1}{s} \sum_{i=1}^s (x_{\nu s+i} - \langle x \rangle_{\nu,s})^2 \right]^{1/2}. \quad (3.2)$$

Then, from each point in the window ν the local mean is subtracted and the cumulative time series, the *local profile* $Y_{\nu,s}(j)$, is calculated by

$$Y_{\nu,s}(j) = \sum_{i=1}^j (x_{\nu s+i} - \langle x \rangle_{\nu,s}) \quad : \quad j = 1, \dots, s \quad (3.3)$$

yielding – based on its extrema – the *range*

$$R_{\nu,s} = \max_{j=1}^s [Y_{\nu,s}(j)] - \min_{j=1}^s [Y_{\nu,s}(j)]. \quad (3.4)$$

Together with Eqs. (3.2) the *local rescaled range* $R_{\nu,s}/S_{\nu,s}$ and finally the *Hurst rescaled range* as the average over all windows ν can be calculated,

$$[R/S](s) = \frac{1}{[N/s]} \sum_{\nu=0}^{[N/s]-1} \frac{R_{\nu,s}}{S_{\nu,s}}. \quad (3.5)$$

Now, Eq. (3.5) is evaluated for many scales $s \in \mathbb{N} : 1 < s \leq N$. From linear regression in a double-logarithmic plot the *Hurst exponent* H is derived,

$$[R/S](s) \sim s^H. \quad (3.6)$$

A value $H > 0.5$ indicates long-range persistence, while $H < 0.5$ is associated with anticorrelations. Uncorrelated (independent random behavior) is retrieved for $H = 0.5$. It was shown that $H \approx (1+\beta)/2 = (2-\gamma)/2$ [HUNT 1951; MANDELBROT AND NESS 1968] where the latter two expressions equal the fluctuation exponent α , see Sects. 1.2, 3.1.2, and Eq. (1.24).

3.1.2. Fluctuation Analysis (FA)

Fluctuation analysis (FA) which was already briefly introduced and used to define long-range dependence in Sect. 1.2 is quite similar to Hurst-R/S analysis. It is, however, based on the theory of a random walk. The time series $\{x_k\}_{k=1,\dots,N}$ is therefore assumed to describe the steps of a random walker. Then the cumulative time series

$$Y(j) = Y_j = \sum_{k=1}^j x_k \quad , \quad j = 1, \dots, N \quad (3.7)$$

denotes the *FA-profile*⁴ of $\{x_k\}$ and characterizes the position of the random walker at discrete times t_k . In order to study scaling the time series is divided into $[N/s]$ non-overlapping segments of width s and for each segment the squared displacement of the random walker is obtained by

$$F_{\text{FA},\nu}^2(s) = [Y((\nu+1)s) - Y(\nu s)]^2 \quad : \quad \nu = 0, 1, \dots, [N/s] - 1. \quad (3.8)$$

³For an improved version in English see [MANDELBROT 1982].

⁴Later a mean-subtracted version will just be referred to as the *profile*.

After averaging over all segments this yields the fluctuation function $F_{\text{FA}}(s)$, i.e., the square root of the mean squared displacement. A scaling law can be obtained from evaluating $F_{\text{FA}}(s)$ for many scales s ,

$$F_{\text{FA}}(s) = \langle F_{\text{FA},\nu}^2(s) \rangle^{1/2} = \left[\frac{1}{[N/s]} \sum_{\nu=0}^{[N/s]-1} F_{\text{FA},\nu}^2(s) \right]^{1/2} \sim s^{\alpha_{\text{FA}}} . \quad (3.9)$$

The exponent α_{FA} is called the *fluctuation exponent*. Uncorrelated fluctuations lead to $\alpha_{\text{FA}} = 1/2$, while $\alpha_{\text{FA}} > 1/2$ indicates positive temporal correlations, and $\alpha_{\text{FA}} < 1/2$ anti-correlations. Note that integrating the time series according Eq. (3.7) is required to ensure a self-affine structure for which a scaling law can be obtained [BUNDE AND HAVLIN 1994]. If the profile was not derived before FA or any of the fluctuation analysis methods described in the following, only time series that are characterized by a fluctuation exponent larger than 1 could be handled. In particular this requirement is violated for anti-correlated fluctuations.

FA is the simplest fluctuation analysis method to show the relationship between the fluctuation exponent⁵ α and the correlation exponent γ . However, this relationship is not exact as we will see shortly, although, several papers assume an exact relationship. In the following I partially employ mathematical properties of the auto-correlation function which are given in [e. g., HONERKAMP 1994]. A summary of the proof is given in [KANTELDHARDT *et al.* 2001]. Consider the squared version of Eq. (3.9) together with Eq. (3.8)

$$\begin{aligned} F_{\text{FA}}^2(s) &= \left\langle \left(\sum_{k=1}^{(\nu+1)s} x_k - \sum_{k=1}^{\nu s} x_k \right)^2 \right\rangle = \left\langle \left(\sum_{k=\nu s+1}^{(\nu+1)s} x_k \right)^2 \right\rangle = \left\langle \sum_{k,l=\nu s+1}^{(\nu+1)s} x_k x_l \right\rangle \\ &= \frac{1}{[N/s]} \sum_{\nu=0}^{[N/s]-1} \sum_{k,l=1}^s x_{\nu s+k} x_{\nu s+l} = \sum_{k,l=1}^s \langle x_{\nu s+k} x_{\nu s+l} \rangle . \end{aligned}$$

Now it is usually argued that this term can be expressed by the auto-covariance function [Eq. (1.9a)] or by the auto-correlation function [Eq. (1.10b)]

$$F_{\text{FA}}^2(s) = \sum_{k,l=1}^s \text{Cov}(x_k, x_l) = \text{Var}(x) \sum_{k,l=1}^s C(x_k, x_l)$$

which in the case of weak stationarity only depends on the separation $|l - k|$ and the variance reduces to a constant c .

$$F_{\text{FA}}^2(s) = c \sum_{k,l=1}^s C(|l - k|) \quad (3.10)$$

Note, that Eq. (3.10) is not exact since the correct averaging would take place over the windows ν . Even if strongly overlapping windows (one step at a time) are considered, Eq. (3.10) does not exactly yield the standard auto-covariance. However, this inconsistency can be neglected for very long time series, i. e., in the limit $N \rightarrow \infty$, and for overlapping windows. In the approach involving non-overlapping windows this approximation causes differences between observed and theoretical slopes (α values) in particular for short time series. In a next step one can expand the summation over the auto-correlation function in the following way:

$$\begin{aligned} \sum_{k,l=1}^s C(|k - l|) &= sC(|0|) + (s-1)C(|1|) + \dots + (s - (s-2))C(|s-2|) + \\ &\quad (s - (s-1))C(|s-1|) + (s-1)C(|-1|) + \dots \\ &\quad + (s - (s-1))C(|1-s|) \end{aligned}$$

⁵Since the following relationship is used for all similar fluctuation analysis methods α_{FA} is denoted here and on the next page by α to emphasize the generality [see also discussion in Sect. 3.1.3].

yielding

$$\sum_{k,l=1}^s C(|k-l|) = sC(0) + 2 \sum_{m=1}^{s-1} (s-m)C(m). \quad (3.11)$$

Inserting Eq. (3.11) into (3.10) leads to

$$F_{\text{FA}}^2(s) = c \left[sC(0) + 2 \sum_{m=1}^{s-1} (s-m)C(m) \right] \quad (3.12)$$

For uncorrelated data the correlation function vanishes except for a zero time lag ($C(m) = 0 : \forall m \neq 0$). Hence, for uncorrelated data only the first term needs consideration, leading to

$$F_{\text{FA}}^2 \sim s \iff F_{\text{FA}} \sim s^{1/2}, \quad (3.13)$$

and thus, the fluctuation exponent for an uncorrelated time series (white noise) satisfies $\alpha = 0.5$. In the case of long-term persistence the auto-correlation function decays per definition according to a power law with correlation exponent γ , and hence, for large scales $s \gg 1$ the second term in Eq. (3.12) can be approximated yielding

$$\begin{aligned} F_{\text{FA}}^2(s) &= c \left[sC(0) + 2 \int_1^{s-1} sm^{-\gamma} - m^{1-\gamma} dm \right] \\ &= c \left[sC(0) + 2 \left(\frac{s(s-1)^{1-\gamma} - s}{(1-\gamma)} - \frac{(s-1)^{2-\gamma} - 1}{(2-\gamma)} \right) \right] \\ &\sim s + s^{2-\gamma}. \end{aligned} \quad (3.14)$$

In the long-term persistent limit $0 < \gamma < 1$. Thus, the left part of Eq. (1.24) follows from

$$F_{\text{FA}} \sim s^{(2-\gamma)/2}$$

together with Eq. (3.9)

$$\alpha = 1 - \frac{\gamma}{2}. \quad (3.15)$$

3.1.3. Detrended Fluctuation Analysis (DFA)

Analyses of real data as for instance temperature recordings, river runoff time series, heartbeat, or respiration are generally hampered by nonstationarities such as piecewise trends and/or oscillatory components. Since Hurst-R/S analysis and FA do not take nonstationarities into account, correlation results obtained from either of both are at risk of misinterpretation. Unattended trends can affect a fluctuation analysis, e. g., yield spurious scaling behavior or crossovers in the fluctuation function. Periodicities, on the other hand, might induce twists in the fluctuation function with positions depending on the period of the oscillation and amplitudes depending on the amplitude of the oscillation [see also Fig. 3.2].

To overcome this problem Peng *et al.* invented the *detrended fluctuation analysis (DFA)* in the context of studying DNA sequences. They integrated local detrending into the FA procedure [PENG *et al.* 1994, 1995]. Peng *et al.* originally considered the most simple 'detrending' approach by removing in each window ν the *local mean* in a similar way as Hurst did in 1951 [HURST 1951]. However, the concept can easily be generalized to higher order detrending [BUNDE *et al.* 2000]. Later, Kantelhardt *et al.* generalized DFA to study multifractality in time series by introducing detrended fluctuation functions of higher-moments [KANTELHARDT *et al.* 2002]. In spite of the monofractal DFA being a subset of *Multifractal Detrended Fluctuation Analysis (MF-DFA)* introduced in Sect. 3.3.1, I separately describe the DFA algorithm in following to provide a basis for its application to study scaling in heartbeat and respiration during sleep as presented in Sect. 3.2.

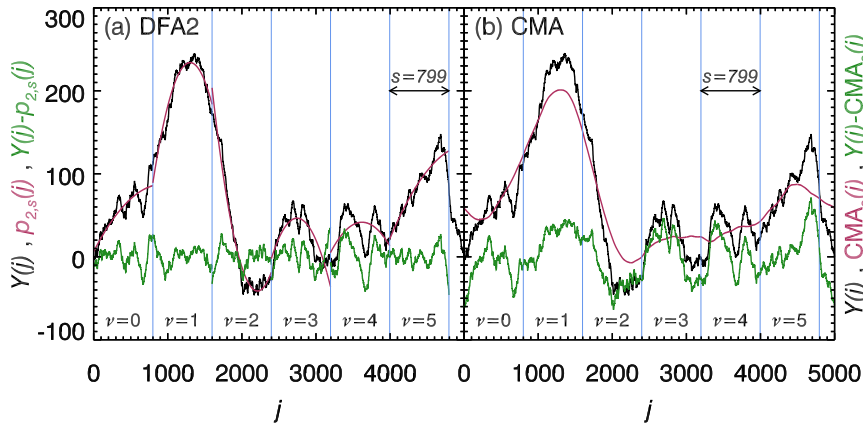


Figure 3.1.: Profile $\{Y_j\}_{j=1,\dots,N}$ of $f^{-\beta}$ noise $\{x_k\}_{k=1,\dots,N}$ [$\beta = 0.75$, $N = 5000$; black]. (a) Fitted detrending 2nd-order polynomials for the MF-DFA2 [purple], (b) centered moving averages considering cyclic continuation [purple] for the MF-CMA algorithm in segments of scale $s = 799$. Green curves are (a) detrended and (b) CMA subtracted profiles.

The DFA algorithm consists of four steps:

Step 1:

Analogously to the FA methodology in Sect. 3.1.2, the *profile* Y of a recording $\{x_k\}_{k=1,\dots,N}$ is derived according to

$$Y(j) = Y_j = \sum_{k=1}^j (x_k - \langle x \rangle) \quad (3.16)$$

where⁶ $j = 1, \dots, N$ and the subtraction of the mean $\langle x \rangle = N^{-1} \sum_{i=1}^N x_i$ is not mandatory since it would be removed by the later detrending in *Step 2*; compare with the FA-profile in Eq. (3.7). Removing the mean value ensures $Y(N) = 0$ which allows a cyclic continuation of the signal. While this could be helpful for short time series, a global mean might not be meaningful in strongly nonstationary signals.

Step 2:

The profile in Eq. (3.16) is divided into non-overlapping windows⁷ $\nu : \nu = 0, \dots, 2[N/s] - 1$ of width s , $s \in \mathbb{N}$ [see Fig. 3.1(a) for an illustration]. In order not to neglect data points at the end of the signal if N is not a multiple of the scale s and to improve statistics in shorter time series the segmentation starts (i) from the very beginning of the time series yielding the first $[N/s]$ consecutive segments, and (ii) from the very end of the time series yielding the next $[N/s]$ windows. Within each window ν n th-order fitting polynomials $p_{n,\nu} = \sum_{l=0}^n a_l x^l$ are calculated by least-squares regression and the sum of *squared local residuals of regression*⁸ (local variance) is derived:

$$F_{\text{DFA}n,\nu}^2(s) = \frac{1}{s} \sum_{i=1}^s \{Y(\nu s + i) - p_{n,\nu}(i)\}^2 \quad (3.17a)$$

for the forward direction and $\nu = 0, \dots, [N/s] - 1$ and

$$F_{\text{DFA}n,\nu}^2(s) = \frac{1}{s} \sum_{i=1}^s \{Y(N - (\nu - [N/s] + 1)s + i) - p_{n,\nu}(i)\}^2. \quad (3.17b)$$

for the backward direction and $\nu = [N/s], \dots, 2[N/s] - 1$, respectively.

Step 3:

Similarly to FA, studying averaged local fluctuations for many different scales⁹ $s \geq n + 2$ yields a scaling exponent α_{DFA} if the fluctuations follow a power law, see [TAQQU *et al.* 1995] for an

⁶Sometimes one includes a value $j = 0$ corresponding to a $Y_0 = 0$ which motivates a cyclic continuation of the profile after subtracting the mean value yielding $Y_N = 0$.

⁷ $[N/s] = \text{int}(N/s)$

⁸For that reason DFA is in the literature sometimes referred to as *residuals of regressions method*.

⁹A polynomial $p_{n,\nu}$ can be uniquely constructed from $n + 1$ grid points. In order to obtain a non-vanishing residual of regression at least $n + 2$ points are necessary.

analytical proof with $n = 1$ (DFA1),

$$F_{\text{DFA}}(s) = \left[\frac{1}{2^{\lfloor N/s \rfloor}} \sum_{\nu=0}^{2^{\lfloor N/s \rfloor} - 1} F_{\text{DFA},\nu}^2(s) \right]^{1/2} \sim s^{\alpha_{\text{DFA}}} . \quad (3.18)$$

Step 4:

From linear fits to $F_{\text{DFA}}(s)$ in a double-logarithmic plot the fluctuation exponent α_{DFA} can be obtained [see Figs. 1.1(f), 3.2, or 3.4 for examples]. Note that the variances in Eqs. (3.17) increase with increasing scale s , and thus, $F_{\text{DFA}}(s)$ is a monotonous function. Uncorrelated fluctuations in the data lead to $\alpha_{\text{DFA}} = 1/2$, while $\alpha_{\text{DFA}} > 1/2$ indicates positive temporal correlations, and $\alpha_{\text{DFA}} < 1/2$ anti-correlations.

The relation between α_{DFA} , the spectral exponent β [Eq. (1.20)], and the correlation exponent γ [Eq. (1.19)] is not as easily shown in an analytic way as for FA. However, it was proven that detrending does not affect the scaling behavior [HENEGHAN AND MCDARBY 2000]. For both limits of very small scales and very large scales deviations from a power law are often observed even in data constructed, e.g., by employing the Fourier filtering technique [Sect. 1.5.2]. In the first case the number of data points per window ν barely exceeds $n + 1$ and polynomial regression is very good yielding only small residuals and a systematically reduced fluctuation function $F_{\text{DFA}}(s)$. For very large scales the number of non-overlapping windows $\lfloor N/s \rfloor$ is small, hence, statistics becomes worse resulting in stochastic fluctuations in $F_{\text{DFA}}(s)$. For the same reason only scales up to $N/4$ should be considered reliable.

The characteristics and performance of DFA in various situations were comprehensively tested by several authors. For instance crossovers between different scaling regimes and the influence of polynomial trends and periodicities on DFA results were empirically studied by [KANTEHARDT *et al.* 2001] who also suggested dividing DFA fluctuation functions by a correction function obtained from shuffled data to correct the deviations on very small scales, see Fig. 3.2. Focusing on DFA1 Hu *et al.* provide analytical solutions for crossovers, trend scaling, and periodicities [HU *et al.* 2001], while Chen *et al.* study the influence of nonstationarities [CHEN *et al.* 2002] and find that cutting out up to 50% of the data points does not change positive long-term correlations but strongly affects anti-correlated scaling. The study was completed more recently by investigations on effects of nonlinear transformations [CHEN *et al.* 2005].

Today there are more than 850 papers employing DFA to study datasets from various fields of interest such as geoscience (temperature recordings, river runoff data, solar activity, wind speed recordings), medicine (physiological data such as heartbeat, brainwave recordings, respiration, gait), econophysics (asset return, volatilities), or solid state physics. It was even used as a basic tool to approach extreme events in extreme value statistics, see for instance [BUNDE *et al.* 2002] and [MEYERS 2009] for a recent review.

However, there were two critical inquiries on the limitations of DFA which should be mentioned. Firstly, it was argued that DFA – as a heuristic approach to studying long-range memory in time series – does not have an established limiting distribution which would be needed for specifying confidence intervals and hypothesis testing. Therefore, DFA should be considered rather as a diagnostic tool than a method for drawing statistical inference [RUST 2007]. While this is indeed true for a single dataset, results can be compared with findings obtained from a DFA of many surrogate time series (characterized by statistical properties one wishes to probe for). This comparison will allow assessing estimation errors and defining confidence intervals.

Secondly, it was reported that DFA is sensitive but not specific for detecting long-range dependence in signals, i.e., if long-range dependence is present in the signal it is identified by DFA but from finding a fluctuation index $\alpha > 0.5$ long-range persistence should not generally be concluded [MARAUN *et al.* 2004]. Nevertheless, I disagree with the strong statement of Maraun *et al.* which was obtained from studying three superimposed AR(1) processes only at scales much smaller than the decay time of the slowest AR(1) component, i.e., in the non-asymptotic regime. For larger scales DFA does clearly indicate uncorrelated behavior even for the Maraun model. This issue will be revisited and discussed in Appendix E.2.

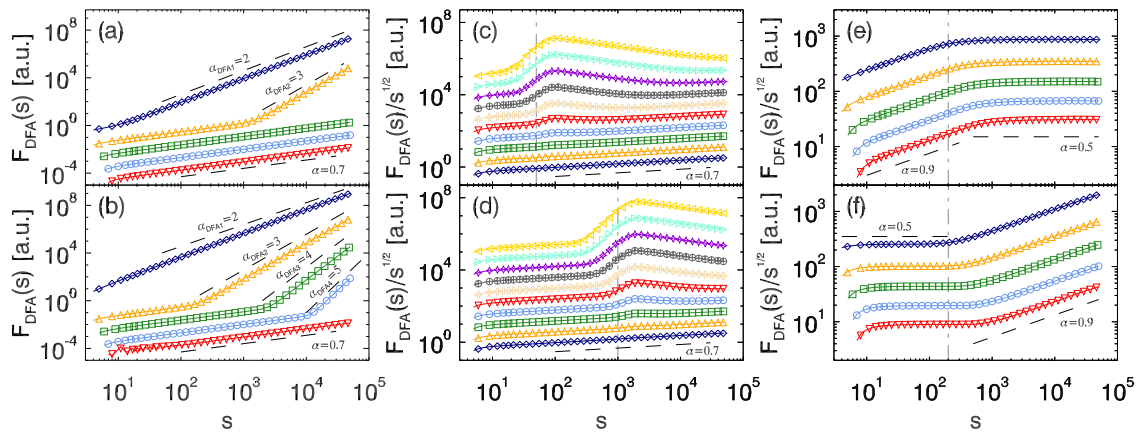


Figure 3.2.: Summary of important DFA characteristics. (a-d) DFA-fluctuation functions of long-term persistent monofractal data ($N = 200000, \alpha = 0.7$) with additional polynomial trends Ax^o [(a) $o = 2, A = 10^{-6}$ (b) $o = 4, A = 10^{-15}$; employing from top to bottom DFA1, DFA2, DFA3, DFA4, DFA5], and with additional periodicities $A \sin(2\pi x/T)$ [(c) $T = 50$, (d) $T = 1000$; from top to bottom $A = 25.6, 12.8, 6.4, 3.2, 1.6, 0.8, 0.4, 0.2, 0.1, 0.05$; employing DFA3]. (e,f) DFA-fluctuation functions of long-term persistent monofractal data with constructed crossover at scale $s_x = 200$ from correlated [$\alpha = 0.9$] to uncorrelated behavior [$\alpha = 0.5$; (e)] and from uncorrelated to correlated behavior [same α ; (f)] employing different orders of DFA [from top to bottom: DFA1 to DFA5; same symbols and colors as in (a,b)]. Fluctuation functions [arbitrary units] are shifted in (a-b) and divided by $s^{1/2}$ in (c-f) for clarity. In all panels dashed black lines indicate theoretical slopes and gray dashed lines mark periods (c,d) or crossovers (e,f) used in the model. Trends of order p cause crossovers in DFA n up to order $n = p$; the limit slope is $\alpha_{DFA_n} = n + 1$ [(a,b)]. Periodicities can disturb fluctuation functions depending on period T and amplitude A (c,d). Observed crossover positions depend on the DFA order; larger order shifts observed crossover towards larger scales (e,f). Each curve was obtained by averaging 200 configurations.

3.1.4. Centered Moving Average Analysis (CMA) – And Other Monofractal Fluctuation Analysis Methods

DFA and Hurst-R/S analysis are doubtlessly the most popular scaling methods to estimate power-law correlations. However, the computational effort due to the polynomial regression step in DFA and the jumps of the fitted polynomials at the edges of the windows led to the suggestion of numerous somewhat related fluctuation analysis algorithms which all provide certain advantages but also suffer certain limitations. None of them has been widely used, yet.

By definition the standard DFA algorithm yields to discontinuities between polynomial fits of neighboring non-overlapping windows. It was argued that this unlikely matches real (rather continuous) trends in the data and detrended moving average methods were advertised to overcome such limitation, however, at the price of detrending capabilities. The studies of Vandewalle *et al.* on moving averages [VANDEWALLE AND AUSLOOS 1998] motivated Alessio *et al.* to substitute the polynomials $p_{n,\nu}$ in Eqs. (3.17) by a backward moving average [ALESSIO *et al.* 2002] yielding the *backward moving average analysis (BMA)*. Its characteristics were further investigated and employed to study financial data in [CARBONE *et al.* 2004a,b]. However, BMA turned out to fail even for linear trends in the profile, i. e., constant trends in the data.

In a similar way a forward moving average analysis or a *centered moving average analysis (CMA)* can be defined [ALVAREZ-RAMIREZ *et al.* 2005], see also [BASHAN *et al.* 2008] for a recent review on detrended fluctuation analysis variants and moving averaging methods. Especially, the CMA has the advantage of local mean detrending by including both the dynamics of noise in the past and in the future, and it worked well for linear trends. Moving averages are in principle low pass filters. They can be calculated during runtime, and due to their generally much less computational costs in evaluation compared with DFA, they allow for a better statistics when overlapping windows are considered. Note that considering overlapping windows is also possible in DFA, however, computational loads increase significantly especially on large scales.

The CMA algorithm also comprises four steps:

Step 1:

Let $\{x_k\}_{k=1,\dots,N}$ denote the considered time series with $x_k = x(t_k)$. Then, the profile is calculated

by Eq. (3.16) as in DFA. The subtraction of the mean is again not mandatory, because it would be eliminated by the subtraction of local means in *Step 3*.

Step 2:

A centered moving average of an odd window length s (identified as scale) is obtained for (almost) every point j of the profile,

$$\text{CMA}_s(j) = \frac{1}{s} \sum_{i=-(s-1)/2}^{(s-1)/2} Y_{j+i}, \quad (3.19)$$

see Fig. 3.1(b). Note that the scales s , i.e., the window widths, in CMA must be odd in contrast to DFA where s can be even or odd. For all indices j at the edges of the profile, i. e., $1 \leq j < (s+1)/2$ and $N-(s-1)/2 < j \leq N$, a centered moving average does not exist. One might either ignore these points or use weighted averages of corresponding smaller incomplete windows instead. However, this might cause edge effects especially in short time series. A better approach is the cyclic continuation of the time series by connecting the very last part of the integrated signal (profile) to the beginning. When the profile is obtained following Eq. (3.16) there is no sudden jump at the connecting point. Not removing the mean value, however, will lead to a sudden jump and falsify the results. In case of a very long time series one might not want to cyclically continue the time series due to other nonstationarities such as trends. Then, however, the very beginning and the very end will not contribute much, anyway, due to large statistics.

Subsequently, the profile is again subdivided in $2[N/s]$ non-overlapping windows ν (segmentation starts at the very beginning and the very end of the signal), see Fig. 3.1(b) for the forward direction. For each window $\nu = 0, \dots, 2[N/s] - 1$ the variance (fluctuation) of the profile and the centered moving average is determined by

$$F_{\text{CMA},\nu}^2(s) = \frac{1}{s} \sum_{i=1}^s \{Y(\nu s + i) - \text{CMA}_s(\nu s + i)\}^2 \quad (3.20a)$$

for the forward direction and $\nu = 0, \dots, [N/s] - 1$, and

$$F_{\text{CMA},\nu}^2(s) = \frac{1}{s} \sum_{i=1}^s \{Y(N - (\nu - [N/s] + 1)s + i) - \text{CMA}_s(N - (\nu - [N/s] + 1)s + i)\}^2. \quad (3.20b)$$

for the backward direction and $\nu = [N/s], \dots, 2[N/s] - 1$, respectively. The centered moving averages in Eqs. (3.20) perform the detrending in CMA (compared to polynomials $p_{n,\nu}$ in DFA). In addition to constant trends in the profile CMA also removes linear trends because the centered average includes an equal number of points from the past and from the future. This explains the advanced performance compared to other detrended moving average methods such as BMA.

Note that I consider non-overlapping windows in this thesis for a better comparability with the DFA algorithm presented in Sect. 3.1.3. Then CMA is related to DFA1. However, overlapping windows can be considered at reasonable computational costs since computing the sums in Eqs. (3.20) for the window $\nu + 1$ reduces to subtracting the leading overlap from the sum corresponding to window ν and adding values from the overlap with window $\nu + 2$. In contrast, the DFA method [Sect. 3.1.3] requires a separate polynomial regression for each window. I suggest an adaptive overlap length which increases with the scale s in order to improve statistics especially on large scales.

Step 3:

Analogous to Eq. (3.18) fluctuations from all windows ν are averaged and calculated for many different scales s to obtain the CMA fluctuation function

$$F_{\text{CMA}}(s) = \left[\frac{1}{2[N/s]} \sum_{\nu=0}^{2[N/s]-1} F_{\text{CMA},\nu}^2(s) \right]^{1/2} \sim s^{\alpha_{\text{CMA}}}. \quad (3.21)$$

Step 4:

The fluctuation exponent α_{CMA} can finally be derived from a linear fit to the double-logarithmic plot of Eq. (3.21) if F_{CMA} follows a power-law.

CMA has two immediate advantages over DFA: (i) Systematically reduced values due to a 'well-suited regression' on small scales ($s < 10$) do not occur, and (ii) due to an enhanced statistics, because of overlapping windows (coming at 'no' computational costs), larger scales are reliably accessible compared with DFA. Nevertheless, higher order detrending is not possible with all moving-average methods and an application to data with strong trends is not possible. For the same reason a trend classification can not be achieved while trend orders can be quantified by comparing results from different detrending orders n in DFA.

I suggested a multifractal generalization of CMA [SCHUMANN AND KANTELHARDT 2010b] which will be introduced in Sect. 3.3.2, tested, and compared with MF-DFA, see Sect. 3.3.1. Note that to my opinion today's computational power, even provided by main stream CPUs, allows for analyzing data of reasonable length, e.g., up to $N = 100000$ data points, by employing DFA. Polynomial fitting requires a matrix inversion only once per scale (window size); beyond this, fitting is reduced to a simple matrix multiplication. For repeatedly high-load analyses of long datasets one might even take advantage of modern graphics-processor units (GPUs) which are specialized in fast matrix-operations¹⁰.

Another possible approach to study fluctuations in time series is closely related to wavelet analysis [see Sect. 1.3]. It takes advantage of the fact that certain wavelet bases are orthogonal to disturbing features in the signal. For instance n th-order Haar wavelets¹¹ are orthogonal to polynomial trends of the same order n . They can be utilized to remove such trends in a fluctuation-analysis algorithm similar to DFA [KOSCIELNY-BUNDE *et al.* 1998a,b; ROMAN *et al.* 2008]. There are two possible reasons why this algorithm did not become as popular as DFA: (i) No generally used acronym was established, i.e., abbreviations such as WLn , FAHW, WTA, or WTN coexist, and (ii) this algorithm was introduced in a slightly awkward way without a mathematically required rescaling. This led to the wrong assumption¹² WLn would perform worse compared with DFA_n . In Appendix E.1 I will discuss the methodology of WLn where Eqs. (3.17) for a Haar basis simply reduce to squared higher-order differences. These can be faster computed compared with residuals of regressions required in DFA. I employ WLn together with DFA to model data consisting of three superimposed AR(1) time series considering the same parameters as in [MARAUN *et al.* 2004] and illustrate why WLn and DFA_n provide exactly the same detrending capabilities and yield equivalent fluctuation functions for a correct rescaling, see Appendix E.2.

3.2. Fluctuations During Nocturnal Sleep

3.2.1. Impact of Undetected Heartbeats and Extrasystoles on DFA

Beat-to-beat interval time series (RRI), see Sect. 2.2 for a definition, often exhibit a spiky structure, which is originated either in heartbeats missed by the beat detection software (technical aspect) or in ectopic heartbeats such as extrasystoles (physiological aspect). In the first case large interbeat intervals occur which are roughly an integer multiple of the average RRI. Extrasystoles, on the other hand, are often characterized by a significantly smaller RRI followed by a compensating pause¹³ which maintains the average 'timing' of the heart.

¹⁰A common n th-order polynomial-regression algorithm to curves $\mathbf{y} = \{y_i\}_{i=1,\dots,s}$ starts with the Vandermonde matrix $V = (\mathbf{1}, \mathbf{t}, \mathbf{t}^2, \dots, \mathbf{t}^n)$ where $\mathbf{1}$ denotes the s -elements vector $(1, 1, \dots, 1)$ and $\mathbf{t}^i = (1, 2^i, \dots, s^i)$ is the vector of grid points to the power i . Then the fit matrix follows $F = (V^T V)^{-1} V^T$ with $(\cdot)^T$ and $(\cdot)^{-1}$ being the transposed matrix and the inverse. Finally, the fitted curve $\tilde{\mathbf{y}}$ is obtained by $\tilde{\mathbf{y}} = F\mathbf{y}$.

¹¹Or better Haar-wavelet alike functions that fulfill the principle requirements of a wavelet, i. e., vanishing mean and compact support. I will further denote such functions as higher-order Haar-wavelets for simplification.

¹²In the following I use the acronym suggested in the original publication [KOSCIELNY-BUNDE *et al.* 1998a].

¹³Here only the timing is considered while the deformed normal beat in the ECG recording is not further considered. See Sect. 2.2 for details.

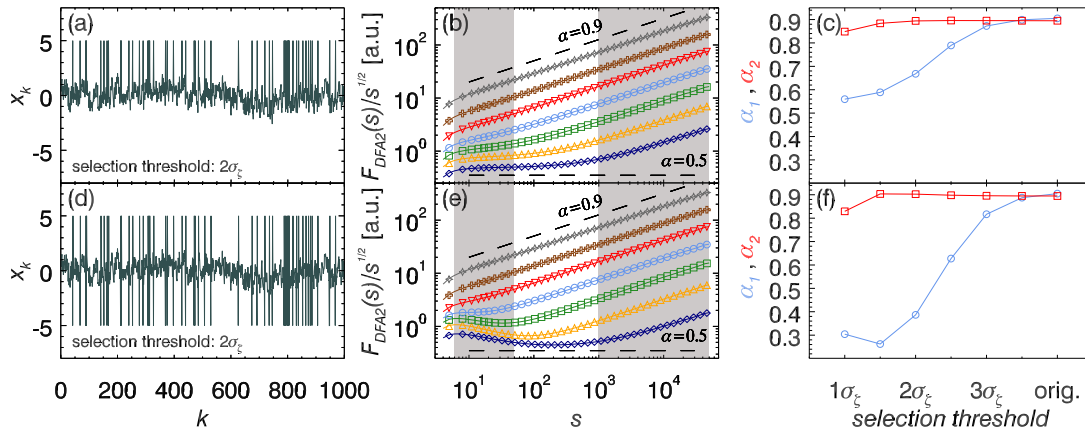


Figure 3.3.: Impact of two different types of artifacts on DFA2 which are often observed in RRI time series: (a-c) heart beats missed by peak detector cause longer beat-to-beat intervals [spikes type I], (d-f) extrasystoles consist of a shorter interval followed by a compensatory pause [spikes type II]. In a long-term persistent signal $\{x_k\}_{k=1,\dots,200000}$ [$\alpha = 0.9$] elements x_k are randomly replaced by a value of (a-c) 5 and (d-f) -5 if an associated random number ζ_k [$\{\zeta_k\}$ distributed as $\mathcal{N}(0,1)$] satisfies $|\zeta_k| > r\sigma_\zeta$ with $r \in \mathbb{R}^+$, $\sigma_\zeta = 1$. In (d-f) elements following a spike were additionally set to a value of 5. In (b,e) DFA2-fluctuation functions are shown; from top to bottom: signal without artifacts [gray diamonds], signals with artifacts of $p \approx 0.05\%$ [$r = 3.5$, brown crosses], $p \approx 0.27\%$ [$r = 3$, red triangles down], $p \approx 1.2\%$ [$r = 2.5$, light blue circles], $p \approx 4.6\%$ [$r = 2$, green squares], $p \approx 13.4\%$ [$r = 1.5$, yellow triangles up], $p \approx 31.7\%$ [$r = 1$, blue diamonds]. Percentages p are derived from the Gaussian error function $p = 1 - \text{erf}(r/\sqrt{2})$ with $\text{erf}(x) = 2/\sqrt{\pi} \int_0^x \exp\{-t^2\} dt$. Panels (c,f) illustrate scaling exponents α calculated from linear fits to $\log F(s)$ vs. $\log s$ within (i) a small scales range α_1 [$s \in [6, 50]$; blue circles], and (ii) a large scales range α_2 [$s \in [10^3, 5 \cdot 10^4]$, red squares]. Ranges are marked by gray bars in (b,e).

Clearly, such disturbances in RRI signals affect fluctuation-analysis results, and therefore, corresponding changes in the fluctuation function as well as effects on derived scaling exponents have to be studied. Although, Chen *et al.* qualitatively studied changes in the DFA1 fluctuation function induced by spikes in long-term correlated data [CHEN *et al.* 2002]¹⁴ they did neither systematically study higher order detrending nor did they quantify implications for fluctuation exponents on different scales. Fluctuation functions obtained from RRI signals often exhibit a characteristic crossover between two scaling regimes. Therefore, two different fluctuation exponents are defined in heartbeat data: The exponent that characterizes scaling on short scales is denoted by α_1 and the exponent corresponding to long scales is denoted by α_2 . Before I present results which I obtained from real physiological time series I would like to motivate why a (unfortunately time-consuming) beat classification with the utmost care must precede all serious attempts to study power-law scaling in heartbeat data.

Consider a long-term correlated time series $\{x_k\}_{k=1,\dots,N}$ of zero mean ($\mu_x = 0$) and unit variance ($\sigma_x^2 = 1$) which was generated by Fourier filtering [see Sect. 1.5.2] and subsequently disturbed by adding randomly occurring spikes. After generation each data point x_k is associated with a normally distributed random number ζ_k (with mean $\mu_\zeta = 0$ and variance $\sigma_\zeta^2 = 1$; typically denoted by $\mathcal{N}(0,1)$). An elements x_k is replaced by a spike if the associated random number ζ_k satisfies $|\zeta_k| > r\sigma_\zeta = r$ with the tuning parameter $r \in \mathbb{R}^+$. Figure 3.3(a) shows a fragment of such a time series where selected elements are replaced by the value 5. This type (further called type I) of constructed model data is related to missed heartbeats during the peak detection. For the second type of spikes (further called type II) resembling certain extrasystoles¹⁵ I replaced the selected elements in the signal with a value of -5 (representing ventricular beats) and the succeeding element by a value of 5 (representing the compensatory pause), see Fig. 3.3(d).

Results for different percentages of spikes obtained from DFA2 are depicted right of the corre-

¹⁴Please note that Chen *et al.* write they use DFA2 but instead only remove linear trends from the 'integrated signal' (profile) which is indeed DFA1 in the standard definition according to the original work [BUNDE *et al.* 2000].

¹⁵Although most extrasystoles are followed by a compensating pause, they might also occur additionally between normally timed heartbeats. This would result in two spikes that are related to type I spikes but are pointing down.

sponding model in Figs. 3.3(b,e). From the fluctuation function it is already apparent that even a small number of spikes strongly affects short-range scaling while long-range persistence, on the other hand, is practically unaffected. For type II spikes the effect is stronger because each small value in the signal is followed by a large value, compare Figs. 3.3(b,e) and 3.3(c,f). However, note that the effect does not exclusively come from twice as many spikes (down and up) compared with type I spikes but can be elucidated by their impact on the profile: Type I spikes yield nonstationarities expressed by jumps to larger values which occur on average – for a fixed scale s – equally often in each window ν , except for very small scales. Hence, corresponding polynomial fits will be affected in a similar way. Moreover, such jumps represent trends of order 0 which are removed by DFA2. In the presence of many spikes smaller windows ‘appear’ more uncorrelated which explains the limit of $\alpha_1 = 0.5$ for type I spikes, see lower blue curve in Fig. 3.3(b) and the change in α_1 scaling behavior shown in Fig. 3.3(c). In contrast, for type II spikes the profile itself is disturbed by spikes pointing down – at a position k of a spike in the signal the profile is reduced by 5 (spike down) and in the next step, $k + 1$, this reduction is compensated by adding 5. Second-order polynomials (DFA2)¹⁶ cannot well approximate such spikes in the profile, in particular on small scales s . The more the scale is increased the less the spikes disturb a polynomial regression, and the correct scaling ($\alpha = 0.9$) is obtained, see Figs. 3.3(e,f).

Hence, windows containing spikes result in a too large local fluctuation $F_\nu(s)$ [see Eq. (3.17)]. As the percentage of spikes increases more windows exhibit spuriously large local fluctuations, and the resulting DFA fluctuation function $F_{\text{DFA}}(s)$ [Eq. (3.18)] for very small scales, e.g. $s < 15$, might even become larger than for intermediate scales as is observed for the blue curve in Fig. 3.3(e). Consequently, anti-correlated behavior¹⁷ could be concluded from corresponding fluctuation exponents α_1 .

Figures 3.3(c,f) report the full results from studying the dependence of both scaling exponents α_1 and α_2 on ratio of spikes in the data. While α_2 is practically unaffected by both types of spikes, α_1 exhibits uncorrelated behavior for approximately 2.4% spikes ($|\zeta_k| > 2.25\sigma_\zeta$) and anti-correlations for a larger percentage of type-II spikes. The dramatical effects of spikes on short-term scaling exponents imply that careful beat classification must precede any fluctuation analysis unless one is only interested in long-term persistence.

3.2.2. Fluctuations in Heartbeat and Respiration

In order to better understand autonomous control and its regulation during sleep the correlation structure in heartbeat and respiration has been studied in several databases for disease-free subjects and patients suffering from various diseases. In particular short-term scaling exponents were identified to discriminate different stages of heart failures, e.g., chronic heart failure or multiple organ dysfunction syndrome, see for example [HUIKURI *et al.* 2009] and references therein. However, previous studies were not based on a large database such as SIESTA [Sect. 2.3] comprising approximately 350 whole-night recordings of disease-free subjects. Most of the results from employing DFA2 to heartbeat and respiration which I present and discuss in the following were published in [SCHUMANN *et al.* 2008b, 2010a].

Data Preparation

In order to separately study correlations within respiratory data and heartbeat data for different sleep stages as well as nocturnal wakefulness I divide all recordings into segments corresponding to wake, light sleep S1, light sleep S2, deep sleep (S3 & S4 combined, as suggested in [IBER *et al.* 2007]), and REM sleep. From each segment the first and last 30s are disregarded since sleep stage determination during transitions is sometimes complicated and possibly unreliable. Results from light sleep S1 are skipped for the moment because of insufficient statistics [see Fig. 2.9 or brown curves in Fig. 3.7]. However, I will partially include results for light sleep S1 in Chaps. 4 and 5. Heartbeat time positions (R-peaks) were extracted from the ECG data using the semi-automatic peak detector *Raschlab* developed by the cardiology group of Klinikum Rechts der Isar, Munich

¹⁶And n th order polynomials for DFA n .

¹⁷Here only induced by sequences ‘0’, –5, 5, ‘0’ where ‘0’ represents the value before or after the type II spike.

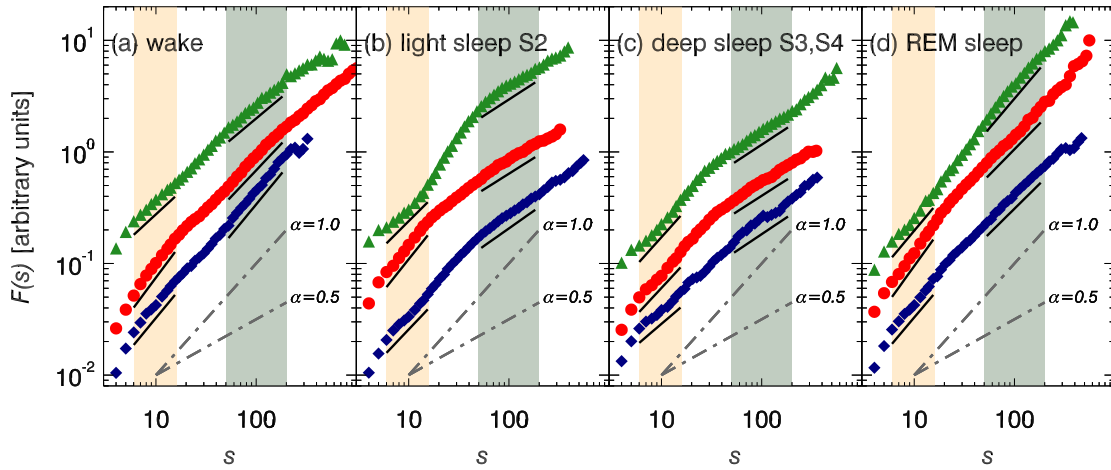


Figure 3.4: Examples of DFA2 heartbeat fluctuation functions for different sleep stages and representative subjects from three age groups, from bottom to top: young - blue diamonds, intermediate age - red circles, and elderly - green triangles up. Yellow and gray shaded bars indicate the fitting regimes for $\alpha_{RR,1}$ ($6 \leq s \leq 16$ heartbeats) and $\alpha_{RR,2}$ ($50 \leq s \leq 200$ heartbeats). The slopes of the solid black lines are identical with these fitted exponents. For comparison gray dash-dotted lines indicate slopes of $\alpha = 1/2$ (uncorrelated behavior) and $\alpha = 1$ ($1/f$ noise). Fluctuation functions and fits are vertically shifted for clarity.

Germany [SCHNEIDER 2005]. A beat classification (normal beat, ventricular beat, artifact) was assigned to each R-peak by the detector and checked by visual inspection. The series of time intervals between consecutive heart beats (RRI) was calculated, and RR intervals were excluded if (i) either the beat (R-peak) before the interval or the one after it was not normal, (ii) the calculated interval was shorter than 330ms or longer than 2000ms, or (iii) the interval was more than 30% shorter or more than 60% longer compared with the preceding interval. The purpose of the last filter was to eliminate extrasystoles and ectopic beats unnoticed by the peak detector, see also Fig. 3.3 and related discussion. Furthermore, all sleep stage segments containing less than 100 normal-to-normal intervals or more than 5% excluded intervals were treated as unreliable and fully disregarded in the analysis.

Recorded oronasal airflow data were processed by determining the times and values of the signals' maxima and minima, representing the ends of the expiration and inspiration phases, respectively¹⁸. Since noise in the data mainly consists of spikes (outliers of type I), a simple threshold filter is sufficient. All data points exceeding a threshold of 95% of the maximum value or dropping below 95% of the (negative) minimum value within a moving time window are clipped to the corresponding threshold values. Data was resampled at 4Hz before identifying maximum and minimum values. In addition a classification scheme assigning to each event a reliability depending on (i) the length of the identified breathing cycle, (ii) the difference between cutoff threshold and extremal point, and (iii) a comparison with averages over three preceding and three following breathing cycles was implemented.

I applied the described filters separately for each subject and each night, taking into account all reliable segments for the same stage. Preceding Detrended Fluctuation Analysis (DFA2) all excluded intervals were cut out and the gaps were joined. This procedure was shown not to affect the DFA results for positively correlated data even if up to 50% of the data is removed [CHEN *et al.* 2002]. Note that I did not join different segments from the same sleep stage type but derived local fluctuations $F_{DFA2,\nu}(s)$ [Eqs. (3.17)] separately for each segment in order to avoid strong discontinuities at the joining point.

Fluctuation functions obtained from heartbeat data usually exhibit a crossover between two different scaling regimes. For that reason I distinguish slopes $\alpha_{RR,1}$ for small scales ($6 \leq s \leq 16$ heartbeats) and slopes $\alpha_{RR,2}$ for larger scales ($50 \leq s \leq 200$ heartbeats). Note that for the calcu-

¹⁸Oronasal airflow was obtained by temperature measurements (thermistor). In the study it was assumed that during inspiration inhaled air cools down the thermistor while during expiration exhaled air warms up the thermistor.

lation of long-range fluctuation exponents (in DFA) the upper boundary is usually set to $s = N/4$ instead of $s = 200$. Because the number of transitions between different sleep stages, and hence, the duration of data fragments varies between different subjects, I have chosen a limit of $s = 200$ to achieve good statistics (averages over many windows) and to ensure a comparability of results. In contrast to heartbeat no established crossover is observed in respiration in general. Hence, it can be characterized by just one fluctuation exponent α_{RES} . From the finding of preferential 4 : 1 cardiorespiratory coupling (which will be discussed in detail in Chapt. 5), i.e., on average a breath cycle spans four heartbeats, I have defined an associated fitting range of $12 \leq s \leq 50$ breaths for comparability with $\alpha_{\text{RR},2}$.

Short-term correlations quantified by $\alpha_{\text{RR},1}$ are related to the HF-band. This can be shown by a simple approximation. Recall that for DFA a scale correction depending on the detrending-order has to be applied because observed crossovers are shifted towards larger scales compared with the real crossover, see Fig. 3.2(a,b). For DFA2, $s_{\text{real}} \approx s_{\text{observed}}/2.5$ applies [KANTELHARDT *et al.* 2001]. Hence, a considered scaling range [6, 16] heartbeats transforms to a real scaling range of [2.4, 6.4] heartbeats which corresponds to the frequency band [0.156, 0.417]Hz under the simplified assumption of an average heartbeat interval of 1s. The HF band is usually associated with [0.15, 0.4]Hz and parasympathetic activity [see Sect. 2.2 and HRV TASK FORCE 1996]. Scaling exponents $\alpha_{\text{RR},2}$ and α_{RES} , on the other hand, describe long-range correlations associated with the LF and VLF bands. They thus reflect cerebral dynamics in addition to autonomic control; DFA results for large scales might elucidate additional features of cardiopulmonary control and coupling.

Effects of Normal Aging on Fluctuation Exponents

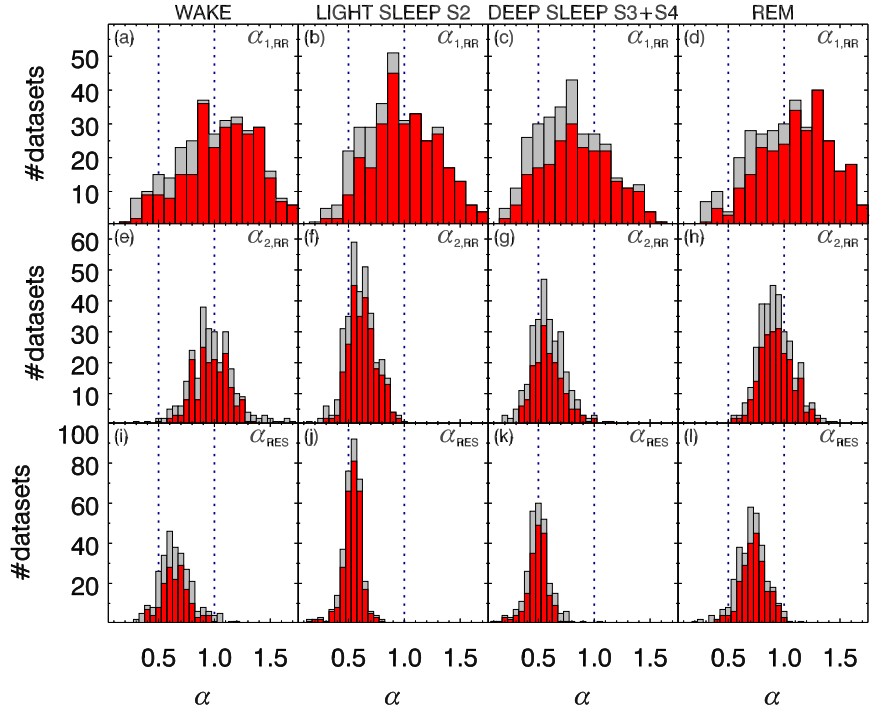
Figure 3.4 shows the heartbeat fluctuation functions $F_{\text{DFA2}}(s)$ of three representative subjects from different age groups: (i) young subjects (20-39 years, lowest curves in each panel), (ii) intermediately aged subjects (40-69 years, center), and (iii) elderly subjects (70-89 years, top) in double-logarithmic plots. Both scaling regimes for $\alpha_{\text{RR},1}$ (characterizing short-term correlations) and $\alpha_{\text{RR},2}$ (characterizing long-term correlations) are marked by gray bars. The slopes of the black solid lines are identical with the fitted values of $\alpha_{\text{RR},1}$ and $\alpha_{\text{RR},2}$ for the presented examples. There are two important observations. First, one clearly sees the presence of long-range correlations ($\alpha_{\text{RR},2} \approx 1 \gg 1/2$) during wakefulness and REM sleep while long-term correlations are weak or absent during light sleep and deep sleep ($\alpha_{\text{RR},2} \approx 1/2$). This finding is consistent results reported in [BUNDE *et al.* 2000; PENZEL *et al.* 2003]. Secondly, age differences in the scaling behavior are apparent, especially when comparing $\alpha_{\text{RR},2}$ for young and elderly subjects during wakefulness and REM sleep, and when comparing $\alpha_{\text{RR},1}$ for young and intermediately aged as well as intermediately aged and elderly during all sleep stages.

In order to further investigate these age-dependencies I calculated DFA2 fluctuation functions for heartbeat and oronasal airflow from 180 disease-free healthy subjects¹⁹ (85 males and 95 females) contained in the SIESTA database [see Sect. 2.3] and derived scaling exponents $\alpha_{\text{RR},1}$, $\alpha_{\text{RR},2}$, and α_{RES} .

Some of the individual fluctuation functions do not very well follow a power law most likely due to unnoticed nonstationarities in the raw data (only a 2nd-order polynomial detrending was performed). To verify the quality of the fits I additionally computed the coefficient of determination r^2 for each slope α and disregarded fits with $r^2 < 0.98$, since these fluctuation functions are not sufficiently close to a power-law. The full results are reported in Fig. 3.5 where I have plotted for each sleep stage histograms of all three α values in gray and marked in red the proportion of those which passed the acceptance criterion. Rechecking the supposedly healthy subjects who failed the power-law test often revealed unrecognized sleep apnea episodes [see Sect. 2.3]. Since the duration of such apneas has a characteristic time scale, a crossover in the DFA scaling function is observed and the power law is violated, see also [SCHMITT AND IVANOV 2007]. Sleep apnea episodes appear mostly during deep sleep with an immediate transition to light sleep, or already during light sleep. Depending on the strength of the apnea event it is often not terminated before an arousal (brief

¹⁹Note that I later use brain-wave recordings from 190 disease-free subjects. The reason for a smaller number here is that some subjects were disregarded due to missing or spoiled (many artifacts) heartbeat or respiration signals.

Figure 3.5.: Histograms of (a-d) $\alpha_{RR,1}$, (e-h) $\alpha_{RR,2}$, and (i-l) α_{RES} in wake state, light sleep S2, deep sleep S3&S4, and REM sleep. Gray histograms show the distributions for all 348 datasets considered in this study, while the α values from fits with $r^2 < 0.98$ or incomplete fitting regimes were excluded for the red histograms. Dotted lines indicate random uncorrelated behavior $\alpha = 1/2$ and strongly correlated behavior $\alpha = 1$. Note that the bins were chosen twice as wide for (a-d) compared with (e-l).



wake episode as short as 3s) occurs. Due to apneas, deep sleep is reduced or even inhibited and sleep becomes fragmented (many arousals) yielding a loss of the regenerative function of sleep.

To study effects of normal aging on the correlation structure in heartbeat and respiration all subjects were classified in seven age groups, each spanning ten years. Figure 3.6 shows mean values and standard errors of the means for $\alpha_{RR,1}$, $\alpha_{RR,2}$, and α_{RES} separately for (i) different sleep stages, (ii) all age groups, and (iii) all subjects, males, and females. Note that I have combined results from signals of both nights (adaptation night and recording night) after checking that differences are not relevant.

Since the distributions in Fig. 3.5 are very close to Gaussians, a Student's t-test can be applied to check the significance of differences [Appendix D.1]. The numerical means and standard deviations (instead of standard errors of the means in Fig. 3.6) for the three α parameters and sleep stages in young, intermediately aged, and elderly subjects are reported in Tab. 3.1. For all combinations of these three age groups significances for their difference were obtained by applying a Student's t-test [Appendix D.1] and are indicated by symbols based on the corresponding p values, see table caption for details.

Heartbeat

The most intriguing finding is an age dependence in heartbeat correlations on short time scales, i. e., in the exponent $\alpha_{RR,1}$, cp. Figs. 3.6(a-d). In the age range from 20-59 years a significant increase in $\alpha_{RR,1}$ is observed across all sleep stages except for wake where the statistical analysis shows no significant difference between the 20-29 year and the 50-59 year group (t-test: $p > 0.05$). This increase is almost independent of gender [see Figs. 3.6(a-d) and Tab. 3.1]. Above 60 years of age a systematic and significant decrease in $\alpha_{RR,1}$ occurs with further aging, except during deep sleep where statistics are insufficient in the elderly groups. Recall from the introduction [Sect. 2.3 and Figs. 2.9(b,c)] that the total time spent in deep sleep is noticeably reduced in elderly subjects which results together with a generally increased occurrence of ectopic beats in the rejection of many segments of data. For instance, the average $\alpha_{RR,1}$ value for the 80-89 year old group during deep sleep as shown in Fig. 3.6(c) is based on only eight $\alpha_{RR,1}$ values from six subjects.

The general picture of a maximum in $\alpha_{RR,1}$ in the age regime of 50-60 years is, nevertheless, unaffected by the considered sleep stage (or wake). It also occurs in the same way for both, males and females, proving a high reliability. However, in the intermediate age group of 40-69 years, the values for females are lower than those for males at a $p < 0.03$ significance level during wakefulness, deep sleep and REM sleep [see Table 3.1]. These differences are an additional indication of an

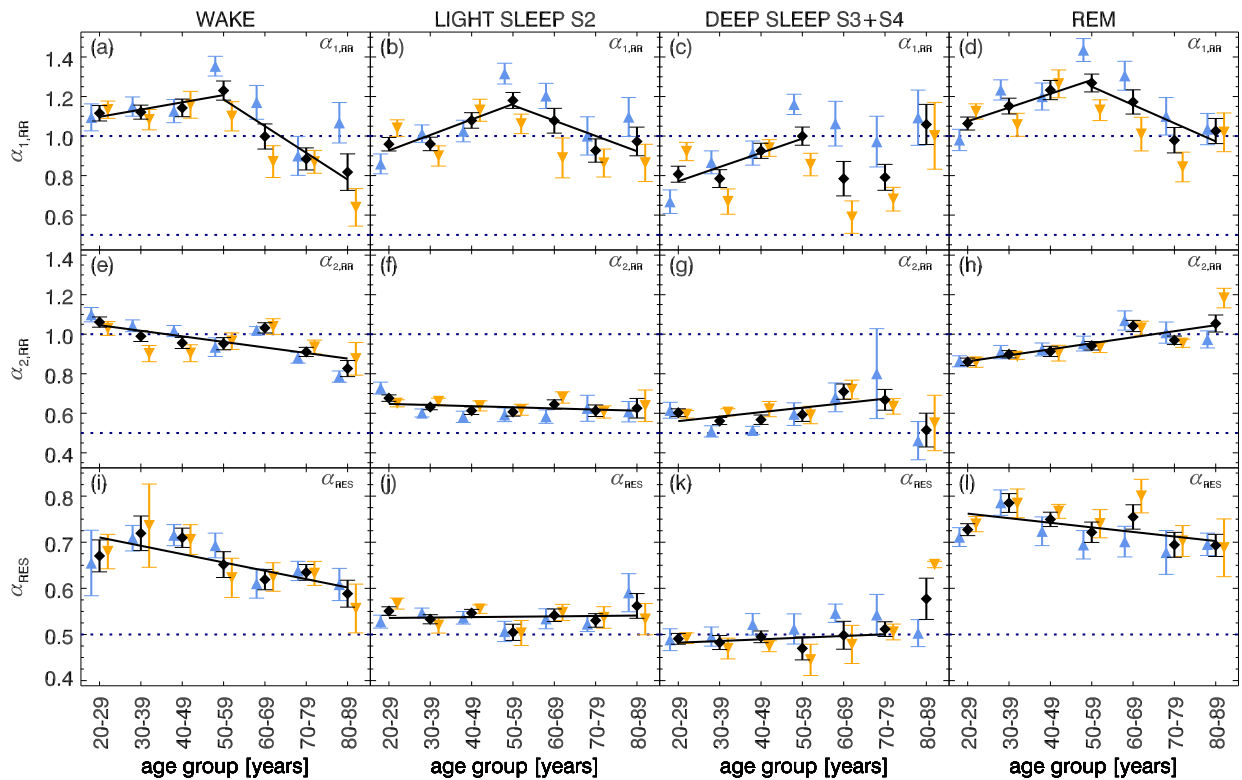


Figure 3.6.: Age dependence of (a-d) heartbeat short-term fluctuation exponents $\alpha_{RR,1}$, (e-h) heartbeat, and (i-l) respiration long-term fluctuation exponents $\alpha_{RR,2}$ and α_{RES} for wakefulness, light sleep S2, deep sleep S3&S4, and REM sleep. The mean values for all subjects [black diamonds], men [blue triangles up], and women [orange triangles down] are shown with error bars representing the standard errors of the means. Black solid lines indicate linear fits to the means based on all age groups, except for $\alpha_{RR,1}$, where two separate fit regimes [20-59 and 50-89 years] were chosen and for deep sleep, where insufficient statistics in elderly did not allow fitting. Note that α values with $r^2 < 0.98$ or incomplete fitting regimes in $F(s)$ were disregarded. The dotted lines mark $\alpha = 1/2$ [uncorrelated behavior] and $\alpha = 1$ [$1/f$ noise].

earlier decay of $\alpha_{RR,1}$ in females as could be speculated from Figs. 3.6(a-d). A possible explanation for this finding seems to require a change in the related control mechanisms which is sufficiently fundamental to affect all sleep stages and wakefulness. Similar rises were reported to emerge at the age of 50 years in evening cortisol²⁰ levels associated with an increase in sleep fragmentation and a decline in REM sleep [VAN CAUTER *et al.* 2000]. High cortisol levels have been identified with physiological stress and an increased cardiac risk. Reduced short-term correlation exponents ($\alpha_{RR,1}$) were shown to be a better indicator for predicting cardiac risk and mortality in infarction patients than standard HRV parameters [MÄKIKALLIO *et al.* 1999; HUIKURI *et al.* 2000].

Further note that disabling the quality check based on r^2 and keeping ectopic beats yielded an additional decrease in $\alpha_{RR,1}$ down to values close to 0.5 indicating uncorrelated behavior. This observation affirms the importance of careful filtering and data preparation, see also Fig. 3.3 and related discussion. Note that the coefficient of determination is typically not examined carefully in clinical applications, and hence, the good performance of $\alpha_{RR,1}$ for predicting cardiac risk and mortality in infarction patients compared with standard HRV parameters [MÄKIKALLIO *et al.* 1999; HUIKURI *et al.* 2000; JOKINEN *et al.* 2003] might partly be originated in a sloppy data preparation. In Elderly more ectopic beats are in general observed which can reduce $\alpha_{RR,1}$ values. A correlation of $\alpha_{RR,1}$ with the number of *ventricular premature complexes (VPCs)* that are also used for cardiac risk assessment [KLEIGER *et al.* 1987; CAIRNS *et al.* 1997] is, thus, not completely surprising.

Besides the most interesting age dependence, my analysis shows significant differences in $\alpha_{RR,1}$ values across sleep stages for all age groups (except the 80-89 years group, where statistics are not sufficient). These differences are comparable to the age differences within each sleep stage.

²⁰A stress hormone.

Measure	$\alpha_{RR,1}$	$\alpha_{RR,2}$	α_{RES}
Wake			
Young	1.12 ± 0.25 †	1.02 ± 0.15 † ◦	0.69 ± 0.16 *
Middle	1.13 ± 0.33 ◦	0.98 ± 0.15	0.66 ± 0.12
Elderly	0.87 ± 0.35 †	0.89 ± 0.14 ‡	0.62 ± 0.10
Light sleep S2			
Young	0.96 ± 0.26	0.65 ± 0.11	0.54 ± 0.07
Middle	1.12 ± 0.29 †	0.62 ± 0.13	0.53 ± 0.08
Elderly	0.95 ± 0.35 ‡	0.60 ± 0.14	0.54 ± 0.10
Deep sleep S3&S4			
Young	0.80 ± 0.29	0.59 ± 0.13	0.49 ± 0.09
Middle	0.93 ± 0.29 ‡ ◦	0.60 ± 0.15	0.49 ± 0.11 ◦
Elderly	0.84 ± 0.35	0.60 ± 0.15	0.52 ± 0.07
REM sleep			
Young	1.11 ± 0.28	0.88 ± 0.13 †	0.75 ± 0.11 *
Middle	1.23 ± 0.33 ‡ ◦	0.95 ± 0.15 †	0.74 ± 0.12 ◦
Elderly	1.00 ± 0.36 †	1.00 ± 0.13	0.69 ± 0.12

Table 3.1.: Mean values and standard deviations for fluctuation exponents α during wakefulness, light sleep stage S2, deep sleep S3&S4, and REM sleep distinguishing three cohort subsets: young [age 20-39], intermediately aged [age 40-69], and elderly [age 70-89]. The null-hypothesis that values for a pair of cohort subsets are drawn from identical distributions was checked by a two-sided heteroscedastic Student's *t*-test. Three significance levels are indicated by symbols, $p < 0.001$ (†), $p < 0.01$ (‡), and $p < 0.03$ (*). The symbols (†, ‡, *) in the line for young subjects refer to the test comparing young and elderly, the symbols in the line for intermediately aged subjects to comparing them with young, and the test in the line for elderly refers to comparing elderly with intermediately aged. Additionally, the symbol ◦ indicates significant differences [$p < 0.03$] between males and females in the same age group.

Specifically, for the 20-29 years old group a significant difference is found between sleep stages with lowest $\alpha_{RR,1}$ values during deep sleep, higher values during light sleep and highest values during REM and wake (see Figs. 3.6(a-d), $p < 0.01$ for deep versus light sleep and light sleep versus wake, and $p < 0.001$ for deep sleep versus REM).

For larger time scales I find $\alpha_{RR,2} \approx 0.9 \gg 1/2$ indicating long-term persistence during wake and REM sleep. In contrast, correlations are almost absent during non-REM sleep, i.e., light sleep and deep sleep, with $\alpha_{RR,2} \approx 0.6$. This confirms the scaling behavior observed previously in a much smaller cohort of young subjects [BUNDE *et al.* 2000; PENZEL *et al.* 2003] as well as in a group of elderly subjects [SCHMITT *et al.* 2009], suggesting a common dependence of $\alpha_{RR,2}$ on sleep stages for all age groups.

The 50-59 year old group, where the maximum in $\alpha_{RR,1}$ occurs, exhibits a similar pattern of lowest values during deep sleep and higher values during light sleep, REM and wake (see Figs. 3.6(a-d)), with $p < 0.01$ for deep versus light sleep, $p < 0.001$ for deep versus REM sleep and no significant differences between wake, REM and light sleep. Comparing the 20-29 year old group with the 50-59 year old group, a statistically significant age difference is obtained within each sleep stage (deep sleep $p < 0.01$, light sleep $p < 0.001$, REM sleep $p < 0.001$) but not wake ($p > 0.05$). The age differences are statistically similar to the differences across sleep stages for each of the two groups. Hence, they indicate that the effect of sleep regulation on $\alpha_{RR,1}$ in heartbeat intervals is comparable to the effect of aging.

When focusing on the age dependence of $\alpha_{RR,2}$, significant changes are observed during REM and wake [see Figs. 3.6(e,h)] while long-term correlation appear to be practically independent of age during non-REM sleep. During REM sleep, $\alpha_{RR,2}$ increases from $\alpha_{RR,2} \approx 0.85$ for young adults (aged 20-29) up to values $\alpha_{RR,2} \approx 1.05$ in the very elderly (aged 80-89). While this increase is statistically significant for the young and middle age groups, there is no significant difference when comparing intermediate age and elderly subjects [see Fig. 3.6(h) and Tab. 3.1]. During wakefulness an opposite behavior is observed, i.e., $\alpha_{RR,2}$ decreases from $\alpha_{RR,2} \approx 1.05$ towards $\alpha_{RR,2} \approx 0.85$ with normal disease-free aging. Except for comparing the young and the intermediate age groups this decrease is statistically significant for all age group combinations [see Fig. 3.6(e) and Tab. 3.1]. During light sleep and deep sleep no significant age dependence in $\alpha_{RR,2}$

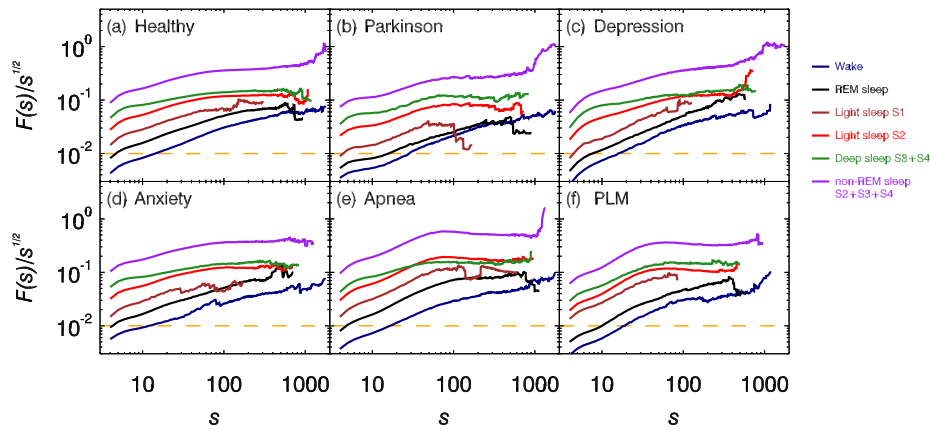


Figure 3.7.: Averaged fluctuation functions considering all healthy subjects (a) and all patients in the same group of disease (b-f) obtained from DFA2. Note that all individuals contribute up to the scale where fluctuation functions for the corresponding sleep stage can be reliably derived [$s \leq N/4$]. On very large scales less individuals contribute. Note the strong crossover which is observed in results for non-REM in sleep apnea and periodic leg movement patients.

is observed [see Figs. 3.6(f,g) and Tab. 3.1]. However, the physiological meaning of described age dependencies is not yet fully understood.

Respiration

Regarding respiration, results for inter-breath intervals obtained only from maxima in the oronasal-airflow signal are presented. I have also checked other respiration proxies (inter-breath intervals from belt recordings and based on signal maxima or minima), but corresponding findings essentially did not differ.

Neglecting the influence of aging, one finds a similar scaling behavior as for the heartbeat at large scales, i. e., $\alpha_{\text{RES}} > 1/2$ for wake states and REM sleep as well as $\alpha_{\text{RES}} \approx 1/2$ for deep sleep [see Figs. 3.6(i-l) and Tab. 3.1], consistent with earlier observations in a much smaller cohort [ROSTIG *et al.* 2005]. Furthermore, it seems that weak long-term correlations in respiration are present during light sleep while absent during deep sleep [see also the histograms in Fig. 3.5]. The overall correlations are, however, much weaker than for heartbeat. Supported by almost identical histograms for males and females (not shown) during all studied sleep stages and wakefulness, there are hardly any gender effects, although intermediately aged females have (weakly significant) smaller and larger averages during deep sleep and REM sleep, respectively [see Figs. 3.6(k-l)].

Looking at the age dependence, one recognizes an opposite aging effect during REM sleep compared with heartbeat: α_{RES} decreases with age while $\alpha_{\text{RR},2}$ increases [compare Figs. 3.6(h,l)]. For wakefulness, both exponents α_{RES} and $\alpha_{\text{RR},2}$ decrease [see Figs. 3.6(e,i)]. Nevertheless, the observed age dependences in α_{RES} during wake and REM are only weakly significant [see Tab. 3.1] due to a more pronounced inter-individual variation compared with heartbeat which manifests in larger error bars in Figs. 3.6(i,l). No significant age dependencies in respiratory correlations are observed during non-REM sleep.

For a comprehensive comparison of these findings with results reported by others I refer the reader to the discussion section of my related paper [SCHUMANN *et al.* 2010a].

3.2.3. Fluctuations in Patients

Since the SIESTA database also contains data from patients suffering from sleep apnea, Parkinson's disease, anxiety, depression, and periodic leg movement syndrome I would like to briefly show averaged fluctuation functions for different diseases for completeness. I suggest further studies of such data as soon as they become available. So far, a systematic study of age-dependence on correlations in heartbeat (or respiration) in patients cannot be done in the same way as presented before because (i) much less recordings are available, and (ii) diseases such as apnea or Parkinson are typically found among elderly people.

For that reason I do not present results from my investigation of aging effects in different diseases in the same way as above but rather average individual fluctuation functions as suggested by various authors in the literature. However, note that due to inter-individual differences averaging fluctuation functions should only be done to get an idea about 'qualitative' effects due to different pathologies.

Figure 3.7 summarizes averaged results from employing DFA2 to healthy subjects and five different diseases. The most pronounced finding is a strong crossover in non-REM sleep for sleep apnea and periodic leg movement subjects (PLM), see red, green, and purple curves in Figs.3.7(e,f). Note that although averages are shown here, this crossover is observed in all individual fluctuation functions for severe sleep apnea ($AHI \gg 10$) and in PLM patients. As explained above, apneas have a characteristic time scale yielding a crossover during deep sleep and light sleep where apneas predominantly occur. However scaling exponents should be obtained from individual fluctuation functions rather than from averaged curves. My results on the scaling in patient's heartbeat and respiration are inconclusive, yet, and although there seem to be some dependences on age they are not further discussed here. I suggest a systematic study in a much larger database as for example the SHHS (Sleep Heart Health Study) database consisting of $N \approx 6000$ recordings which are so far rather unattended due to the enormous labor costs for data preparation²¹.

3.3. Multifractal Fluctuation Analysis Methods

In the previous sections I explored monofractal scaling behavior, i.e., the characterization of fluctuations by a single fluctuation exponent. However, many recordings do not exhibit monofractal scaling behavior captured fully by the scaling exponents²² $h(2)$, β , and γ , but are of more complicated structure that is characterized by many interwoven fractal subsets described by different scaling exponents.

In the simplest extension of a monofractal time series one observes a crossover between small and large time scales s in the fluctuation function $F(s)$, leading to two scaling regimes as observed in a monofractal analysis of heartbeat²³. Other time series have more than one crossover, and others show a spectrum of many different fluctuation exponents due to many interwoven fractal subsets. The latter case can be imagined by different magnitudes of fluctuations obeying different scaling laws, i. e., small fluctuations and large fluctuations are described by different scaling exponents. Hence, a multifractal fluctuation analysis in time series focusses on separating the scaling properties of fluctuations of different magnitude.

Multifractal scaling behavior was first studied in turbulent and chaotic systems [BENZI *et al.* 1984; MUZY *et al.* 1991; KESTENER AND ARNEODO 2004] with later applications to physiology and medicine (e. g., DNA sequences [ARNEODO *et al.* 1995], and heartbeat [IVANOV *et al.* 1999b]), geophysical data (e. g., cloud patterns [ARRAULT *et al.* 1997], climate change [ASHKENAZY *et al.* 2003], precipitation and river runoff [KANTEHARDT *et al.* 2003b], seismic electric signals [VAROTSOS *et al.* 2003], and wind speeds [GOVINDAN AND KANTZ 2004]), econophysics (e. g., price increments and waiting times [OSWIECIMKA *et al.* 2005] and volatility [WANG *et al.* 2006]), and complex systems in general (e. g., eigenvalue spectra [YANG *et al.* 2004]), see [MEYERS 2009] for further applications.

The oldest multifractal analysis method is *multifractal box counting (MF-BOX)* [FEDER 1988] which is briefly described in Appendix E.3. However, it fails in the presence of non-stationarities such as trends since it can analyze only normalized measures rather than time series. This deficiency led to the development of the *wavelet transform modulus maxima (WTMM)* method – a generalized box counting approach based on wavelet transform [MUZY *et al.* 1991, 1994; ARNEODO *et al.* 1995]. In the applied sciences *multifractal detrended fluctuation analysis (MF-DFA)* [Sect. 3.3.1], a generalization of DFA [KANTEHARDT *et al.* 2002] gained more influence due

²¹In addition data protection issues prohibiting a transfer of the data to Europe are not resolved yet.

²²Monofractal fluctuation exponents α are denoted $h(q = 2)$ in this section in order to avoid confusion with the local fluctuation (Hölder) exponent α . The meaning of the moment q will become clear in the following.

²³This is a simplification used as a motivation. However, heartbeat exhibits an even more complicated, multifractal structure with many different scaling exponents [IVANOV *et al.* 1999b].

to the rather complicated and computational involved procedure of the WTMM algorithm [Appendix E.4]. For comparisons of these multifractal analysis methods, see [KANTELHARDT *et al.* 2002, 2003b; OSWIECIMKA *et al.* 2006; TURIEL *et al.* 2006]. The direct comparisons show that MF-DFA is at least equivalent to WTMM, while an application of WTMM needs more care and yields spurious multifractality more often [OSWIECIMKA *et al.* 2006]. For extensions of both methods to higher dimensions, see [KESTENER AND ARNEODO 2004; GU AND ZHOU 2006].

In Sect. 3.1.4 I already mentioned the positive aspects of fluctuation analysis methods based on moving averages. A particularly interesting variant is the CMA technique [ALVAREZ-RAMIREZ *et al.* 2005; BASHAN *et al.* 2008]. Therefore, I suggest an alternative multifractal analysis method, coined *multifractal centered moving average analysis (MF-CMA)* which facilitates a better statistics because less computational costs allow for the consideration of overlapping windows. This results in better performance on large scales ($s > N/4$) compared with MF-DFA. Additionally, MF-CMA works well at small scales ($s < 10$), especially for large negative and large positive moments²⁴, that are problematic in MF-DFA. This characteristics make MF-CMA particularly suited for studying fluctuations in short time series which often arise in applications. However, unlike for MF-DFA higher order detrending is not possible for it. It can thus serve as an easy second method in studying multifractal time series with weak trends, when a comparison of the results of two independent methods is needed to confirm the conclusions.

In order to validate conclusions drawn from a multifractal analysis and to reject spurious scaling behavior a model to generate multifractal surrogate data of well defined properties is required. In Sect. 3.3.4 I suggest a generalized binomial multi-fractal model (GB-MFM), in which both, the long-term correlations (persistence) and the multifractality strength can be tuned easily to any desired value and easy analytical formulas are available.

3.3.1. Multifractal Detrended Fluctuation Analysis (MF-DFA)

MF-DFA [KANTELHARDT *et al.* 2002] is based on the conventional DFA [PENG *et al.* 1994; BUNDE *et al.* 2000; KANTELHARDT *et al.* 2001]. In contrast to MF-CMA [Sect. 3.3.2] it eliminates higher order polynomial trends depending on detrending order. Despite a modification in the last steps, the MF-DFA algorithm is similar to the DFA algorithm which was presented in Sect. 3.1.3.

MF-DFA algorithm:

Step 1 and Step 2:

The first two steps are identical with *Step 1* and *Step 2* in DFA [Sect. 3.1.3], i. e., the profile is calculated following Eq. (3.16) and subsequently to dividing it into $\nu = 0, \dots, 2[N/s] - 1$ non-overlapping windows, squared local fluctuations $F_{\text{DFA},\nu}^2(s)$ are derived according to Eqs. (3.17).

Step 3:

In order to study multifractal structure in the time series, i. e., the influence of fluctuations of different magnitudes on different time scales, Eqs. (3.17) are raised to the power of a real valued parameter q before the averaging over all segments ν in Eq. (3.18). The parameters q are generally referred to as *moments*. The multifractal generalization of Eq. (3.18) is then defined by

$$F_{\text{MF-DFA},q}(s) = \begin{cases} \left[\frac{1}{2[N/s]} \sum_{\nu=0}^{2[N/s]-1} [F_{\text{DFA},\nu}^2(s)]^{q/2} \right]^{1/q} & : q \neq 0 \\ \exp \left[\frac{1}{4[N/s]} \sum_{\nu=0}^{2[N/s]-1} \ln F_{\text{DFA},\nu}^2(s) \right] & : q = 0 \end{cases} . \quad (3.22)$$

²⁴The term 'moment' will be explained shortly. Negative moments are associated with studying the scaling of small fluctuations while positive moments correspond to large fluctuations.

For negative q small fluctuations are dominating Eq. (3.22), while for positive q large fluctuations have a stronger influence. The classical monofractal DFA method is retrieved for $q = 2$, compare Eqs. (3.18) and (3.22). Equation (3.22) constitutes the actual multifractal generalization of the monofractal variant by introducing higher moments q that weight fluctuations in windows ν according to their magnitude. The transition from Eq. (3.18) to Eq. (3.22) can be implemented for any related monofractal method [see Appendix E.1 and in particular Eq. (E.6) for a MF-WL n method].

Step 4:

To investigate the multifractal scaling behavior, i. e., how the generalized fluctuation functions $F_{\text{MF-DFA},q}(s)$ depend on s , Eq. (3.22) has to be calculated for many values of s and for many moments q . Ideally, $F_{\text{MF-DFA},q}(s)$ follows a power law for a certain range of s and a fixed value of q ,

$$F_{\text{MF-DFA},q}(s) \sim s^{h_{\text{MF-DFA},n}(q)} \quad , \quad s \gg 1. \quad (3.23)$$

The *generalized fluctuation exponents* $h_{\text{MF-DFA},n}(q)$ are then inferred by linear fits to the q th-order fluctuation function in a double-logarithmic plot of $F_{\text{MF-DFA},q}(s)$ versus s .

Note that the exponents²⁵ $h(q)$ have a similar meaning in a multifractal fluctuation analysis as the fluctuation exponents α in a monofractal analysis ($q = 2$). This explains the earlier mentioned notation $h(2) = \alpha$.

Theoretically, if $h(q)$ is a constant for all q , the time series $\{x_k\}$ exhibits monofractal structure, otherwise it is of multifractal structure. The inversion remains true: when $\{x_k\}$ is a monofractal time series, $h(q)$ does not depend on q , because the variances in each window ν become equivalent. However, we will see later that even supposedly monofractal data often exhibit spurious multifractality.

3.3.2. Multifractal Centered Moving Average (MF-CMA) Analysis

Inspired from the multifractal generalization of the detrended fluctuation analysis (MF-DFA) which was suggested in [KANTELHARDT *et al.* 2002], I will in the following describe a *multifractal centered moving average analysis (MF-CMA)* as a generalization of its monofractal variant CMA [ALVAREZ-RAMIREZ *et al.* 2005]. The MF-CMA method also comprises four steps. *Step 1* and *Step 2* are identical with its monofractal variant and Eqs. (3.16), (3.19), and (3.20) need to be evaluated. In *Step 3* Eq. (3.21) is generalized in the same way as higher moments q were incorporated in Eq. (3.18) to obtain Eq. (3.22). This yields the MF-CMA fluctuation function,

$$F_{\text{MF-CMA},q}(s) = \begin{cases} \left[\frac{1}{2^{[N/s]}} \sum_{\nu=0}^{2^{[N/s]}-1} [F_{\text{CMA},\nu}^2(s)]^{q/2} \right]^{1/q} & : q \neq 0 \\ \exp \left[\frac{1}{4^{[N/s]}} \sum_{\nu=0}^{2^{[N/s]}-1} \ln F_{\text{CMA},\nu}^2(s) \right] & : q = 0 \end{cases} \sim s^{h_{\text{MF-CMA}}(q)}, \quad (3.24)$$

which is again calculated for many scales s and different moments q in *Step 4*. From linear fits to plots of $\log(F_{\text{MF-CMA},q}(s))$ versus $\log(s)$ generalized fluctuation exponents $h_{\text{MF-CMA}}(q)$ are obtained for fixed q if fluctuations obey power-law scaling. The properties that I discussed below Eqs. (3.22) and (3.23) remain valid.

3.3.3. Standard Multifractality Properties

In the traditional multifractal scaling approach used in multifractal box counting [see Appendix E.3 and FEDER 1988] and WTMM analysis [see Appendix E.4 and MUZY *et al.* 1991, 1994] one studies

²⁵For the moment I drop the subscript MF-DFA n because the following properties remain valid for all multifractal fluctuation analysis methods that are discussed in this thesis.

the partition function,

$$Z_q(s) = \sum_{\nu=0}^{[N/s]-1} |\tilde{p}_s(\nu)|^q = \sum_{\nu=0}^{[N/s]-1} \left| \sum_{k=\nu s+1}^{(\nu+1)s} x_k \right|^q \sim s^{\tau(q)} \quad (3.25)$$

with $\tilde{p}_s(\nu)$ being the box probability in the window ν and $\tau(q)$ the *Rényi exponents*. Multifractality was originally studied on fractal sets. Assume, \mathcal{A} is such a set which is covered by a series of cubes $\{\mathcal{C}_k\}$ of a unit size $\varepsilon \rightarrow 0$. With each cube a probability measure $\mu_k = \mu(\mathcal{C}_k)$ satisfying $\mu(\mathcal{A}) = 1$ is associated. It can then be motivated to define a generalized (fractal) box dimension [OTT 2002]

$$D_q = \frac{1}{1-q} \lim_{\varepsilon \rightarrow 0} \frac{\ln \sum_k \mu_k^q}{\ln(1/\varepsilon)}. \quad (3.26)$$

When the time series is properly normalized to ensure $\sum_k x_k = 1$ the partition function formalism in Eq. (3.25) can be transferred to time series and from $Z_q \sim s^{\tau(q)}$ Rényi exponents can be calculated to study multifractal scaling. Note that for a fluctuation analysis based on the partition function the normalization is indeed not required since the scaling is independent. However, it is required to motivate the equivalence of both approaches by identifying time series element with probability measures.

Under the assumption the time series is stationary and has a compact support with²⁶ $D_0 = 1 = -\tau(0)$, the generalized fluctuation exponents $h(q)$ and the Rényi exponents $\tau(q)$ are equivalent [KANTELHARDT *et al.* 2002].

Similar to the difficulties one faces in proofing the equivalence of the fluctuation exponent, the spectral exponent, and the correlation exponent for DFA [see Sect. 3.1.2 and discussion in Sect. 3.1.3] it is not trivial to show the equivalence of $\tau(q)$ and $h(q)$ for MF-DFA. Nevertheless, under the stationarity condition trends in the data are absent and a higher order detrending is not required. Thus, a *multifractal fluctuation analysis (MF-FA)* is sufficient to access multifractal scaling properties. As I have motivated in Step 4 of the MF-CMA algorithm a multifractal generalization can be easily achieved for any related fluctuation analysis method. Inserting Eq. (3.8) instead of $F_{\text{DFAN},\nu}^2$ in Eq. (3.22) yields the MF-FA fluctuation function

$$\begin{aligned} F_{\text{MF-FA},q}(s) &= \left[\frac{1}{[N/s]} \sum_{\nu=0}^{[N/s]-1} [F_{\text{FA},\nu}^2(s)]^{q/2} \right]^{1/q} \\ &= \left[\frac{1}{[N/s]} \sum_{\nu=0}^{[N/s]-1} |Y((\nu+1)s) - Y(\nu s)|^q \right]^{1/q} \sim s^{h(q)}. \end{aligned} \quad (3.27)$$

From Eq. (3.27) and with the simplification that N is an integer multiple of s one obtains

$$\frac{1}{N} \sum_{\nu=0}^{N/s-1} |Y((\nu+1)s) - Y(\nu s)|^q = \frac{1}{N} \sum_{\nu=0}^{N/s-1} \left| \sum_{k=\nu s+1}^{(\nu+1)s} x_k \right|^q = \frac{1}{N} \sum_{\nu=0}^{N/s-1} |p_s(\nu)|^q \sim s^{qh(q)-1}. \quad (3.28)$$

This yields together with the partition function approach in Eq. (3.25) and again $[N/s] = N/s$

$$\tau(q) = qh(q) - 1. \quad (3.29)$$

Another well established description of multifractal data is the singularity spectrum $f(\alpha)$ describing the dimensions f of subsets of the series characterized by the same singularity strength or *Hölder exponent* α [HALSEY *et al.* 1986]. The Hölder exponent characterizes the local divergence (singularity, α_ν) of box probability densities in the limit $s \rightarrow 0$, $\tilde{p}_s(\nu) \sim s^{\alpha_\nu}$.

²⁶ $D_0 = \lim_{\varepsilon \rightarrow 0} \frac{\ln \tilde{N}_{\mathcal{C}}(\varepsilon)}{\ln 1/\varepsilon}$ is the box dimension where \tilde{N} denotes the number of boxes of edge length $\varepsilon > 0$ needed for covering the curve \mathcal{C} . For a time series $\{x_k\}_{k=1,\dots,N}$ of compact support setting $\tilde{N}(\varepsilon) = N/\varepsilon$ yields a box dimension $D_0 = \lim_{\varepsilon \rightarrow 0} -\frac{\ln N}{\ln \varepsilon} + 1 = 1$. Employing Eq. (3.26) yields the same result.

In the framework of time series analysis the concept of multifractality means that the support of a time series can be subdivided into (fractal) subsets that obey a different scaling described by a local fluctuation exponent α . Theoretically, the Hölder exponent at a position k , α_k can be obtained by studying the scaling of the corresponding local fluctuation $F_k(s) \sim s^{\alpha_k}$ in the limit $s \rightarrow 0$, i.e., in a 'small window'. Unfortunately, very small scales are not accessible with any of the previously described methods due to numerical limitations. Similarly to the probability measure approach, one can study the dimensions $f(\alpha)$ of the fractal subsets of the time series' support that are characterized by the same Hölder exponent α . $f(\alpha)$ can be derived from either $\tau(q)$ via a Legendre transform or from $h(q)$,

$$\alpha = \tau'(q) \qquad f(\alpha) = q\alpha - \tau(q) = q\tau'(q) - \tau(q) \qquad (3.30a)$$

$$\alpha = h(q) + qh'(q) \qquad f(\alpha) = q[\alpha - h(q)] + 1 = q^2h'(q) + 1 \qquad (3.30b)$$

Note that the notation α for the Hölder exponents must not be confused with the notation $\alpha = h(2)$ or $\alpha = H$ (Hurst exponent) frequently used in monofractal studies, i.e., monofractal fluctuation exponents H [Eq. (3.6)], α_{FA} [Eq. (3.9)], and α_{DFA} [Eq. (3.18)] are not equivalent with the Hölder exponent α unless the data is monofractal. The maximum value of $f(\alpha)$ is $D_0 = -\tau(0) = 1$ and occurs for $q = 0$ because this is the dimension of the time series' support and the probability measure of the whole (compact) support is 1 [see e.g., OTT 2002]. On the other hand, $f(\alpha) = 0$ is valid for all values α that do not characterize the scaling at any location k . Monofractal fluctuation exponents (H , α_{FA} , α_{DFA}) are retrieved when $\alpha_k = \text{const.}$ for all subsets of the support; in this case the singularity spectrum only consists of a single point $f(\alpha) = 1$. The width of the singularity spectrum is used to quantify the strength of multifractality and is (in the infinite limit) equivalently described by

$$\Delta h = h(-\infty) - h(+\infty) \equiv \Delta\alpha = \alpha|_{q=-\infty} - \alpha|_{q=+\infty}. \qquad (3.31)$$

However, in real world applications both properties Δh and $\Delta\alpha$ are not directly accessible and one defines a $\Delta h_q = h(-q) - h(+q)$ for a large value of q (I consider $q = 20$ in this thesis) and derives $\Delta\alpha$ from the roots of model²⁷ fits to the singularity spectra $f(\alpha)$ (in the following I will use a quadratic model). This invalidates the strict equality of both quantities in Eq. (3.31) and $\Delta h_q \lesssim \Delta\alpha$.

3.3.4. Generalized Binomial Multi-Fractal Model (GB-MFM)

In order to validate conclusions drawn from a multifractal analysis and to reject spurious scaling behavior a model to generate multifractal surrogate data of well defined properties is required. While monofractal surrogate data can be easily generated by Fourier filtering or the Schreiber-Schmitz method [Sects. 1.5.2 and 1.5.2, or THEILER *et al.* 1992; SCHREIBER AND SCHMITZ 1996], surrogate data tests for multifractal data have usually been restricted to studying randomly shuffled data. Prominent multifractal models are multifractal random cascade processes [MENEVEAU AND SREENIVASAN 1987; GREINER *et al.* 1998; BOGACHEV *et al.* 2008], the multifractal random walk model [BACRY *et al.* 2001], and the binomial multifractal model [see, e. g. FEDER 1988; KANTELHARDT *et al.* 2002]. In the following I will focus on the latter model and suggest a *generalized binomial multi-fractal model (GB-MFM)* in which one can additionally to the standard model tune long-term correlations (persistence), i. e., $h(2)$.

Classical Binomial Multifractal Model

The *deterministic binomial multifractal model* is a time series $\{x_k\}_{k=1, \dots, 2^{n_{\text{max}}}}$ where the k -th element is constructed according to

$$x_k = a^{n_{\text{max}} - \text{CS}\{(k-1)_2\}} (1-a)^{\text{CS}\{(k-1)_2\}} \qquad (3.32)$$

²⁷Although, often quadratic or hyperbolic models are sufficient to describe the singularity spectrum other models might fit better.

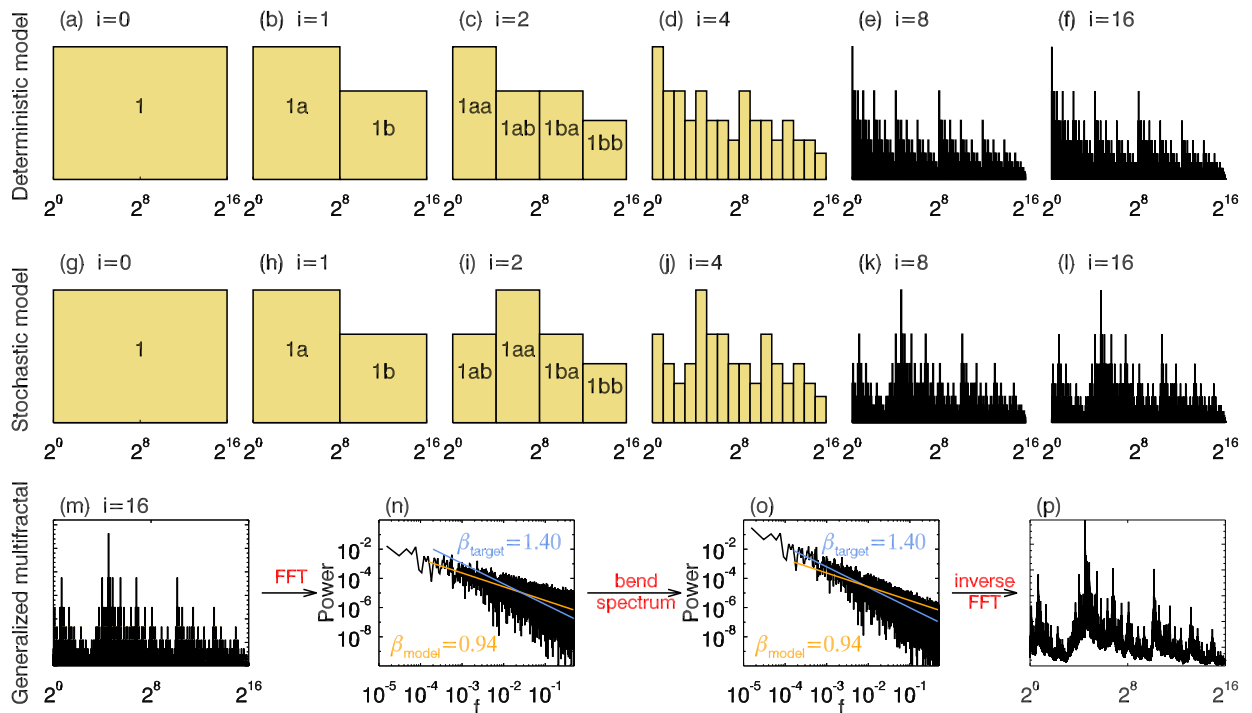


Figure 3.8.: (color online) Generation algorithms of a binomial multifractal for the deterministic case (a-f), the stochastic case (g-l), and the proposed generalized binomial multifractal additionally exhibiting long-term correlations with spectral exponent $\beta = 1.4$ (equivalent with $h(2) = 1.2$) (m-p). Shown are single configurations with $N = 2^{16}$ and a binomial parameter $a = 0.6$. In (a-m) i denotes the number of the iteration. Note that vertical axes are rescaled in each step for visual reasons.

with $a \in \mathbb{R}$ fulfilling $0.5 < a < 1$ the model parameter. The operator $\text{CS}\{\cdot\}$ denotes the checksum, and $(k-1)_2$ is the binary expression of $(k-1)$. For instance, $\text{CS}(26) = \text{CS}(11010) = 3$. Thus the deterministic binomial multifractal is uniquely defined by the parameter tuple (a, n_{\max}) . Note that the dependent parameter $(1-a)$ in Eq. (3.32) is often denoted by b leading to the equivalent term *ab-model* for the binomial multifractal model.

The binomial multifractal can be constructed in $n_{\max} + 1$ iterative steps [see Figs. 3.8(a-f)]: ($i = 0$) start with a constant series of $N = 2^{n_{\max}}$ times the number 1, ($i = 1$) divide the series in two halves and multiply the first with a and the second with $b = (1-a)$, ($i = 2$) divide both halves again in two halves each and multiply the left half with a and the right half with b , ($i = 3, \dots, n_{\max}$) repeat halving and multiplying with a and $b = (1-a)$ until the halves consist of only one element. For $n_{\max} = 16$ this is illustrated in Figs. 3.8(a-f) for iterations $i = 0, 1, 2, 4, 8, 16$. Note that the relation $b = (1-a)$ is in principle not required, but ensures that the norm is preserved for all iterations i , i.e., $\sum_k x_k^{(i)} = 1$.

The *stochastic binomial multifractal* is constructed in a similar way, except for randomly multiplying either the left half with a and the right half with $b = (1-a)$ or vice versa [see Figs. 3.8(g-l)] for the same $n_{\max} = 16$.

For both binomial models the scaling properties follow [KANTELHARDT *et al.* 2002]

$$h(q) = \begin{cases} \frac{1}{q} (1 - \log_2(a^q + (1-a)^q)) & : q \neq 0 \\ -\frac{1}{2}(\log_2 a + \log_2(1-a)) & : q = 0 \end{cases} \quad (3.33a)$$

and

$$\tau(q) = \begin{cases} -\log_2(a^q + (1-a)^q) & : q \neq 0 \\ -1 & : q = 0 \end{cases} \quad (3.33b)$$

The theoretical multifractality strength can then be obtained from the limits $q \rightarrow \pm\infty$ of

Eq. (3.33a),

$$h(-\infty) = \lim_{q \rightarrow -\infty} h(q) = -\log_2(1-a) \quad \text{and} \quad h(+\infty) = \lim_{q \rightarrow +\infty} h(q) = -\log_2(a) \quad (3.34)$$

where I used the common trick to neglect the term $a^q \approx 0$ when $q \rightarrow -\infty$ and $(1-a)^q \approx 0$ for $q \rightarrow +\infty$ justified by the property $0.5 > a > 1$. Together with Eq. (3.31) this yields

$$\Delta\alpha = h(-\infty) - h(+\infty) = -\log_2(1-a) + \log_2(a) = \log_2(a/(1-a)). \quad (3.35)$$

Consequently, the model parameter a follows

$$a = (2^{-\Delta\alpha} + 1)^{-1} \quad (3.36)$$

for a desired multifractality strength $\Delta\alpha$. Besides, $h(2) = \frac{1}{2}(1 - \log_2(a^2 + (1-a)^2))$ [from setting $q = 2$ in Eq. (3.33a)] describes the intrinsic long-term correlations for the ab -model. For instance, $a = 0.6$ leads to $\Delta h_{20} \approx 0.485 < \Delta\alpha \approx 0.585$ while $h(2) \approx 0.972$ and $\beta = 2h(2) - 1 \approx 0.943$.

Again notice that in the standard binomial multifractal model long-range persistence (i. e., $\alpha_{\text{DFA}} = h(2)$) and multifractality strength ($\Delta h_q = h(-q) - h(+q)$, $\Delta\alpha = h(-\infty) - h(+\infty)$) are one-to-one related and cannot be tuned separately; therefore a generalization is needed.

Generalized Binomial Multifractal Model (GB-MFM)

Motivated by the Fourier filtering technique [Sect. 1.5.2] which is employed to generate long-term correlated surrogate data of arbitrary $h(2)$ emanating from a white noise time series ($h(2) = 0.5$) one might incorporate it together with the classical binomial multifractal model in a joint model which I coin *generalized binomial multifractal model (GB-MFM)*. The GB-MFM algorithm thus consists of two steps and is illustrated in Figs. 3.8(m-p):

Step 1: Binomial multifractal

In the first step a time series that obeys stochastic or deterministic binomial multifractal structure is generated according to the formalism described above, e. g., following Eq. (3.32) in the deterministic case. The stochastic variant is used for illustration in Fig. 3.8(m).

Step 2: Fourier filtering

Arbitrary long-term correlations can be generated by employing the Fourier filtering technique [Sect. 1.5.2 and THEILER *et al.* 1992]. (i) The data is fast Fourier transformed (FFT) into the frequency domain [Fig. 3.8(n)]. (ii) Each (complex) spectral coefficient is multiplied by $f^{-\Delta\beta/2}$, where f is the frequency and applying $\beta = 2h(2) - 1$ yields

$$\Delta\beta = \beta_{\text{target}} - \beta_{\text{model}}(a) = 2h_{\text{target}}(2) + \log_2(a^2 - (1-a)^2) - 1 \quad (3.37)$$

being the difference of the desired and the actual (binomial model) spectral exponent [Fig. 3.8(o)]. (iii) The signal is transformed back to the time domain by inverse FFT yielding a realization of the GB-MFM [Fig. 3.8(p)]. Thus, one can obtain all parameters necessary for generating surrogate data of a desired multifractality strength $\Delta\alpha$ and long-term correlations $h(2)$ by Eqs. (3.36) and (3.37). The algorithm is illustrated in Fig. 3.8(m-p) for the stochastic binomial multifractal with $a = 0.6$ and $n_{\text{max}} = 16$ and target long-term correlations of $h(2) = (1.4 + 1)/2 = 1.2$. I thoroughly test the scaling properties of this model in Section 3.3.5.

Recall that the Fourier filtering technique does not preserve the distribution of the time series elements x_k when $h(2) \gtrsim 1.25$, see Sect. 1.5.2. For that reason the Schreiber-Schmitz method was originally suggested [SCHREIBER AND SCHMITZ 1996]. In principle it might be possible to embed the GM-MFM into the Schreiber-Schmitz method by starting with the output of the binomial generator (*Step 1*) instead of random uncorrelated numbers. In such an algorithm, it may be possible to tune also the distribution of the data, besides their auto-correlations (i. e. $h(2)$ or the power spectrum), and their multifractality strength. However, it is known that a different type of multifractality can be induced by broad distributions [KANTELHARDT *et al.* 2002], and hence, it is not automatically clear to which extend the Schreiber-Schmitz method

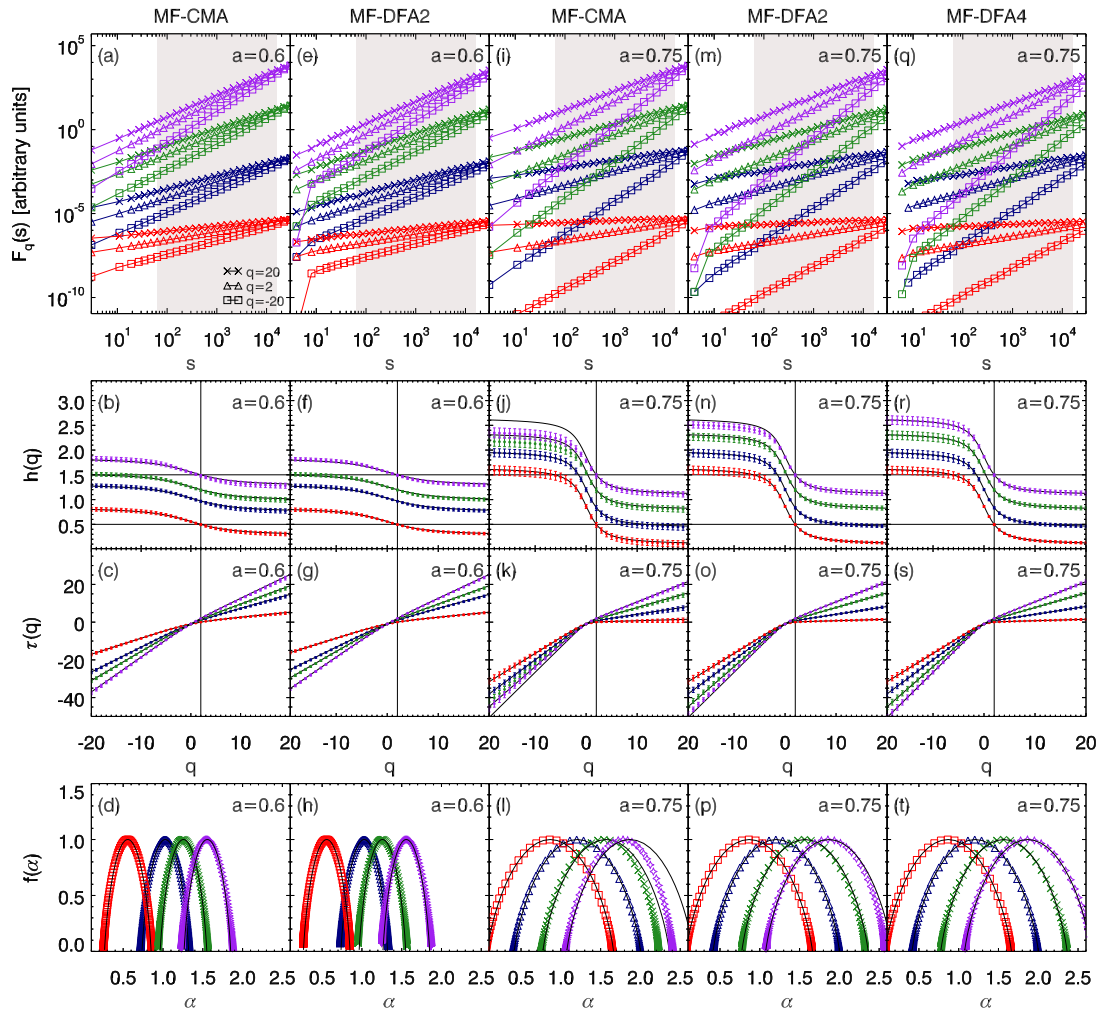


Figure 3.9.: Multifractal analysis of generalized binomial multifractals with parameters $a = 0.6$ and $a = 0.75$ applying (a-d, i-l) MF-CMA, (e-h, m-p) MF-DFA2, and (q-t) MF-DFA4. Fluctuation functions in (a,e,i,m,q) correspond – from top to bottom – to the GB-MFM for $h(2) = 1.5$ [purple], $h(2) = 1.2$ [green], $h(2) = [1 - \log_2(a^2 + (1 - a^2))]/2$ [pure stochastic binomial multifractal, blue], and $h(2) = 0.5$ [red]. For all parameters, results from 1000 configurations of length $N = 2^{16}$ have been averaged. Fluctuation functions are vertically shifted for (i) different moments q [shown $q \in \{-20, 2, 20\}$], and (ii) for different model parameters for clarity. Gray shaded areas mark fitting ranges for obtaining $h(q)$. Further, associated multifractal scaling parameters $h(q)$ and $\tau(q)$ are illustrated in the center panels, and the $f(\alpha)$ spectra are shown in the lower panels. Solid black curves correspond to theoretical behaviors for comparison. For both scaling exponents the monofractal case ($q = 2$) is marked by vertical solid black lines, and additionally in $h(q)$ plots horizontal solid black lines mark the adjusted $h(2) = 0.5$ and 1.5 .

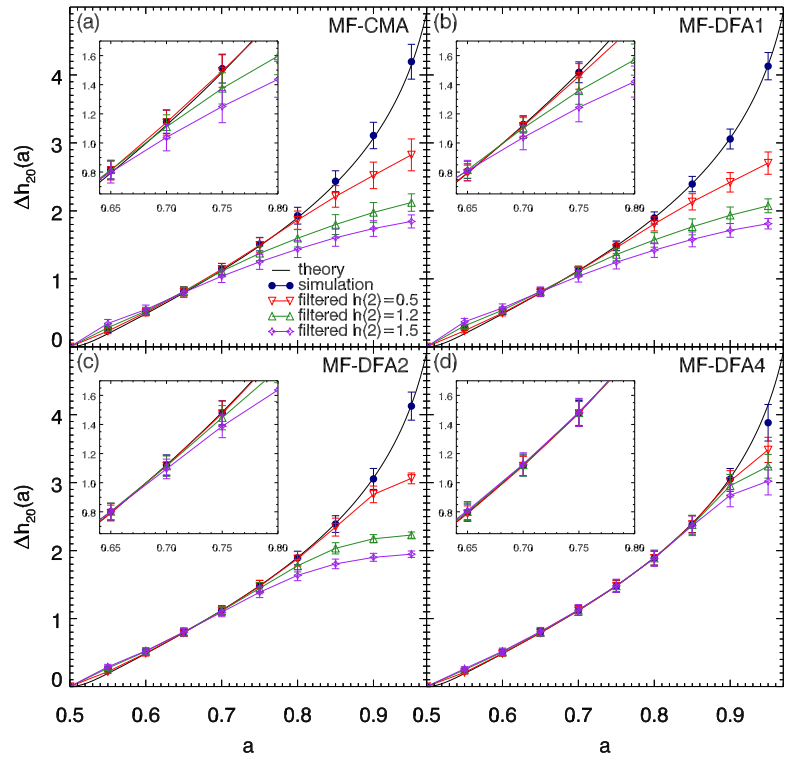
can be incorporated with the GB-MFM. On the other hand, this might pave the way to adjust also multifractal properties originating in broad distributions. Note that one can separate both types of multifractality by randomly shuffling the dataset which destroys multifractality due to correlations but preserves multifractality due to broad distributions. However, so far I did not systematically test a combination of GB-MFM and the Schreiber-Schmitz algorithm.

Although, more general multifractal random cascade processes [MENEVEAU AND SREENIVASAN 1987; GREINER *et al.* 1998] or the multifractal random walk model [BACRY *et al.* 2001] might appear more advanced, I think that for most applications an easier model is preferred, where both important quantities, long-term correlations (i. e., $h(2)$) and multifractality strength (i. e., Δh or $\Delta \alpha$) can be tuned without any additional parameter adjustments and based on an easily implemented procedure.

3.3.5. Analysis of Data from the GB-MFM

Now I want to thoroughly test the GB-MFM model by varying the strength of multifractality (tuned by the parameter a in Step 1 of the model) and the strength of long-term correlations (tuned by adjusting $h(2)$ in Step 2 of the model) and analyse modeled data by employing MF-

Figure 3.10.: Degree of multifractality expressed by $\Delta h_{20} = h(-20) - h(20) < \Delta\alpha$ as a function of the binomial multifractal parameter a for the pure binomial multifractal [blue filled circles] and for the generalized binomial multifractal for three adjusted $h(2)$: 0.5 [red open triangles down], 1.2 [green open triangles up], and 1.5 [purple open diamonds] derived from fluctuation analysis applying (a) MF-CMA, (b) MF-DFA1, (c) MF-DFA2, and (d) MF-DFA4. Insets present magnifications in annotated ranges. Mean values and standard deviations for 1000 configurations are shown. Note, h_{20} is slightly underestimated by MF-DFA4 for $a = 0.95$ due to finite size effects causing a crossover for $q < 0$ within the fit range [64, 16384] used for all data points.



DFA (including tests with different detrending orders) and MF-CMA.

Figure 3.9 shows average results of the fluctuation functions for 1000 configurations of the stochastic version of the GB-MFM model. Setting the main model parameter to $a = 0.6$ (see Figs. 3.9(a-h)) and 0.75 (see Figs. 3.9(i-t)), the data is supposed to exhibit multifractality strengths $\Delta\alpha_{a=0.6} \approx 0.58$ and $\Delta\alpha_{a=0.75} \approx 1.58$, respectively [cf. Eq. (3.35)]. In both cases, the multifractality can be clearly seen in the different slopes (exponents) of the $F_q(s)$ curves in the double-logarithmic presentation. While the MF-CMA, MF-DFA2, and MF-DFA4 curves are shown for $q = -20, 2$, and $+20$ only [see Fig. 3.9(a,e,i,m,q)], the scaling exponents for many values of q can be compared with the expected behavior of the model [see Eq. (3.33a)] in the plots of $h(q)$ [see Fig. 3.9(b,f,j,n,r)]. The four sets of curves belong to different autocorrelations set in the model, characterized by $h(2) = 1.5, 1.2$, original $h(2, a = 0.6) = 0.972$ (or $h(2, a = 0.75) = 0.839$), and 0.5 [from top to bottom]. Note that there are no two-point correlations in the last case.

I find that the procedure of shifting the $h(q)$ curves by using spectral filtering works very well. There are hardly any deviations from the expected behavior of $h(q)$ if $a = 0.6$ [see Figs. 3.9(b,f)] or for MF-DFA4 [see Fig. 3.9(r)]. Clearly, the detrending capacity of MF-CMA and MF-DFA2 is insufficient to obtain the correct $h(q)$ for $a = 0.75$ in particular for negative q and large $h(2)$ [see Figs. 3.9(j,n)]. The reason is the upper limit for scaling exponents: $h(2) \leq n + 1$ for DFA n [KANTELHARDT *et al.* 2001] and $h(2) \leq 2$ for CMA, since it is linearly detrending only. Although, these limits are not strict for $q < 2$, i. e., in the multifractal versions of both methods, significant deviations occur if the real $h(q)$ comes close to the limits. One thus has to select a sufficiently large order n of detrending if large $h(q)$ occur or if results for methods with different detrending order disagree.

In Figs. 3.9(c,g,k,o,s) corresponding results for $\tau(q)$ are shown [see Eq. (3.29)], while Figs. 3.9(d,h,l,p,t) display the corresponding singularity spectra $f(\alpha)$ obtained by Eq. (3.30). Again, deviations from the expected curves can be seen for $a = 0.75$ and MF-CMA as well as MF-DFA2 only. Evidently, the singularity spectra are very well approximated by parabolas. However, no tuning of the shape of the singularity spectra is possible in the GB-MFM.

In Fig. 3.10 results for the strength of multifractality, measured by $\Delta h_{20} = h(-20) - h(20) \lesssim \Delta\alpha$, are shown for the GB-MFM as a function of the model parameter a . For the pure model [blue circles] the theoretical behaviour is fully recovered by all four methods, MF-CMA, MF-DFA1, MF-DFA2, and MF-DFA4. Note that even values $\Delta h_{20} > 4$ can be observed in the MF-CMA

results although this exceeds the possible range of $h(2)$, $0 < h(2) < 2$, by a factor of two. This illustrates that these strict limits for $h(2)$ do not apply for other (in particular negative) values of q .

Ideally, the strength of multifractality should be also preserved for every adjusted $h(2)$. However, as can be seen for model parameters $a > 0.7$, tuning $h(2)$ by Fourier filtering reduces Δh_{20} by a level depending on the applied analysis method and the total difference of the model's intrinsic correlations (β_{model}) and the desired target correlations (β_{target}), i. e., according to $\Delta\beta$ given by Eq. (3.37). Similar, but much weaker problems seem to occur for $a \approx 0.55$, where the multifractality is *increased* by filtering [see also later discussion around Fig. 3.14]. In both cases, the multifractality is fairly well preserved for target $h(2) = 0.5$, i. e., intrinsic correlations of the model can easily be removed for a wide range of a (and thus Δh_q). As already mentioned in discussing Fig. 3.9, a higher order of detrending is required for successfully retrieving the correct $h(q)$ for large $h(2)$ and large a (and thus strong multifractality) in the filtered version of the model. For relatively weak multifractality ($a \leq 0.7$) it is sufficient and computationally convenient to use MF-CMA. MF-DFA1 is comparable to MF-CMA [see Figs. 3.10(a,b)], although our error bars obtained as standard deviations of the results for 1000 configurations are slightly lower for MF-DFA1. For $a \geq 0.75$ one must apply at least MF-DFA2 [see Fig. 3.10(c)], while even higher order detrending is needed for $a \geq 0.85$. MF-DFA4 works up to $a = 0.9$. Note that for MF-DFA4 and $a = 0.95$ the values shown in Fig. 3.10(d) are slightly lower than the theoretical expectation (blue circle does not lie on black curve) due to finite size effects. In fact for negative values of q the associated fluctuation function shows a crossover within the fitting range [64, 16384] used for all values shown in Fig. 3.10 resulting in an underestimation of $h(-20)$ and finally in an underestimation of Δh_{20} . However, I did not want to adjust the range just for a single parameter set.

Taking into account the exact reproduction of $h(q)$ by all methods in the unfiltered version of the GB-MFM one can see that the need for using higher order detrending in analyzing data from the filtered version is most probably due to apparent trends introduced into the data in the second (Fourier filtering) step. However, since such effects are possible also in real data I recommend comparing with high-order MF-DFA if strong multifractality is observed. Nevertheless, surrogate data needed for applications will usually require weaker multifractality ($a < 0.75$), and MF-CMA can then be used for analyses and comparisons.

3.3.6. Surrogate Data Generation by Block Shuffling

It is a common approach to compare fluctuation analysis results from real data with results obtained from the same data after random shuffling, see, e. g. [KANTEHARDT *et al.* 2001, 2002]. The shuffling procedure destroys correlations on all time scales, but preserves the distribution of the elements. A comparison of both results thus reveals all effects of correlations and allows distinguishing effects of correlations from those of (possibly broad) distributions.

However, one might also want to destroy correlations in real data within a certain limited range of time scales only [SCHUMANN AND KANTEHARDT 2010b]. This is particularly appropriate to test hypotheses regarding correlations or correlation-caused multifractality on specific scales, e. g., just below a particular time scale L . In this case there should be no change in the results of fluctuation analysis upon destroying all correlations for $s > L$.

Destroying all correlations above a certain scale L can easily be achieved by shuffling blocks of the data of size L while keeping the order of the values within each block untouched [SCHUMANN AND KANTEHARDT 2010b]. For instance, when non-overlapping segments of width $L = 100$ are randomly shuffled all correlations for scales $L > 100$ are destroyed and the generated surrogate data exhibit uncorrelated and monofractal ($h(q) = 1/2$) behavior for $L > 100$ unless there are remaining effects of broad distributions of the values.

On the other hand, correlations on short scales $s < L$ can be analogously destroyed by shuffling the data within the blocks of size L keeping the order of the blocks unchanged [SCHUMANN AND KANTEHARDT 2010b]. This way, short-term correlations (and possibly related multifractality) can be selectively destroyed. For example, one can check if multifractality in river runoff below

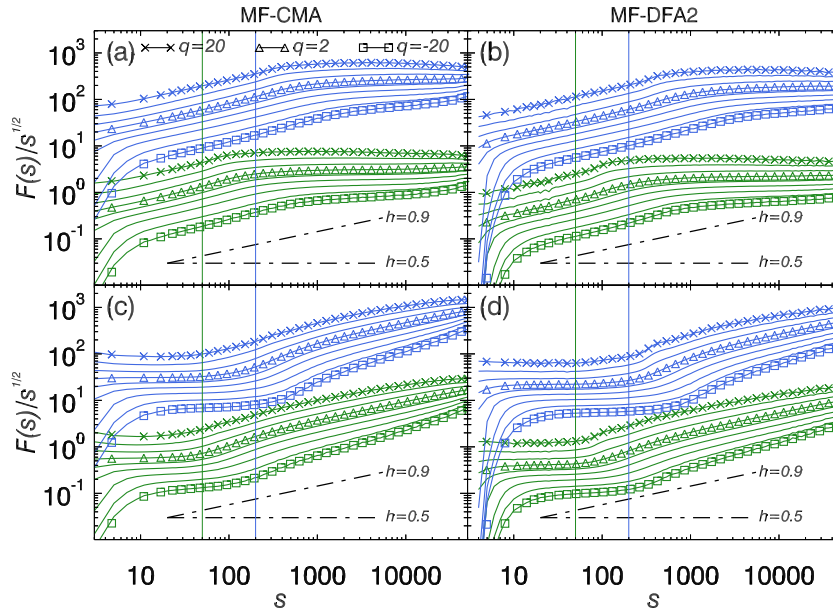


Figure 3.11.: Correlations in long-term correlated data [$h(q) = 0.9$, $N = 100000$, generated by Fourier filtering] are destroyed on large scales by shuffling non-overlapping blocks of size $L = 50$ [bottom, red] and $L = 200$ [top, orange] (a,b), and on small scales by shuffling the data inside non-overlapping blocks of the same size (c,d; same order and color coding). $F_q(s)/s^{1/2}$ is shown for $q \in [-20, -10, -5, -2, 0, 2, 5, 10, 20]$ and MF-CMA (a,c) as well as MF-DFA2 (b,d) averaged over 1000 configurations. Theoretical slopes $h = 0.5$ [uncorrelated] and $h = 0.9$ [model] are indicated by black dashed lines. $F_{q=2}(s)$ is marked by triangles, $F_{q=-20}(s)$ by boxes, and $F_{q=20}(s)$ by crosses. All curves are vertically shifted (i) for different q and (ii) for different parameter sets. Vertical lines in the corresponding color indicate the values of L .

time scales of one year is due to correlations by shuffling the data within blocks of size $L = 365$ days. Furthermore, it should be possible to first shuffle the data within blocks of length L_1 and then shuffle whole blocks of length L_2 to preserve only correlations for $L_1 < s < L_2$. I test the results of both major shuffling modes using MF-DFA and MF-CMA in Sect. 3.4.1.

3.4. Spurious Multifractality in Monofractals

Often multifractal analysis methods are blindly applied to real data and the reliability of scaling obtained by linear fits in the double-logarithmic regime to resulting fluctuation functions (e. g. MF-DFA [Sect. 3.3.1]) or partition functions (e. g. WTMM [Appendix E.4]) is often not properly checked. This Section is dedicated to the question under which circumstances by definition monofractal signals can exhibit a spurious multifractal structure.

Therefore, we check the scaling behavior of various kinds of surrogate data with both multifractal analysis methods, MF-DFA and MF-CMA. In particular we want to point out pitfalls (observations suggesting spurious multifractality) in multifractal analysis of fractal and multifractal data including data with inhomogeneous scaling behavior.

3.4.1. Spurious Multifractality in Block Shuffled Data

As a first example I consider non-multifractal (monofractal) long-term correlated data with $h(2) = 0.9$, i. e., $\gamma = 0.2$, where either (i) correlations on large scales are removed by shuffling data blocks of size L , or (ii) correlations on small scales are removed by shuffling the data within these blocks keeping the order of the blocks. More detailed information on this type of surrogate data were given in Sect. 3.3.6. Figure 3.11 shows fluctuation functions obtained from MF-CMA and MF-DFA2 for two different block lengths $L = 50$ and $L = 200$ where shuffling of entire blocks was done for Figs. 3.11(a,b) and shuffling within these blocks took place to create Figs. 3.11(c,d). Note that I show $F(s)/s^{1/2}$ vs. s , and hence, uncorrelated behavior corresponds to a horizontal plot in this presentation. As can be seen in Fig. 3.11(a) CMA results (i. e., MF-CMA results for $q = 2$) still

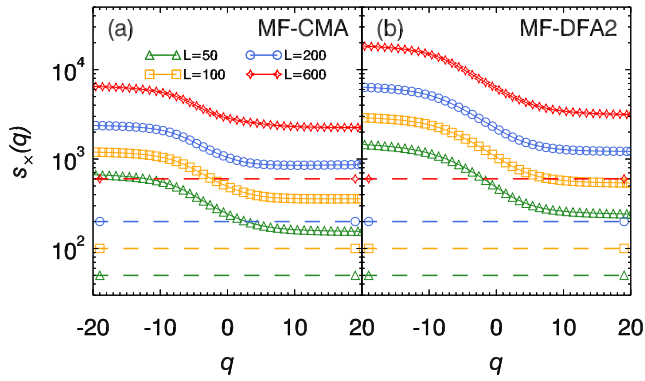


Figure 3.12.: Dependence of observed crossover location s_x on the considered moment q for block-shuffled long-term correlated data [$h(q) = 0.9$, $N = 100000$] for $L = 50$ [green triangles], $L = 100$ [orange squares], $L = 200$ [light blue circles], and $L = 600$ [red stars]. Dashed lines in the same color and symbol indicate the values of L . Results are obtained by MF-CMA (a) and MF-DFA2 (b) averaging 1000 configurations.

seem to indicate correlations up to scales s_x (observed crossover positions) approximately four times larger than the block size L [marked by vertical lines in the same colors]. For DFA2 s_x is even approximately six times larger than L , see Fig. 3.11(b). The observed crossover positions are thus deviating even more from the theoretical crossovers as for data with a crossover directly generated by Fourier filtering: $s_{x,\text{DFA1}} \approx 1.6s_{\text{real}}$ (related to CMA) and $s_{x,\text{DFA2}} \approx 2.5s_{\text{real}}$ [KANTELHARDT *et al.* 2001]

Looking at other moments $q \neq 2$, one finds that the crossover position s_x is strongly dependent on q , as can be seen in all panels of Fig. 3.11. Figure 3.12 systematically shows this dependence for four exemplary block sizes L and for both methods [block sizes from Fig. 3.11 are included in the same colors]. The block size L which can be interpreted similarly to a theoretical crossover is indicated by dashed lines using corresponding colors and symbols. For negative values of q , $q = -20$, the difference is surprisingly large: $s_x/L \approx 32$ (MF-DFA2) and $s_x/L \approx 12$ (MF-CMA); for $q = 2$ values are roughly $s_x/L \approx 8.5$ and $s_x/L \approx 4.5$ while for positive moments $q = 20$ one finds $s_x/L \approx 5.5$ and $s_x/L \approx 3.75$, respectively²⁸. For MF-CMA, s_x is not only smaller (as expected from earlier studies [KANTELHARDT *et al.* 2001; BASHAN *et al.* 2008]) but is also less dependent on q than for MF-DFA2.

Figures 3.11(c,d) show results from long-term correlated data with short-term correlations eliminated by block shuffling. The crossover positions correspond to the cases with eliminated long-term correlations. However, the crossover seems to be more pronounced for negative values of q in this case and somewhat broader in MF-DFA2 compared with MF-CMA. I checked that there are no effects of odd configurations in the plots.

Having a q dependent crossover at s_x [as shown for non-multifractal data in Figs. 3.11 and 3.12] represents a dangerous pitfall for conclusions regarding multifractality. If (part of) such a broad crossover happens to be in the considered fitting regime for calculating the slopes $h(q)$, spurious multifractality will be observed. This is illustrated in Fig. 3.13, where the same long-term correlated data ($h(q) = 0.9$) without multifractality is considered with and without block-shuffling. Figure 3.13 shows the averaged MF-DFA2 [top] and MF-CMA [bottom] fluctuation functions for both types of non-multifractal data together with the full multifractal analysis: fitted generalized Hölder exponents $h(q)$ for different fitting regimes [as indicated in Fig. 3.13(a)] and derived singularity spectra $f(\alpha)$. The results show that a certain level of apparent multifractality ($\Delta\alpha \approx 0.2$) is already observed in the purely long-term correlated data due to finite-size effects, even though the corresponding fitting regime includes nearly three orders of magnitude ($30 < s < 20000$). The data with crossover at $L = 200$ generated by block shuffling exhibits even stronger spurious multifractality ($\Delta\alpha \approx 0.3$) if the fitting regime is not changed. Fitting in smaller regimes yields strongly regime-dependent results. None of them is consistent with the expected monofractal scaling behavior even if the crossover is not within the fitting regime. A spurious 'inverted' multifractality is observed on short time scales ($30 < s < 400$), where $h(q) = 0.9$ is expected, and even stronger ($\Delta\alpha \approx 0.35$) spurious normal multifractality on large time scales ($4000 < s < 20000$), where $h(q) = 0.5$ is expected since the correlations above $L = 200$ were destroyed by block shuf-

²⁸These values are very roughly rounded to give a general idea, indeed there are noticeable differences between values obtained from different block sizes L and quotients may even vary by 1.

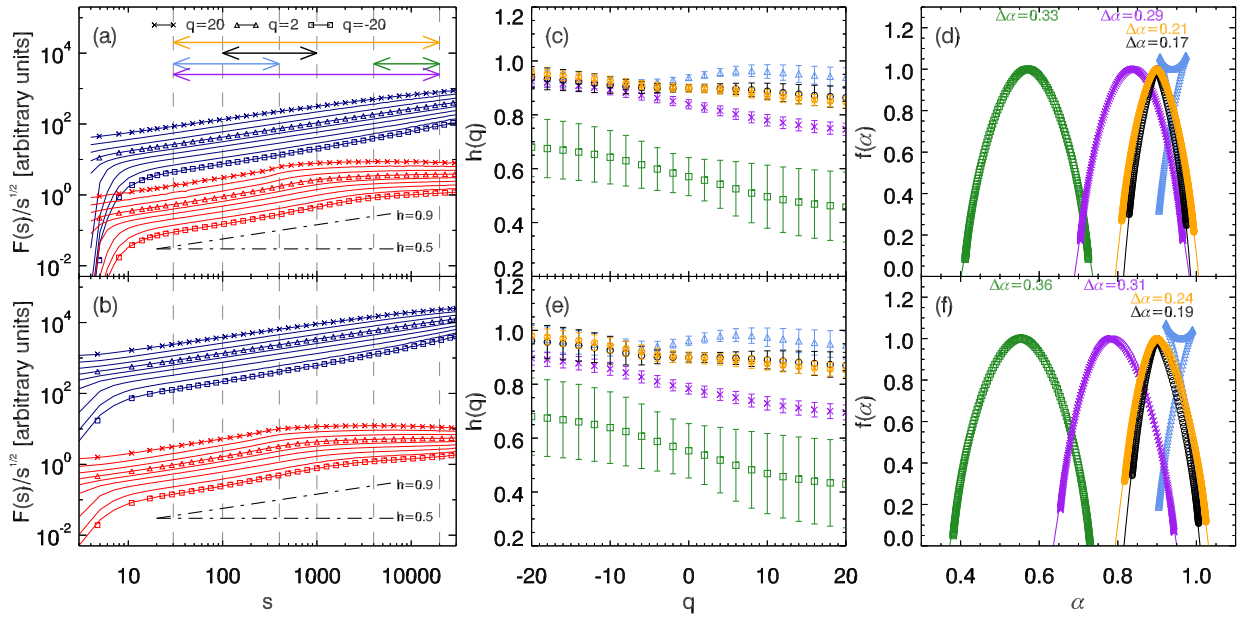


Figure 3.13.: Comparison of multifractal analysis results from purely long-term correlated data [$\alpha = 0.9$, $N = 100000$, top blue curves in (a,b)] and the same data after additional shuffling of non-overlapping blocks [$L = 200$, bottom red curves in (a,b)] employing MF-DFA2 (a,c,d) and MF-CMA (b,e,f). All results are based on $N_c = 1000$ different configurations. In (a,b) multifractal fluctuation functions $F_q(s)$, $q \in [-20, -10, -5, -2, 0, 2, 5, 10, 20]$ are shown. Colored arrows mark different fitting regimes for obtaining $h(q)$; from top to bottom: (i) for purely long-term correlated data $s \in [30, 20000]$ (orange), $s \in [100, 1000]$ (black), and (ii) for shuffled data $s \in [30, 400]$ (blue), $s \in [4000, 20000]$ (green), and $s \in [30, 20000]$ (purple). In the same color coding $h(q)$ is illustrated in (c,e), and $f(\alpha)$ in (d,f). Values for $\Delta\alpha$ are obtained from the roots of second order polynomial fits.

fling. The 'inversed' singularity spectrum (see blue points in Fig. 3.13(d,f)) is in fact a typical sign of crossover effects disturbing the scaling behavior. Note that the unexpectedly large spurious multifractality in the large s regime, where $h(q) = 0.5$ should be expected after the block shuffling, can be explained as follows. Looking at Eqs. (3.20), (3.24), (3.17), and (3.22) the number of windows ν becomes one in the limit of large scales ($s \rightarrow N$), leading to only one term in the sums in Eqs. (3.24) and (3.22). Therefore, the fluctuation functions must become independent of q and converge in one point for $s \rightarrow N$, which can only be achieved by different, slopes depending on q , i. e., apparent multifractality. This observation constitutes a deficiency of fluctuation analysis methods in general.

These results indicate that a 'blind' multifractal analysis, where $h(q)$ or $f(\alpha)$ is automatically calculated without looking at the scaling behavior of the fluctuation functions, is very dangerous. A crossover in the data creates spurious multifractality and further increases the apparent $\Delta\alpha$ above the levels expected due to finite size effects. Even comparing the results of two analysis methods with different detrending capability does not help in these cases. Therefore, careful checks of possible crossovers and comparisons involving different fitting regimes are needed before conclusions regarding multifractality should be drawn for real data unless the calculated $\Delta\alpha$ values are much larger than those obtained for non-multifractal data here.

3.4.2. Spurious Multifractality Due to Finite-Size Effects and Nonstationary Correlations

In order to study systematically, down to which Δh_{20} (and $\Delta\alpha$) real multifractality can be detected reliably by MF-CMA and MF-DFAn in data without crossovers in the following results for monofractal and multifractal data are compared. I find that the non-zero numerical values of Δh_{20} and $\Delta\alpha$ calculated from MF-DFA2 and MF-CMA results of non-multifractal data depend mainly on $h(2)$. Since this dependence is much stronger than the N dependence of these finite-size effects, detailed results are presented in Fig. 3.14.

Figures 3.14(a-c) show Δh_{20} and $\Delta\alpha$ as well as the ratio of the two parameters versus $h(2)$ for

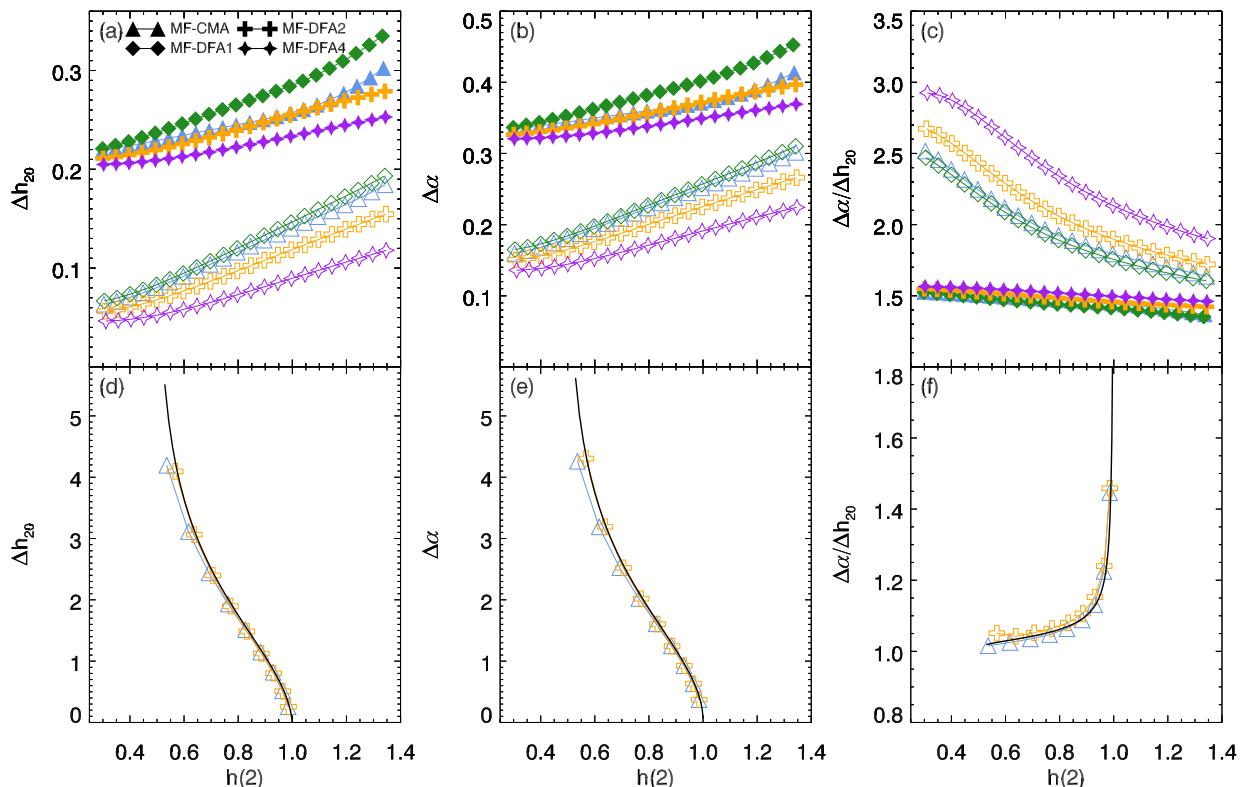


Figure 3.14.: Degree of multifractality expressed by Δh_{20} and $\Delta\alpha$ and their ratio for MF-CMA [triangles] and different orders of MF-DFA [$\circ(1)$ diamonds, $\circ(2)$ crosses, $\circ(1)$ stars]. Open symbols in (a-c) refer to monofractal long-term correlated data of $h(2) \in [0.3, 1.35]$, $N = 100000$; filled symbols refer to results from a generalized binomial multifractal [$a = 0.55$, $N = 2^{16}$] with tuned $h(2) \in [0.3, 1.35]$ as described in Sect. 3.3.5. Open symbols in (d-f) denote results for pure stochastic binomial multifractals [without tuning $h(2)$] from bottom to top for parameters $a = [0.55, 0.6, 0.65, 0.7, 0.75, 0.8, 0.85, 0.9, 0.95]$ and only for MF-CMA and MF-DFA2. Black curves illustrate the theoretical behavior. Note: Although results become stable very quickly each point in every panel is derived by averaging $N_c = 1000$ configurations.

both, monofractal data generated by Fourier filtering [open symbols] and multifractal data from the GB-MFM [$a = 0.55$; filled symbols; see Sect. 3.3.4 for model details]. One clearly observes spurious multifractality for the monofractal signals increasing with $h(2)$ up to a $\Delta h_{20} \approx 0.2$ and $\Delta\alpha \approx 0.3$, respectively. These strengths of finite-size multifractality effects are basically the same for MF-DFA1 and MF-CMA, but become smaller for MF-DFA n with $n > 1$. Thus, when multifractality characterized by $\Delta h_{20} \approx 0.2$ is found in real world data, this result cannot prove multifractality on its own. Further tests are necessary, e.g., by comparing results for different detrending orders n . Supposedly multifractal time series showing $\Delta h_{20} \leq 0.2$ or $\Delta\alpha \leq 0.3$, respectively, might indeed be monofractal, in particular if $h(2)$ is large, i. e., in the non-stationary regime $h(2) > 1$. Therefore, I suggest being very careful with conclusions regarding multifractality if $\Delta h_{20} \leq 0.2$ and/or $\Delta\alpha \leq 0.3$. An additional effect which might partially be responsible for the observed spurious multifractality in non-multifractal data might be an altered distribution of values due to the Fourier filtering technique. In studying the Schreiber-Schmitz method [see Sect. 1.5.2] I found that the distribution of values is foremost notably changed for $h(2) > 1.25$ [see also Fig. 1.3 for an example with $h(2) = 1.5$]. However, since a similar increase in Δh_{20} and $\Delta\alpha$ is observed for $h(2) < 1$ and in particular around $h(2) = 0.5$, I doubt that a broad distribution is an appropriate explanation. Such hypothesis could easily be checked by shuffling the data that destroys multifractality due to correlations but preserves multifractality due to a broad distribution [KANTELHARDT *et al.* 2002].

The same trends with $h(2)$ are observed for multifractal data, see the filled symbols in Figs. 3.14(a-c). Considering the GB-MFM with $a = 0.55$ (corresponding to $\Delta h_{20} = 0.192$ and $\Delta\alpha = 0.290$), I find the numerical values of these quantities also increasing with $h(2)$, just as for the monofractal data [see Figs. 3.14(a,b)]. The ratio of both quantities, however, is fairly constant [see Fig. 3.14(c)]

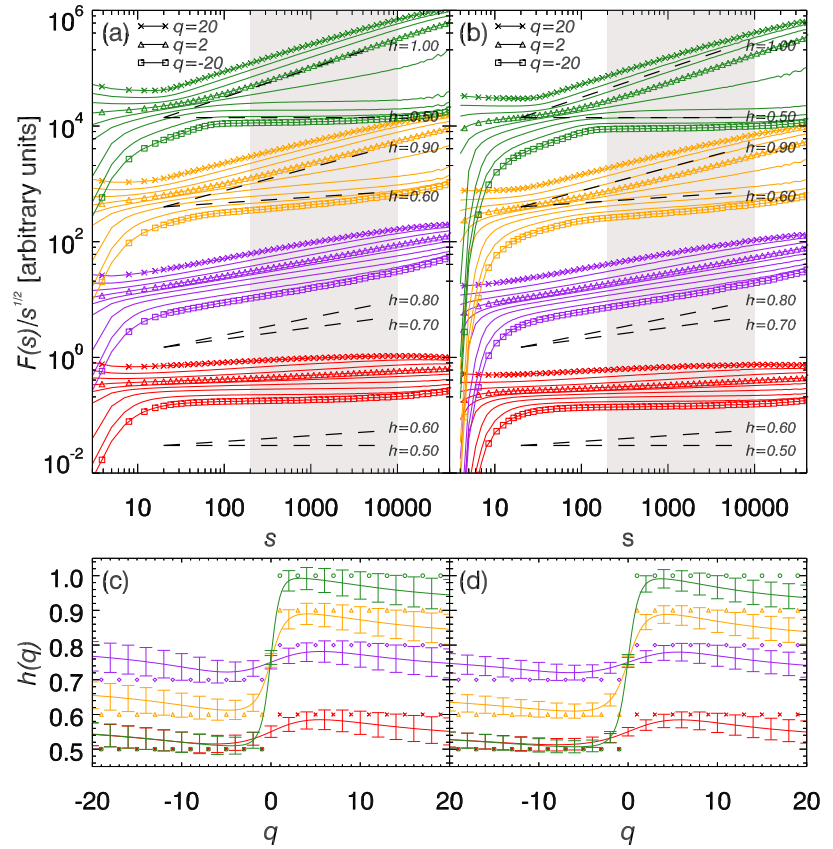


Figure 3.15: Multifractal analysis of two joined monofractal long-term correlated data series [$N = 100000$ each]. Scaled results for (a) MF-CMA and (b) MF-DFA2 are presented for $q \in \{-20, -10, -5, -2, 0, 2, 5, 10, 20\}$ with triangles marking $q = 2$, boxes $q = -20$, and crosses $q = +20$. Black dashed lines indicate theoretical slopes for both patches [from bottom to top] $(h(2)_{\text{first}}, h(2)_{\text{second}}) = (0.5, 0.6)$ [red], $(0.7, 0.8)$ [purple], $(0.6, 0.9)$ [yellow], and $(0.5, 1.0)$ [green]. All curves are vertically shifted (i) for different q and (ii) different parameter sets. Gray shaded areas indicate the fitting range. Parts (c,d) show the numerical $h(q)$ behavior [same order for $q > 0$ and color coding as in (a,b)]; errorbars from 1000 configurations; symbols mark theoretical values for a corresponding bi-fractal.

and strictly below 1.6, unlike the behavior for monofractal data. High ratios $\Delta\alpha/\Delta h_{20} > 2$ are thus clearly indicative of spurious multifractality.

Results for the pure binomial multifractal model without modified long-term correlations are presented in Figs. 3.14(d-f). The value of $h(2)$ is close to 1 for weak multifractality ($a \approx 0.5$) and approaches 0.5 for strong multifractality ($a \rightarrow 1.0$). Consequently, Δh_{20} and $\Delta\alpha$ drastically increase with decreasing $h(2)$. The numerical results are very close to the theoretical curves. The ratio $\Delta\alpha/\Delta h_{20}$ converges to 1 in the limit of strong multifractality as shown in Fig. 3.14(f). The results show that both methods work very well for strong multifractality, and the parameters Δh_q and $\Delta\alpha$ become equivalent in this limit.

3.4.3. Spurious Multifractality Due to Patchy Correlation Behavior

As described in Section 3.3.3 real multifractal time series consist of interwoven fractal subsets with the points in each subset (with fractal dimension f) characterized by different Hölder exponents α (describing the local scaling behavior). If, however, these subsets are not fractal, there is no real multifractality. In particular, a time series consisting of large patches of monofractal data with each patch being characterized by a different (but not q dependent) scaling exponent $h(q) = \alpha$ cannot be regarded as a multifractal. In fact, analyzing each patch separately would clearly reveal the monofractal (and nonstationary) nature of the data in this case. In practice, however, the positions of the patches might not be known, and therefore one might be tempted to study the whole non-stationary time series by a single multifractal analysis procedure. A practical example is the fluctuation behavior of human heartbeat, which has been studied by looking at whole 24h recordings [PENG *et al.* 1995] and by splitting them into daytime and nighttime [IVANOV *et al.* 1999a] as well as different sleep stages [BUNDE *et al.* 2000], rest and exercise [KARASIK *et al.* 2002]. Although, consequences of *patchy data* on a monofractal DFA analysis were studied in [CHEN *et al.* 2002] their impact on a multifractal analysis, e.g., when employing MF-DFA or MF-CMA, were not studied before. Therefore, I now consider the simple model of independently generated and joined long-term correlated time series of $N = 100000$ elements each characterized by different monofractal scaling behavior ($h(2)_{\text{first}}$ and $h(2)_{\text{second}}$).

Figure 3.15 shows the spurious multifractality appearing for such data. Obviously, both methods, MF-CMA and MF-DFA2 seem to indicate rather strong multifractality (or better: bi-fractality) if h_{first} and h_{second} are sufficiently different, see the two top sets of curves in Figs. 3.15(a,b). One can see that the larger fluctuation exponent is retrieved in the limit of large positive q while the smaller one appears for negative q . The strange shapes of the corresponding $h(q)$ curves shown in Figs. 3.15(c,d), however, clearly indicate that there is something wrong with this multifractality – for real multifractal data one would expect a monotonously decaying $h(q)$ curve, i.e., $h(-|q|) > h(|q|)$. In general, any segment of $h(q)$ with *positive* slope should be considered as a sincere warning that there are problems with the observed scaling behavior.

If, on the other hand, both exponents h_{first} and h_{second} differ by just 0.1 the scaling behavior appears as nearly monofractal, see the two bottom sets of curves in Figs. 3.15(a,b). In this case the fitted slopes $h(q)$ meander between h_{first} and h_{second} , see Figs. 3.15(c,d). Except for crossovers appearing at smaller scales for MF-CMA (originating in the different detrending order) there are no significant differences between the results of MF-CMA and MF-DFA2.

To understand what is observed let us first recall that stitching together two monofractal patches of different fluctuation exponents should result in a *pseudo bi-fractal* when studied as a whole by MF-CMA or MF-DFA. I use the attribute 'pseudo' here because although a fluctuation analysis yields non-monofractal behavior the series is not characterized by interwoven fractal subsets which I consider to be an integral part of multifractality (or, bi-fractality). In a real bi-fractal series any sufficiently long subset ensuring reliable statistics exhibits bi-fractal scaling. In the joined-monofractals case, however, any subset that does only contain parts of either half is immediately identified as a monofractal.

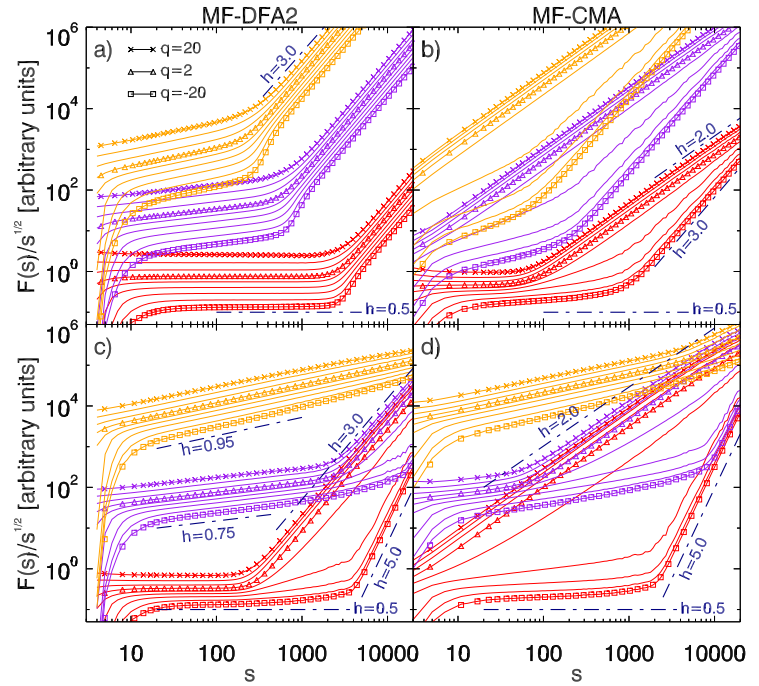
Next it is necessary to understand why the larger scaling exponent is retrieved for large positive moments q and the smaller scaling exponent for large negative moments. Therefore, consider the fluctuation function (exemplarily for MF-DFA; analogous for MF-CMA and other related methods) in Eq. (3.22). Since in the algorithm non-overlapping windows are considered only one window contains information of both patches each characterized by $h(2)_{\text{first}}$ and $h(2)_{\text{second}}$, respectively. The q th moment fluctuation function is linear in $F_{\text{MF-DFA},\nu}^q$; let without loss in generality be $h(2)_{\text{first}} \geq h(2)_{\text{second}}$, and hence,

$$\begin{aligned}
 F(s) &\approx [F_{\text{first}}^q + F_{\text{second}}^q]^{1/q} \\
 &\sim [s^{qh(2)_{\text{first}}} + s^{qh(2)_{\text{second}}}]^{1/q} \approx \begin{cases} 2s^{h(2)} & : h(2) = h(2)_{\text{first}} \approx h(2)_{\text{second}}, q \neq 0 \\ s^{h(2)_{\text{first}}} & : h(2)_{\text{first}} > h(2)_{\text{second}}, q \gg 0 \\ s^{h(2)_{\text{second}}} & : h(2)_{\text{first}} > h(2)_{\text{second}}, q \ll 0 \end{cases} \quad (3.38)
 \end{aligned}$$

where the first ' \approx ' is used since the equality is violated by the window containing parts of both patches for most scales s . At this juncture, above argumentation remains valid for overlapping windows (MF-CMA or statistically enhanced MF-DFA) since although the number of windows containing the joint of both scaling regimes increases, the number of windows belonging to either one regime does increase as well.

The discussed property has serious consequences for any multifractal analysis in long datasets where spurious multifractality might be rooted in many joined monofractal subsets. For instance multifractality which has been reported in 24h heartbeat by various authors, see [SASSI *et al.* 2009] for a recent example, has to be challenged. Although heartbeat data is sometimes subdivided into daytime and nighttime segments, e.g., 6h segments each in [IVANOV *et al.* 1999b], subdivision should be done even more carefully according to certain sleep stages during night or activity vs. rest during daytime. Nevertheless, to my own opinion and experience with multifractal analyses of heartbeat during different sleep stages [not discussed in this thesis] it is unlikely that reported multifractality is completely spurious. This is supported by a recent paper [DING *et al.* 2007] whose results on the other hand appear to my own experience in a much larger database (SIESTA) a little too smooth considering the strong inter-individual variations in heartbeat, and I urge the reader to question associated results.

Figure 3.16.: Multifractal analysis of long-term correlated data [$N = 100000$, $\langle x_k \rangle = 0$, $\langle x_k^2 \rangle = 1$] with additional trends. (a,b) 2nd-order trend Ax^2 ; $h = h(2) = 0.95$, $A = 0.0001$ [orange]; $h = 0.75$, $A = 10^{-5}$ [purple]; $h = 0.5$, $A = 10^{-7}$ [red]. (c,d) 4th-order trend Ax^4 ; $h = 0.95$, $A = 10^{-19}$ [orange]; $h = 0.75$, $A = 10^{-17}$ [purple]; $h = 0.5$, $A = 10^{-15}$ [red]. Scaled fluctuation functions $F_q(s)/s^{1/2}$ obtained by (a,c) MF-DFA2 and by (b,d) MF-CMA for $q \in [-20, -10, -5, -2, 0, 2, 5, 10, 20]$ with triangles marking $q = 2$, boxes for $q = -20$, and crosses for $q = +20$. Blue dashed lines indicate slopes for initial correlations or linear fits to fluctuation functions on large scales. All curves are vertically shifted (i) for different q and (ii) for different parameter sets.



3.4.4. Spurious Multifractality in Data With Trends

It is known that trends of different order affect monofractal DFA, see Figs. 3.2(a,b) or [KANTELHARDT *et al.* 2001; HU *et al.* 2001; RYBSKI AND BUNDE 2009]. Since CMA is comparable to DFA1 (linear detrending in the profile, removal of local means in the signal) one expects to observe effects of linear or higher order trends in those results as well. However, it was not studied so far if these effects are different for different moments q in the corresponding multifractal versions of the methods.

In Fig. 3.16 I study the crossovers observed for monofractal long-term correlated data with additional quadratic [Figs. 3.16(a,b)] and fourth order polynomial [Figs. 3.16(c,d)] trends using both multifractal analysis methods, MF-CMA and MF-DFA2 [parameters in figure's caption]. Since both of them cannot eliminate these trends, crossovers at positions s_{\times} related to the strengths of the trends are expected from previous studies. Comparing Figs. 3.16(a,b) one clearly observes the expected crossover behavior for MF-DFA2, while MF-CMA fails to reveal any usable information about the underlying scaling except for the weakest trend (bottom curves). The monofractal partial result which was already reported for monofractal analyses ($q = 2$) is contained in each curve group and marked by open triangles up. Clearly the detrending capability of MF-CMA is too weak for strong trends here.

Interestingly though, all fluctuation functions exhibit strong spurious multifractal (or better rather bi-fractal) scaling on large time scales, where the positive moments ($q > 0$) have slopes of $\approx n + 1$ (with n the detrending order), while the negative moments ($q < 0$) have slopes $t + 1$ (with t the order of the trend). These properties can in principle be analytically derived by evaluating the following scheme (sketched for MF-DFA):

Assume that both components, the correlated noise x_k and the trend $t_k = Ak^o$ of order o are uncorrelated with each other and additively superimposed. Then it follows for the superimposed profile (linear) $Y_{x+t} = Y_x + Y_t$, and together with their individual n th-order detrending polynomials in the ν th window, $p_{n,\nu,x}$ and $p_{n,\nu,t}$, one finds for the corresponding superimposed DFA fluctuation function

$$F_{\text{DFAn},\nu,x+t}^2(s) = \frac{1}{s} \sum_{i=1}^s \{Y_x(\nu s + i) - p_{n,\nu,x}(i) + Y_t(\nu s + i) - p_{n,\nu,t}(i)\}^2. \quad (3.39)$$

Here, I have only considered non-overlapping windows for the forward direction for simplicity. Similar expressions can easily be obtained for the backward direction and/or overlapping windows. Since I assumed noise and trend to be uncorrelated it follows that both detrended profiles are

uncorrelated, and hence, all terms

$$\sum_{i=1}^s (Y_x(\nu s + i) - p_{n,\nu,x}(i)) (Y_t(\nu s + i) - p_{n,\nu,t}(i)) \approx 0 \quad (\text{for large } s) \quad (3.40)$$

yielding the superimposed q th moment MF-DFA fluctuation function

$$F_{\text{MF-DFA}n,x+t,q}(s) = \left[\frac{1}{[N/s]} \sum_{\nu=0}^{[N/s]-1} [F_{\text{DFA}n,\nu,x}^2(s) + F_{\text{DFA}n,\nu,t}^2(s)]^{q/2} \right]^{1/q}. \quad (3.41)$$

Equation 3.41 does not trivially separate because in general $q \in \mathbb{R}$, and thus, the binomial theorem does not apply, here. To find an exact solution: (i) the least-square fit of the desired detrending polynomial to the profile has to be obtained analytically employing software tools capable of symbolic analysis, (ii) results have to be inserted in Eq. (3.39) followed by Eq. (3.41), and (iii) the leading terms for both limits $q \rightarrow \infty$ and $q \rightarrow -\infty$ have to be identified. For a much simpler example see [HU *et al.* 2001] where the exact solution for the monofractal DFA1 ($q = 2$, linear detrending polynomial) considering a quadratic trend in the profile (linear trend in the signal) is discussed. Note that this conjecturally simple example already yields a rather complicated formula. One can imagine that the analytical expression for the generalized multifractal case and the trends shown in Fig. 3.16 has an even more complex structure. However, the behavior of $F_{\text{MF-DFA}n,x+t,q}(s)$ in Eq. (3.41) can be approximated in the limit of small s and large s where either stochastic components (from x_k) or trend components (from Ak°) dominate, yielding

$$F_{\text{MF-DFA}n,x+t,q}(s) \approx \begin{cases} F_{\text{MF-DFA}n,x,q}(s) & : n + 2 \leq s \lesssim N \\ F_{\text{MF-DFA}n,t,q}(s) & : s_x \gtrsim s \leq N/4. \end{cases} \quad (3.42)$$

This can easily be understood by imagining a stochastic component superimposed by a quadratic trend which pans over the whole dataset and is detrended by a linear function (as in MF-DFA1). For small scales the regression line approximates the quadratic trend rather well due to a small curvature. Thus, local fluctuations in the windows ν are dominated by stochastic components rather than trend components, finally yielding a q th-moment MF-DFA function similar to the one obtained by separately analyzing the stochastic signal. On the other hand on large scales $1 \ll s \leq N/4$ the fitting straight does rather badly approximate the trend which leads to large fluctuations not at all representing the behavior of the noise. Fluctuations of the stochastic component are eclipsed. Analogously, both limits can be explained for higher order trends and detrending where the detrending order is smaller than the trend order.

But, why do positive q exhibit a scaling of $n + 1$ with n being the detrending order and negative q a scaling of $t + 1$ with trend order t ? So far, I was not able to derive a convincing analytical expression. However, in their simple toy model for monofractal DFA1 Hu *et al.* have shown that the monofractal fluctuation function depends on nonlinear terms of the series length N and nonlinear terms containing the scale s [HU *et al.* 2001]. While Hu *et al.* neglect purely s -dependent terms since $s < N$ and $q = 2 > 0$ for a monofractal analysis, such approximation is no longer generally valid in the multifractal case where terms containing N will still dominate moments $q > 0$ but terms in s with $s < N$ will dominate moments $q < 0$. Hence, a different behavior of the multifractal fluctuation function can be expected assuming similar terms in an exact solution. The Hu *et al.* model is related but not equivalent (if moments q are involved the analytical expression will be different!) to the MF-CMA (which is not exactly the same as MF-DFA1) case in Fig. 3.16(b). Simplifying their reported results yields for the largest components $F(s) \sim s^3 + Ns^2$. Together with the above argumentation and the assumption that similar superscripts are retrieved in the generalized q th-moment fluctuation function this would roughly yield a scaling of $h(q < 0) = 3$ and $h(q > 0) = 2$, respectively, in the multifractal case. Both scaling exponents are observed in Fig. 3.16(b). Nevertheless, an exact multifractal expansion of Eq. (3.41) allowing for a verification of this hypothesis remains to be done. The same is true for

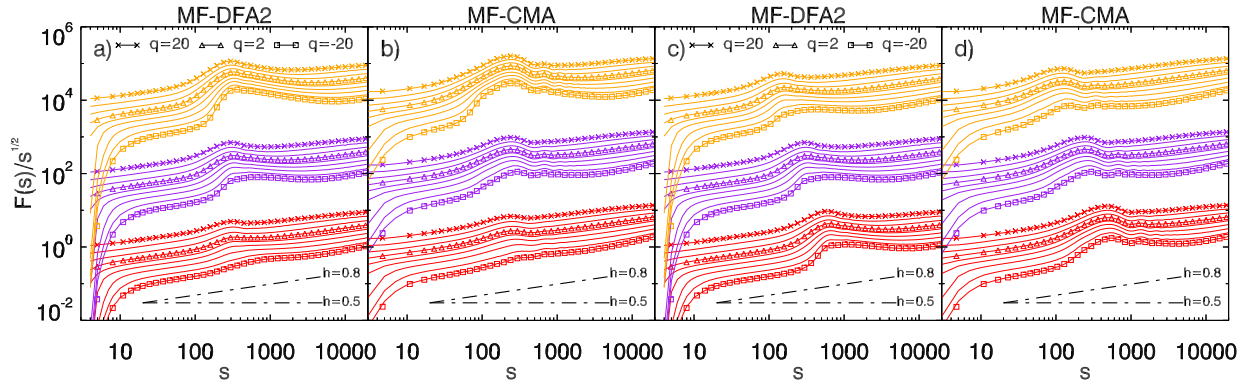


Figure 3.17.: Multifractal analysis of long-term correlated data [$h(q) = 0.8$, $N = 100000$] with additional periodicities (a,b) of period $T = 200$ and amplitude $A = 0.5$ [red], $A = 1$ [purple] and $A = 2$ [orange], and (c,d) of amplitude $A = 1$ and period $T = 100$ [orange], $T = 200$ [purple] and $T = 400$ [red]. The noise was normalized to zero mean and unit variance. Scaled fluctuation functions $F_q(s)/s^{1/2}$ have been obtained by (a,c) MF-DFA2 and by (b,d) MF-CMA for $q \in [-20, -10, -5, -2, 0, 2, 5, 10, 20]$ with triangles marking $q = 2$, boxes for $q = -20$, and crosses for $q = +20$. Black dashed lines indicate the theoretical slopes $h = 0.8$ as well as uncorrelated behavior [$h = 0.5$]. Again all curves are vertically shifted (i) for different q and (ii) for different parameter sets.

the positions s_{\times} of the crossover which apparently strongly depend on q in the cases of spurious multifractality.

Be aware that this scaling behavior has no relation with any multifractality or bi-fractality at all and is only induced by the trends and application of fluctuation analysis methods of 'too' low order. For all examples in Figs. 3.16(a,b) MF-DFA3 would fully eliminate the trends and therefore show no crossover, while MF-DFA5 would be needed to achieve full detrending in Figs. 3.16(c,d).

3.4.5. Spurious Multifractality in Data With Periodicities

Real world data, e. g., time series obtained from temperature or precipitation recordings, are often disturbed by nearly periodic trends due to, e. g. annual variations. From monofractal investigations it is known that even weak periodicities in the data can spoil its scaling behavior [KANTELHARDT *et al.* 2001; HU *et al.* 2001]. Effects of periodicities (arrhythmias) can also be observed in heartbeat and to my experience often during light sleep especially in apnea patients. To check whether periodic trends can cause spurious multifractality I analyze long-term correlated data with additional periodicities of different amplitudes and frequencies. Results obtained by MF-CMA and MF-DFA2 can be found in Fig. 3.17. Obviously, all moments q are affected by the periodicities. The position of the distortions in the fluctuation functions depends directly on the period T (see Figs. 3.17(c,d)) while the strength of the distortions depends on the amplitude A of the periodicities (see Figs. 3.17(a,b)).

However, the strengths of the disturbing effects are also different for different moments q leading to a possible pitfall regarding conclusions about multifractality. In particular the regime just below the twists exhibits different slopes with larger $h(q)$ for negative q . Such effect seems to be stronger for MF-DFA2 than for MF-CMA, compare Figs. 3.17(a,b) in the range $100 < s < 200$. This might lead to a spuriously decaying $h(q)$ curve when blindly fitting over the distortions. Note, that MF-CMA fluctuation functions show weak additional oscillations directly following the initial meander due to only constant detrending while sinusoids can be piecewise approximated by quadratic detrending in MF-DFA2.

4. Investigating Quasiperiodicities

This chapter is devoted to studying periodicities and more importantly quasiperiodicities in time series. The latter term will be defined shortly. In particular I will focus on two recently developed methods – namely *Phase Rectified Signal Averaging (PRSA)* and *Bivariate PRSA (BPRSA)* – which are capable of detecting and studying quasiperiodicities in univariate, bivariate, and even multivariate time series.

As a motivation why studying periodicities in recorded data is of importance recall that many natural systems exhibit cyclicity on different time scales. Among the numerous examples in biological and physiological systems are cardio-respiratory rhythms whose mutual phase-synchronization will be studied in further detail in Chapt. 5, rhythmic motions of limbs in walking, rhythms underlying the release of hormones and gene expression, membrane potential oscillations, oscillations in neuronal signals, and circadian rhythms [see, e. g., TYSON 2002; GLASS 2001]. Aside from living systems oscillations can be found in geophysical data, e.g., for the El-Niño phenomenon, sunspot numbers, and ice age periods [VON STORCH AND ZWIERS 2001] or in economics, e.g., stock exchange. In many cases several signals capturing different components of such complex systems can be recorded simultaneously. A particular example are polysomnographic recordings such as provided by the SIESTA database [see Sect. 2.3]. In order to elucidate a complex system, including its control chains and feedback loops, knowledge about the interactions between different components generating periodicities is desired. Consequently, there is a need for identifying periodicities in one recorded signal together with the direction of causal relations to periodicities in other signals.

Traditional tools used to tackle such questions are cross-correlation analysis [see Sect. 1.1] and transfer function analysis [SCHLITTEGEN AND STREITBERG 1999]. However, there are three major drawbacks of both methods: (i) only rather stationary data can be studied, (ii) a linear relationship between the signals is usually assumed, and (iii) the identification of causalities is hindered by the fact that the exchange of the two signals under study is identical with time inversion. Non-stationarities are a major problem when analyzing signals of long duration [PRIESTL 1988; PENG *et al.* 1994; BOX *et al.* 1994; BROCKWELL AND DAVIS 2003; KANTZ AND SCHREIBER 2004]. Many internal and external perturbations are continuously influencing the system and causing interruptions of the periodic behavior. The interruptions often 'reset' the regulatory mechanisms resulting in phase de-synchronization of the oscillations. The signals thus become *quasi-periodic*, consisting of many periodic patches as well as noise and trends. In addition, there might be causal inter-relationships between two signals X and Y that cannot be revealed by the traditional methods. For illustration, assume that a large increase *and* a large decrease in X (later termed trigger signal) cause *the same* specific effect in Y (later termed target signal), while there is no such effect in Y if X remains unchanged. In this situation with an essentially nonlinear coupling between the signals, both, cross-correlation analysis and spectral analysis cannot reveal the effect, see Sect. 1.1 for methodology. They show the superposition of the two branches of the interaction with opposite signs, i.e., no effect. Even if the effects on Y were different for increases and decreases of X , one could see some relation but could not distinguish the two effects. Hence, one needs a method that can separately study effects in Y which might occur in response to different causes in X , and vice versa. A separation of effects with different typical duration or frequency scale seems also appropriate for distinguishing frequency-band selective inter-relationships between X and Y .

Firstly, I will describe and review the *Phase Rectified Signal Averaging (PRSA)* method which was originally introduced in the context of assessing cardiac-arrest risk after an index myocardial infarction event and tested in a large data base comprising all together 2711 post-infarction patients ($N = 1455$ in the Munich cohort [ISAR-I, see Sect. 2.4.1], $N = 656$ in the London cohort, and $N = 600$ in the Oulu cohort) [BAUER *et al.* 2006a,b]. In particular I will present and discuss

new PRSA results as well as circadian-, diabetes-, and age dependencies of the PRSA based risk-classification parameter *Deceleration Capacity (DC)* which I obtained from the Munich cohort (ISAR-I) [KANTELHARDT *et al.* 2007]. Further, univariate PRSA is employed to sleep data from the SIESTA database separately for different sleep stages [SCHUMANN *et al.* 2010a]. The second part of this chapter is dedicated to a generalization of PRSA to a *bivariate phase rectified signal averaging (BPRSA)* [SCHUMANN *et al.* 2008a] which is somewhat related to *cross-correlation analysis (CCA)* [see Eqs. 1.9] but gives additional insights into the system under surveillance — I will address advantages of BPRSA compared with CCA, discuss its performance and robustness in the presence of nonstationarities. Finally, a sketch will be given how the method can further be generalized towards a *Multivariate Phase Rectified Signal Averaging (MPRSA)*.

4.1. Univariate Phase Rectified Signal Averaging (PRSA)

Let $X = \{x_i\}$, $i = 1, \dots, N$ be a long time series¹ representing the signal under investigation which in this thesis will either be artificial data or heartbeat data, in the bivariate case together with blood pressure [Sect. 4.2]. Nevertheless, the methodology is not limited to this type of data but can easily be ported to data from various other sources².

In addition to periodicities and correlations of interest, X may contain non-stationarities, noise and recording artifacts. One example for such signal is the series of time intervals between successive heartbeats (RRI) [see Sect. 2.2]. Univariate *Phase Rectified Signal Averaging (PRSA)* was shown to reduce the signal to a much shorter sequence keeping all relevant quasi-periodicities but eliminating non-stationarities, artifacts, and noise [BAUER *et al.* 2006b]. PRSA is based on the assumption that certain 'typical oscillatory patterns' are present throughout the signal. Such *quasi-periodic oscillations* are characterized by non-constant frequencies throughout the signal and additional interruptions in their periodic cycles. Usually, internal or external perturbations – for instance, cardiac arrhythmias or activity changes – lead to *phase jumps*: an oscillator stops and then resumes its operation with a random phase offset that is not related with the phase of the oscillations before the interruption. Both phase jumps and frequency variations destroy the auto-coherency of the signal and broaden characteristic peaks in its power spectrum yielding a diffuse frequency localization. Additionally, random noise components from various sources disturb an analysis. The previous chapter, Chapt. 3, was exclusively dedicated to studying the characteristics of such noise components by various multifractal detrending fluctuation analysis methods. Now, I aim at a somewhat complementary goal. In a fluctuation analysis oscillatory components disturb a homogeneous scaling behavior – recall the influence of oscillations presented for the monofractal ($q = 2$) case in Fig. 3.2 – and, moreover, can imply spurious multifractality as depicted in Fig. 3.17. Fluctuations, on the other hand, disturb studies aiming at understanding oscillatory dynamics. Hence, a methodical framework for enhancing quasi-oscillatory traces hidden in the signal by simultaneously attenuating random fluctuations is needed.

In addition to such rather technical desire there is the medical requirement to distinguish oscillatory components that are associated (in phase) with the deceleration of the heart, i.e., increases in beat-to-beat intervals, and acceleration of the heart, i.e., decreases in beat-to-beat intervals. The reason are two complementary parts of the autonomous nervous system [see Sect. 2.2] being responsible for either of the two. The sympathetic autonomous nervous system affects the acceleration of the heart while the parasympathetic autonomous nervous system is responsible for steering its deceleration. Although parasympathetic activation is faster than sympathetic activation [HRV TASK FORCE 1996] we recognize sympathetic effects more quickly. For instance, when we are suddenly frightened or get up quickly from supine to upright position our heart rate

¹At least long enough to result in approx. 100 anchor points [see description of PRSA algorithm in Sect. 4.1.1].

Commonly, I suggest a minimum of $N = 1000$ data points, roughly resulting in 500 anchor points assuming a series characterized by a homogeneous distribution of increasing events and decreasing events.

²Although results are not presented in this thesis I have applied (bivariate) phase rectified signal averaging to geophysical data, e.g. El Niño datasets (Sea Surface Temperature (SST) from different locations in the Pacific), Southern Oscillation Index (SOI), North Atlantic Oscillation Index (NAO), sunspot data, or All Indian Rainfall Index a proxy of Monsoon activity.

increases fast. The parasympathetic deceleration of the heart, on the other hand, appears to be rather slow. This can manifest for example as a longer time that our bodies need to calm down after exercise compared with the rather quick speedup before. A separate analysis of both effects would be helpful for researching different components of autonomic control. In addition, it is believed that results can be exploited to improve mortality-risk assessment due to the empirical observation that in high-risk patients the heart’s ability to slow down (parasympathetic effect) is diminished compared with healthy subjects or subjects with a positive prognosis after an index infarction event [PRIORI *et al.* 2001; HUIKURI *et al.* 2009].

Obviously, the desired method needs to combine typical, i.e., *average* information from many times of the same event, i.e., *the same phase* by simultaneously reducing noise. Parasympathetic activation resulting in the heart’s deceleration is just one example of such an event. For that reason my collaborators successfully suggested to align similar events together with their surroundings, i.e., *phase rectify* the signal, and average to enhance the features while reducing the out-of-phase noise.

Before describing the PRSA method in detail I would like to mention that although the idea behind PRSA was originally developed independently, it is similar to *event-locked functional magnetic resonance imaging (efMRI)*, *event-related potentials (ERP)* based on electro-encephalographic (EEG) data, or its magneto-encephalographic (MEG) pendant *event-related fields (ERF)* analysis which have been applied to tackle brain and central nervous system related questions in physiology, (cognitive) psychology, or linguistics during the last two decades, see e.g. [LUCK 2005; POLICH 2003; BUXTON 2002] for an overview. For instance in efMRI studies it is common to expose a subject to certain stimuli, e.g., showing a photograph of the well known actress Jennifer Aniston³, at a well-defined time and record changes in neural activity (measured by blood oxygen-level dependent (BOLD)-fMRI) before, during, and after exposure [QUIAN QUIROGA *et al.* 2005]. For statistical reasons the experiment is repeated several times including intermediate ‘no-stimulus’ or even ‘counter-stimulus’ episodes to reset the brain activity to baseline activity. Scans are then aligned with respect to stimulus onset and activity profiles are averaged. By comparing the ‘normal’ brain activity, i.e., without exposure, with the ‘stimulated’ brain activity one can identify brain regions that were especially active or inactive upon stimulation and study their dynamics. In sleep EEG it has been found that aligning recordings at times of occurring sleep spindles and averaging recovers the respiratory cycle [ACHERMANN 2009].

4.1.1. PRSA Algorithm With Variants

The PRSA algorithm comprises 3 steps which are illustrated in Fig. 4.1:

Step 1: Definition of Anchor Points

Anchor points are selected in the time series $X = \{x_i\}$ according to signal-specific features one wants to study. There are several possibilities: in the most simple version of the PRSA method the anchor points correspond to increases (or, alternatively, decreases) in the signal as is depicted in Fig. 4.1(a) where red points mark such anchor points for increase events. A point x_i qualifies as an anchor point if $x_i > x_{i-1}$ (or, alternatively, $x_i < x_{i-1}$) for triggering on increases (or decreases, respectively). Alternatively, one may define the anchor points by comparing sums (or, equivalently, averages) of T successive values of the time series before and after the anchor point candidate x_i in order to study a lower frequency regime,

$$\sum_{j=0}^{T-1} x_{i+j} > \sum_{j=1}^T x_{i-j} \quad (4.1a)$$

$$\sum_{j=0}^{T-1} x_{i+j} < \sum_{j=1}^T x_{i-j}, \quad (4.1b)$$

³Actress Jennifer Aniston is well known from playing “Rachel Green” in the American comedy show “Friends”.

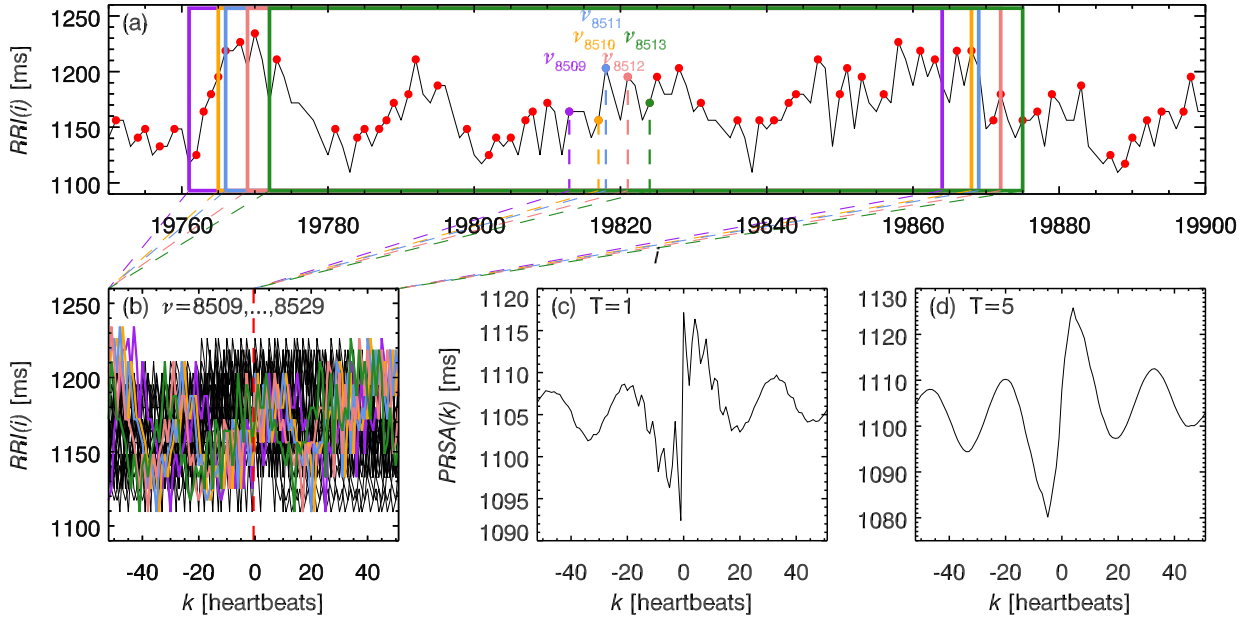


Figure 4.1.: Illustration of the PRSA technique: (a) Randomly chosen fragment of a 24h beat-to-beat interval signal from a post-infarction subject [72 years old, male survivor with diabetes] from the ISAR study. Anchor points [red filled circles] are selected in the time series $RRI(i)$ according to Eq. (4.1a) with $T = 1$. Exemplarily, only 5 of altogether 33162 identified anchor points, i.e., ν_{8509} [purple], ν_{8510} [orange], ν_{8511} [blue], ν_{8512} [coral], and ν_{8513} [green], are depicted together with their corresponding surroundings of length $2L$ [in same colors; here $L = 52$ for clarity] defined around each anchor point. (b) Surroundings of all anchor points are aligned at their anchor positions [here: only windows $\nu_{8509, \dots, 8519}$ are shown]. (c) PRSA curve, $PRSA(k)$, from averaging over all surroundings obtained in such way from the whole heartbeat signal [$N=79474$]. (d) PRSA curve derived analogously to (a-c) but by setting $T = 5$ in the anchor condition in Eq. (4.1a). Larger parameters T act as frequency low-pass filters. One clearly observes a fast oscillation likely related to respiration [period roughly 4 heartbeats per breath cycle] which is especially present [coherent] during ± 20 heartbeats around a deceleration event [an increase in heartbeat intervals], and a slow oscillation [period approx. 27 heartbeats] that is believed to be related with blood pressure oscillations.

where the simplest case is retrieved for setting $T = 1$. The parameter T sets an upper frequency limit for the periodicities that can be detected by PRSA (a kind of low pass filter, compare also Figs. 4.1(c,d)).

In principle other boolean valued functions $F : \Omega \rightarrow \{0, 1\}$ can serve as more sophisticated anchor criteria where Ω is the sample space of X and F assigns to every point $x_i \in \Omega$ the value true for the condition 'is an anchor' or false for the condition 'is not an anchor'⁴. This allows studying more complex structures in signals, e.g., two consecutive increases followed by a decrease and an increase, again. However, F must capture a 'typical' pattern yielding a sufficiently large number of selected anchor points to ensure a successful denoising in Step 3 of the algorithm (see below). If F returned a value 'true' for only one data point, PRSA would become meaningless.

Typically, in the case of selecting simple increases, approximately half of all points of the time series will qualify as anchor points. It can be shown mathematically that the PRSA is most sensitive for strictly periodic oscillations with frequency $f \approx 1/(2.7T)$ [BAUER *et al.* 2006b]: in order to calculate the parameter T for which the PRSA can most sensitively detect sinusoidal signals with frequency f consider – instead of the sums in Eqs. (4.1) – the following integral, $\frac{1}{T} \int_0^T \sin(2\pi f x) dx = \frac{1 - \cos(2\pi f T)}{2\pi f T}$. Finding the maximum of this expression yields $T \approx 2.33/(2\pi f) \approx 1/(2.7f)$. Numerical simulations have shown that this value changes to $f \approx 1/(2.5T)$ if the signal contains many phase jumps (non-stationarities).

In general, quasi-periodic oscillations in a noisy time series X will result in anchor points [Eq. (4.1)(a)] predominantly found in the phase of the steepest ascent (or decent [Eq. (4.1)(b)]), i.e., when the phase of the signal itself is close to 0 (or close to π). The phase information

⁴Note that F is meant as an abstract object where a value x_i (with known position i in $\{x_i\}$) is plugged in and a value 1 or 0 is returned. F might involve other points x_j , $j \neq i$ for the anchor decision.

of the oscillations is thus obtained from the signal itself, and the signal can be *phase-rectified* using the anchor points. Although it was not explicitly mentioned in the original work on PRSA, heartbeat data is almost always disturbed by artifacts and/or ectopic beats which must not qualify as anchor points, but should remain in the dataset to ensure correct timing. Especially, in infarction patients a large number of disturbing extrasystoles⁵ is characteristic, see Figs. 3.3(a,d) and 4.2(a) for both artificial and real examples. To overcome this problem originally an additional 5%-*threshold* was incorporated with the anchor definitions in Eqs. (4.1): only x_i with $0.95x_{i-1} \leq x_i \leq 1.05x_{i-1}$ qualify as anchor points. This filters out practically all ectopic beats but might be too strict⁶. From my own experience with semi-automatic QRS-peak detection software and the SIESTA database I suggest seriously reconsidering the threshold for each database under investigation. In SIESTA I implemented thresholds performing much better in sleep data: $0.7x_{i-1} \leq x_i \leq 1.6x_{i-1}$.

Step 2: Definition of Surroundings

Windows, i.e., surroundings, of length $2L$ are identified around each anchor point x_{i_ν} , $\nu = 1, \dots, M$ (see colored boxes in Fig. 4.1(a) for 5 examples with $L = 52$); M is the total number of anchor points. The surrounding of x_{i_ν} is

$$x_{i_\nu-L}, x_{i_\nu-L+1}, \dots, x_{i_\nu}, \dots, x_{i_\nu+L-2}, x_{i_\nu+L-1}. \quad (4.2)$$

The parameter L has to be chosen larger than the expected coherence time of the periodicities in the signal; it must definitely exceed the period of the slowest oscillation that one wants to detect. Note, that it is in principle possible to define an arbitrary surrounding $x_{i_\nu-L_1}, \dots, x_{i_\nu}, \dots, x_{i_\nu+L_2}$ where $L_1, L_2 \in \mathbb{N}$. When $L_1 \neq L_2$ different time spans preceding and succeeding the anchor event are captured. Usually, we choose L to be a power of two in order to support a Fourier- or wavelet analysis subsequent to Step 3 (however, not in Fig. 4.1 for clarity).

All anchor points with indexes i_ν smaller than $L + 1$ and larger than $N - L + 1$, i.e., at the very beginning and at the end of the time series, have incomplete surroundings. The same holds for windows containing missing data points due to, e.g., measurement artifacts, instrument failure, or outliers. In contrast to the original algorithm, I suggest including such incomplete windows in Step 3 to improve statistics especially in datasets with more than just a few artifacts.

Step 3: Phase Rectification and Averaging

All windows ν , $\nu = 1, \dots, M$ are aligned at their anchor points x_{i_ν} as depicted in Fig. 4.1(b), and the phase-rectified signal average PRSA $_X(k)$ is obtained by averaging over all windows [see Fig. 4.1(c) for $T = 1$ and Fig. 4.1(d) for $T = 5$],

$$\text{PRSA}_X(k) = \frac{1}{M} \sum_{\nu=1}^M x_{i_\nu+k}, \quad k = -L, \dots, 0, \dots, L-1. \quad (4.3)$$

If $x_{i_\nu+k}$ is a missing data point, it is replaced by 0, and M is substituted by M_k denoting the number of non-missing points at position k . Including windows with missing data points yields better statistics and allows investigation of time series with artifacts. In general a well-behaved average PRSA (k) can be expected when there are at least 100 to 1000 anchor points, i.e., $N = 200$ to $N = 2000$ for the length of the record⁷.

In the average in Eq. (4.3), non-periodic components (not phase-synchronized with the anchor points), i.e., non-stationarities, non-identified artifacts, and noise, cancel out. Only events that

⁵The number of extrasystoles has also been used to address cardiac risk in the past. However, extrasystoles are equally prominent features in EEG recordings of sportsmen and elderly, although, corresponding individuals are otherwise considered disease-free or 'healthy' subjects.

⁶For a beat-to-beat interval of 1000ms this only includes changes ± 50 ms which is to my opinion too small in at least healthy subjects characterized by a large heart rate variability compared with infarction subjects. However, my test with other thresholds in the ISAR data did not significantly alter the results due to the rather long datasets of $N > 80000$ elements.

⁷Of course this is not an exact number but depends on the source signal X . Given numbers are empirical values from my experience with medical data from various databases.

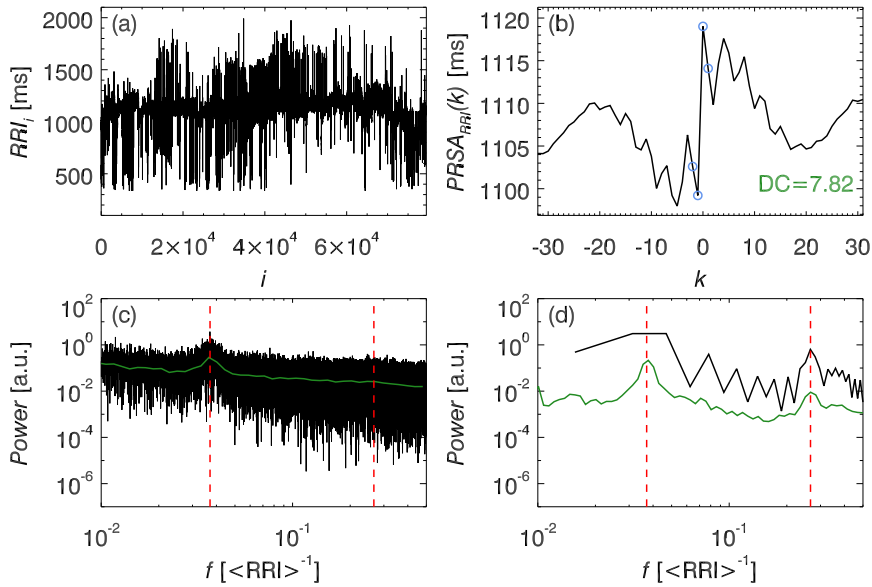


Figure 4.2.: (a) Original 24h beat-to-beat interval signal [post-infarction patient, many ventricular beats, survivor, diabetes type 2]. (b) Corresponding $\text{PRSA}_{\text{RRI}}(k)$ curve triggered on increasing intervals [$T = 1$, $L = 32$]. Two frequency components are immediately recognized [periods: ≈ 3.75 heartbeats (fast respiratory component) and ≈ 27 heartbeats (although a little too slow, likely a blood pressure related component)]. (c,d) Power spectra [black curves] of the signals shown in (a,b). The Spectra are logarithmically averaged such that the green curves have the same number of elements: (c) based on the black spectrum, (d) based on a recalculated PRSA curve [$L = 2048$] to include more periods of the slower oscillation and get a better frequency resolution. Red dashed lines indicate both frequency components. The slow component is well captured by both PRSA and the directly obtained spectrum. The fast component, clearly found in (d), is not seen in (c). Peaks are generally more pronounced in (d). Central points contributing to Deceleration Capacity ($\text{DC}=7.82$) according to Eq. (4.5) are marked in blue in panel (b).

have a fixed phase relationship with the anchor points, i.e., periodicities and quasi-periodicities, 'survive' the procedure [see Fig. 4.1(c,d)]. $\text{PRSA}_X(k)$ represents important features of the original data containing all quasi-periodicities aligned with phase zero in the center (at $k = 0$). Applying the PRSA before traditional spectral analysis significantly improves the quality of the spectra in the presence of noise and non-stationarities, see Fig. 4.2 and [BAUER *et al.* 2006b; KANTELHARDT *et al.* 2007].

Differences between PRSA curves obtained by applying either of the two criteria in Eqs. (4.1) will indicate missing time reversal symmetry of the original signal. Hence, nonlinear and non time-reversal invariant processes, with different phenomena occurring during increasing and decreasing parts, can be studied in detail. Such asymmetry has been reported in high-risk infarction subjects [BAUER *et al.* 2006a], but was challenged in a much smaller cohort (20 survivors and 20 non-survivors) by [WESSEL *et al.* 2007]. Optionally, it might be meaningful to weight the windows according to some criteria, e.g., according to the magnitude of the change at each anchor position. With anchors defined at increases Eq. (4.3) becomes

$$\text{PRSA}_{X,\text{weighted}}(k) = \sum_{\nu=1}^M c_{i_\nu} x_{i_\nu+k}, \quad k = -L, \dots, 0, \dots, L-1. \quad (4.4)$$

with weights c_{i_ν} , e.g., $c_{i_\nu} = (x_{i_\nu} - x_{i_\nu-1}) / \sum_{\mu=1}^M (x_{i_\mu} - x_{i_\mu-1})$. Other weights can be defined as well. When I subtract from the PRSA curve its mean value⁸ to compare results from different individuals I will in the following denote the corresponding curve by $\text{PRSA}_{\text{mr}}(k)$.

4.1.2. Interpretation of PRSA Curves

Figure 4.2 shows the performance of the PRSA technique on biological data, where a (non-stationary, not pre-processed, and noisy) 24 hours long-term recording of heartbeat intervals [Fig. 4.2(a)] is depicted together with the corresponding PRSA transformation employing an anchor criterion according to Eq. (4.1a) with $T = 1$ [Fig. 4.2(b)].

In the PRSA-transformed data [Fig. 4.2(b)] two relevant quasi-periodicities can be observed by eye: (i) a rather fast oscillatory component with a period of roughly 4 heartbeats which is coherent for approximately 20 heartbeats before and after the trigger event and related to respiration (4 heartbeats typically occur per breathing cycle in this subject), and (ii) a slow oscillation with a period of approximately 27 heartbeats which might be related to blood pressure oscillations⁹. Please note, during the time span of 24 hours the subject does not breathe at a fixed rate. Slight frequency variations and thus yield a broadened power spectrum (green curve) in Fig. 4.2(d). Subjects underlying controlled conditions with a forced-breathing rhythm show a much more coherent fast component apparent in PRSA curves for much longer time shifts k . I could observe this effect in data from other projects which I analyzed for collaborators in Oulu, Finland (stimulated sympatho-vagal activation data) and in Halle (intense care patients dying from multiple organ dysfunction syndrome (MODS)). This effect can be used to check to which extent subjects in studies with controlled respiratory rhythms are following the instruction. In every study with supposedly forced breathing which was at my disposal there were some subjects that did not at all follow such stipulation.

Figures 4.2(c,d) show power spectra associated with the signals in Figs. 4.2(a,b) in black color. The directly from the PRSA curve [Fig. 4.2(b); $N = 2L = 64$] calculated PRSA-power spectrum [black in Fig. 4.2(d)] is rather rough compared with the strongly fluctuation power spectrum in Fig. 4.2(c) of the complete RRI recording ($N=79473$). In the latter case one usually overcomes this problem by logarithmic binning — the result is shown in green. To compare the PRSA-power spectrum and the standard power spectrum with each other I have calculated a finer sampled PRSA-power spectrum [green in Fig. 4.2(d)] based on a longer PRSA curve ($2L = 4096$). Then I have adjusted the bin size for logarithmically smoothing the spectrum in Fig. 4.2(c) to ensure a similar number of elements in both spectra. Note obtaining a longer PRSA curve does not at all affect the 64 center points but includes more information about the anchor events' past and future.

From the standard power spectrum a spectral exponent β [cp. Eq. (1.20)] can be derived to characterize long-term correlations (if power-law correlations are present), see Sect. 1.2. This is also possible from PRSA-power spectra if the sampling is fine enough. However, the obtained spectral exponent β_{PRSA} is not identical with β , $\beta_{\text{PRSA}} = 2\beta - 2$ [BAUER *et al.* 2006b]. In conclusion, PRSA does not render standard spectrum analysis obsolete but might add useful information about quasi-oscillatory components – here it clearly identifies the fast component which is not captured by the standard power spectrum.

In $\text{PRSA}_X(k)$ all periodicities are aligned in the center, i. e. for $k = 0$, and decay towards larger positive or negative k if the coherence time is finite [see, e. g. Figs. 4.2(b) and 4.1(c,d)]. This has two important consequences: (i) the central peak of the PRSA curve contains contributions of all (quasi-) periodicities in the original signal and (ii) the decay of the oscillations towards large $|k|$ conveys information about their coherence time. In addition, an asymmetry of the PRSA curve will indicate a break of time reversal symmetry, which cannot be seen in any power spectra. Hence, in some applications it can be useful to characterize $\text{PRSA}_X(k)$ by certain values or slopes at specific distances from the center. Such parameters, however, will have to be selected according to specific problems, and no general characterization of $\text{PRSA}_X(k)$ or all quasi-periodicities in the original data can be expected from them. One of such characteristic values that has been defined

⁸This is for a stationary signal equivalent to subtracting the mean from the signal before calculating PRSA curves. However, due to artifacts, which are filtered in the PRSA algorithm, it is often more applicable to remove the mean of the PRSA curve.

⁹I do by purpose not obligingly associate slow oscillations with so called Mayer waves or blood pressure oscillations since this topic is still controversially discussed, see [JULIEN 2006] for a review.

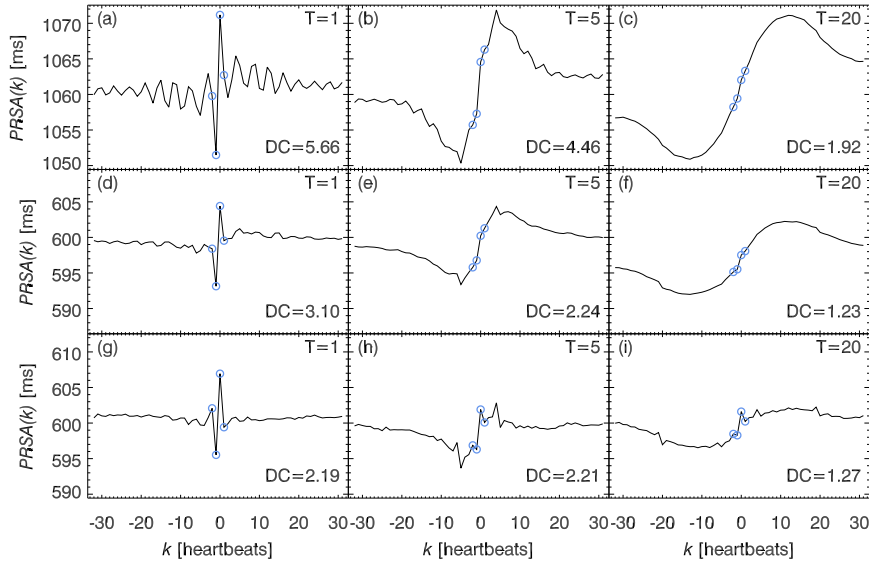


Figure 4.3.: Phase-rectified signal averages aligned at heartbeat decelerations [increasing beat-to-beat interval] according to anchor criterion Eq. (4.1a) for three representative patients taken from the ISAR-I database: in rows: (a-c) male 67y, survivor, low risk class [DC=5.68], (d-f) male, 59y, survivor, intermediate risk class [DC=3.19], (g-i) female, 72y, nonsurvivor, high risk class [DC=2.21]; in columns: different anchor parameters (a,d,g) $T=1$, (b,e,h) $T=5$, and (c,f,i) $T=20$. Blue circles mark values contributing to deceleration capacity (DC) following Eq. (4.5). The average value (PRSA(k)) corresponds to the mean interbeat time interval for each patient. The vertical range of all plots is the same (22ms). Note, the x-axis index k is not exactly associated with real time but is 'heartbeats' which can roughly be translated into time units by multiplication with the average beat-to-beat interval $\langle \text{PRSA}(k) \rangle$. For larger T all three patients (increasing risk from top to bottom) become less distinguishable using DC, see also Fig. 4.5.

to assess the risk of sudden cardiac death events in myocardial-infarction patients is *Deceleration Capacity (DC)*.

4.1.3. PRSA Curves of Cardiac Data

For all $N = 1455$ post-infarction patients in the ISAR-I database [Munich cohort, see Sect. 2.4.1] PRSA curves¹⁰ were calculated considering different values of the width parameter T in both Eqs. (4.1) and visually compared by my collaborators at the German Heart Center in Munich. They found and validated¹¹ a difference in the overall shape of PRSA curves as well as an asymmetry between PRSA curves obtained separately from triggering on increases [Eq. (4.1a)] and decreases [Eq. (4.1b)] in RRI depending on the subjects' mortality¹² [BAUER *et al.* 2006a]. For illustrating these findings in Fig. 4.3 I have chosen three representatives from the ISAR-I database and calculated PRSA curves anchored at heartbeat decelerations according to Eq. (4.1a) for $T = 1$ [Figs. 4.3(a,d,g)], $T = 5$ [Figs. 4.3(b,e,h)], and $T = 20$ [Figs. 4.3(c,f,i)].

The first patient (male, 67y) in Figs. 4.3(a-c) survived at least two years¹³ after index myocardial infarction ('low risk', for the definition of the risk classification, see below Eq. (4.5) or [BAUER *et al.* 2006a]). The second patient (male, 59y) in Figs. 4.3(d-f) also survived for at least two years but was classified with 'intermediate risk'. The third patient (female, 72y) in Figs. 4.3(g-i) died 24 days after the initial myocardial infarction and was classified with 'high risk'.

Due to anchoring at heartbeat decelerations the center spike always occurs at position $k = 0$ for $T = 1$, but might be smeared for anchor definitions with $T > 1$. It is most pronounced for the

¹⁰In this original study the standard PRSA was used without considering incomplete windows and without more carefully checking for ectopic beats. Therefore, the method slightly deviates from the one I suggest here.

¹¹The validation was done by employing PRSA blinded to $N = 600$ subjects from the Oulu cohort and $N = 656$ subjects from the London cohort.

¹²In this chapter I will also use the term *cardiac risk* which is [here](#) understood as the risk to die of sudden cardiac death (SCD) within 2 years after an initial myocardial infarction.

¹³In the ISAR-I study there was originally a follow up period of two years after myocardial infarction. Patients who are still alive after this time period are classified as survivors.

low-risk patient and significantly smaller for the high-risk patient. This property indicates a more pronounced heartbeat regulation by the autonomous nervous system and a larger cardiovascular response to external and endogenous inputs for the low-risk patient. A reduced reflexive-type responsiveness has been reported in congestive heart failure subjects compared to healthy subjects [BERNAOLA-GALVAN *et al.* 2001].

If one employs anchor point criteria based on the comparison of more than two heartbeat intervals ($T > 1$), high frequency components are partially suppressed in the PRSA curve and low frequency periodicities are dominant in all three patients. This suppression is rather strong in low-risk patients [Figs. 4.3(h,i)] compared with poorer suppression in high-risk patients [Figs. 4.3(h,i)]. Here, increasing the value of T in Eqs. (4.1) corresponds to adding a kind of risk-dependent low-pass filter which might prove useful for risk stratification in addition to the amplitude of the central spike.

4.1.4. Wavelet Analysis of PRSA Results

Besides quantifying oscillatory components in PRSA curves by spectral analysis [Fig. 4.2(d)] one might employ wavelet analysis which allows not only for a frequency decomposition of the signal but also for associating specific times with these components [see Sect. 1.3 and SCHUMANN 2004]. In the following I consider wavelet amplitudes obtained from the discrete convolution of a mother wavelet of scale s with the PRSA curve according to Eqs. 1.26b and 1.30. Note that I drop the 'prime' in the shift parameter k' of the wavelet for better comparability with the shift parameter k in PRSA. The obtained time information can be used to study coherence¹⁴ and time asymmetry in the PRSA curves. Figures 4.4(A,B) show the wavelet amplitude of all nine PRSA curves from Fig. 4.3 employing two different mother wavelets: (A) a 1st-order Gaussian wavelet [Eq. (1.27b); depicted in Fig. 4.4(Ak)] and (B) a 6th-order Morlet wavelet [Eq. (1.27c); depicted in Fig. 4.4(Bk)]. Here I show results from employing two wavelets to point out that the choice of the wavelet function is important and wavelet amplitude figures have to be interpreted with care. In Fig. 4.4 I have normalized each panel separately to ensure unit total power and in addition use the same pseudo-logarithmic color model [cf. Figs. 4.4(Aj,Bj)] for all corresponding plots.

An often neglected property of wavelet transform that severely affects interpretations of results is the general inequality of wavelet scale s and Fourier wavelength λ as obtained from power spectra. Thus, a large wavelet amplitude at a scale s^* does not necessarily imply an oscillation at a frequency $f = 1/s^*$. The reason for such inconvenience is the rather smeared localization of the wavelet in Fourier space which is the price for a certain localization of the wavelet in sample space. Recall Fourier analysis where sine functions have a perfect (delta-peaked) localization in Fourier space but no localization at all in sample space. This property can be thought of as a type of uncertainty relation. Now, each wavelet has a characteristic relation between sample space localization and frequency space localization. The 1st-order Gaussian wavelet has a rather good localization in sample space but is quite smeared in frequency space compared with the 6th-order Morlet wavelet which has a good frequency localization (the real part are damped cosine functions) but a less optimal time localization. Choosing a wavelet is a decision on the ratio between time and frequency resolution. While the Morlet wavelet is a better choice when one is interested in frequency resolution, e. g., periodicities in the PRSA curve, the Gaussian wavelet is better suited to study times of changes in frequency components.

By wavelet transforming pure sinusoids of fixed frequency and studying its relation to the observed frequency one finds $\lambda \approx 2.679s$ for the 1st-order Gaussian wavelet and $\lambda \approx 1.03s$ for the 6th-order Morlet wavelet. Because the typical patterns in physiological time series are oscillations and an adjustment of scales in corresponding wavelet-amplitude plots is not required ($1.03 \approx 1$), I personally prefer using the 6th-order Morlet wavelet. For instance features observed at scales $s_{\text{Gauss}} = 1$ in Fig. 4.4(A) correspond to features at $s_{\text{Morlet}} \approx 2.6$ in Fig. 4.4(B) which itself can

¹⁴In this chapter coherence time is understood as the time span for that a certain oscillatory component is present in the PRSA curve. This corresponds with the width of 'bands' that are established in wavelet-amplitude plots by compact sequences of large amplitudes for different time shifts k and a fixed scale s .

directly be read in units heartbeat. The Gaussian wavelet, on the other hand, is a good choice to study fluctuations [see Appendix E.4].

A second important pitfall when using a 1st-order Gaussian is the strong influence of the kernel function. From looking at Fig. 4.4(A) one might get the impression that around the center position ($k = 0$) there are slow oscillations of a broad frequency range ($s = 2, \dots, 32$) whose coherence time is increasing towards larger scales s . While there are indeed such oscillations in the corresponding PRSA signals [cp. Fig. 4.3] the smeared appearance here comes from the unfavorable frequency localization and the asymmetry of the wavelet kernel [see Fig. 4.4(Ak)]. The kernel resembles the central peak in PRSA curves for anchors according to Eq. (4.1a). With an increasing wavelet scale large wavelet amplitudes are obtained in a broader range around the center at $k = 0$. The self-repeating (*self-reproducing*) structure of smeared areas – here bounded by sharp blue lines – which is particularly pronounced at small scales (striped character) is only partially originated in the oscillatory PRSA curves but mainly in the convolution with the Gaussian kernel (good time localization). Such artifacts are sometimes referred to as *self-reproducing kernel* artifacts. Although, the Morlet wavelet in principle suffers from the same problem it is much less pronounced due to the wavelets' symmetry together with a weaker time localization, compare Figs. 4.4(A,B). Keeping both possible pitfalls in mind one can interpret Figs. 4.4(A,B). Both main components, which were discussed in the previous section, are observed: (i) a high frequency respiratory component (roughly $s \in [1, 4]$ heartbeats) is especially pronounced for $T = 1$ around the center position ($k = 0$) in Figs. 4.4(Ba,Bd,Bg) but less obvious in the corresponding panels employing a 1st-order Gaussian wavelet [Figs. 4.4(Aa,Ad,Ag)]. Results from the Morlet wavelet moreover nicely allow an identification of associated coherence times for each subject. In the low-risk post-infarction patient [Fig. 4.4(Ba)] a respiratory component of 4 heartbeats period is clearly noticed during the whole observed time span (± 32 heartbeats). While this could already be obtained from PRSA curves [cp. Fig. 4.3] wavelet plots additionally describe variations (extended red area) in frequency hardly seen in PRSA signals. Obviously, the coherence time of 4 : 1 respiration, i.e., 4 heartbeats occur per breathing cycle [see Chapt. 5 for a systematic analysis of cardio-respiratory synchronization], decreases with cardiac risk – coherent 4 : 1 respiration is observed in the intermediate-risk patient [Fig. 4.4(Bd)] for approx. ± 20 heartbeats before and after heartbeat deceleration and is notably diminished (approx. ± 7 heartbeats) in the high-risk patient [Fig. 4.4(Bg)]. Note, that coherence properties are difficult to extract from corresponding panels in Fig. 4.4(A) utilizing a Gaussian wavelet due to the reproducing kernel. Another property which can be perceived in Fig. 4.4(B) compared with Fig. 4.4(A) is the shift of wavelet power from respiratory components (plots for $T = 1$) towards slow oscillations (plots for $T = 20$). Please note that this shift comes from increasing the anchor width T and is not a property of the subjects. However, note low-frequency quasi-periodicities are more pronounced in low-risk patients than in high-risk patients as indicated by orange areas in Figs. 4.4(Ba,Bg). To investigate their coherence times, one would have to increase the window length L (fixed to 32 here). This correlates with the opinion found among cardiologists of reduced blood pressure regulation capabilities (baroreflex) in high-risk patients assuming slow oscillations being related to blood pressure oscillations.

As earlier reported in [BAUER *et al.* 2006a; KANTELHARDT *et al.* 2007] PRSA curves for example analyzed by a wavelet transform are usually more asymmetric for high-risk patients compared with intermediate-risk patients or even low-risk patients. Although, such symmetry characteristics can be observed in Figs. 4.4(B) for the Morlet wavelet they are much easier recognized in Figs. 4.4(A) employing the Gaussian wavelet. For example Gaussian wavelets were used to extract features in heartbeat data as markers of pathologic deviations in [IVANOV *et al.* 2001].

4.1.5. Definition of Deceleration Capacity (DC)

From studying PRSA curves in all 1455 post-infarction patients of the Munich cohort it was observed that the simple parameter *Deceleration Capacity DC* is a superior parameter to assess total mortality in infarction patients compared with (the current *gold standard*¹⁵) left ventricular

¹⁵In medicine a *gold standard* or nowadays *criterion standard* refers to a well established standard diagnosing procedure, scoring parameter, or benchmark that is regarded as definitive. Newly suggested parameters and procedures

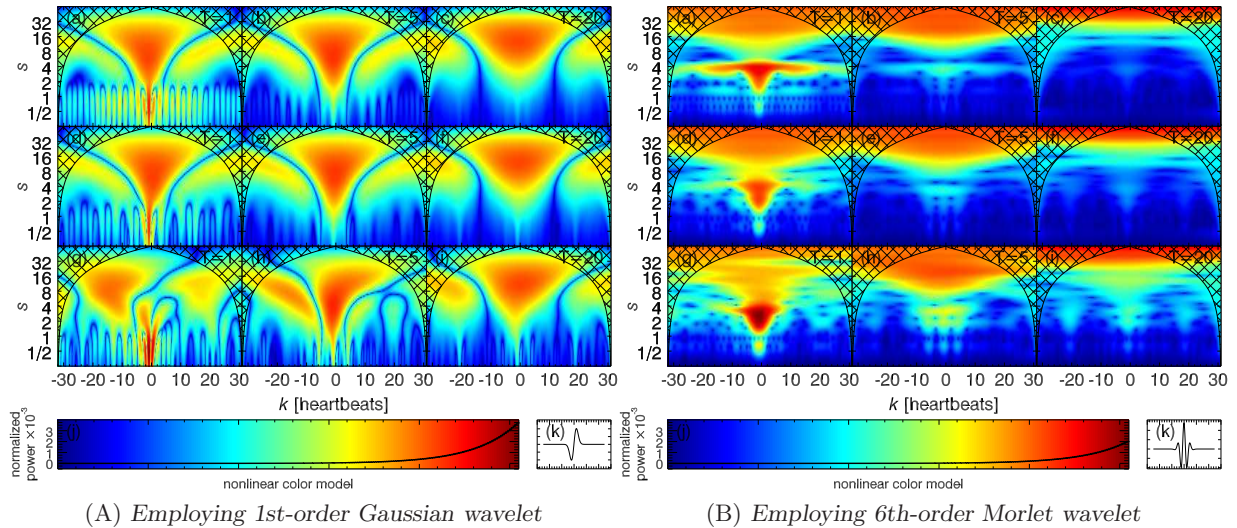


Figure 4.4.: Wavelet power vs. scale obtained from PRSA shown in Fig. 4.3 according to Eq. (1.30) utilizing (A) a 1st-order Gaussian wavelet and (B) a 6th-order Morlet wavelet – subpanels in rows [same in (A,B)]: (a-c) male 67y, survivor, low risk class [DC=5.68], (d-f) male, 59y, survivor, intermediate risk class [DC=3.19], (g-j) female, 72y, nonsurvivor, high risk class [DC=2.21]; in columns: results from anchor criterion Eq. (4.1a) (a,d,g) $T=1$, (b,e,h) $T=5$, and (c,f,j) $T=20$. Cross-checked area marks cone of influence [area of edge effects]. (j) applied non-linear color model and (k) a sketch of the employed wavelet (A) $w_{\text{Gau}\beta(1)}$ and (B) $w_{\text{Morlet}(6)}$. Wavelet power was normalized to satisfy unit total power in each subpanel and the same approximately logarithmic color models in (A_j,B_j) are applied to all subpanels in (A) and (B). For clarity and a smoother plot scales $1 > s \geq 0.25$ were ‘artificially’ included by enhancing time resolution via repeating each point in the PRSA curves 4 times before the wavelet transform. Pay attention: Wavelet scale is generally not an equivalent of Fourier wavelength [see text]: for a (A) 1st-order Gaussian $\lambda[\text{heartbeats}] \approx 2.679s$ and (B) 6th-order Morlet wavelet $\lambda[\text{heartbeats}] \approx 1.03s$ meaning scales s in (B) can directly be associated with units heartbeat. Wavelet-power asymmetry increases with risk and average-anchor parameter T tunes a risk-dependent low-pass-frequency filter.

ejection fraction (LVEF)¹⁶ [BAUER *et al.* 2006a; KANTELHARDT *et al.* 2007]. DC is calculated from the PRSA curve of RRI time series¹⁷ in units *milliseconds* employing the anchor definition in Eq. (4.1a) with $T = 1$ by

$$\text{DC} = \frac{1}{4} [\text{PRSA}_{\text{RRI}}(0) + \text{PRSA}_{\text{RRI}}(1) - \text{PRSA}_{\text{RRI}}(-1) - \text{PRSA}_{\text{RRI}}(-2)] . \quad (4.5)$$

From systematically testing the classification capabilities of DC to identify survivors and non-survivors two threshold values were defined in the ISAR study: ‘low-risk’ of death was associated with $\text{DC} > 4.5\text{ms}$, ‘intermediate risk’ with $2.5\text{ms} < \text{DC} \leq 4.5\text{ms}$, and ‘high risk’ with $\text{DC} \leq 2.5\text{ms}$ [BAUER *et al.* 2006a]. Note, in Fig. 4.3 I used Eq. (4.5) to derive ‘DC’ values for other values of T , too. Although DC was exclusively defined for $T = 1$, I kept the notation ‘DC’ for comparison. Above threshold values were obtained for $T = 1$ only.

The performance of a predictor such as DC is often quantified by *Receiver-Operator-Characteristics (ROC)* curves plotting the *true positive rate = sensitivity* versus the *true negative rate = specificity* [see Appendix D.4 for details]. The larger the *area under the curve (AUC)*¹⁸ the better the prediction. The diagonal connecting (0% sensitivity, 100% specificity) and (100% sensitivity, 0% specificity) represents the random choice case, i.e., taking an arbitrary patient and ‘throwing a coin’ to decide if he would belong to the group of survivors or non-survivors, yielding $\text{AUC}=0.5$. Figure 4.5(a) compares DC with two other established parameters for SCD-risk assessment confirming its superiority.

have to be compared with such gold standard to judge their performance and quality. An hypothetically ideal gold standard satisfies 100% sensitivity at 100% specificity [comprehensively defined in Appendix D.4].

¹⁶LVEF is defined by the quotient $(\text{EDF}-\text{ESV})/\text{EDF}$ where EDF is the end-diastolic volume and ESV the end-systolic volume. EDF and ESV can be assessed by left ventricular angiography, radionuclide scanning, or echocardiography.

¹⁷In the original work 24h heart-beat-interval (RRI) time series sampled at 128Hz were analyzed.

¹⁸In finance mathematics AUC is called *coefficient of concordance (CoC)*.

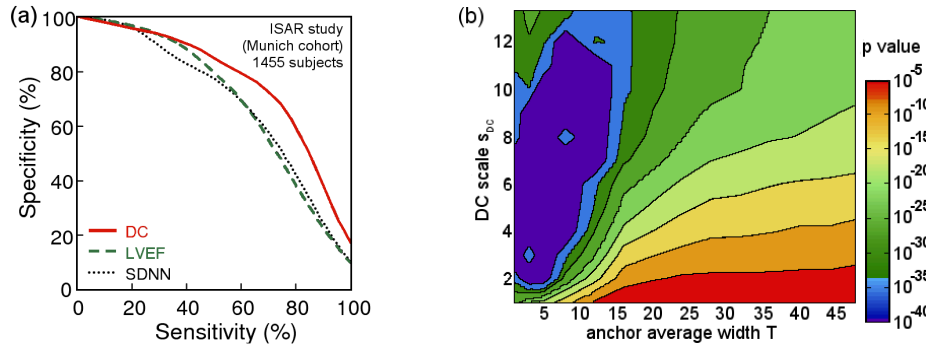


Figure 4.5.: (a) Receiver-Operator curves indicating performance of three parameters used for cardiac risk classification: (i) Left-ventricular ejection fraction [LVEF, the current gold standard; $AUC=0.70$], (ii) standard deviation of normal-to-normal beat intervals [SDNN; $AUC=0.68$], and (iii) PRSA based Deceleration Capacity [DC; $AUC=0.77$]. The area under the curve [AUC] is used to compare performance [the larger the better]. Note, curves were obtained via a bootstrapping algorithm and an additional smoothing of the 'staircase like' resulting ROC curve yielding somewhat imprecise ROC curves at the lower right edge, see Appendix D.4. In principle [without smoothing] all curves should pass the point (100%-sensitivity,0%-specificity). (b) DC values are derived for different scales s_{DC} by $DC(s_{DC}) = 1/(2s_{DC}) \left[\sum_{i=0}^{s_{DC}-1} PRSA(i) - \sum_{i=-s_{DC}}^{-1} PRSA(i) \right]$ where PRSA curves are obtained for different average widths T in an anchor condition following Eq. (4.1). The significance of the statistical association with mortality was calculated using the non-parametric Mann-Whitney-U test. Corresponding p-values are color-coded, see Appendix D.2 and D.3 for methodology. Figure adapted from [KANTELHARDT et al. 2007].

Note that although DC has been associated with the central Haar wavelet coefficient I personally find that using the term wavelet in this case is rather dangerous since PRSA and DC are not equivalent to a wavelet transform. One might argue, considering a Haar-wavelet basis [see Sect. 1.3] and deriving the wavelet transform only for the center position of the PRSA signal (no translation in the wavelet transform) the DC value is identical with the central Haar-wavelet coefficient of scale $s = 2$. However, this is only true when the specific Haar-mother wavelet is used and amplitude rescaled, and no translation and dilatation of the mother wavelet is performed.

Nevertheless, one can address the question whether the DC definition in Eq. (4.5) is an optimal predictor of SCD or other anchor-average widths T in Eqs. (4.1) together with other scales s of the 'Haar alike' convolution kernel. Results from systematically varying both parameters are shown in Fig. 4.5(b). This approach led originally to choosing $T = 1$ and $s = 2$ for the definition of DC as presented in Eq. (4.5) and with an anchor criterion based on decelerations according to Eq. (4.1a).

Since the DC parameter quantifies the central spike of the PRSA curve around deceleration events and thus determines the capacity of the central nervous system to quickly decelerate heartbeat it is called deceleration capacity (DC). Since decelerations are triggered by vagal activation DC has been associated with parasympathetic activity [BAUER et al. 2006a]. Analogously, a similar risk indicator might be defined based on a PRSA curve obtained by anchor points corresponding to accelerations [Eq. (4.1b)] yielding a parameter *Acceleration Capacity* (AC) following the same definition in Eq. (4.5). Nevertheless, AC was reported to perform much worse [BAUER et al. 2006a].

4.1.6. Age Dependence in Post-Infarction DC

Aging strongly affects human physiology as has been discussed in Sect. 3.2.2. The question arises about aging effects in DC values. This would have consequences for DC threshold values currently suggested for risk classification without considering the patient's age.

Although a multivariate analysis adjusted for age, presence of diabetes mellitus, and history of myocardial infarction showed that only deceleration capacity (DC), left ventricular ejection fraction (LVEF) and mean heart rate are associated with total mortality [BAUER et al. 2006a], there is definitely a systematic dependence of DC on age. Figure 4.6(a) shows, for all patients that survived the 24 months follow-up period (but independent of the DC risk category), the age dependence of DC [displayed are medians and both 25% and 75% quartiles as error bars;

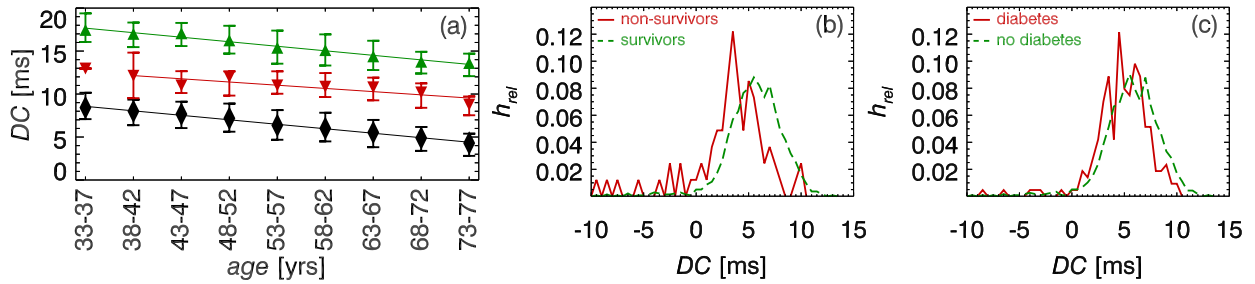


Figure 4.6.: (a) Age dependence of DC for survivors [ISAR-I study]. The symbols show the medians of the DC values for the specific age groups: males [green triangles up, values shifted up by 9ms, fit: $DC/ms = 12.4 - 0.11 \text{ age/yrs}$], females [red triangles down, values shifted up by 5ms, fit: $DC/ms = 10.1 - 0.07 \text{ age/yrs}$], males and females combined [black diamonds, fit: $DC/ms = 12.2 - 0.10 \text{ age/yrs}$]. The error bars indicate the values of upper and lower quartiles. (b,c) Normalized histograms of the DC values after projection onto an age of 60 years for (b) non-survivors [red continuous curve] and survivors [green dashed curve], (c) survivors with diabetes [red continuous curve] and without diabetes [green dashed curve]. The average values of DC are (b) 3.21ms and 5.64ms for non-survivors and survivors [a standard t-test yields $p < 10^{-5}$ for the equivalence of both histograms] and (c) 5.03ms and 5.75ms for the diabetes and the non-diabetes group, respectively [t-test yields $p < 0.01$ for equivalence].

black diamonds = all patients, red triangles down = females, green triangles up = males]. An approximately linear decrease of DC with age is clearly observed. The trend is nearly identical for both, men and women – together yielding $DC/ms \approx 12 - \text{age}/10 \text{ yrs}$. Note however, that the age range of the study is limited by 75 years, and there are hardly any patients below the age of 35 years. It is not clear, however, if this decrease of DC should indicate an increased risk of cardiac death or just corresponds to the generally higher risk of death for older people due to a reduced parasympathetic tone.

Five percent of the 1455 post-infarction patients did not survive the two years follow-up period after an index myocardial infarction event. Based on the observed age-dependence in Fig. 4.6(a) DC values for both survivors and non-survivors can be age-corrected by projecting all values to those corresponding to age 60 years in the same patient using obtained regression formulas separately for males and females. Histograms of age-corrected DC values from both groups are depicted in Fig. 4.6(b). Although, there is a certain overlap of the histograms, a standard two-sided heteroscedastic Student's t-test [Appendix D.1] yields the probability $p < 10^{-5}$ for the equivalence of both histograms. Such result is not surprising considering that DC was explicitly designed to separate survivors and non-survivors, but shows the weak influence of aging on the parameter.

Seventeen percent of the patients in the study (242 out of 1455) suffered from diabetes mellitus (in addition to the myocardial infarction). Diabetes mellitus is associated with autonomic dysfunction. I therefore aimed to analyze DC in the 17% of the patients presenting this disease. Since the ratio of diabetes patients is larger among the old patients, the age dependence studied would already result in a decreased DC value for the diabetes patients. Hence, I have again corrected all DC values by the linear trend observed in Fig. 4.6(a); all values are rescaled to those corresponding to the age of 60. Figure 4.6(c) shows the histograms of DC values for patients with and without diabetes mellitus. Although, there is a larger overlap of the histograms as in Fig. 4.6(b), a standard two-sided heteroscedastic Student's t-test yields the probability $p < 0.01$ for the equivalence of both histograms which is in medical applications still believed to be quite significant¹⁹. Hence, DC values are significantly smaller for the patients with additional diabetes compared with diabetes-free patients which might indicate an increased cardiac risk [see also Sect. 4.1.7].

4.1.7. Circadian Rhythm in PRSA Results

Studying the evolution and stability of DC with dataset length I realized two effects: (i) a strong inter-individual variability which was not surprising considering my experience with other med-

¹⁹In most medical applications three significance levels are generally considered: (i) $p < 0.001$ strongly significant, (ii) $p < 0.01$ 'good' significance, (iii) $p < 0.03$ 'still' significant.

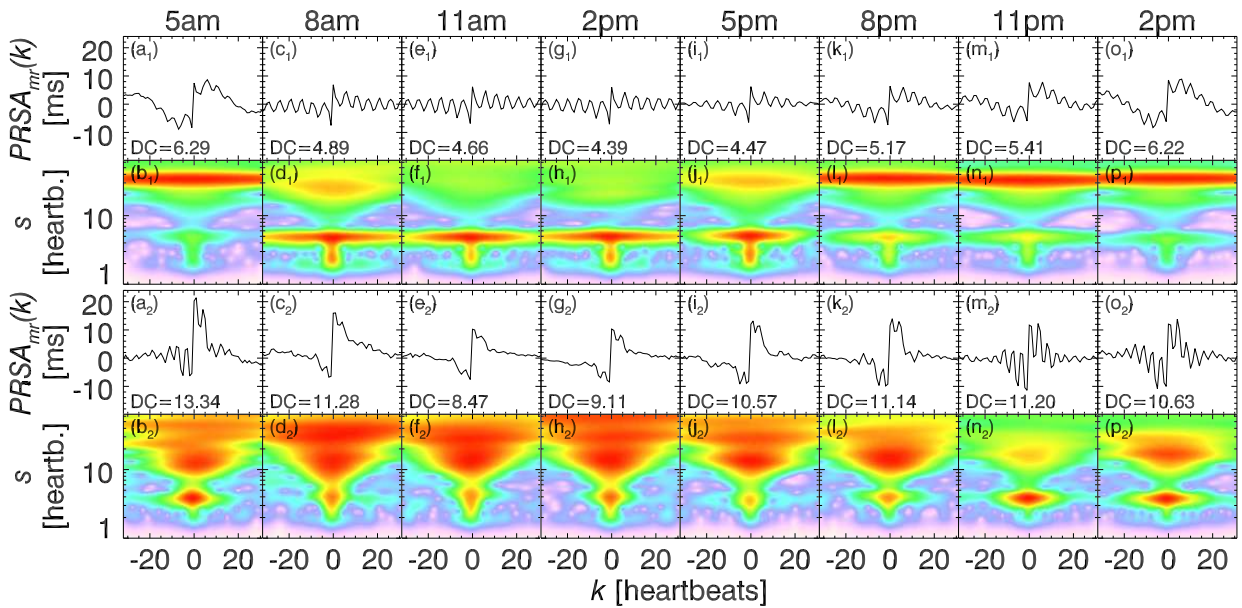


Figure 4.7.: Circadian influence on PRSA and DC based on 24h ECG recordings of two patients after an index myocardial infarction; both male survivors without diabetes: (a_1-p_1) 49 years old, (a_2-p_2) 44 years old For 3h ECG fragments [initial time indicated at the very top] the phase-rectified signal averages with means subtracted are shown on top of the corresponding wavelet power using a 6th order Morlet wavelet. PRSA is shown in the range $k \in [-32, 31]$ but wavelet power was obtained from a longer PRSA signal [$L = 256$] to improve statistics, In the top individual two frequency components are coherent for a longer time: (i) a respiratory component [$s = 4$ heartbeats] is especially pronounced during daytime in panels (c_1-j_1) and (ii) a likely blood pressure related component [$30 < s < 40$ heartbeats] is most apparent during the evening and bedtime hours (a_1, b_1, k_1-p_1) . The bottom patient exhibits: (i) less coherent and less localized respiratory components [$2 \leq s \leq 5$ heartbeats; (a_2, b_2, m_2-p_2) bedtime coherence approx. 15 heartbeats compared with (c_1-l_1) 5 heartbeats during daytime left and right of trigger event] and (ii) less located slow oscillations where higher frequencies [$s \approx 15$ heartbeats] are less coherent over time. DC values are lower during daytime compared with night time in both subject.

ical databases and (ii) a variation of DC values separately obtained from different parts of the signal. This observation suggested studying the time dependence of DC in 24-hour heartbeat data, i. e., the circadian rhythm effect on DC. Figure 4.7 shows PRSA curves and corresponding wavelet power obtained in segments of 3 hours duration each starting at 5am in the morning for two representative examples of male survivors without diabetes from the same age group. It is immediately observed that PRSA curves and thus DC values are different during daytime and evening/bedtime hours. This is not surprising considering known physiological differences between daytime wakefulness and sleep [IVANOV *et al.* 1999a, 2001; KANTELHARDT *et al.* 2002; PENZEL *et al.* 2003]. Looking closer at DC values one finds a monotonous change in DC where values are lowest around noon and the early afternoon and highest during the early morning (peak around 4am to 5am). In sleep research the circadian rhythm²⁰ regulating the timing of sleep is well known besides its antagonist, the homeostatic mechanism regulating sleep intensity. In order to determine circadian activity in humans (and vertebrates in general) two proxies are monitored: (i) The level of melatonin hormone (*the hormone of night*) which is predominantly produced during sleep time with the highest concentration around 4am; and (ii) the core body temperature which practically oscillates inversely to melatonin concentration [see Fig. 4.8(c)].

I have derived and visually inspected PRSA curves, wavelet power, and DC values from all 1455 patients (ISAR-I study) by generating similar figures as depicted in Fig. 4.7. Average DC results with respect to daytime (same 3 hours segments as in Fig. 4.7) are shown in Figs. (4.8)(a,b) separately for survivors versus non-survivors as well as for patients with diabetes versus those not suffering from diabetes mellitus. It can be observed that (i) DC values follow a circadian rhythm similarly to the schematic melatonin rhythm and that DC values of non-survivors and

²⁰To be more precise: While in cardiology the *circadian rhythm* refers to a 24-hour rhythm in general, it is refined in sleep research to a rhythm that originates in the suprachiasmatic nucleus (SCN), a group of cells in the hypothalamus.

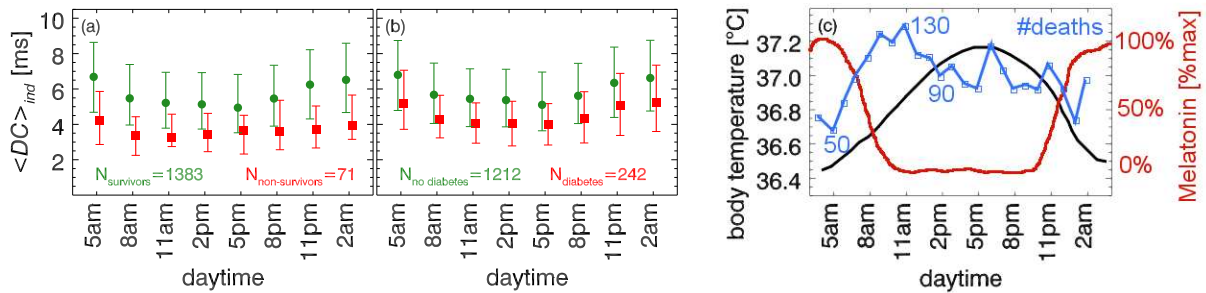


Figure 4.8.: DC determined in non-overlapping windows of 3h versus daytime based on the ISAR study: (a) Survivors [green filled circles] vs. non-survivors [red filled squares] and (b) no diabetes [green filled circles] vs. diabetes [red filled squares]. Shown are median values and both the 25% quartile and the 75% quartile. Note that green and red plots in (a,b) are horizontally shifted by -15min and $+15\text{min}$ for clarity. A clear decrease in DC is observed from the early morning towards the afternoon. Average values [not shown] follow practically the same curves and standard errors are very small. During evening and bedtime hours DC increases again. (c) Hand drawn sketches of core body temperature [black], percentage melatonin concentration [maximum conc. at approx 4am = 100%, red; values taken from BENLOUCIF *et al.* 2008], and number of deaths [blue; $N=2203$, values from MULLER *et al.* 1987] — for comparison.

diabetes patients are systematically lower compared with survivors and non-diabetes patients. This supports the popular opinion among medical doctors that diabetes increases the cardiac risk.

The observed decrease in DC during the morning [$DC(5\text{am}) > DC(8\text{am}) > DC(11\text{am})$; Figs. 4.8(a,b)] is consistent with the finding of a reduced DC value during REM sleep when recalling that most time spend in REM sleep occurs before awakening in the morning. It is further in full accordance to the observation that most sudden cardiac deaths occur in the morning between 7am and 11am [see Fig. 4.8(c) and MULLER *et al.* 1987; MÜLLER-NORDHORN *et al.* 2001]. Limitations of circadian results comprise the neglected age dependence here. I have shown that DC reduces with aging in the ISAR-I database, and I will report and illustrate a similar systematic age dependence of DC during sleep in Sect. 4.1.10. This suggests that aging is in also affecting the daily cycle of DC values.

The observed 24-hour rhythm in DC might additionally be related to the circadian cycle known from sleep research and its daily synchronization with the day-night cycle via the eyes and the visual cortex [compare Figs 4.8(a,b) with (c) where both proxies of the circadian rhythm show a qualitatively similar (or inverse) time course]. Such synchronization might be less effective in elderly compared with young. The observation of an irregular sleep onset, i.e., practically at all day times drowsiness might occur, and a much more fragmented sleep in elderly supports the 'less' effective synchronization hypothesis. In Sect. 5.2.6 I will discuss my research concerning cardiorespiratory coupling in 190 healthy subjects during sleep. I find a significant decrease with aging in percentage of of times where respiration and heartbeat are phase synchronized²¹ during light sleep and deep sleep. However, note that although the circadian cycle is strongly related to sleep, cardiorespiratory synchronization might but must not be unrelated with the here observed variation in DC.

I would like to remark that in principle even a *local DC*, i.e., the time series of DC values obtained separately for each anchor-point surrounding can be obtained. This time series turned out to have multifractal structure (not presented here) which is in accordance with multifractal structure in heartbeat intervals, see among many others [IVANOV *et al.* 1999b].

4.1.8. Quasioscillations Across Sleep Stages

Data recording during sleep are much shorter, i.e., approximately 7.8 hours of data per night are available, compared with 24 hours in Sect. 4.1.7. Daytime- and age-dependent DC findings discussed there already suggest a time dependence of DC during sleep and wake. As I have discussed in Sect. 2.3 polysomnographic (sleep) data is subdivided according to five stages —

²¹The term phase synchronization will become clear in the beginning of Chapt. 5

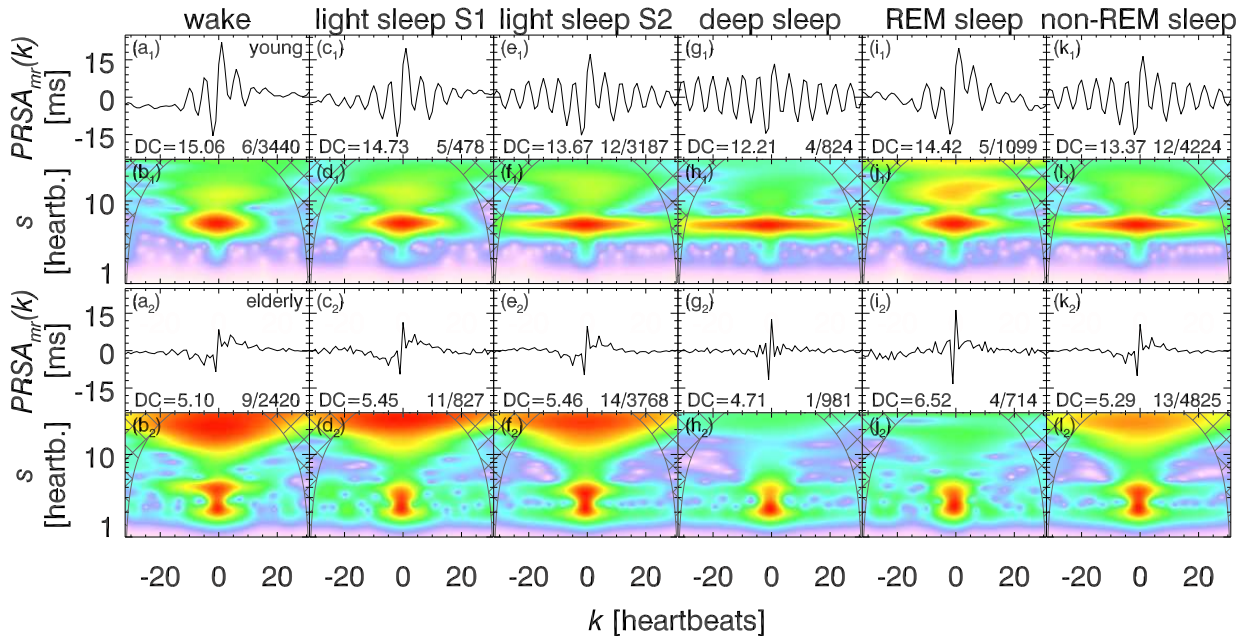


Figure 4.9.: PRSA analysis results obtained separately for nocturnal wake, light sleep [stages 1 and 2], deep sleep, REM sleep, and non-REM sleep [light sleep and deep sleep, combined] in two representative disease-free subjects from the SIESTA database: (a_1-l_1) a healthy 32 years old female and (a_2-l_2) a 78 years old female [apnea-hypopnea-index $AHI=4.0$]. Shown are phase-rectified signal averages with subtracted means above their corresponding wavelet power utilizing a 6th-order Morlet wavelet. Wavelet power was normalized in each panel to ensure a total power of one. Power increases from white to red; a pseudo-logarithmic color model stretched in both the very low power range and the large power range was employed separately in each panel guaranteeing a qualitative but not quantitative comparability between panels. In panels devoted to PRSA curves associated Deceleration Capacity (DC) values are shown next to the 'number of different segments from the same sleep stage' / 'total number of windows contributing to the shown PRSA curve'. In young healthy subjects a long-coherent oscillatory component of rather narrow frequency bandwidth is apparent during deep sleep [in (h_1) approx. 5 heartbeats per breath cycle]. The coherence time decreases towards light sleep S2 and often even further towards light sleep S1. It is small during REM sleep and wake. In elderly coherence is notably decreased during all sleep stages (sometimes still longer during deep sleep) and respiratory frequency bandwidth is increased. It is typical to find additional slow wave oscillations (likely blood pressure related) compared to young.

Nocturnal wakefulness (arousals), light sleep S1 and S2, deep sleep, and REM sleep — which are associated with different physiological states of the autonomous nervous system. Hence, it is interesting how oscillatory components (observed by PRSA curves) change with sleep stages. Therefore, I subdivided the data from all 608 ECG recordings in the SIESTA database (disease-free and diseased considering both adaptation and recording night when possible) according to the annotated sleep stages and obtained PRSA curves together with their wavelet transforms to study frequency components and their timing and coherence. From PRSA curves I calculated DC values separately for each sleep stage.

Fig. 4.9 shows PRSA curves and their corresponding wavelet transforms separately for wakefulness [(a_i, b_i) ; $i = 1, 2$], light sleep S1 [(c_i, d_i)], light sleep S2 [(e_i, f_i)], deep sleep [(g_i, h_i)], REM sleep [(i_i, j_i)], and non-REM sleep [light sleep and deep sleep together; (k_i, l_i)] of a young [female age 32; $i = 1$] and an elderly [female age 78; $i = 2$] disease-free representative from the SIESTA database. Both subjects are considered healthy according to the SIESTA study protocol [MEMBERS OF SIESTA EU PROJECT 1998] although this classification should be challenged in some cases from a cardiologist's point of view.

For young disease-free subjects in the SIESTA database [see also Figs. 4.10(a_1-l_1) for an additional disease-free young subject] strong evidences of coherent respiration related periodicities (3 to 5 heartbeats per breath) seem to be typical. The corresponding frequency band ($f = 1/s$) is particularly narrow during non-REM sleep, i. e., good coherence during non-REM sleep. The coherence length is maximal during deep sleep and decreases towards light sleep S2 and further towards light sleep S1 [see Figs. 4.9(c_1-h_1, k_1, j_1) and 4.10(c_1-h_1, k_1, j_1)]. Light sleep S1 [Figs. 4.9(c_1, d_1)] is a

transition stage between wakefulness and light sleep S2. It often occurs transiently and/or only for a short period²². Coherence times of respiratory components during light sleep S1 are normally larger than corresponding times observed during nocturnal wakefulness (shorter coherence); and they are smaller compared with light sleep S2 (longer coherence). However, in some disease-free subjects coherence results from light sleep S1 appear to be more similar to wakefulness while in other subjects results are more similar to light sleep S2. Note the atypical large coherence length during wake in the healthy subject shown in Fig. 4.10. It suggests that this subject breathes at a regular rate which might be related to a relaxed condition before again falling asleep. During REM sleep and wakefulness respiratory components typically appear to be more random yielding (i) a broader associated frequency band, i.e., respiration does not occur at such a fixed frequencies as during deep sleep, and (ii) a much shorter coherence time [cp. Figs. 4.9(i₁,j₁) and Figs. 4.9(a₁,b₁) with Figs. 4.9(g₁,h₁)].

In young subjects the wavelet power in the slow oscillation range is reduced during all sleep stages compared with respiratory components. However, a few young subjects also exhibit strong traces of such slow oscillations during REM sleep, wakefulness, and sometimes even during light sleep S1 (when it is closer related to wake than to light sleep S2) but never during light sleep S2 and deep sleep. In elderly subjects which are classified as healthy by the SIESTA group the picture is quite opposite [see Figs. 4.9(a₂-l₂)]. The previous sharp and coherent structure of respiratory components has been changed in particular during non-REM sleep, implying a reduced synchrony in typical respiratory patterns. These patterns are quickly out of phase as the distance from the anchored heartbeat deceleration increases and thus cancel out in the averaging step [Eq. (4.3)]. Moreover, respiratory frequencies appear not as fixed as in young. Both effects are expressed by a smeared out (different frequencies) and localized (short coherence) wavelet power around $k = 0$ in the corresponding scales range. There are two possible implications: (i) real respiratory patterns change with aging, or (ii) respiratory components are less present in heartbeat intervals due to a reduced cardiorespiratory coupling in elderly. Chapter 5 deals with the analysis of inter-signal coupling. In particular, cardiorespiratory phase synchronization for SIESTA data is studied in Sect. 5.2.3 finding a reduction of cardiorespiratory phase synchronization with aging especially during light sleep S2 and deep sleep [see Fig. 5.10]. Further, note the increased power of slow wave oscillations which are otherwise a typical feature in sleep apnea subjects [see discussion Fig. 4.10]. The sleep stage characteristics shown for single subject are like fingerprints which are mainly identical when comparing results from adaptation night and recording night.

4.1.9. Quasioscillations in Patients

Figure 4.10 shows one representative subject from the SIESTA database classified disease-free (healthy) [(a₁-l₁); for comparison] and four representative patients suffering from (obstructive) sleep apnea [(a₂-l₂)], Parkinson's disease [(a₃-l₃)], anxiety [(a₄-l₄)], and depression²³ [(a₂-l₂)]. In most patients suffering from severe sleep apnea (AHI \gg 10) a strong frequency-localized slow oscillation is typical and often observed during all sleep stages, however, sometimes reduced during deep sleep. More importantly breathing related wavelet power (fast component) is severely diminished except for deep sleep which even seems totally unaffected (sharp, long coherence) in some individuals. For many Parkinson patients sleep stage differences of oscillatory patterns are weakened, however, in elderly additional slow components sometimes appear which might be related to an undetected sleep apnea.

A typical feature in anxiety patients are extended areas of slow oscillations during all or most sleep stages. However, especially some young anxiety patients look very similar to healthy subjects but often with reduced respiratory coherence. Such picture is even more pronounced in depression patients who can practically not be distinguished from healthy subjects although some elderly

²²For that reason light sleep S1 related data of long-enough duration ensuring a certain statistical reliability is not available for each dataset. In Figs. 4.9 and 4.10 I present selected subjects and patients having sufficiently long episodes of each sleep stage.

²³Depression was identified including a self-rating score [MEMBERS OF SIESTA EU PROJECT 1998]. Hence, it might be difficult to scientifically quantify the strength of the depression.

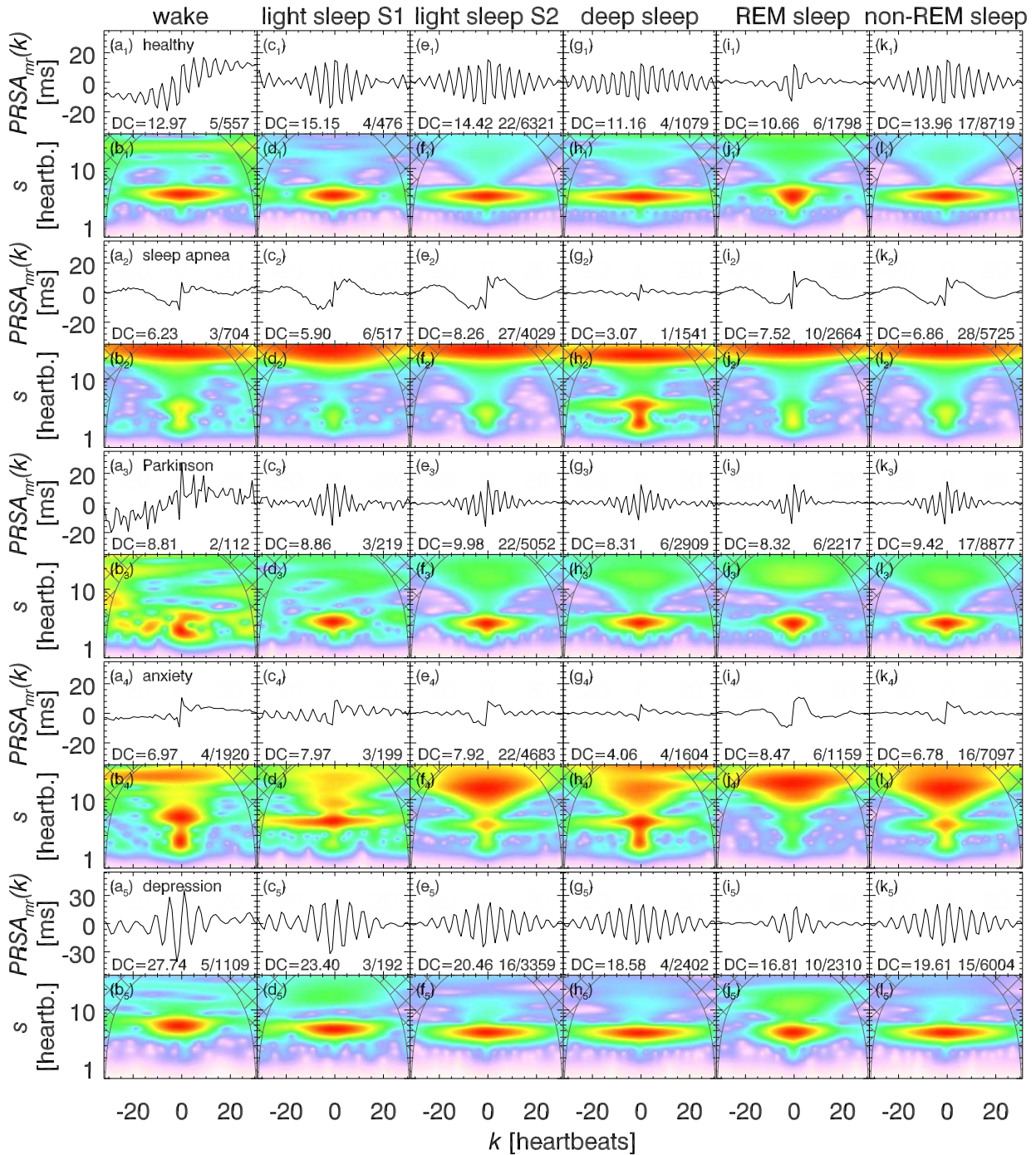


Figure 4.10.: PRSA results for 5 typical representatives from the SIESTA database being healthy or diseased; separately for nocturnal wake, light sleep [stages 1 and 2], deep sleep, REM sleep, and non-REM sleep [light sleep and deep sleep, together]. Shown are mean-removed phase-rectified signal averages above their corresponding wavelet power utilizing a 6th-order Morlet wavelet [Fourier scale = wavelet scale s times 1.03] for a (a_1 - l_1) 35 years old healthy female; (a_2 - l_2) 38 years old male sleep apnea patient [apnea-hypopnea-index (AHI) of 82.8]; (a_3 - l_3) 61 years old female Parkinson patient [AHI=1.2]; (a_4 - l_4) 56 years old female anxiety patient [AHI=0.9]; and (a_5 - l_5) 35 years old female depression patient. Wavelet power was normalized in each panel to ensure total power one. Power increases from white to red; a pseudo-logarithmic color model stretched in both the very low power range and the large power range was employed separately in each panel guaranteeing a qualitative but not quantitative comparability between panels. In panels devoted to PRSA curves associated Deceleration Capacity (DC) values are shown next to the number of different segments from the same sleep stage / total PRSA surroundings contributing to the shown PRSA. Note the different Y-axis used in (a_5 - k_5). All diseases exhibit typical pattern in wavelet power, except for depression which here appears to be similar to healthy [see text for a detailed discussion].

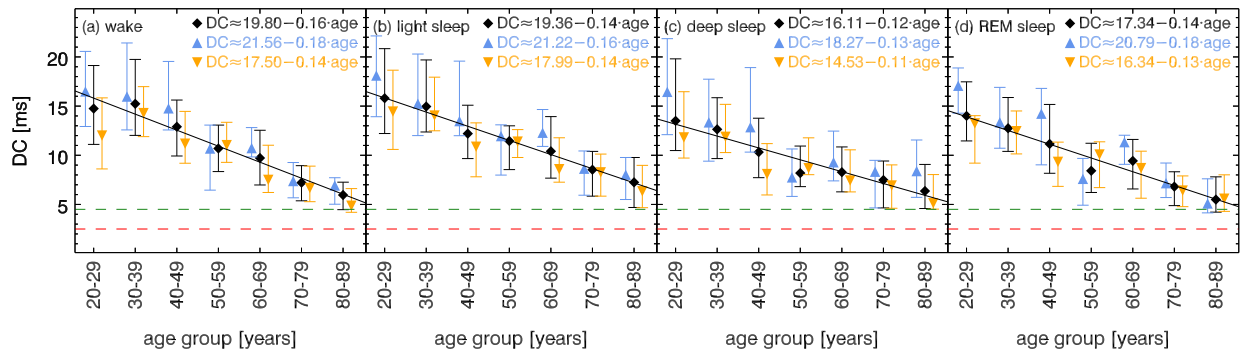


Figure 4.11.: Deceleration capacity (DC) versus age for (a) nocturnal wakefulness, (b) light sleep $S2$, (c) deep sleep $S3\&S4$, and (d) REM sleep for all subjects [black diamonds], males [blue triangles up], and females [orange triangles down]. Plotted are median values and both quartiles $Q25$ and $Q75$ as lower and upper errors bars, respectively. Solid straight lines are linear fits to the medians for all subjects; the formulas of the separate fits for males and females are printed in the top right corner. Red and green dashed lines indicate risk levels previously defined for post-infarction patients: high cardiac risk $DC < 2.5ms$ and low cardiac risk $DC > 4.5ms$. Taken from [SCHUMANN et al. 2010a]

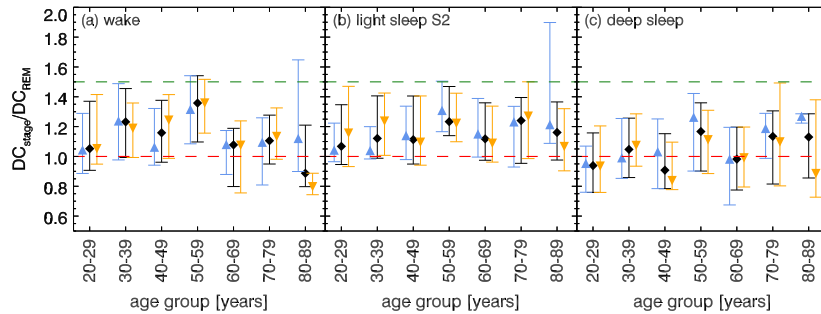


Figure 4.12.: Age dependence of DC ratios: (a) DC_{wake} / DC_{REM} , (b) $DC_{light\ sleep\ S2} / DC_{REM}$, and (c) $DC_{deep\ sleep\ S3\&S4} / DC_{REM}$ for all subjects [black diamonds], males [blue triangles up], and females [orange triangles down]. Shown are medians and quartiles as in Fig. 4.11. Taken from [SCHUMANN et al. 2010a]

seem to have incipient sleep apnea. This suggests that anxiety and depression do not significantly affect quasi-oscillatory components in heartbeat.

Incidental apnea episodes which according to SIESTA study rules, however, did not yield a classification as apnea patient are typically observed in all Elderly subjects within the SIESTA database. Further systematic investigation on disease identification algorithms based on these qualitative observations is required in a larger database recorded using much more DC specified classification rules as has been employed in the SIESTA study.

4.1.10. Aging Effects on DC Across Sleep Stages

To investigate effects of healthy aging on DC during sleep I divide the heartbeat data from all disease-free subjects according the same age groups as were used in Sect. 3.2.2. Light sleep $S1$ is again neglected for the same reasons as discussed earlier. The results that are discussed in the following can also be found in [SCHUMANN et al. 2010a].

For deriving DC based statistical parameters I only considered values in the range $0 \leq DC \leq 40ms$ to be reliable. Median DC values from including all disease-free subjects in the same age group are depicted in Fig. 4.11.

A significant decay from younger subjects towards older subjects is obvious in all sleep stages. The slope of the decay is, however, smaller for females than for males (see different symbols and regression equations printed in the figure but not shown). In particular young females (age 20-29) exhibit surprisingly low DC values especially during wake. If one would exclude this age group from the study, the differences of DC slope for males and females during wakefulness would vanish. In general, DC values for males and females become more similar with aging in all states and merge for the oldest group except during deep sleep. Recall that deep sleep is significantly reduced among elderly yielding a reduced statistics.

When exploring individual DC values I recognized lower values during REM sleep and deep sleep than during light sleep and wakefulness for most of the subjects. To test this observation Fig. 4.12

shows the mean ratios over DC_{REM} and their standard deviations. In case of a lower DC during REM sleep the ratios are > 1 . This is observed for young subjects during wake and for all age groups during light sleep S2, i. e., $DC_{\text{REM}} < DC_{\text{wake}}$ and $DC_{\text{REM}} < DC_{\text{light sleep}}$. The results during deep sleep are inconclusive. Employing a paired Student's t test [see Appendix D.1] comparing all DC value combinations I found highly significant differences ($p \ll 0.0001$) for the combinations wake vs. REM sleep, light sleep vs. REM sleep, wake vs. deep sleep, and light sleep vs. deep sleep. Marginally significant differences ($p < 0.05$) occurred for wake vs. light sleep. The DC values during deep sleep and REM sleep were not significantly different.

The observed sleep-stage related changes in DC can be compared with changes in long-term heartbeat correlations during different sleep stages [Sect. 3.2.2] to improve the understanding of cardiovascular regulation during sleep. In addition, the results might be applied for the detection of sleep stages based on ECG instead of more complicated brain recordings. Another possible application is the identification of anomalous autonomic regulation associated with certain disorders.

4.2. Bivariate PRSA (BPRSA) and Multivariate PRSA (MPRSA)

The previously explored concept of univariate PRSA can be generalized to study interrelations between two signals X and Y or even more than two signals. While I will mainly focus on the first case and explain *bivariate phase rectified signal averaging (BPRSA)* which was published in [SCHUMANN *et al.* 2008a], I only briefly mention the even more general case of *multivariate phase rectified signal averaging (MPRSA)*.

As I have discussed in Sect. 2.1 autonomous control is established by the sympathovagal balance, i. e., the ratio between parasympathetic and sympathetic tone. Recall that the empirical observation that this balance is affected by age, gender [VALLADARES *et al.* 2008], and more importantly by certain pathologies led to the development of the PRSA method to separately investigate sympathetic and parasympathetic effects in heartbeat [see Sect. 4.1]. Moreover, the association of cardiac dysfunction and a history of myocardial infarction with a reduced parasympathetic activity [PRIORI *et al.* 2001, and references therein] motivated the suggestion of the PRSA-based parameter DC for mortality-risk assessment, Sect. 4.1.3.

However, as I have also mentioned in Sect. 2.2 the cardiovascular system includes the blood vessels in addition to the heart. Blood pressure is simultaneously controlled by the autonomous nervous system and linked to the regulation of the heart. One important autonomic control loop between both components is the baroreflex, a homeostatic regulation that maintains a 'stable' blood pressure. An elevated blood pressure reflexively causes the blood pressure to decrease and vice versa. It is controlled through several stretch sensitive mechanoreceptors (baroreceptors). Activation of the baroreceptor results in a inhibition of sympathetic components and activation of parasympathetic or vagal components. Due to an initially elevated blood pressure, activated baroreceptors tend to decrease cardiac output via a decrease in contractility resulting in a lower heart rate and finally in a decrease in blood pressure. A low blood pressure level relaxes the mechanoreceptor and stops the sympathetic inhibition and resulting in an increased contractility, heart rate, and blood pressure. It is believed that cardiovascular illnesses disturb the baroreflex and parameters that include blood pressure information might even further improve mortality predictors as LVEF or DC [Sect. 4.1.3]. Thus, the detection of quasi-periodicities reflecting regulation processes of the autonomic cardiac nervous system that coincide either with increases or decreases of blood pressure in long-term records of human heartbeat is of high clinical relevance. Autonomic dysfunction is closely related to cardiac mortality and susceptibility to life-threatening arrhythmic events [LOWN AND VERRIER 1976]. The assessment of heart rate variability (HRV) by the PRSA based deceleration capacity (DC) parameter [BAUER *et al.* 2006a] was shown to be superior to spectral parameters proposed earlier for risk prediction [BIGGER *et al.* 1992]; for a recent review on DC and different other nonlinear parameters used in total mortality risk assessment see [HUIKURI *et al.* 2009]. Hence, a PRSA based method that respects the coupling of heartbeat *and* blood pressure (BPRSA), i. e., phase rectifies heartbeat at times where blood pressure increases (or decreases)

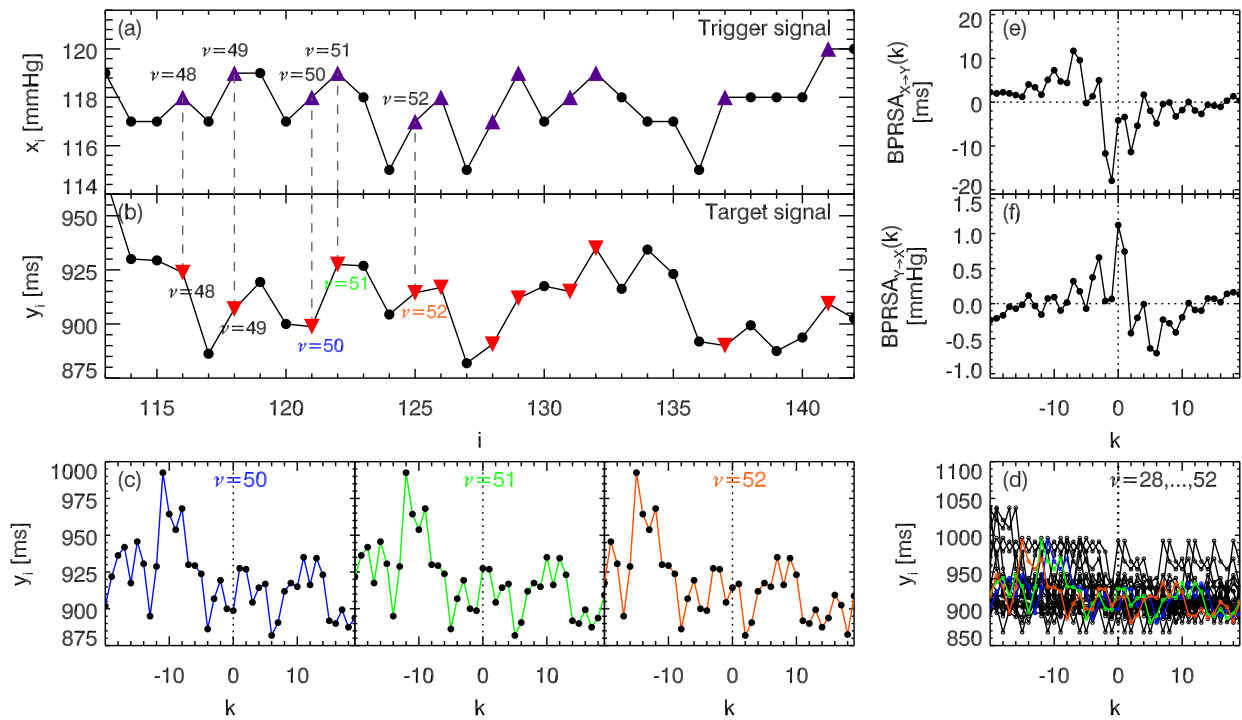


Figure 4.13.: Illustration of the BPRSA technique: Shown are fragments of (a) a blood pressure recording [trigger signal X] and (b) a heartbeat interval (RRI) time series [target signal Y]. According to Eq. (4.1a) anchor points x_{i_ν} are selected in X [(a); violet triangles up] and identified with corresponding points in Y [(b); red triangles down] which are used as new anchors y_{i_ν} . For each y_{i_ν} , surrounding windows $y_{i_\nu-L}, \dots, y_{i_\nu}, y_{i_\nu+L-1}$ are defined [(c) three example windows $\nu = 50, 51, 52$ of many more; anchor in the center] and aligned at anchor positions [(d) windows $\nu = 28, \dots, 52$; examples from (c) are shown in same colors]. (e) All surroundings $\nu = 1, \dots, M$ with M the total number of windows are averaged yielding $\text{BPRSA}_{X \rightarrow Y}(k)$ which illustrates changes in heartbeat at increasing blood pressure. (f) Likewise, changes in blood pressure caused by increases in heartbeat can be studied by exchanging trigger and target signal, $\text{BPRSA}_{Y \rightarrow X}(k)$.

and vice versa, seems to be promising for the definition of an advanced risk predictor that is even more superior.

4.2.1. BPRSA Algorithm

Both BPRSA and MPRSA algorithms are nearly identical with the univariate approach described in the previous subsection [Sect. 4.1], except for the usage of different signals. I here illustrate the BPRSA recipe using heartbeat and blood pressure signals commonly studied to quantify baroreflex sensitivity, i.e., the variation of the time intervals between successive heartbeats in reaction to changes in blood pressure.

Step 1:

Anchor points are defined in a similar sense as before – e.g., according to Eq. (4.1a) – based on the *trigger signal* $X = \{x_i\}, i = 1, \dots, N$ which is for example systolic blood pressure [purple triangles up in Fig. 4.13(a)]. Subsequently, corresponding anchor points $i_\nu, \nu = 1, \dots, M$ are identified in the *target signal* $Y = \{y_i\}$ which are for example heartbeat intervals (RRI) [red triangles down in Fig. 4.13(b)]. Note, triggering on certain features in the trigger signal (e.g. increases in blood pressure) does not necessarily imply anchors at the same features (e.g. increases in RRI) in the target signal since a response might be time delayed.

Step 2:

Surroundings of width $2L$ are defined around each anchor in the target signal [Fig. 4.13(c)] (analogous to *Step 2* in the univariate PRSA algorithm).

Step 3:

Similarly to *Step 3* in the univariate PRSA all surroundings are aligned at their anchor positions and averaged with respect to previously discussed 'missing points' or 'incomplete surroundings' yielding the bivariate phase rectified signal average

$$\text{BPRSA}_{X \rightarrow Y}(k) = \frac{1}{M} \sum_{\nu=1}^{M_k} y_{i_\nu+k}, \quad k = -L, \dots, 0, \dots, L-1 \quad (4.6)$$

with $M_k \leq M$ is the number of valid points of Y at position k and M is the total number of anchor surroundings. BPRSA is a non-symmetric algorithm, i.e., the exchange of trigger signal X and target signal Y will result in a different BPRSA curve addressing a different question, e.g., how changes in heartbeat affect systolic blood pressure [cp. Figs. 4.13(e),(f)]. More complex boolean or weighted anchor criteria, even ones based on more than one trigger signal, are possible. The latter defines a *multivariate PRSA (MPRSA)* which is briefly sketched in Sect. 4.2.9.

4.2.2. Limitations of Cross-Correlation Analysis

Cross-correlation analysis (CCA) is a well established tool to quantify time-domain linear interrelations between two signals and has already been briefly introduced in Sect. 1.1. Although, CCA has been employed in many applications, only a few authors have specifically addressed its reliability [PETERSON *et al.* 1998; WELSH 1999; VIO AND WAMSTEKER 2001]. For two discretely measured signals $\{x_i\}$ and $\{y_i\}$, $i = 1, \dots, N$, the (biased) *normalized cross-correlation function* is most commonly defined as in Eq. (1.9b); for convenience the essential part of both equations is repeated and the notation is adapted to the notation of BPRSA by setting $s = k$. To avoid confusion I denote this adapted version by $\widetilde{\text{Cov}}_{xy}(k)$.

$$\widetilde{\text{Cov}}_{xy}(k) = \begin{cases} \frac{1}{N\sigma_x\sigma_y} \sum_{i=1}^{N-k} (x_i - \mu_x)(y_{i+k} - \mu_y) & : k = 0, 1, \dots \\ \frac{1}{N\sigma_x\sigma_y} \sum_{i=1-k}^N (x_i - \mu_x)(y_{i+k} - \mu_y) & : k = -1, -2, \dots \end{cases} \quad (4.7)$$

where again $\mu_\alpha = \frac{1}{N} \sum_{i=1}^N \alpha_i$ and $\sigma_\alpha = \left[\frac{1}{N} \sum_{i=1}^N (\alpha_i - \mu_\alpha)^2 \right]^{1/2}$ are means and standard deviations of both series $\alpha = x, y$, respectively. This definition assumes that both μ_α and σ_α do not vary in time, i.e., they do not depend on the segments of the time series selected for the study. This corresponds to the assumption of weak stationarity. Strong stationarity additionally requires constancy of all other moments [see Sect. 1.1]. For studies discussing the replacement of μ_x and μ_y by local estimates, e.g., running averages, see [SCARGLE 1989; PRESS *et al.* 1992]. Note, however, that some cross-correlations might be reduced or eliminated by this so-called pre-whitening procedure, which is therefore unsafe.

Another problem of cross-correlation functions is that the exchange of the two signals X and Y corresponds to replacing k by $-k$, i.e., time inversion. Hence, causality relations between the two series can hardly be assessed. In general, the points of $\widetilde{\text{Cov}}_{xy}(k)$ are highly auto-correlated, e.g., $\widetilde{\text{Cov}}_{xy}(k)$ is strongly correlated with $\rho_{xy}(k+1)$. I.e., neighboring points in $\widetilde{\text{Cov}}_{xy}(k)$ are stronger correlated with each other than neighboring points in the original time series [WELSH 1999; JENKINS AND WATTS 1969]. This *self-correlation* causes long living trends in $\widetilde{\text{Cov}}_{xy}(k)$, e.g., a slow decay after a peak, which is at risk of misinterpretation.

Furthermore, the sum in Eqs. (4.7) runs over $N - k$ terms, while it is divided by N instead of $N - k$. This procedure corresponds to a standard averaging procedure only in the limit of very long data ($N \rightarrow \infty$). Nevertheless, most statistical toolkits employ the definition [Eqs. (4.7)], because the convolution theorem and fast Fourier transform can be used to speed up the calculations significantly in this case by application of the Wiener-Khinchin theorem. Some authors even argue for an increase in precision because the normalization $1/N$ reduces the mean-square variance of $\widetilde{\text{Cov}}_{xy}(k)$ (see, e.g., [JENKINS AND WATTS 1969]). However, this non-matching prefactor results in a bias towards zero with increasing time lag k for small N , causing a triangular-shaped behavior of

$\widetilde{\text{Cov}}_{xy}(k)$. Consequently, the value of $|k| > 0$ for the center of a peak in $\widetilde{\text{Cov}}_{xy}(k)$ is systematically underestimated [WELSH 1999]. There are different opinions about which normalization should be used. I am personally convinced that the correction factor $N/(N-k)$ which transforms $\widetilde{\text{Cov}}_{xy}(k)$ from Eqs. (4.7) into the (unbiased) *correctly normalized cross-correlation function*²⁴

$$\widetilde{\text{CCF}}_{XY}(k) = \begin{cases} \frac{1}{(N-k)\sigma_x\sigma_y} \sum_{i=1}^{N-k} (x_i - \mu_x)(y_{i+k} - \mu_y) & : k = 0, 1, \dots \\ \frac{1}{(N-k)\sigma_x\sigma_y} \sum_{i=1-k}^N (x_i - \mu_x)(y_{i+k} - \mu_y) & : k = -1, -2, \dots \end{cases} \quad (4.8)$$

should be used to obtain reliable results except for very long data and small $|k|$. For small $|k|$ and large N the correction factor approaches 1.

If the considered data is not fully stationary, one might want to use only the values x_i with $i = 1, \dots, N-k$ and y_i with $i = k+1, \dots, N$ for calculating $\mu_{x,k}$, $\mu_{y,k}$, $\sigma_{x,k}$, and $\sigma_{y,k}$. This approach is known as *local cross-correlation* in literature; it is equivalent to the Pearson r_{xy} (product-moment) correlation coefficient for the two overlapping pieces. Since the partial means and standard deviations will depend on k , the computational effort is significantly increased. The bias mentioned in the previous paragraph is not completely removed in this approach [WELSH 1999] (although it is weaker than for the standard definitions [Eqs. (4.7)]. In addition, problems with autoregressive moving average processes (ARMA) were reported [JENKINS AND WATTS 1969]. Since the cross-correlation approach does not work well for non-stationary data anyway, we do not consider local cross-correlation here.

4.2.3. Interpretation of BPRSA Curves

In BPRSA, anchor points usually occur in all parts of the trigger signal X . The average of $\text{BPRSA}_{X \rightarrow Y}(k)$ for all k will, thus, be approximately the global average of the whole target signal, i.e., μ_y . Consequently, subtraction of this mean from $\text{BPRSA}_{X \rightarrow Y}(k)$ yields positive and negative values as in the cross-correlation function. $\text{BPRSA}_{X \rightarrow Y}(k) - \mu_y$ can thus be interpreted in a similar way as an unnormalized cross-correlation function. If one divides by the global standard deviation, σ_y , the resulting quantity

$$\text{BPRSA}_{X \rightarrow Y}^{(\text{norm})}(k) = \frac{\text{BPRSA}_{X \rightarrow Y}(k) - \mu_y}{\sigma_y} \quad (4.9)$$

is also normalized. Hence, it can be compared with $\text{CCF}_{X,Y}(k)$ in Eqs. (4.8) and interpreted in a similar way. Note that – different from cross-correlation analysis – this rescaling is just the last step, and μ_y does not enter into the calculation of $\text{BPRSA}_{X \rightarrow Y}(k)$. Hence, the shape of the curve cannot be affected by non-stationarities, i.e., inaccurate μ_y . There is no practical advantage of normalized BPRSA, unless the behavior of the curves for different signals, e.g., triggering directions ($X \rightarrow Y$) and ($Y \rightarrow X$), shall be directly compared. However, the global mean μ_y and global standard deviation σ_y might not exist due to non-stationarities and in this case normalization is not recommended.

In some applications it is even preferred to study the unnormalized BPRSA curves. For example, in quantifying the influence of blood pressure upon heartbeat regulation via the baroreflex mechanism in the human cardiovascular system, the variation of the time intervals between successive heartbeats in reaction to increases in blood pressure needs to be measured [example used for method illustration in Fig. 4.13]. In this case the units of both signals have to be kept, and the measure characterizing the baroreflex must have the unit ms/mmHg, i.e., time difference divided by pressure difference. In fact, cross-correlation studies can only yield either quantities without units (if normalized) or quantities which are products of both original units. Quantities with the unit of only one original series or their ratio (as needed for the baroreflex) cannot be obtained.

²⁴I changed the notation from 'xy' to capital letters to ensure comparability with the notation I use for BPRSA following [SCHUMANN *et al.* 2008a].

Hence, there is no way to obtain a meaningful measure for the baroreflex from a cross-correlation analysis, although the baroreflex is a typical example of a meaningful inter-relation between two components of a complex system.

Effects occurring in $\text{BPRSA}_{X \rightarrow Y}(k)$ for $k > 0$ can be easily recognized as consequences of the triggering events in the trigger signal X . On the other hand, effects seen in $\text{BPRSA}_{X \rightarrow Y}(k)$ for $k < 0$ are likely to be causes for the actual triggering events. Note that a similar conclusion is also valid for the cross-correlation function $\text{CCF}_{X,Y}(k)$, since effects observed for $k > 0$ and $k < 0$ are probably due to interactions from signal X onto signal Y and vice versa. However, BPRSA allows separating these causality effects from nonlinear effects, as we will see in the following.

Altogether, four BPRSA curves can be defined, compared with one cross-correlation function: $\text{BPRSA}_{X \rightarrow Y}^{\nearrow}(k)$ (triggering on increases in X), $\text{BPRSA}_{X \rightarrow Y}^{\searrow}(k)$ (triggering on decreases in X), $\text{BPRSA}_{Y \rightarrow X}^{\swarrow}(k)$, and $\text{BPRSA}_{Y \rightarrow X}^{\nwarrow}(k)$ (triggering on Y). By comparing these curves, additional information on the linearity of the interactions and time reversal symmetry can be obtained. In the following we will use the symbols \nearrow and \searrow for BPRSA curves obtained by triggering on increases and decreases in the trigger signal only when necessary for distinction. In all other cases $\text{BPRSA}_{X \rightarrow Y}$ means $\text{BPRSA}_{X \rightarrow Y}^{\nearrow}$.

If the interaction from signal X to signal Y is linear, we will find $\text{BPRSA}_{X \rightarrow Y}^{\nearrow}(k) = -\text{BPRSA}_{X \rightarrow Y}^{\searrow}(k)$, since increases and decreases in X must cause opposite effects in Y . Accordingly, $\text{BPRSA}_{Y \rightarrow X}^{\swarrow}(k) = -\text{BPRSA}_{Y \rightarrow X}^{\nwarrow}(k)$ shows that the interaction from Y to X is linear. If the interaction between both signals is fully symmetric, time inversion is equivalent with exchanging the signals, $\text{BPRSA}_{X \rightarrow Y}^{\nearrow(\text{norm})}(k) = \text{BPRSA}_{Y \rightarrow X}^{\swarrow(\text{norm})}(-k)$ and $\text{BPRSA}_{X \rightarrow Y}^{\searrow(\text{norm})}(k) = \text{BPRSA}_{Y \rightarrow X}^{\nwarrow(\text{norm})}(-k)$. Deviations from this behavior show non-symmetric coupling as do deviations from $\text{CCF}_{X,Y}(k) = \text{CCF}_{X,Y}(-k)$ in cross-correlation analysis. However, this can be checked independent of the linear or nonlinear character of the interactions between the signals. Note that normalized BPRSA must be considered in this case, Eq. (4.9). It is straightforward to write down similar relations for testing further hypotheses regarding the inter-relations between both signals.

4.2.4. Comparison of Cross-Correlation Analysis and BPRSA

In this subsection I will discuss how BPRSA overcomes the above described disadvantages of cross-correlation analysis.

1. *Causality and nonlinear interactions.* As we have shown in the previous subsection, more information on the linearity or nonlinearity of the interactions and on time-reversal symmetry can be obtained from BPRSA curves than from the cross-correlation function.

2. *Time delays.* The estimation of (positively or negatively) time-delayed inter-relations between both signals is straightforward, just as in cross-correlation analysis.

3. *Missing data and outliers.* BPRSA can easily cope with missing data (e.g., measurement artifacts, instrument failure, or outliers) in both series X and Y . Invalid values in X just cannot become anchor points. Invalid values in Y will be disregarded [see text following Eq. (4.3)].

4. *(Non-)stationarity of the data.* In the definition of BPRSA [Sect. 4.2.1, in particular Eq. (4.6)] neither means nor standard deviations of both signals X and Y are needed. Hence, no direct problems arise for non-stationary data. In particular data with a piecewise constant trend, which is often observed in medical data recordings, will cause no problems in BPRSA, because Eq. (4.6) is a simple linear arithmetic averaging procedure. The deviations from a small or large local average will have the same weight in this averaging procedure. Hence, BPRSA does not need pre-whitening of the data before analysis. Cross-correlation analysis, on the other hand, will be disturbed severely by a piecewise constant trend, because the deviations $x_i - \mu_x$ from the global average will be dominated by this trend [see Sect. 4.2.8 for an example]. The same holds for an oscillating trend in the target signal Y which is uncorrelated with the trigger signal X . However, such a trend in X will selectively cause anchor points and thus disturb also BPRSA; consequently more anchor points, i.e., longer data, will be needed!

A slowly varying, monotonous (e.g., polynomial) trend in the target signal will bend the BPRSA curve, since the local means are different in the beginning and at the end of the signal and in the

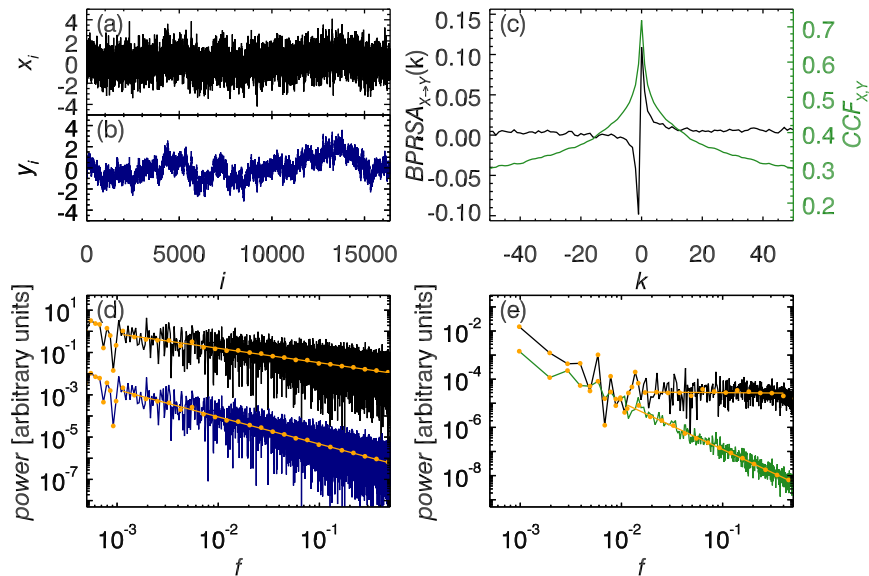


Figure 4.14.: Filter-properties of BPRSA and cross-correlation function for differently correlated noises with $\mu_x = \mu_y = 0$, $\sigma_X = \sigma_Y = 1$. The time domain (a,b) and frequency domain (d) plots of $1/f^\beta$ -noise with spectral exponents $\beta_X = 0.7$ [black curves, shifted] and $\beta_Y = 1.3$ [magenta curves] are shown next to the $BPRSA_{X \rightarrow Y}$ [black] and $CCF_{X,Y}$ [blue] in (c) and their correctly normalized and correspondingly color-coded power spectra with $\beta_{BPRSA_{X \rightarrow Y}} \approx 0$ [shifted] and $\beta_{CCF_{X,Y}} \approx 2$ in (e). The two long-term correlated noises were generated by Fourier filtering [Sect. 1.5.2] with different β , starting both procedures with the same original white noise [not shown]. For all spectra logarithmic binning and linear fitting [yellow dots and lines] were applied to estimate β .

beginning and at the end of each segment. However, this bending is definitely not stronger than a similar bending of the cross-correlation function. Trends in the trigger signal X will modify the fraction of anchor points for increases and decreases, which has little effect on $BPRSA_{X \rightarrow Y}(k)$ unless these trends are very strong.

5. Enhanced auto-correlations. Unlike the cross-correlation function [WELSH 1999; JENKINS AND WATTS 1969], which is often dominated by low frequencies, BPRSA does not show artificially enhanced auto-correlations. On the contrary, low frequencies are reduced due to the filtering characteristics (see next point). This makes BPRSA particularly attractive for studying signals with underlying $1/f$ - rather than white noise. Note that $1/f$ -noise is prevalent, e.g., in medical and geophysical data.

6. Filtering characteristics. Figure 4.14 compares the spectral properties of both, cross-correlation analysis and BPRSA. Since many interesting data contain long-term auto-correlations [cp. Sect. 1.2 for definition and Chapt. 3] and are characterized by $1/f$ -noise in their power spectra, $P(f) \sim f^{-\beta}$ with β around 1, consider two such noise series (see Fig. 4.14(a,b)) with $\beta_x \approx 0.7$ and $\beta_y \approx 1.3$ (see Fig. 4.14(d)). The power spectrum of the cross-correlation function decays as f^{-2} (see Fig. 4.14(e)). It is thus dominated by low-frequency components. The BPRSA curve, on the other hand, yields a nearly flat power spectrum (see also Fig. 4.14(e)). Therefore, additional peaks and quasi-periodicities can be noticed and determined much easier.

The filtering characteristics of BPRSA can be explained as follows. The scaling behavior of the BPRSA spectrum is influenced by the anchoring procedure in the trigger signal and by the averaging of the target signal. We want to estimate the probability $p(f)$ that an oscillating component with frequency f , $y_f = A_y \sin(2\pi ft)$ in the target signal Y affects $BPRSA_{X \rightarrow Y}(k)$ under the condition that an oscillation with the same frequency f , $x_f = A_x \sin(2\pi ft)$ causes anchor points in the trigger signal X . Firstly, x_f has to cause anchor points at positions t_ν , meaning $x_f(t_\nu)$ has to be larger than $x_f(t_\nu - \Delta t) \approx x_f(t_\nu) - \Delta t x'_f = x_f(t_\nu) - \Delta t 2\pi f A_x \cos(2\pi f t_\nu)$ for anchor criterion Eq. (4.1a). This is a valid approximation except for very high frequencies f . The deviation $x_f(t_\nu) - x_f(t_\nu - \Delta t) = \Delta t 2\pi f A_x \cos(2\pi f t_\nu)$ becomes maximal for $t_\nu = n/f$ with any integer n . Since anchor points t_ν are primarily generated at or close to phase zero of the considered component x_f , the later averaging is phase-rectifying in terms of the trigger signal. The value of the maxima $x_f(t_\nu) - x_f(t_\nu - \Delta t)$ is $2\pi \Delta t f A_x$ and thus the probability p_x to anchor

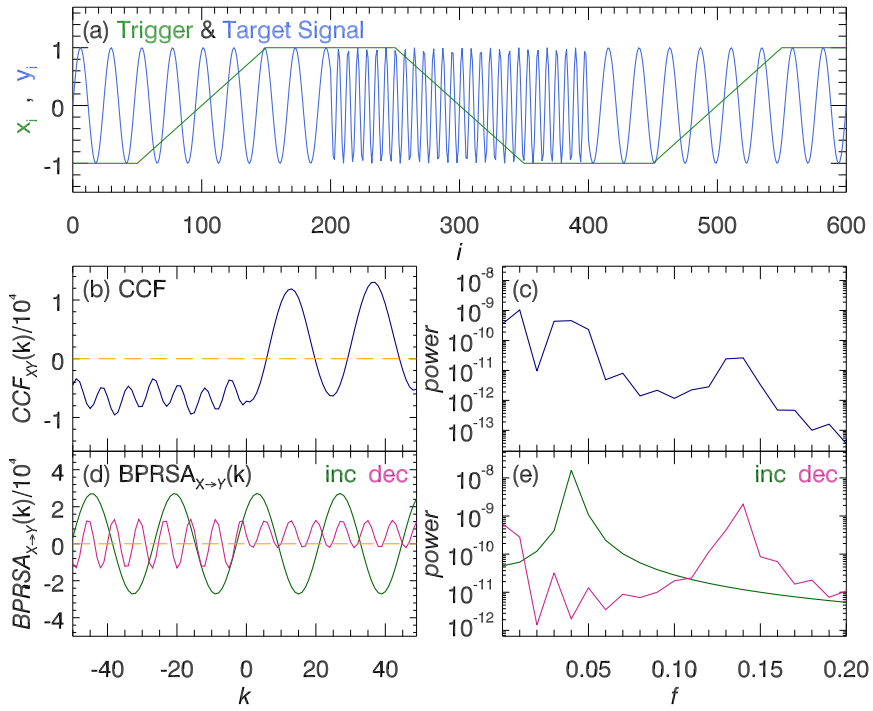


Figure 4.15.: Idealized model illustrating the idea of BPRSA to distinguish different oscillatory components in the target signal which correspond to a certain phase of the trigger signal. (a) Target signal Y [blue] composed of two pure sinusoids with $f_1 = 0.042$ 1/sample units (s.u.) and $f_2 = 0.136$ (s.u.) $^{-1}$ together with trigger signal X [green; here a simple flattened sawtooth signal whose flanks symbolize times of signal increase and signal decrease]. (b) Cross-correlation function $CCF_{X,Y}$ and (d) $BPRSA_{X \rightarrow Y}$ of both signals in (a) employing an anchor criterion according [green, increases] Eq. (4.1a) and [violet, decreases] Eq. (4.1b). (c,e) Power spectra of $CCF_{X,Y}$ and $BPRSA_{X \rightarrow Y}$. While BPRSA can clearly distinguish between oscillations occurring simultaneously to an increase or a decrease in the trigger signal, CCF only qualitatively identifies both components.

is proportional to $A_x f$. On the other hand, the component y_f has an effect proportional to its amplitude A_y due to the averaging procedure of Eq. (4.3) and therefore $p_y \sim A_y$. The amplitude of the considered spectral components in $BPRSA_{X \rightarrow Y}(k)$ is thus determined by $A_x A_y f$. If one considers two signals X and Y consisting of correlated noise with power spectra

$$P_x(f) \sim A_x^2 \sim f^{-\beta_X} \quad \text{and} \quad P_y(f) \sim A_y^2 \sim f^{-\beta_Y} \quad (4.10)$$

it follows

$$P_{BPRSA}(f) \sim (p_x p_y)^2 \sim A_x^2 f^2 A_y^2 \sim f^{-\beta_X - \beta_Y + 2} = f^{-\beta_{BPRSA}} \quad (4.11)$$

with $\beta_{BPRSA} = \beta_X + \beta_Y - 2$, yielding $\beta_{BPRSA} \approx 0$ if both β_X and β_Y are close to one or their average is close to one.

Since BPRSA has significant advantages over cross-correlation analysis for studying data with $1/f$ noise and/or nonlinear interaction as well as non-stationary data, one can imagine several applications. Next, I describe four specific situations (with and without noise) and illustrate the performance of BPRSA on model data.

4.2.5. Example I: Event Modulated Oscillations

As already mentioned before there exist applications where a signal Y exhibits typical oscillatory structure at certain phases of a signal X . A prominent physiological example is *respiratory sinus arrhythmia* (RSA), i.e., the modulation of heartbeat with respiration. During inspiration heartbeat is accelerated while it is decelerated during expiration. RSA is especially pronounced in dogs and was also reported to improve the efficiency of pulmonary gas exchange [HAYANO *et al.* 1996; YASUMA AND HAYANO 2004]. Hence, there are heartbeat (quasi-)oscillations of different period associated with inspiration and expiration. Another example is the previously discussed baroreflex. Figure 4.15 shows a simple toy model comprising a signal (target signal) constructed from

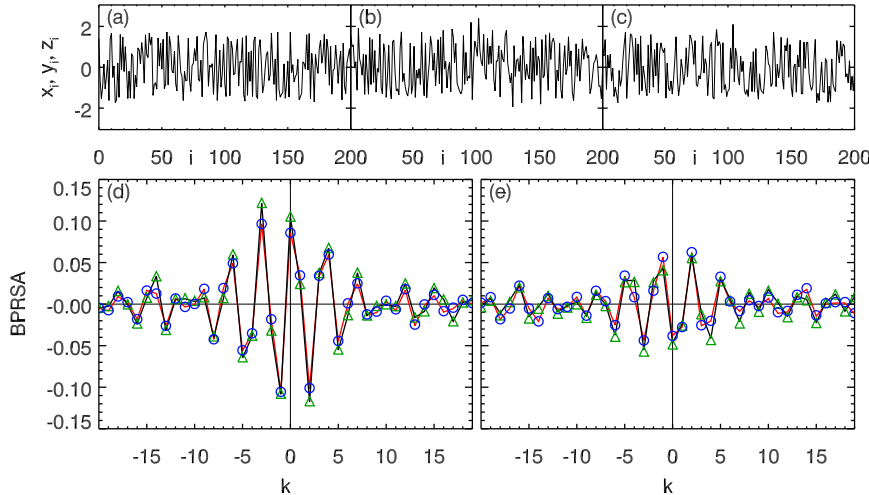


Figure 4.16.: Samples of the noise series X [(a), pure noise], Y [(b), generated from X by Eq. (4.12) with $c_1 = 0.2$], and Z [(c), $c_1 = -0.1$]. The HF band [$f \in [0.25, 0.35]$ reciprocal sampling units] is used for the bandpass filtering, and the total length of the data is $N = 16384$. BPRSA results for $\alpha = Y$ (d) and $\alpha = Z$ (e): $\text{BPRSA}_{X \rightarrow \alpha}$ [black solid lines], $\text{BPRSA}_{\alpha \rightarrow X}$ [red solid lines], $-\text{BPRSA}_{X \rightarrow \alpha}$ [green triangles], $-\text{BPRSA}_{\alpha \rightarrow X}$ [blue circles] are shown. The points are connected for visual reasons only; all values are dimensionless.

two different periodic components which are present at different phases of a second signal (trigger signal). It illustrates the idealized capability of BPRSA to distinguish both effects of different autonomous control (heartbeat deceleration=vagal activation, heartbeat acceleration=sympathetic predominance). Since all data points of both signals contribute to the cross-correlation function it is not capable to extract which oscillatory component was present at times of trigger signal increases (or, alternatively decreases) [Figs. 4.15(b,c)]. BPRSA on the other hand can clearly distinguish both components since anchor points are chosen exclusively during increasing (or decreasing) events in the trigger signal [Figs. 4.15(d,e)].

However, while this concept does work as desired in examples similar to the illustrated one the performance strongly depends on the 'order' and 'density' of anchor points. In long datasets, where anchor points of opposite anchor criteria (signal increases and decreases) are strongly interwoven, oscillations coexisting with either criterion survive in the BPRSA averaging step because the surrounding width L will be larger than the distance to the next anchor of opposite criterion. Thus, each window and as a result the BPRSA will contain (quasi-)oscillations from both criteria. For that reason, when studying the baroreflex, oscillatory components associated with either blood pressure increase or blood pressure decrease can never successfully be distinguished by BPRSA since heartbeat and blood pressure signals oscillate at a similar frequency (each heartbeat is followed by a maximum – systole – in blood pressure). However, distinction is possible for RSA (heartbeat and respiration) on scales smaller than a respiratory cycle. Nevertheless, one might still benefit from such property in systems where events that one wants to separate are defined by more complicated anchor criteria other than simple increases and decreases in the trigger signal and which, hence, occur more rarely.

4.2.6. Example II: White Noises with Linear Relation

May $X = \{x_i\}$ and $\tilde{Y} = \{\tilde{y}_i\}$ denote two independent white noise signals with zero mean and unit variance. Based on \tilde{Y} the signal $Y = \{y_i\}$ is generated by introducing a linear unidirectional coupling with X in a certain frequency band. This is generated by calculating the linear combination of \tilde{Y} and one or more bandpass filtered components of X ,

$$y_i = \tilde{y}_i + \sum_j c_j \text{BP}_i^{(j)}(X). \quad (4.12)$$

The bandpass filtering is done in Fourier space, and $\text{BP}_i^{(j)}(X)$ denotes the i -th element of the series obtained from the related j -th bandpass filter operator acting on X . The prefactors c_j include the coupling strengths $|c_j|$ and directions $\text{sgn}(c_j)$. Finally, Y is normalized to obtain zero mean and unit variance. Fig. 4.16(a) illustrates the original noise X , while Figs. 4.16(b,c) show Y and Z for two different values of c_1 and $c_j = 0, \forall j > 1$.

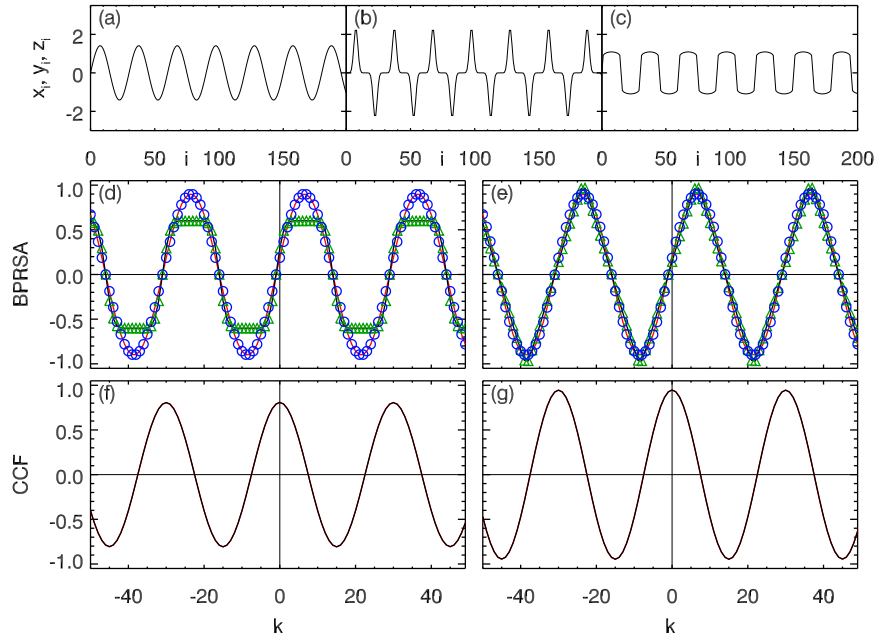


Figure 4.17.: (a) Sinusoidal signal X and nonlinearly coupled signals (b) Y and (c) Z according to Eq. (4.13). (d) $BPRSA_{X \rightarrow Y}$ [black solid lines], $BPRSA_{Y \rightarrow X}$ [red solid lines], $-BPRSA_{X \rightarrow Z}$ [green triangles], $-BPRSA_{Z \rightarrow X}$ [blue circles], (e) $BPRSA$ for Z instead of Y accordingly; panel (f) shows $CCF_{X,Y} = CCF_{Y,X}$ and (g) $CCF_{X,Z} = CCF_{Z,X}$ [black on red solid lines]

Different coupling strengths $|c_1|$ are reflected by different amplitudes of $BPRSA_{X \rightarrow \alpha}(k)$ and $\alpha = Y, Z$, while a different coupling direction results in a different sign of $BPRSA_{X \rightarrow \alpha}(k)$ [cp. Figs. 4.16(d,e)]. Since linear coupling is considered here, $BPRSA_{X \rightarrow \alpha}(k) = -BPRSA_{X \leftarrow \alpha}(k)$ as discussed in Sect. 4.2.3 and illustrated in Figs. 4.16(d,e). There is no advantage over $CCF_{X,Y}(k)$ which is a linear method and looks very similar in this example [not plotted].

4.2.7. Example III: Nonlinear Relation

The response of the BPRSA to nonlinearly coupled trigger and target signals strongly depends on the type of the coupling. The most simple nonlinear coupling is the absolute value. Let us assume a sinusoidal trigger signal X without noise and a target signal Y that only contains the absolute value of X , yielding a frequency doubling. When calculating the BPRSA all oscillations cancel out and $BPRSA_{X \rightarrow Y}(k) = BPRSA_{Y \rightarrow X}(k) = 0$. In the presence of additional $1/f$ -noise the BPRSA will basically show features of the noise and possibly finite size effects. The same holds for similar nonlinear coupling, e.g., raising to an even power. On the other hand, this elimination of higher harmonics might be an advantage if one wants to clarify a complex relationship between two unknown signals.

Now, we study nonlinear coupling without frequency doubling. Three simple oscillating series are defined by

$$x_i = \sin(2\pi fi), \quad y_i = (x_i)^9, \quad z_i = \text{sgn}(x_i) |x_i|^{1/9}. \quad (4.13)$$

and illustrated in Figs. 4.17(a-c). The large power of 9 has been chosen for visual reasons only; it enhances the differences as does the absence of noise. The cross-correlation analysis [see Figs. 4.17(f,g)] cannot distinguish (i) the cases $X \rightarrow Y$ and $X \rightarrow Z$ as well as (ii) both possible analysis directions. Studying only the cross-correlation function could thus lead to the false conclusion of equivalently related signals Y and Z . BPRSA, on the other hand, can clearly distinguish the four cases except for $BPRSA_{Y \rightarrow X}(k) = BPRSA_{Z \rightarrow X}(k)$. However, one has to keep in mind that the shape of the BPRSA curve needs not be the same as the original target signal [cp. Figs. 4.17(b,d)]. A presence of noise might disturb the BPRSA signal, making the identification of characteristics in trigger and target signal more difficult, depending on the signal to noise ratio.

4.2.8. Example IV: Influence of Trends in the Signal

Now let X and Y be two independent $1/f$ -noise signals with zero mean and unit variance generated by Fourier filtering. Furthermore, be a periodic component $A \sin(2\pi fi)$ incorporated in

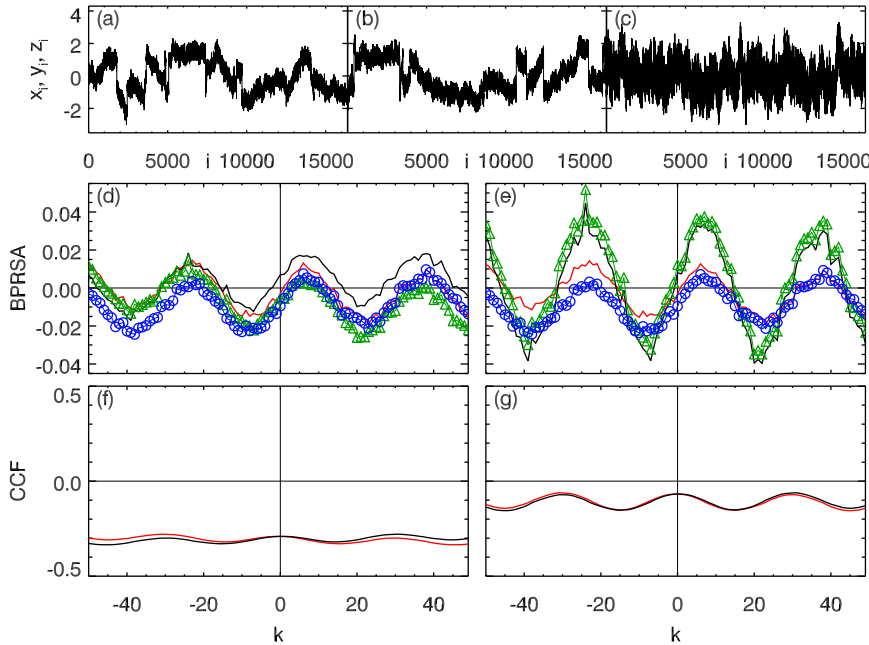


Figure 4.18.: Sinusoids with frequency $f = 1/30$, amplitude $A = 0.5$, and normalized additional $1/f$; length $N = 16384$. In (a,b), different partial trends of random offset, slope and duration were added; (c) is the same as (b) but without trends. (d) BPRSA results for Y : $\text{BPRSA}_{X \rightarrow Y}$ [black solid lines], $\text{BPRSA}_{Y \rightarrow X}$ [red solid lines], $-\text{BPRSA}_{X \rightarrow Y}$ [green triangles], $-\text{BPRSA}_{Y \rightarrow X}$ [blue circles]. (e) BPRSA for Z replacing Y accordingly. Panel (f) shows $\text{CCF}_{X,Y}$ [black], $\text{CCF}_{Y,X}$ [red] and (g) $\text{CCF}_{X,Z}$ [black], $\text{CCF}_{Z,X}$ [red] accordingly. The points are connected for visual reasons only; all values are dimensionless.

both signals. Additionally, non-stationarities are introduced by adding piecewise linear trends as follows: Start with some initial value for the slope a_1 and the initial offset a_0 . At random positions, the offset and the slope are changed randomly within a previously defined range; the trends added to X and Y are independent [see Figs. 4.18(a,b)]. For comparison a third signal Z that equals Y is defined without additional non-stationary trends [Fig. 4.18(c)].

Trends in the trigger signal will hardly affect the identification of the anchor points, because the anchor criteria defined in Eqs. (4.1) is only based on local fluctuations. Note, that this might be different when using a more sophisticated boolean anchor function as discussed earlier [compare BPRSA directions $Y \rightarrow X$ and $Z \rightarrow X$ in Fig. 4.18(d,e)].

On the other hand, the influence of trends in the target signal cannot be neglected [see Fig. 4.18(e)]. In case of a significant global trend in the target signal, e.g., more decreasing parts than increasing parts, the global trend will be present in the BPRSA curve, although it is diminished. Note, that due to trends which do not cancel out completely, $\text{BPRSA}_{X \rightarrow Y}(k) \neq -\text{BPRSA}_{Y \rightarrow X}(k)$ in general [compare solid lines and triangles in Figs. 4.18(d,e)]. When the BPRSA shows no trend at all, the target signal is either characterized by no trends or the duration and slopes of increasing and decreasing trends cancel out.

As an implication of the different influences of trends in the trigger and target signal one can identify which signal is disturbed by trends by comparing the BPRSA for opposite trigger-target directions ($X \rightarrow Y$, $Y \rightarrow X$). This is inherently impossible with cross-correlation analysis since the algorithm does not distinguish between both signals. Besides, trends are harmful for the definition of a global mean and thus disturb the standard cross-correlation analysis. Therefore, its results may suggest a wrong correlation behavior. In Figs. 4.18(f),(g) one finds, by chance, anti-correlated behavior although the signals themselves, i.e., the sinusoids, are strongly positively correlated. For the same reason a normalized BPRSA as defined in Eq. (4.9) cannot be applied here. Of course, in this simple example the use of the local cross-correlation function, which is based on local means rather than on a global mean, might help to remove the influence of the trends.

4.2.9. Towards a Multivariate Analysis

As I have mentioned in Sect. 4.2.1 it is possible to define more sophisticated anchor criteria compared to Eqs. (4.1) which includes more than one signal and promotes BPRSA to a multivariate variant. For instance, the typical behavior of a target signal Y can be studied around points in time (anchors) with increases of a *first trigger signal* X_1 and positive values of a *second trigger signal* X_2 . This defines a conditional anchor criterion in *Step 1* of the BPRSA algorithm. As a

specific example of such conditional anchor criterion consider the three signals heartbeat intervals, respiratory phase, and blood pressure describing component of the cardiovascular system. One could study characteristic heartbeat intervals (target signal Y) around increasing systolic blood pressure (first trigger signal X_1) coinciding with a certain respiratory phase such as inspiration (second trigger signal X_2).

When more than one trigger signal is involved in a BPRSA variant, I denote the method *multivariate phase rectified signal averaging (MPRSA)*. First attempts revealed promising results for the investigation of baroreflex properties, see also [BAUER *et al.* 2009].

The capabilities of MPRSA could, for instance, prove useful for verifying the respiratory gating theory which is still controversially discussed among medical doctors, for a review see [ECKBERG 2003]. Respiratory gating theory basically deals with the coupling between respiration, heartbeat, and baroreflex and claims that respiration modulates the latter two. While the coupling between respiration and heartbeat is known (and accepted) as respiratory sinus arrhythmia (RSA) [see Sect. 2.2.2], the coupling between baroreflex and respiration is not well understood. According to [ROTHLISBERGER *et al.* 2003] who studied the baroreflex during forced breathing and apnea²⁵ there is a 'strong temporal ordering' of spontaneous baroreflex sequences which reflects respiratory gating of sympathetic outflow. Rothlisberger *et al.* consider a parallel increase in blood pressure and RRI (acceleration of the heart) as an 'up' sequence which occurs shortly before and after onset of expiration, and a decrease in systolic blood pressure accompanied by a deceleration of the heart as 'down' sequence that occurs during late expiration and inspiration. In contrast, respiratory gating seems not to affect the gain of baroreflex oscillations (amplitude of influence) because they were found to be independent of breathing or apneas [ROTHLISBERGER *et al.* 2003]. However, the original studies only included a few short recordings (ten subjects, 3min spontaneous breathing, 3min apnea, and 2min hyperventilation) and the generality of both findings and gating theory should be tested in a larger database.

Further possible applications of PRSA methods in biology and physiology include rhythmic motions of limbs in walking, muscle contractions, rhythms underlying the release of hormones that regulate growth and metabolism, periodicities in gene expression, membrane potential oscillations, oscillations in neuronal signals, and circadian rhythms [TYSON 2002; GLASS 2001]. I believe that the range of suitable applications for the PRSA methods also include quasi-periodic geophysical data, e. g., data describing the El-Niño phenomenon, the activity of the sun, and ice age periods [VON STORCH AND ZWIERS 2001]. In addition, the analysis of complex elastic wave patterns to study seismic events or to determine material properties of granular matter might be improved by them. The study of non-stationary quasi-periodic complex waveforms is also a common task in the analysis and recognition of speech or music.

²⁵Here apnea is a deliberate interruption in breathing during wake and not related to sleep apnea.

5. Quantifying Interrelation by Synchronization Analysis Methods

Synchronization phenomena are a topic in physics with a long history dating back to Christian Huygens suffering from a sickness. While confined to bed he observed that two clocks on the wall tend to mutually synchronize after time even when started at different phases [HUYGENS 1673]. Although classical cross-correlations and cross-coherences can be thought of as a linear type of synchronization [QUIAN QUIROGA *et al.* 2002], most authors consider synchronization to be a nonlinear phenomenon. In the concept of Nonlinear Dynamics synchronization is understood as an adjustment of rhythms observed in oscillating objects (oscillators) due to a (sufficiently weak) interaction (coupling) [PIKOVSKY *et al.* 2001]. A typical property of such oscillators is that a small perturbation is followed by a transient process and after some time a restoration of the original rhythm. In theoretical nonlinear dynamics the common approach is to study model systems described by equations (deterministic or stochastic) and a known coupling. Time series analysis on the other hand is a somewhat complementary approach where the underlying system is mostly unknown and the aim is to extract the dynamics, coupling, and more importantly derive model equations by studying the output of the system.

In the introduction part we have seen how interrelation between time series can be defined employing linear (classical) 'synchronization' methods, i.e., cross-correlation analysis and cross-coherence analysis. The concept of cross-correlation has been further developed in a wider sense in Chapt. 4. While methods such as cross-correlation analysis still benefit from their simpleness, they are, unfortunately, rather unsuitable for studying physiological time series where nonstationarities are common, see Chapt. 4. In the context of signals from physiological sources, e.g., heartbeat, respiration, or the human electroencephalogram (EEG), nonlinear methods have proven to be helpful. In this chapter I will explore concepts of nonlinear synchronization analysis to quantify interrelation of multi-variate time series (at least two signals), apply them to sleep data from the SIESTA database [Sect. 2.3] and introduce a related method capable of studying interrelated amplitude and frequency signals in multivariate data. The latter method was coined *Cross-modulation analysis* in our paper [GANS *et al.* 2009] and we successfully applied cross-modulation analysis to study effects of Parkinson's disease on the coupling structure between different physiologically important oscillatory components in the brain during sleep [STUMPF *et al.* 2010].

5.1. Introduction to Synchronization Analysis

5.1.1. Concepts of Characterizing and Detecting Synchronization

Nonlinear synchronization analysis aims at understanding and quantifying nonlinear interrelations between nearly periodic signals. Such periodic signals can be imagined as emerging from the dynamics of a set of self-sustained oscillators each responsible for the generation of an oscillation with a certain frequency. Interrelated periodic signals could thus be modeled by introducing a certain coupling between two or even more such oscillators in the sense that the dynamics of one oscillator is to some extent plugged into the equations describing the dynamics of the other oscillator. Neglecting qualitative work already done by Huygens and his successors such coupled oscillators have been intensely studied in physics for over 40 years now, dating back to the pioneering work of Winfree who did an early simulation on populations of generalized relaxation oscillators (as meaningful for firing neurons) [WINFREE 1967], or Kuramoto who introduced the coupled oscillator model to biological and chemical systems [KURAMOTO 2003]. A nice popularly written review can be found in [STROGATZ AND STEWART 1993], in the revised book by Winfree

[WINFREE 2001], or more recently online [PIKOVSKY AND ROSENBLUM 2007].

Periodic self-sustained oscillators can theoretically be described in terms of a stable limit cycle of a nonlinear dynamical system whose dynamics is fully captured by combining all system relevant variables into a vector $\vec{x}(t)$ where $\dot{\vec{x}}(t) = f(\vec{x}(t))$ describes the dynamics [PIKOVSKY *et al.* 2001]. A periodic solution is then given by $\vec{x}_0(t) = \vec{x}_0(t + T_0)$ with period T_0 . The phase ϕ associated with an oscillator is then some coordinate along the limit cycle – in mathematics we say ϕ parametrizes the motion along a cycle. The phase ϕ monotonously increases with time along the cycle and gains a value of 2π per complete cycle. Hence, an angular frequency (natural frequency of the oscillation)

$$\frac{d\phi}{dt} = \omega_0 = \text{const.} = \frac{2\pi}{T_0} \quad (5.1)$$

can be defined.

When two self-sustained oscillators are bidirectionally coupled by some coupling functions Q_1 and Q_2 , their dynamics can be described by the following model equations

$$\begin{aligned} \dot{\phi}_1 &= \omega_1 + \epsilon Q_1(\phi_1, \phi_2) = \omega_1 + \epsilon \sum_{k,l} a_1^{k,l} e^{ik\phi_1 + il\phi_2} \\ \dot{\phi}_2 &= \omega_2 + \epsilon Q_2(\phi_1, \phi_2) = \omega_2 + \epsilon \sum_{k,l} a_2^{l,k} e^{il\phi_1 + ik\phi_2} \end{aligned} \quad (5.2)$$

where the last term is the Fourier series of the 2π periodic coupling function and ϵ is the coupling strength¹. Substituting the unperturbed case $\phi_{1,2} = \omega_{1,2}t$ in the sums it becomes obvious that most summands correspond to 'relatively fast' oscillations ($i \cdot \text{const} \cdot t$ in the exponent) except for the resonant case ($\text{const} \approx 0$, $l\omega_1 \approx -k\omega_2$) which could be described by a rational frequency ratio ($k = nj$; $l = -mj$; $n, m \in \mathbb{N}^+$)

$$n\omega_1 = m\omega_2 \quad (5.3)$$

and finally yields

$$\begin{aligned} \dot{\phi}_1 &= \omega_1 + \epsilon q_1(n\phi_1 - m\phi_2) \\ \dot{\phi}_2 &= \omega_2 + \epsilon q_2(m\phi_2 - n\phi_1) . \end{aligned} \quad (5.4)$$

The coupling functions $q_{1,2}$ simplify the Fourier sums which can be written as $q_1(\Delta\phi_{n,m}) = \sum_j a_1^{nj, -mj} \exp\{ij\Delta\phi_{n,m}\}$ and $q_2(-\Delta\phi_{n,m}) = \sum_j a_1^{mj, -nj} \exp\{-ij\Delta\phi_{n,m}\}$ by introducing the *generalized phase difference* or relative phase

$$\Delta\phi_{n,m} = n\phi_1 - m\phi_2 . \quad (5.5)$$

Inserting Eq. (5.5) in Eqs. (5.4) yields

$$\frac{d(\Delta\phi_{n,m})}{dt} = -(m\omega_2 - n\omega_1) + \epsilon q(\Delta\phi_{n,m}) , \quad (5.6)$$

where the leading term $m\omega_2 - n\omega_1$ denotes the *frequency detuning* (frequency mismatch) and measures the difference of the coupled oscillators. From studying the stability, i.e, finding solutions of $d(\Delta\phi_{n,m})/dt = 0$, one obtains a stable fix point for $\Delta\phi_{n,m} = \text{const.}$ Thus,

$$|n\phi_1 - m\phi_2| = \text{const.} \quad (5.7)$$

which is known as *phase locking* and, in the case of self-sustained coupled oscillators, immediately yields after differentiation the equivalent term

$$n\dot{\phi}_1 = m\dot{\phi}_2 \quad (5.8)$$

¹Some authors, e.g., Arkady Pikovsky, call it 'amplitude' which might be misleading in the following context where (instantaneous) amplitudes will refer to enveloping curves of oscillating signals determined by a Hilbert transform.

which is referred to as *frequency locking* or *frequency entrainment*. Real world oscillators, however, are constantly perturbed by external forces or influenced by noise resulting in a violation of the strict equality in Eqs. (5.7) and (5.8).

$$|\Delta\phi_{n,m}| = |n\phi_1 - m\phi_2| < \text{const} = |n\phi_1 - m\phi_2 - \delta(t)| \quad n\dot{\phi}_1 \approx m\dot{\phi}_2 \quad (5.9)$$

The noise induced perturbation $\delta(t)$ causes the generalized phase difference to fluctuate around the unperturbed phase difference. Hence, the frequencies $\dot{\phi}_{1,2}$ have to be substituted by expectation values $\Omega_{1,2} = \langle \dot{\phi}_{1,2} \rangle$, i.e., the mean frequencies observed over time. Unfortunately, due to the (time) averaging $n\Omega_1 = m\Omega_2$ might be satisfied by chance even for uncoupled oscillators. Therefore, the unrestricted application of Eq. (5.8) is not longer possible and studying *phase synchronization* or more precisely *phase locking* has become more popular in practice.

The advantage of phase synchronized systems is obvious in the presence of noise where the naturally noise-induced phase diffusion, i.e., phase fluctuations around a stable fix point in a potential yielding non-constant periods of oscillation [PIKOVSKY *et al.* 2001], is significantly reduced in synchronized states. However, phase slips, although reduced in their occurrence, can still occur. Note that the phases $\phi_{1,2}$ are not cyclic in $[0, 2\pi]$ but can take any value in \mathbb{R} . For practicality reasons one often maps the generalized phase difference into the interval $[0, 2\pi]$ and studies the distribution of the *cyclic relative phase differences*,

$$\Delta\Psi_{n,m}(t) = \Delta\phi_{n,m}(t) \bmod 2\pi. \quad (5.10)$$

This distribution shows a peak in the case of phase locking in a statistical sense, see also Fig. 5.1(b,c). It is important to note that signal amplitudes might be uncorrelated while phase-locking takes place. Linear synchronization analysis methods, which do not study phase interrelation but the pure signals, might overlook the synchronization.

Descriptive Meaning of the Integers n , m

So far the integers n and m were a rather technical asset to describe the frequency ratio in the resonant case, recall Eq. (5.3). Before, I discuss how phases φ are defined for real data it might be helpful to establish some understanding of n and m as it will occur in the latter application in Sects. 5.2 and 5.3. Consider the cardiorespiratory system [Sect. 2.2] and its most prominent signals heartbeat and oronasal airflow (a respiration proxy). As was discussed earlier the human heart beats approximately four times per breath (1x inspiration + 1x expiration)² – heartbeat is approximately four times faster than respiration. Hence, the phase associated with heartbeat (φ_2) grows four times faster than the phase of respiration (φ_1), i.e., while heartbeat evolves along cumulative phases from 0 to $4 \cdot 2\pi = 8\pi$ airflow only passes through phases from 0 to 2π . Thus, when studying their mutual interdependence (later, in particular, phase synchronization) one has to take this ratio $n : m = 4 : 1$ into account, that is, the respiratory phase has to be multiplied by 4 to be comparable with the phase of heartbeat ($4\varphi_1 = 1\varphi_2$). In this example phase-locking is reached when the condition $|\Delta\varphi_{4,1}| = |4\varphi_1 - 1\varphi_2| < \text{const}$ [Eq. (5.9)] is satisfied. Equivalently, the frequency of heartbeat (ω_2) is 4 times larger than for respiration (ω_1) yielding $4\omega_1 = 1\omega_2$ for the corresponding frequency locking condition in Eq. (5.9).

5.1.2. Defining Instantaneous Amplitudes, Phases, and Frequencies

Studying synchronization in the following will refer to studying signals in the phase locking regime according to the first part of Eq. (5.9). Since the approach discussed here is not based on some known model whose dynamics should be studied but rather focuses on the dynamics captured by observation, i.e., by measuring time series, the first step in an analysis is dedicated to the definition of phases for such discrete signals.

²Note, this is an approximation only used for illustration. Of course the correct cardiorespiratory 'timing' strongly depends on the medical and physiological state of the individual, i.e., sleep vs. awake, rest vs. exercise, healthy vs. diseased, speaking vs. quiet, calm vs. scared, and many others. The distribution among different ratios during sleep is studied in Sect. 5.2.6, see also Fig. 5.11 for an overview.

General Approach and Point processes

Consider a stable periodic oscillation whose instantaneous phase can then be expressed by the instantaneous angular velocity $\nu(\theta) = d\theta/dt$ via the integral transformation

$$\phi = \omega_0 \int_0^\theta [\nu(\theta)]^{-1} d\theta \quad (5.11)$$

where θ is in general a non-uniformly rotating 2π periodic angular variable and $\omega_0 = 2\pi/T$ is the frequency of the self-sustained oscillation. Note, that in this definition non-uniformly means the rotation can locally be described by any arbitrary angular velocity. The important characteristics of the phase are monotonousness and a 2π gain per cycle but not necessarily a constant instantaneous gain.

For real world data, however, the instantaneous velocities $\nu(\theta)$ are usually unknown for at least some time increments and thus the phase definition in Eq. (5.11) cannot be applied. For point processes such as pulse trains (spike trains) or heartbeat (in the sense of beat positions) one might estimate the phases locally by linear interpolation. Under the assumption that during the time interval $[t_k, t_{k+1}]$, for instance associated with the time interval between the k -th and $(k+1)$ -th heartbeat, a phase gain of 2π is generated it follows from the point-direction equation of linear functions for any time $t : t_k \leq t \leq t_{k+1}$

$$\phi(t) = 2\pi \frac{t - t_k}{t_{k+1} - t_k} + 2\pi k . \quad (5.12)$$

Continuous and Evenly Discretized Signals

Most physiological signals, although discretely sampled, as for instance respiration or the human electroencephalogram (EEG), are not point processes and thus a different concept is needed. When thinking about phases of continuous signals one immediately remembers the canonical solutions of the wave equation³ being plane waves, $\Psi(x, t) = A(t)e^{i(kx - \omega t)}$ where $\varphi(t) = (kx - \omega t)$ is the instantaneous phase.

If an arbitrary⁴ signal can be complemented in such way that it produces a similar expression, it is straightforward to define instantaneous phases and instantaneous amplitudes for the signal. The solution of the problem dates back to Gabor [GABOR 1946] who introduced the Hilbert transform, originally invented by David Hilbert in 1905 during his work on analytical functions, to signal analysis.

The basic idea is to complement an arbitrary real valued signal $x(t)$ (discretization yields a time series) by its imaginary counterpart $i\tilde{x}_H(t)$ to obtain an analytic signal $\check{x}(t)$. The latter allows for the definition of an *instantaneous amplitude* $A(t)$ and an *instantaneous phase* $\varphi(t)$.

$$\check{x} = x(t) + i\tilde{x}_H(t) = A(t)e^{i\varphi(t)} \quad (5.13)$$

The imaginary part of Eq. (5.13) is conveniently given by the Hilbert transform being the convolution of the real signal $x(t)$ with the function $1/(\pi t)$:

$$(\mathcal{H}x)(t) = \tilde{x}_H(t) = \frac{1}{\pi} \text{P.V.} \int_{-\infty}^{+\infty} \frac{x(t')}{t - t'} dt' \quad (5.14)$$

where P.V. denotes the Cauchy principal value. For discrete time series solving Eq. (5.14) is often not straightforward, however, from the convolution theorem it follows that

$$\begin{aligned} \mathcal{F}\left((\mathcal{H}x)(t)\right) &= \mathcal{F}\left(\tilde{x}_H(t)\right) = \mathcal{F}\left(x(t)\right)\mathcal{F}\left(\frac{1}{\pi t}\right) = \mathcal{F}\left(x(t)\right)(-i\text{sgn}(\nu)) \\ \tilde{x}_H(t) &= \mathcal{F}^{-1}\left(-i\text{sgn}(\nu)\mathcal{F}\left(x(t)\right)(\nu)\right)(t) \end{aligned} \quad (5.15)$$

³You might also think of the Schrödinger equation of a free particle $i\hbar \frac{\partial}{\partial t} \psi(\mathbf{r}, t) = H\psi(t)$ with $H = -\frac{\hbar^2}{2m} \Delta + V(\mathbf{r}, t)$ and $V(\mathbf{r}, t) = 0$ which then takes the form of the wave equation.

⁴This is not quite correctly formulated since the analytical completion algorithm presented in the following requires the signal to fulfill two prerequisites: (i) a narrow-banded power spectrum, and (ii) the signal must fluctuate around zero. Here, I understand 'arbitrary' in this sense.

where $\mathcal{F}(g(x)) = \hat{g}(\nu) = \int_{-\infty}^{\infty} g(x)e^{-2\pi i\nu x} dx$ indicates the forward Fourier transform⁵ and $\mathcal{F}^{-1}(\hat{g}(\nu)) = g(x) = \int_{-\infty}^{\infty} \hat{g}(\nu)e^{+2\pi i\nu x} d\nu$ is the inverse (backward) Fourier transform, ν denotes the frequency, and $\text{sgn}(\nu)$ is the signum function. Note the negative sign in front of the signum function⁶. Some authors tend to define the Fourier transform in a different way, yielding a positive sign or even an additional prefactor. Nevertheless, $\tilde{x}_H(t)$ can conveniently be calculated by transforming the signal to Fourier space, multiplying the result by $-i\text{sgn}(\nu)$, and transforming it back to time domain.

Having obtained an analytical signal according to Eq. (5.13) the *instantaneous amplitude* signal $A(t)$ and the *instantaneous phase* signal $\varphi(t)$ can be derived. Based on the latter one might define the *instantaneous frequency* signal $f(t)$ as the time derivative of the instantaneous phases which must not be confused with the frequency ν from the Fourier transform.

$$A(t) = \sqrt{x^2(t) + \tilde{x}_H^2(t)} \quad , \quad \varphi(t) = \text{atan2}(\tilde{x}_H(t), x(t)) \quad , \quad (5.16)$$

$$f(t) = \frac{d\varphi(t)}{dt} = \lim_{\Delta t \rightarrow 0} \frac{\varphi(t) - \varphi(t + \Delta t)}{\Delta t}$$

Note the `atan2` function⁷ in the definition of $\varphi(t)$. It implements an additional sign logic compared to the standard $\arctan(\tilde{x}_H(t)/x(t))$ function in order to obtain phase values $-\pi < \varphi \leq \pi$ rather than $-\pi/2 < \varphi \leq \pi/2$.

After introducing the basic concepts of calculating instantaneous amplitudes, phases, and frequencies from a continuous analytical signal approach we have to discretize the formulas in order to deal with time series. Therefore, the fast Fourier transform (FFT) substitutes the continuous FT, and Eqs. (5.16) become

$$A_k = \sqrt{x_k^2 + \tilde{x}_{H,k}^2} \quad , \quad \varphi_k = \text{atan2}(\tilde{x}_{H,k}, x_k) \quad , \quad f_k = \frac{\varphi_k - \varphi_{k+1}}{\Delta t} \quad (5.17)$$

where the index k indicates discrete times $t_k, k = 1, \dots, N$ and Δt now has the meaning of the sampling. The algorithm can be further simplified by realizing that the multiplier $-i\text{sgn}(\nu)$ means that negative frequencies have to be multiplied by a factor of $+i = \exp\{i\pi/2\}$, i.e., phases are shifted by $+\pi/2$, and positive frequencies by a factor of $-i = \exp\{+i\pi/2\}$, i.e., phases are shifted by $-\pi/2$. Thus, the Hilbert transform can easily be obtained by swapping real- and imaginary parts after the forward FFT and negating the real part for negative frequencies and the imaginary part for positive frequencies⁸. Further, note that time series are in general real valued sequences and thus the discrete Fourier transform satisfies a Hermitian redundancy, meaning $\mathcal{F}(x)(\nu) = \overline{\mathcal{F}(x)(N - \nu)}$ where N is the number of elements in the series and $\overline{\quad}$ denotes the complex conjugate. Thus, calculation can be further simplified. Modern FFT algorithms as `fftw` take advantage of this property [Frigo *et al.* 2003].

Although, Eqs. 5.17 can in principle be calculated without limitation, the Hilbert transform in Eq. 5.14 requires input signals with (i) a narrow frequency band width and (ii) oscillations around zero in order to result in meaningful complements, i.e., in meaningful instantaneous amplitudes,

⁵I employ the unitary ordinary frequency definition of the Fourier transform which requires no normalization factor for simplification.

⁶Here I use $\mathcal{F}(1/(\pi t)) = 1/\pi \text{ P.V.} \int_{-\infty}^{\infty} \frac{e^{-2\pi i\nu t}}{t} dt$ which can be solved straightforwardly by the residue theorem from complex analysis $\oint_{\mathcal{C}} g(z) dz = 2\pi i \sum_{k=1}^n \text{Res}_{a_k}(g)$ with $\text{Res}_{a_k}(g)$ the k th residue of g at the position a_k and the sum over all n residues within the closed curve \mathcal{C} . Now, the closed loop can be generalized for integrals of the type $\int_{-\infty}^{\infty}$, and in our case the residual lies on the real axis ($a_1 = 0$), thus contributing only half per residual. In addition the direction of the curve matters, i.e., $\text{P.V.} \int_{-\infty}^{\infty} g(z)e^{iz} dz = +\pi i \sum_{k=1}^n \text{Res}_{a_k}(g)$ and $\text{P.V.} \int_{-\infty}^{\infty} g(z)e^{-iz} dz = -\pi i \sum_{k=1}^n \text{Res}_{a_k}(g)$ yielding $\mathcal{F}(1/(\pi t)) = 1/\pi \text{ P.V.} \int_{-\infty}^{\infty} \frac{e^{-2\pi i\nu t}}{t} dt = \{-i : \forall \nu > 0, +i : \forall \nu < 0, 0 : \nu = 0\} = -i\text{sgn}(\nu)$ since the frequency ν can take both positive and negative values. The author explicitly warns of sloppy use of signs in the literature! When the Fourier transform is defined as in this thesis (“-” in the exponential for the forward direction and “+” for the backward direction) the signum function must get a negative sign.

⁷The function `atan2` is available in most programming languages.

⁸ $\nu < 0$: $+iz = \exp\{i(\varphi + \pi/2)\} = \cos(\varphi + \pi/2) + i \sin(\varphi + \pi/2) = -\sin \varphi + i \cos \varphi = -\mathfrak{I}\mathfrak{m}(z) + i\mathfrak{R}\mathfrak{e}(z)$
 $\nu > 0$: $-iz = \exp\{i(\varphi - \pi/2)\} = \cos(\varphi - \pi/2) + i \sin(\varphi - \pi/2) = \sin \varphi - i \cos \varphi = \mathfrak{I}\mathfrak{m}(z) - i\mathfrak{R}\mathfrak{e}(z)$

phases, and frequencies. When these two prerequisites are not fulfilled, obtained amplitudes are, for instance, not enveloping the input signal x_k . For an extended discussion on Hilbert transform see [BOASHASH 1992].

An important issue that has to be considered when employing the analytical completion algorithm is that the Hilbert transform assumes signals to be sinusoidal which might not always be the case. For example human gait time series resemble rectangular functions characterized by abruptly decaying flanks where only the top part is of sinusoidal shape (see Fig. 1(a) in [BARTSCH *et al.* 2007] for an example). In such cases a wavelet based approach where the analyzing wavelet is chosen according to the typical pattern is better suited. Note, in [BARTSCH *et al.* 2007] consecutive heel strikes (and toe offs) of the left and right foot are considered as a point process and phases are defined in a similar way as presented in Eq. (5.12).

Wavelet Based Phases

Based on the wavelet coefficients obtained from the convolution of the signal $x(t)$ and a translated and dilated mother wavelet Ψ capturing the 'typical pattern' [$WT_\Psi(s, t) = x(t) * \overline{\Psi(t/s)}$; see also Sect. 1.3] both instantaneous phases and instantaneous amplitudes can be defined analogously to the presented Fourier (Hilbert) approach for a given scale s

$$WT_\Psi(s, t) = A(s, t)e^{i\varphi(s, t)}. \quad (5.18)$$

Since all signals studied in this thesis are rather sinusoidal or point processes this approach will not further be investigated.

5.1.3. Quantifying Mutual Synchronization

When the essential quantities such as instantaneous phases and instantaneous amplitudes (not for point processes) have been defined for bivariate (or even multivariate) data, their mutual interaction has to be quantified. Several methods have been suggested during the last decade. For example Paluš introduced the mutual information to phase-synchronization analysis, where $I(\varphi_1, \varphi_2) = \int_{-\pi}^{\pi} \int_{-\pi}^{\pi} p_{1,2}(\varphi_1, \varphi_2) \log\{p_{1,2}(\varphi_1, \varphi_2)/(p_1(\varphi_1)p_2(\varphi_2))\} d\varphi_1 d\varphi_2$ vanishes in the absence of phase synchronization and is positive otherwise (p_1, p_2 probability distributions of phases φ_1, φ_2 and $p_{1,2}$ is there joint-probability distribution) [PALUŠ 1997]. The concept of information theory was also adapted by Tass in his measure ρ utilizing the Shannon entropy [see below]. He additionally suggested a conditional measure λ based on a stroboscopic approach where the phase of the second oscillator is observed at times where the phase of the first oscillator has a fixed value (phase stroboscope = look at φ_2 when φ_1 is fixed), $\lambda = \langle \varphi_2 \bmod 2\pi n | \varphi_1 \bmod 2\pi m = \theta \rangle_{0 \leq \theta < 2\pi}$ [TASS *et al.* 1998]. It has been suggested quantifying horizontal episodes in cardiorespiratory synchrograms (cyclic phase $\Psi_m(t) = \varphi(t) \bmod 2\pi m$ at discrete incidences t_i plotted vs. t_i [SCHÄFER *et al.* 1998, 1999, see also Sect. 5.2]. They indicate synchronized segments compared to non-synchronized episodes where phase differences are not stable over a certain time [TOLEDO *et al.* 1999]. Phase synchronization in a stochastic sense was studied by Neiman [NEIMAN *et al.* 1999] who considered excitable media, i.e., the FitzHugh-Nagumo equations⁹ modeling neuron-firing activity, and derived the cross-diffusion coefficient describing the spreading in time of an initially localized phase-differences distribution. If the diffusion coefficient decays constantly phase locking appears (see [ANISHCHENKO *et al.* 2000] for an application to heartbeat synchronized by external stimuli such as sound or light). Finally, Rosenblum showed that phase synchronization might also be studied by calculating the first Fourier mode of the cyclic phase differences $\gamma_{n,m} = (\langle \cos \Delta\Psi_{n,m} \rangle_t^2 + \langle \sin \Delta\Psi_{n,m} \rangle_t^2)^{1/2}$ which becomes 1 in the case of perfect phase synchronization and is 0 in the absence of synchronization [ROSENBLUM *et al.* 2001].

In the following I will introduce in more detail three of the mentioned quantification approaches which became most popular in research, i.e., the Shannon entropy based index ρ , the Fourier

⁹Originally termed 'Bonhoeffer-van der Pole model' by FitzHugh the FitzHugh-Nagumo model is a favorite model for reaction-diffusion systems used to simulate electrically excitable media such as heart tissue [IZHIKEVICH AND FITZHUGH 2006]. Model equations follow (i) $\dot{V} = f(V) - W + I + \partial^2 V / \partial x^2$, (ii) $\dot{W} = a(bV - cW)$ where V is a 'voltage-like variable' capturing regenerative self-excitation via a positive feedback loop, W is a 'recovery variable' tuning a slower negative feedback, I is the injected current, and a, b, c are parameters for tuning.

mode index γ , and the synchrogram method. In addition I will demonstrate based on the SIESTA data, an automatism that allows for conveniently studying synchrograms for large databases. It goes beyond and (in our experience) performs better than an alternative suggestion of Toledo in [TOLEDO *et al.* 1999].

Entropy Based Synchronization Index

As has been motivated in the previous section phase locking takes place when the cyclic relative phase difference's ($\Delta\Psi_{n,m}$) distribution is peaked, see Eq. (5.10) and associated discussion. Hence, synchronization strength can be studied by plotting $\Delta\Psi_{n,m}$ histograms and identifying and quantifying possible clusters. When such a cluster of phase differences follows, e.g., a Gaussian distribution, the signals under investigation exhibit a certain dominating phase relationship most of the time [cf. Fig. 5.1(b)]. On the contrary, $\Delta\Psi_{n,m}$ might vary completely random (uniformly distributed) resulting in a flat histogram non-synchronized signals, see Fig. 5.1(a). While such qualitative evaluation of synchronization might be helpful as a first approach or for a limited number of data it is rather unsatisfying for large datasets as typically occur in sleep studies or other long-term recordings. Examples are found in human brain wave recordings, heartbeat, and respiration.

In order to quantify the strength of mutual synchronization between two signals of interest by a single synchronization index ρ , Tass suggested a measure based on the Shannon entropy in the framework of a nonidentical Rössler system¹⁰ and tested it at magnetoencephalograms (MEG) and records of muscle activity (EMG) of a subject suffering from Parkinson disease [TASS *et al.* 1998]. In a first step a cyclic relative phase difference $\Delta\Psi_{n,m}(t_k)$ between two instances, whose mutual synchronization one is interested in, is obtained for each discrete time t_k , $k = 1, \dots, N$. Then the distribution of $\Delta\Psi_{n,m}(t_k)$ is depicted in a histogram of M bins with a bin width of $b = 2\pi/M$, [see Fig. 5.1(a-c) for an illustration]. Considering p_l as the probability of the l -th bin one can derive the Shannon entropy¹¹ [SHANNON AND WEAVER 1949] by

$$S = - \sum_{l=1}^M p_l \ln p_l . \quad (5.19)$$

If the differences $\Delta\Psi_{n,m}$ are, in the simplest case, uniformly distributed the bin probabilities satisfy $p_l = 1/M$; $\forall l$ yielding a maximal Shannon entropy

$$S_{\max} = - \ln \frac{1}{M} \quad (5.20)$$

and both signals are not phase synchronized, see Fig. 5.1(a). In the other limit a perfect synchronization is expressed by a quasi-delta peaked histogram, i.e., ideally only one bin is characterized by a probability different from zero ($\exists l' : p_{l'} = 1 \wedge p_l = 0 \forall l \neq l'$; [Fig. 5.1(c)]), yielding

$$S_{\min} = 0 . \quad (5.21)$$

Hence, a suitable index to quantify the strength of phase synchronization based on the histogram of $\Delta\Psi_{n,m}$ is [TASS *et al.* 1998]

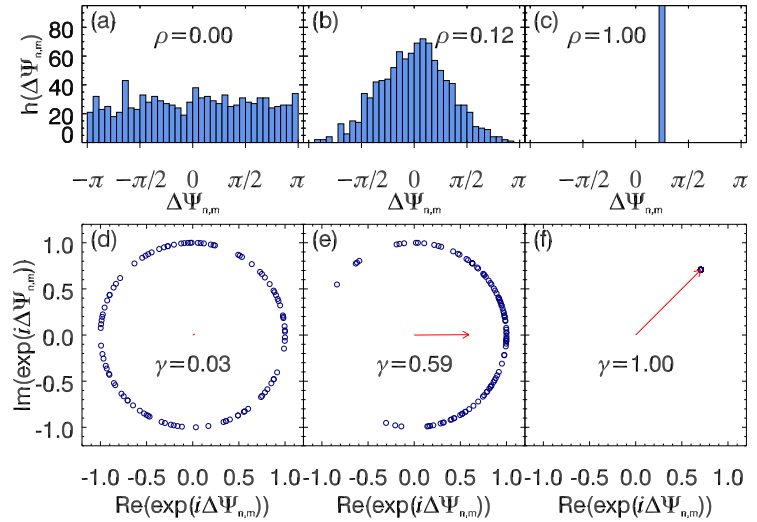
$$\rho_{n,m} = \frac{S_{\max} - S}{S_{\max}} . \quad (5.22)$$

Obviously, $\rho_{n,m} \approx 0$ for the independent, i.e., non-synchronized case with $S \approx S_{\max}$ and $\rho_{n,m} \approx 1$ for the perfect phase synchronization $S \approx S_{\min}$. Here I use the symbol “ \approx ” instead of the

¹⁰Two coupled Rössler oscillators in 3d as considered in [TASS *et al.* 1998] follow: $\dot{x}_{1,2} = -\omega_{1,2}y_{1,2} - z_{1,2} + \xi_{1,2} + \epsilon(x_{2,1} - x_{1,2})$, $\dot{y}_{1,2} = \omega_{1,2}x_{1,2} + 0.15y_{1,2}$, and $\dot{z}_{1,2} = 0.2 + z_{1,2}(x_{1,2} - 10)$ with $\omega_{1,2} = 1 \pm 0,015$ and $\xi_{1,2}$ denotes Gaussian noise with pair correlation $\langle \xi_i(t)\xi_j(t') \rangle = 2D\delta(t-t')\delta_{i,j}$ where δ is the Kronecker symbol and D is a constant to tune the noise amplitude.

¹¹Note, the Shannon entropy is a special case ($q = 1$) of the Rényi entropy (a generalized box counting) $H_q(s) = \frac{1}{1-q} \ln \sum_{l=1}^{N(s)} p_l^q$ of an observable \mathbf{x} where $q \geq 0$ and only boxes B_l with a positive measure $p_l = \mu(B_l) = \int_{B_l} d\mu(\mathbf{x}) > 0$ are contributing [RÉNYI 1961]. The 'boxes' B_l with a side length $s \rightarrow 0$ might thus be disjoint, i.e., the covering might have 'holes'. Employing the rule of l'Hospital it follows: $\lim_{q \rightarrow 1} H_q = - \lim_{q \rightarrow 1} \left\{ \frac{\sum_{l=1}^{N(s)} p_l^q \ln p_l}{\sum_{l=1}^{N(s)} p_l^q} \right\} = - \sum_{l=1}^{N(s)} p_l \ln p_l = H_1 = S$ having used $\sum_{l=1}^{N(s)} p_k = 1$.

Figure 5.1.: Quantification of synchronization based on the cyclic phase difference $\Delta\Psi_{n,m}$. Synchronization indexes ρ (a-c) and γ (d-f) are shown for three illustrative examples: phase differences are uniformly distributed [no synchronization, (a,d)], Gaussian distributed [notedly synchronized, (b,e)], and delta peaked [perfect synchronization, (c,f)]. For each example $N=1000$ phase differences were generated. Lower panels show phases mapped into the complex plane and red arrows illustrate their complex average which length corresponds to the synchronization index γ . Although, γ was obtained from all $\Delta\Psi_{n,m}$ only every 10-th difference is plotted in (d-f) for clarity.



theoretical “=” to make clear that in the application both limits are not exactly obtained due to a limited bin width and/or numerical issues introduced by the Hilbert transform. Moreover, note that the choice of the bin width b generally must be adapted by a trial and error approach. For an unknown dataset it might not be always determined which bin width (or which number of bins) is optimal. Usually, one optimizes b so that enough elements fall into each bin while the overall distribution shape is preserved. Thus, the Shannon entropy based synchronization index $\rho_{n,m}$ is not parameter free. In a sense, ρ can be thought of as characterizing the deviation of the relative phase distribution from a uniform distribution.

Intensity of the First Fourier Mode

Maybe the most prominent index to quantify the strength of phase synchronization between two signals is based on studying the intensity of the first Fourier mode of the cyclic relative phase difference $\Delta\Psi_{n,m}$, see Eq. (5.10) [ROSENBLUM *et al.* 2001]

$$\gamma_{n,m}(t) = \sqrt{\langle (\cos \Delta\Psi_{n,m}(t)) \rangle^2 + \langle (\sin \Delta\Psi_{n,m}(t)) \rangle^2} = |\langle e^{i\Delta\Psi_{n,m}} \rangle| \quad (5.23)$$

where the second expression immediately follows from recalling the Euler formula for complex numbers. Thus, the synchronization index γ is the complex average of the cyclic phase difference and its derivation can be visualized in the complex plane as depicted in Fig. 5.1(d-f). When the phase differences are uniformly distributed, i.e., the signals are not phase synchronized, they cover the unit circle uniformly, and thus, their average is $\gamma = 0$ except for stochastic deviations due to a limited dataset [Fig. 5.1(d)]. In the case of a delta-peaked distribution (perfect synchronization) all points merge in the associated complex representation yielding $\gamma = 1$ [Fig. 5.1(f)]. In general $0 \leq \gamma \leq 1$. For a clearly peaked (monomodal) distribution a cluster point exists on the unit circle and a ‘large’ value of $\gamma < 1$ indicates synchronous behavior. Since noise always affects data measured from complex systems the latter case is generally found in the presence of phase-synchronization, see also Figs. 5.1(b,e) for a normally-distributed example.

Note that calculating γ is parameter free, i.e., no number of bins has to be optimized and hence γ is especially suited for automation compared with ρ in Eq. (5.22). However, γ bears a possible pitfall in the case of a bimodal (or multimodal) phase-difference distribution where many contributions might cancel out on the unit circle yielding a small or even vanishing value of γ although the signals are still somewhat synchronized. For instance, assume a bimodal-delta-peaked $\Delta\Psi_{n,m}$ distribution where $\Delta\Psi_{n,m}$ is either $\pi/4$ or $5\pi/4$ and both groups have equal weight. Then all components would cancel out in the average yielding $\gamma = 0$. When different parts of such signal are characterized by a different phase difference this can easily be avoided by studying the time average in Eq. (5.23) for different parts of the signal, separately. In general, plotting phase difference distributions is recommended to get some impression about the behavior before an automation and application to a large database as available from sleep laboratories.

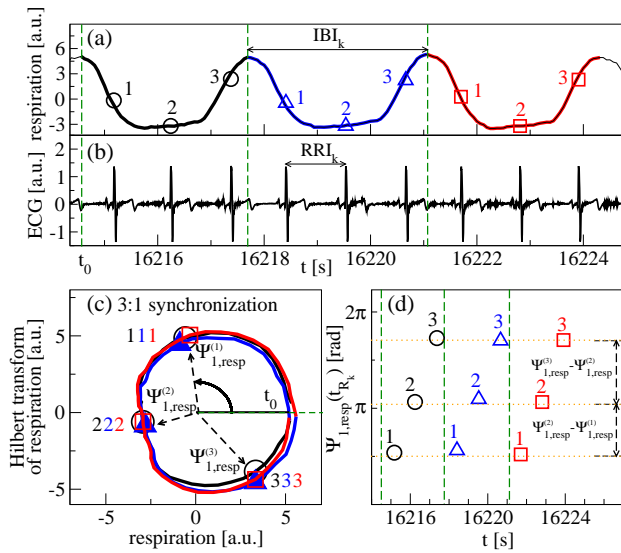


Figure 5.2.: Synchrogram method: (a,b) Three consecutive breathing cycles [colors black, blue, red] are shown above a simultaneously recorded ECG signal. The inter-breath-interval [IBI] is approximately 3 times longer than the beat-to-beat interval [RR]. For respiration [continuous signal] the instantaneous phase is calculated by a Hilbert transform [HT; Eq. (5.14)] and integrated to obtain a cumulative phase signal $\phi_{resp}(t) \in \mathbb{R}^+$ [see text]. (c) Respiration plotted versus its HT; each breath cycle appears as a circle [same colors as in (a)]; the cyclic respiratory phases [for $m = 1$] $\Psi_{1,resp}(t)$ manifest as angles. (d) At the time of each heartbeat $\Psi_{1,resp}(t_{R_k})$ is obtained and plotted versus t_{R_k} . The formation of three parallel horizontal lines [yellow dotted lines] implies 3 : 1 phase synchronization in this example. Green vertical dashed lines indicate the beginning of each breath cycle in (a-d).

Synchrogram Method

The synchrogram method introduced by Schäfer in the framework of studying cardiorespiratory synchronization [SCHÄFER *et al.* 1998, 1999] is a stroboscopic method that aims at exploring $n : m$ phase synchronization between two oscillators where one oscillator is described by a continuous¹² signal and the second signal is a point process. The point process is understood as a sequence of discrete time points t_k with $k = 1, \dots, N$.

As an example consider the cardiorespiratory system where respiration is the continuous signal and heartbeat is point process described by the R-peak positions at times t_{R_k} , see Fig. 5.2(a,b). Now, the idea behind synchrogram analysis is to study the phase of the continuous signal at time positions t_k defined by the point process. “The continuous signal is stroboscopically illuminated at incidents of a second signal that are described by the point process. In my example this means we study the phase of respiration at times t_{R_k} of heart beats. When two oscillators are phase synchronized Eq. (5.9) is satisfied.

Let $\Phi_2(t) = \Phi_{point}(t) \in \mathbb{R}^+$ be the cumulative phase¹³ of the point process and $\Phi_1(t) = \Phi_{continuous}(t) \in \mathbb{R}^+$ is the cumulative phase of the continuous signal in the phase locking condition defined in Eq. (5.9). However, in the application we often calculate *instantaneous* phases $\varphi_{continuous}(t)$ via a Hilbert transform [Eqs. (5.14), (5.17)] and $-\pi < \varphi_{continuous}(t) \leq \pi$ which must not be confused with $\Phi_{continuous}(t)$. In order to study arbitrary ratios $n : m$ according to Eq. (5.9) we require the cumulative phase $\Phi_{continuous}(t)$. Before we can integrate the instantaneous phases we must map them to the interval $[0, 2\pi)$ by adding 2π to negative values.

After calculating $\Phi_{continuous}(t)$ we obtain the cyclic phase¹⁴

$$\Psi_{m,continuous}(t) = \Phi_{continuous}(t) \bmod 2\pi m, \quad (5.24)$$

i. e., $\Phi_{continuous}$ mapped into the interval $[0, 2\pi m)$. Note that we have generated a phase signal with a period of m adjacent cycles from the original signal. In the next step the phases $\Psi_{m,continuous}(t)$ are examined at the times t_k associated with the point process. In our example this means we obtain $\Psi_{m,respiration}(t_{R_k})$ [marked by symbols in Fig. 5.2(a)]. Finally the values $\Psi_{m,continuous}(t_k)$ are plotted versus t_k to obtain the synchrogram, see Fig. 5.2(d) for a short fragment spanning only 3 breath cycles or 6 heart beats. In the presence of $n : m$ phase synchronization n parallel horizontal lines are observed. When the point process and the continuous signal do not synchronize, points in the synchrogram do not align in parallel lines. For a longer synchrogram episode see Fig. 5.6 which is based on an improved synchrogram method that is discussed in the following.

¹²Note that in practice such continuous signal, e. g. respiration, is indeed sampled. In the following I use the term ‘continuous’ for signals that were sampled with a sampling rate much higher than the features under investigation.

¹³Here indicated by Φ instead of ϕ in Eq. (5.9) to indicate that it is a sampled quantity and not a continuous one.

¹⁴Note the single subscript m in Ψ_m being not a difference compared with $\Delta\Psi_{n,m}$ that obeys two indexes n, m [Eq. (5.10)]. Most authors do not put a Δ to indicate phase differences; this is done in this thesis for clarity.

5.2. Automated Synchrogram Analysis

Although, the synchrogram method has proven to be very powerful in a variety of applications, e.g., in studying cardiorespiratory synchronization [SCHÄFER *et al.* 1998, 1999; WU AND HU 2006], the synchronization of heartbeat and music [KUSUNOKI *et al.* 2003], or cardio-locomotion coupling [GILAD *et al.* 2003], it was only applied to a relatively limited data source. Most publications deal with just a few (< 10) very short datasets (some seconds to some minutes). In large databases containing many multivariate, and long recordings visual inspections of many hours of synchrograms (SIESTA: 7.5h times 608 datasets equals 4560h of synchrogram) are not practically impossible.

Toledo *et al.* suggested a method to study the flatness in synchrograms by incorporating the synchronization index γ [see Sect. 5.1.3] into the synchrogram method [TOLEDO *et al.* 2002]. They successfully employed this method to study phase-synchronization in healthy subjects and heart-transplant patients, finding an abundant cardio-respiratory synchronization in the latter group. Moreover, they found in by construction unsynchronized surrogate data that some synchronized episodes occur randomly [TOLEDO *et al.* 2002]. The first finding is not surprising taking into account that cardio-respiratory synchronization can be associated with a diminished heart rate variability (HRV) immanent in patients suffering from cardiac diseases¹⁵.

In Toledo's method the phase synchrogram is subdivided into n subgroups where during episodes exhibiting n parallel these horizontal lines are complete separated from each other. After transforming the cyclic phases $\Psi_m(t_k)$ into the complex plane, a geometrical average over points from the same subgroup is obtained, i.e., the synchronization index γ in Eq. (5.23) is calculated, and the associated (average) phase is subtracted from the individual phases. That way, the n formerly parallel lines merge. Their vertical width is computed in a sliding window and serves as a measure of synchronization.

In the following I will describe another automated synchrogram analysis which is also based on dividing the synchrogram into n subgroups – hence it is somewhat similar to the Toledo approach – but then focuses on studying the n horizontal lines directly by means of standard deviation. This method is employed in the following to study cardio-respiratory synchronization in healthy subjects from the SIESTA database and to answer the question whether it is reliable to derive cardio-respiratory synchronization from a respiration proxy extracted from heartbeat data [HAMANN *et al.* 2009]. Our study had four major aims: (i) For the first time we studied cardio-respiratory synchronization in a large database (about 350 datasets of healthy subjects), (ii) we distinguished sleep stages associated with different physiological states, (iii) we studied effects of aging and overweight, and (iv) we approached the question whether it is possible to waive recording respiration without essentially compromising synchronization results. The latter could be advantageous in an ambulatory setup in terms of complexity and costs.

5.2.1. Reconstruction of Respiration from Heartbeat

A simple reconstruction of respiration from heartbeat is based on the respiratory sinus arrhythmia (RSA) mechanism [Sect 2.2]. Recall that respiration influences the sympatho-vagal autonomous nervous system. While inspiration enhances sympathetic components followed by an increase in heart rate, expiration suppresses sympathetic and activates vagal components resulting in a heart rate decrease. It is important to note that RSA is *not* equivalent to cardiorespiratory synchronization. While RSA yields a cyclical variation of heart rate, cardiorespiratory synchronization is only observed when heartbeats occur at the same instantaneous phases within the breathing cycle for a period of several consecutive breaths. Both phenomena can occur independent of each other although an increased RSA might reduce cardiorespiratory synchronization [SCHÄFER *et al.* 1998, 1999].

In spectral analysis of RRI data [see Fig. 5.3] two prominent peaks are often observed corresponding to the LF (0.04 – 0.15Hz) and the HF (0.15 – 0.4Hz) frequency bands [see Fig. 2.3 and related

¹⁵In fact a reduced HRV is used as an indicator of Chronicle Heart Failure (CHF) and a predictor of Sudden Cardiac Death (SCD).

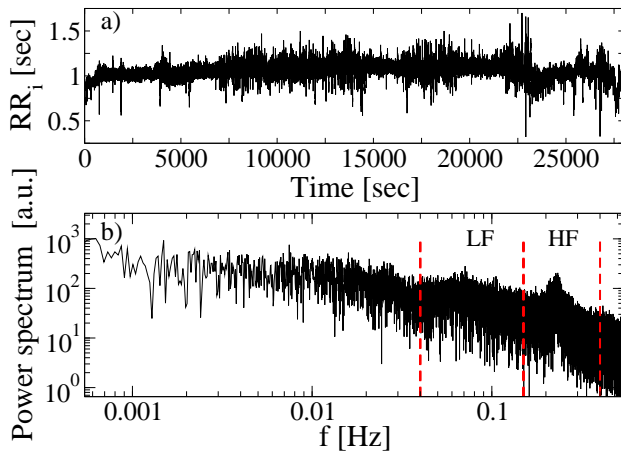


Figure 5.3.: (a) Heartbeat interval time series RR_i from a healthy young subject during sleep. (b) Power spectrum of the signal shown in (a). The LF band [0.04 – 0.15Hz] is assumed to reflect blood pressure oscillations, whereas the HF band [0.15 – 0.4Hz] reflects respiration via the RSA effect. It can thus be used to reconstruct the respiratory signal.

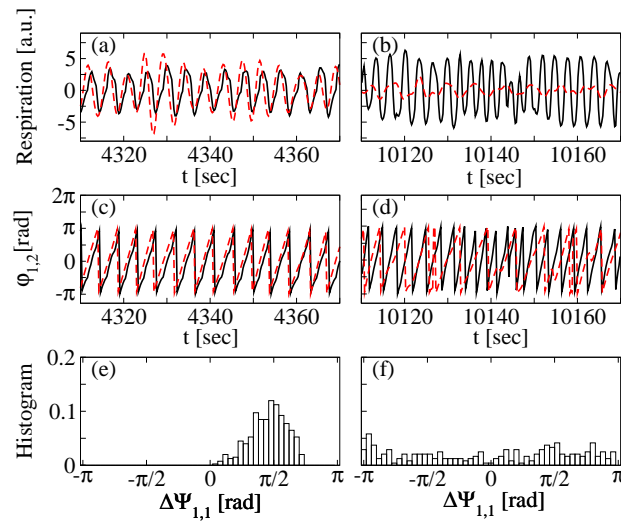


Figure 5.4.: Analysis of respiration signals. (a,b) Recorded oronasal airflow [black solid line] is compared with the respiratory signals reconstructed from heartbeat [red dashed lines] for two segments of a recording from a healthy subject. (c,d) Instantaneous phases calculated from the oronasal airflow [$\varphi_1(t)$, black solid line] and from the reconstructed respiration [$\varphi_2(t)$, red dashed line] are compared for the same segments. (e,f) Histogram of the phase differences $\varphi_1(t) - \varphi_2(t)$ between real and reconstructed respiration signals. The peak in (e) indicates that the reconstructed signal resembles the original signal with an unimportant systematic phase shift of approximately $\pi/2$. The uniform distribution in (f) indicates that the respiratory signal could not be reconstructed, probably due to a diminished influence of the breathing upon the heartbeat signal, i. e., very weak RSA.

discussion in Sect. 2.2, or HRV TASK FORCE 1996]. While the LF band has been associated with both sympathetic and parasympathetic activity; the corresponding peak might be related to blood pressure oscillations (Mayer waves), the HF band was associated with vagal components only [HRV TASK FORCE 1996].

It has been shown that HF spectral power is significantly influenced by breathing volume and breathing rate, i. e., changing the breathing pattern alters the HF spectral components [HIRSCH AND BISHOP 1981; BROWN *et al.* 1993; PENTTILÄ *et al.* 2001]. Therefore, respiratory components can be extracted from a heartbeat interval time series by Fourier filtering, i. e., applying a bandpass filter adjusted to HF components. This way, the RSA effect can be exploited for the reconstruction of the respiration signal from heartbeat intervals.

Employing this technique, respiration was reconstructed for all healthy subjects in the SIESTA database (for adaptation night and recording night). Together with the real respiration signal (ornasal airflow) it was resampled at 4Hz (low pass filter) to eliminate high frequency fluctuations which might disturb the Hilbert transform. Note, that this also ensures the same sampling frequency since respiration recorded at frequencies 16Hz, 20Hz, 100Hz, or 200Hz depending on the sleep laboratory.

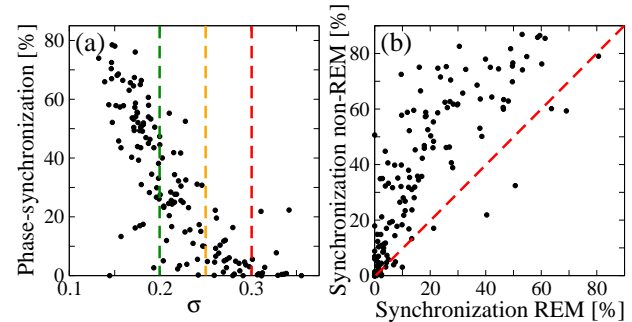
5.2.2. Assessing Reconstruction Quality

Figures 5.4(a,b) show two exemplary parts of both, recorded respiration (solid black) and ECG based reconstructed respiration (dashed red), where the latter was derived by employing the technique described above. The corresponding instantaneous phase signals obtained from Hilbert transforms are shown in Figs. 5.4(c,d). Let in the following $\varphi_1(t)$ denote the instantaneous phase of measured airflow and $\varphi_2(t)$ be associated with the phases of reconstructed respiration. It is clearly seen that the reconstruction works well in the region shown in Figs. 5.4(a,c), while it

	whole night	wake	REM	non-REM
all	30.5 (150)	17.9 (150)	17.8 (149)	35.9 (150)
$\sigma \leq 0.2$	47.9 (74)	33.3 (33)	44.0 (33)	52.3 (88)
$\sigma \leq 0.25$	39.5 (110)	25.1 (95)	25.5 (95)	44.3 (117)
$\sigma \leq 0.3$	33.2 (136)	20.6 (129)	19.2 (137)	37.4 (143)

Table 5.1.: Average synchronization between recorded oronasal airflow and ECG based reconstructed breathing within different sleep stages in percent. Results are shown for all subjects and for subjects characterized by different relative fluctuations σ of the reconstructed breathing. Numbers in brackets denote the number of considered individuals in the respective group.

Figure 5.5.: (a) Percentage of synchronized time between real and reconstructed respiration signals vs. relative fluctuations σ of the reconstructed respiration for whole nights. Values $0.2 < \sigma < 0.3$ seem appropriate to exclude subjects with failing reconstruction of respiration. (b) Synchronization percentage during REM sleep vs. non-REM sleep; each plot represents one subject. The reconstruction is more reliable during non-REM sleep.



completely fails in the fragment depicted in Figs. 5.4(b,d). A simple approach to quantify the reconstruction quality is studying histograms of corresponding phase differences within windows of limited time. Such histograms of corresponding phase differences are depicted in Figs. 5.4(e,f). If recorded and reconstructed respiration signals resemble each other, they exhibit 1 : 1 phase synchronization and the histogram is strongly peaked [Fig. 5.4(e)]. For not synchronized signals, i. e., when the reconstruction fails, all phase differences have identical probability and the histogram is flat [Fig. 5.4(f)]. This can be computationally checked either by calculating standard synchronization indexes, e.g., ρ and γ introduced in Sect. 5.1.3 or by a direct study of the histograms. In the SIESTA data of healthy subjects one finds that the standard indexes strongly depend on the noise level, sudden phase jumps (slips), and artifacts. In addition, they do not fully vanish for unsynchronized surrogate data, e.g., for reconstructed respiration from one subject and the measured oronasal airflow from another. A similar effect of non-vanishing random synchronization in cardio-respiratory (heartbeat and respiration) surrogates was reported in another study by Toledo in [TOLEDO *et al.* 2002].

Me and my collaborator Ronny Bartsch, thus, decided to classify the synchronization between real and reconstructed respiration not based on histograms but by studying the relation of their cumulative phases. These are calculated from the instantaneous respiratory phases $\varphi_j(t)$, $j = 1, 2$, both defined in $(-\pi, \pi]$, by

$$\Phi_j(t) = \varphi_j(t) + 2\pi n, \quad j = 1, 2 \quad (5.25)$$

where the calculation starts with $n = 0$ and proceeds by incrementing n if the instantaneous phase $\varphi_j(t)$ drops by a value larger than π . Ideally, a new breathing cycle would start with a drop in phase by 2π , compare Figs. 5.4(a,c) and (b,d). However, smaller values occur in practice due to limited time resolution, noise, etc. In rare cases, when the instantaneous phase increases by more than π , n is decremented.

The two respiratory signals can be considered synchronized when the cumulative phase signals $\Phi_1(t)$ and $\Phi_2(t)$ run parallel to each other. This can simply be captured by calculating the mean phase differences $\Delta\Phi_\nu = \langle \Phi_1(t) - \Phi_2(t) \rangle_\nu$ and the corresponding standard deviations $\hat{\sigma}_\nu$ within windows ν of length 30s, i. e., 120 data points due to 4Hz sampling. The two signals are defined as synchronized if the standard deviation $\hat{\sigma}_\nu$ is below 0.5rad. This way, we obtained for each subject the overall percentage of synchronized 30s windows for the whole night as well as separately for wake, REM sleep and non-REM sleep (cf. Table 5.1).

Figure 5.5(a) shows the percentage of whole-night synchronization between both respiratory signals (30s, and $\hat{\sigma} < 0.5\text{rad}$) as a function of the relative fluctuations σ of the reconstructed respira-

tion. Considering the time intervals between phase increases of 2π in the cumulative reconstructed respiratory phases $\Phi_2(t)$, σ is defined as the quotient of the standard deviation of these breathing intervals over the mean breathing interval. Since the respiratory data is sometimes nonstationary, σ is calculated for windows of $T_\sigma = 300\text{s}$ and then these values are averaged over the whole night. Each point in Fig. 5.5(a) represents one subject from the SIESTA database¹⁶. It is obvious that there are subjects where the reconstruction is rather successful (large percentage of correctly, i. e., synchronous reconstructed respiration), while for others it more or less fails. The value of σ is usually larger for subjects with failing reconstruction. The relative fluctuations of the reconstructed respiration, i. e. σ , can thus be used as an approximate parameter for the quality of the reconstruction. Consequently, in the following results regarding reconstructed cardiorespiratory synchronization are compared taking into account just subjects with values of σ below given thresholds [see also Table 5.1]. Parameters characterizing the height of the peak in the HF band of the power spectrum [see Fig. 5.3(b)] did not qualify as better replacements for σ in classifying good and bad reconstruction of respiration.

Figure 5.5(b) shows the percentage of synchronization between both respiratory signals during REM sleep versus the corresponding percentage during non-REM sleep in the same subject. Again, each point represents one subject. One clearly observes that well reconstructed respiration is found rather during non-REM sleep than during REM sleep, since more subjects are found above the diagonal in Fig. 5.5(b). This observation is stable for different thresholds for σ , see Table 5.1. Except for $\sigma \leq 0.2$, results for wakefulness and REM sleep are basically the same, also reflecting the well known statistical resemblance of REM and wake stages.

5.2.3. Description of an Automated Synchrogram Approach

Since we originally developed the algorithm in order to study cardio-respiratory synchronization during nocturnal sleep in a set of 150 healthy subjects in the SIESTA database, I will illustrate the methodology using this data. The results of the complete study are presented in the next subsections. The reader might find both algorithm and results presented in our paper [HAMANN *et al.* 2009] and be advised that the method can immediately be ported to any other bivariate set of signals (continuously sampled signal and a point process) in which one wants to analyze phase synchronization.

Step 1: Calculation of Instantaneous Phases

After data preparation [see Sect. 5.2.1] instantaneous phase signals $\varphi_1(t)$ and $\varphi_2(t)$ are calculated for measured airflow and reconstructed respiration, respectively, by employing Hilbert transform.

Step 2: Calculation of Continuous Phases

From instantaneous phases φ_j , $j = 1, 2$ (defined in $(-\pi, \pi]$) cumulative respiratory phases $\Phi_j(t)$ are calculated following Eq. (5.25).

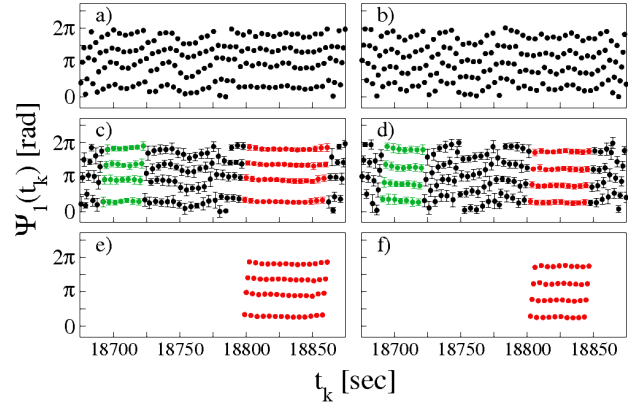
Step 3: Stroboscopic Illumination of Phases

Subsequent to detecting beat positions t_k employing a QRS-detector¹⁷ the cardiorespiratory synchrogram is obtained by mapping the times $t_k = \sum_{i=1}^k RR_i$ of the heartbeats onto the continuous cumulative phases $\Phi_j(t)$ and wrapping it into $[0, 2\pi m)$ yielding $\Psi_m(t_k)$. Figures 5.6(a,b) illustrate two representative parts of corresponding synchrograms for measured oronasal airflow (a) and reconstructed breathing (b). In these synchrograms for studying phase synchronization of n heartbeats within one ($m = 1$) breathing cycle ($n : 1$ coupling), $\Psi_{1,j}(t_k) = \Phi_j(t_k) \bmod 2\pi$ is plotted versus t_k . In areas with $n : 1$ phase synchronization n parallel horizontal lines appear. The lines vanish if synchronization breaks down. Figures 5.6(a,b) show events of $4 : 1$ phase synchronization. The similarities between (a) and (b) indicate a good reconstruction quality

¹⁶Due to very time consuming heartbeat detection we analyzed data from only 150 subjects at this time. The worst 40 recordings from the BERLIN lab were still missing.

¹⁷Here I employed the semi-automatic detector RaschLab of the LibRasch package [SCHNEIDER 2005] and additionally inspected its output for each subject – a tremendously time consuming part of the study compared with the analysis itself.

Figure 5.6.: Examples illustrating the automated synchrogram method for real [left] and reconstructed [right] respiration signals. Symbols in (a,b) show the instantaneous respiratory phases at the time of the heartbeats. (c,d) means and standard deviations of the phases, calculated in time intervals of length $\tau = 30$ s around each point in the horizontal lines. (e,f) Phase points with a standard deviation larger than the threshold were deleted and then sequences shorter than the threshold T were also deleted. Red and green marked elements fulfill the standard deviation criterion, but sequences in green being shorter than the minimal duration T are deleted. Note that T must be slightly smaller for reconstructed breathing [right], since the continuous segments are shorter.



in the considered time window. Arbitrary synchronization ratios $n : m$, i. e., the occurrence of n heartbeats during m breathing cycles, can be studied easily considering synchrograms of $\Psi_{m,j}(t_k) = \Phi_j(t_k) \bmod 2\pi m$ versus t_k and again looking for n parallel horizontal lines.

Step 4: Automated Detection of Synchronized Episodes

To study data of many subjects and nights it is necessary to automatically detect and distinguish synchronized and unsynchronized areas in the synchrograms [BARTSCH *et al.* 2007]. Therefore, a centered moving average filter of window length τ is applied separately for every $r = 1, \dots, n$ heartbeats observed within the m considered breathing cycles in the following sense: (i) m breathing cycles which are assumed to be in the center of the averaging window are taken and the number n of heartbeats occurring within these m breathing cycles is counted. The times of these heartbeats are denoted as $t_c^{(r)}$, (ii) a regularly spaced phase interval associated with each single heartbeat event at center position $\Delta\psi_m^{(n)} = 2\pi m/n$ is calculated, (iii) all phases $\psi_m(t_k)$ belonging to neighboring breathing cycles within the time interval $\mathfrak{T}_r = [t_c^{(r)} - \tau/2, t_c^{(r)} + \tau/2]$ are averaged with respect to their dedicated phase range $\mathfrak{R}_r = [(r-1)\Delta\psi_m^{(n)}, r\Delta\psi_m^{(n)}]$, $r = 1, \dots, n$:

$$\langle \Psi_m^{(r)} \rangle(t_c^{(r)}) = \frac{1}{N_{\mathfrak{R}_r}} \sum_{t_k \in \mathfrak{T}_r} \Psi_m^{(r)}(t_k) \quad (5.26)$$

Here, $N_{\mathfrak{R}_r}$ denotes the number of points occurring in the time window \mathfrak{T}_r and in the phase range \mathfrak{R}_r as obtained from the synchrogram. Note, that even when n heartbeats occur during m breathing cycles at the center position, there might be a different number of heartbeats during other m breathing cycles within the same considered moving average window of width τ . Additionally to the average one calculates for each of the r heartbeats a standard deviation $\hat{\sigma}_r$. Next, every value $\Psi_m^{(r)}(t_k = t_c^{(r)})$ during the centered m breathing cycles is replaced by the corresponding mean value $\langle \Psi_m^{(r)}(t_k) \rangle$ as illustrated for $n = 4$ and $m = 1$ in Figs. 5.6(c,d). In addition, the four different $\hat{\sigma}_r$ are shown as error bars. This 'straightens' the parallel lines indicating synchronized episodes compared with the plain synchrogram in Figs. 5.6(a,b) and makes them more pronounced.

Step 5: Deletion of Unsynchronized and Short Episodes

In the final step shown in Figs. 5.6(e,f) all points in the synchrogram are removed where the condition $\hat{\sigma}_r < 2\pi m/n\delta$ is violated and only episodes of constant n that are longer than a minimum period T are kept [green episodes in Figs. 5.6(c,d) are too short]. The standard deviation parameter $\delta \in \mathbb{R}^+$ allows for continuous tuning of the methods sensitivity. From the remaining synchronized episodes, one can determine the percentage of synchronized episodes compared with the total sleep duration.

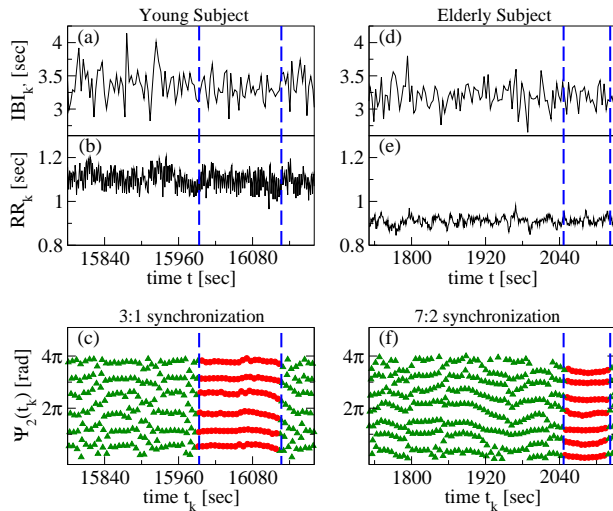


Figure 5.7.: Illustration of higher order cardiorespiratory synchronization [$m = 2$] studied by employing the suggested automated synchronogram analysis in a young subject (a-c) versus an elderly subject (d-f). Shown are 400s fragments of (a,d) an inter-breath-interval signal [IBI], (b,e) the corresponding heart-beat-interval signal [RR], and (c,f) the automated synchronogram [$m = 2$, $\Psi_2(t_k)$ vs. t_k] with marked synchronized episodes [in red] versus time. Blue dashed lines mark the beginning and the end of the synchronized episodes. In the young subject $6 : 2 = 3 : 1$ synchronization is depicted while there is a $7 : 2$ episode in the elderly subject. Note the smaller beat-to-beat intervals [larger heart rate] and the lower variability in the older subject, which is typical for an increased cardiac risk often found in elderly. Surprisingly, the length of the cardio-respiratory synchronization episode is significantly larger in the younger subject despite a much larger heart rate variability [HRV].

5.2.4. Optimizing Synchronogram Evaluation Parameters

For the suggested automated analysis of phase synchronograms three parameters need to be optimized [BARTSCH *et al.* 2007]: (i) the (time) width τ of the moving average filter, (ii) the standard deviation limit parameter δ , and (iii) the minimum episode duration T . In order to optimize the parameters their influence on the overall whole-night phase synchronization was studied, comparing results for real data¹⁸ (heartbeat and oronasal airflow) with those for (unsynchronized) surrogate data. The surrogate data was in this case obtained by randomly combining heartbeat data from one subject with breathing data from another subject.

Figure 5.8(a) shows the whole-night phase-synchronization percentage for different δ and T . As expected, the largest ratio of synchronized episodes was found for small T and small δ (i. e., a large limit for the standard deviations). However, in this case, a rather large number of synchronized episodes is also reported for the unsynchronized surrogate data. The ratio of the mean percentage of synchronization in real data over the mean percentage in surrogate data increases from 1.6 for $T = 20$ s to 3.4 for $T = 40$ s. However, for $T = 40$ s only very few synchronization episodes were detected. We therefore suggested choosing $\delta = 5$ and $T = 30$ s to optimize the ratio between correctly detected real synchronization episodes and falsely detected synchronization episodes in surrogate data. Together with $\tau = 30$ s these parameter values provide a good separation and, furthermore, the time parameters coincide with the time interval of 30s used in sleep stage classification. Note that δ has a similar influence on the results as T (not shown in detail), while τ just weakly affects the results.

When comparing synchronized episodes for real and reconstructed respiration [see red episodes in Figs. 5.6(e,f) for an example], one observes in general shorter synchronized episodes for the reconstructed respiration. This is due to instabilities in the reconstruction process. We thus adjusted $T_{\text{rec}} = 24$ s for reconstructed breathing, keeping both τ and δ at the same values and $T = 30$ s. This led to similar total synchronized time in both respiratory signals, see Fig. 5.9.

5.2.5. Phase Synchronization with Reconstructed Breathing

Figure 5.9(a) shows the whole-night percentages of cardiorespiratory synchronization for the real respiration [left sub-panel] and the reconstructed respiration [right sub-panel] considering subsets of the 150 subjects¹⁹ with σ below and above the indicated thresholds [see Sect. 5.2.2 for

¹⁸Although, I here show results from the original dataset (only 112 subjects where heartbeat was obtained by an unpublished experimental beat detector of Stephan Zschiegner [ZSCHIEGNER 2004]) I would like to note that during the study presented in [HAMANN *et al.* 2009] we rechecked the parameters using the data obtained in Halle by employing the peak detector RaschLab [SCHNEIDER 2005].

¹⁹SIESTA without Berlin lab where ECG data quality required more attention and which I only finished in April 2009.

Figure 5.8.: Medians, upper and lower quartiles [bars] and means [filled symbols] of total-night-synchronization rates (a) versus T for all original data [black dotted bars and circles] and surrogate data [magenta striped bars and triangles], left of dotted line $\delta = 6$, right of dotted line $\delta = 5$. (b) The results for optimized parameters [for $\delta = 5$ and $T = 30$ s] are shown versus body mass indexes [BMI] and gender for wakefulness [blue dotted bars and circles], REM sleep [orange blank bars and triangles], and non-REM sleep [green striped bars and diamonds]. Note the similar synchronization behavior in all subgroups. This figure is based on the original data set of 112 subjects and is adapted from [BARTSCH *et al.* 2007].

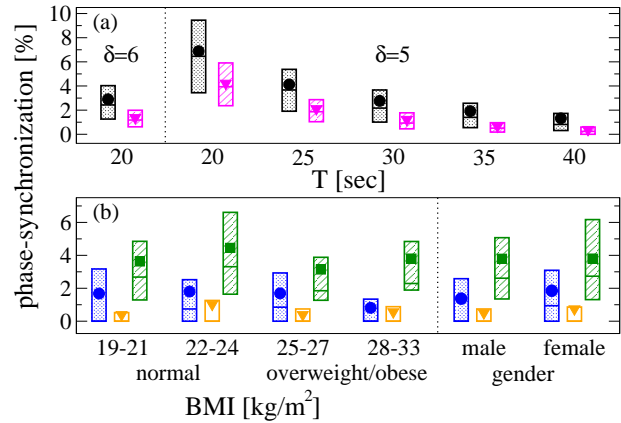
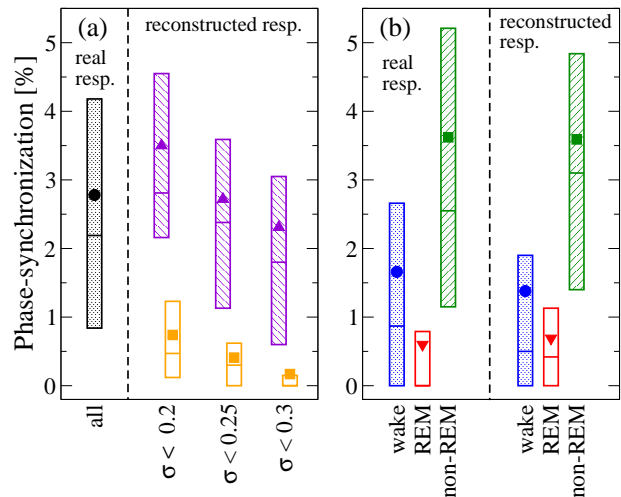


Figure 5.9.: (a) Median, upper and lower quartile and mean [dot] of percentage of phase synchronized time regarding heartbeat and real breathing signal [left]. The three sets on the right show the results for heartbeat and reconstructed respiration for different σ . The violet striped bars represent the values for subjects with σ below the threshold value and the dark yellow blank bars for breathing signals with σ above the threshold. (b) Cardiorespiratory synchronization percentages for real respiration signals [left set] and reconstructed respiration signals [$\sigma < 0.25$, right set] during different sleep stages [wake=blue, REM=red, non-REM=green].



definition]. The close similarity of the results for real and reconstructed respiration prove that cardiorespiratory synchronization can be calculated based solely on heartbeat data. Comparing the values with those in the left sub-panel, it seems that the limit $\sigma < 0.25$ is most appropriate – median and mean are comparable with results from real respiration. For Fig. 5.9(b) the data has been split into parts of wakefulness, non-REM sleep, and REM sleep. Again there is a close similarity for the results based on real respiration and reconstructed respiration. The main finding of drastically reduced cardiorespiratory synchronization during REM sleep and enhanced cardiorespiratory synchronization during non-REM sleep compared with wakefulness is fully confirmed.

5.2.6. Higher Order Cardiorespiratory Synchronization and Age Dependence

Until now only total phase synchronization (all ratios $n : m$ combined) was studied during REM sleep and non-REM sleep [HAMANN *et al.* 2009]. Additionally, Figs. 2.9(b,c) underpin the general observation of tremendous changes in sleep structure during human lifetime. E. g., in elderly the time spent in deep sleep is decreased in favor of additional and more frequent arousals accompanied by prolonged light sleep episodes. This motivates a more systematic study of aging effects in cardiorespiratory phase synchronization.

Therefore, I now consider heartbeat and oronasal airflow from all 190 disease-free subjects contained in the SIESTA database in an automated synchrogram analysis. I separate results according to (i) different synchronization ratios, i.e., $n : 1$, $n : 2$, or $n : 3$, (ii) the subject's individual age, and (iii) different physiological states during sleep. For two illustrative examples of higher order cardio-respiratory phase-synchronization in a young subject versus an elderly subject see Fig. 5.7. All results obtained from a full analysis are shown separately for nocturnal wakefulness, light sleep S1, light sleep S2, deep sleep, and REM sleep in Fig. 5.10. The bar plots were obtained by averaging $n : m$ phase-synchronization rates for an integer number of heartbeats n

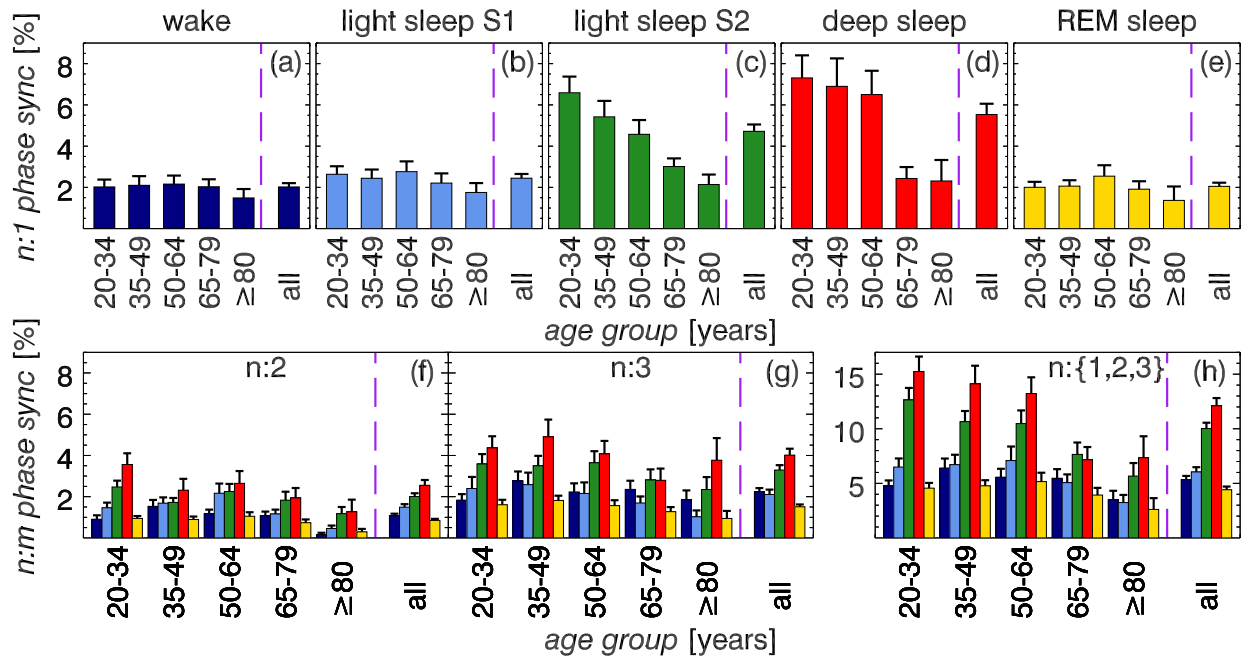


Figure 5.10.: Cardiorespiratory phase-synchronization results from 190 healthy subjects during average 7.8h habitual sleep separately for different sleep stages and for different age groups [left of purple dashed line] versus all subjects [right of purple dashed line]. (a-e) $n : 1$ phase synchronization separately [from left to right] for (a) nocturnal wakefulness [dark blue], (b) light sleep S1 [light blue], (c) light sleep S2 [green], (d) deep sleep [red], and (e) REM sleep [yellow]. (f-h) Phase-synchronization results of other ratios [sleep stages in same order and color coding as in (a-e)]: (f) $n : 2$, (g) $n : 3$, and (h) combined $n : 1$, $n : 2$, and $n : 3$ [notice the different percentage-axis]. Shown are averages in the respective group together with standard errors. Note, the similarities and quasi age independence during wakefulness, light sleep S1, and REM sleep. Percentage of phase synchronization increases with increasing sleep depth from wake to deep sleep [recall REM sleep not being 'deep']. Synchronization during REM sleep is less pronounced for all ratios and during all sleep stages.

occurring during a fixed number of respiratory cycles $m = 1, 2, 3$ over all healthy subjects within the corresponding age range (15 years width²⁰). Figures 5.10(a-e) concentrate on percentage $n : 1$ phase-synchronization, i.e., all episodes where $n \in \{1, 2, 3, 4, 5, 6, 7, 8\}$ heartbeats occur per breath cycle ($m = 1$) are combined, across nocturnal wakefulness and for different sleep stages [see Fig. 5.11 for details on single synchronization ratios]. Analogously obtained results for ratios $n : 2$ (combining segments where $n \in \{3, 5, 7, 9, 11, 13, 15\}$ heartbeats occur during 2 breath cycles) and $n : 3$ ($n \in \{4, 5, 7, 8, 10, 11, 13, 14, 16, 17, 19\}$ heartbeats per 3 breaths) are illustrated in Figs. 5.10(f,g) using the same percentage-axis range as in Figs. 5.10(a-e) for comparison.

Although, percentage $n : 1$ phase-synchronization is slightly increased during light sleep S1 it appears to be more or less similar during nocturnal wakefulness, light sleep S1, and REM sleep [Figs. 5.10(a,b,e)]. Contrarily, the proportion of $n : 1$ phase-synchronization across light sleep S2 and deep sleep is notably larger for all age groups [Figs. 5.10(c,d)] – in young synchronization during light sleep S2 (or, deep sleep) is roughly larger by a factor of 3 (or, even 3.5) than during wake or REM sleep. However, levels for all sleep stages seem to merge towards the oldest group (≥ 80) where $n : 1$ phase-synchronization is, despite still being slightly enhanced during deep sleep and light sleep S2, less different when comparing all stages with each other.

A strong age dependence is observed during light sleep S2 and deep sleep where percentage phase-synchronization decreases from 6.59% and even 7.31% in young to 2.14% and 2.31% in elderly. Especially, during deep sleep a tremendous break down in phase-synchronization appears during the transition from age group 50–64 years to the next age group 65–79 years. When looking closer at corresponding results from other sleep stages a noticeable change in cardiorespiratory coupling is also observed, but much less pronounced. In wake, light sleep S1, and REM sleep percentage phase-synchronization slightly increases until it reaches its maximum for the age group 50–64

²⁰Although, a 95 years old female contributes to the oldest group ≥ 80 she is the only one above 90 years. Thus, in a strict sense the last group is not as homogeneous as the others.

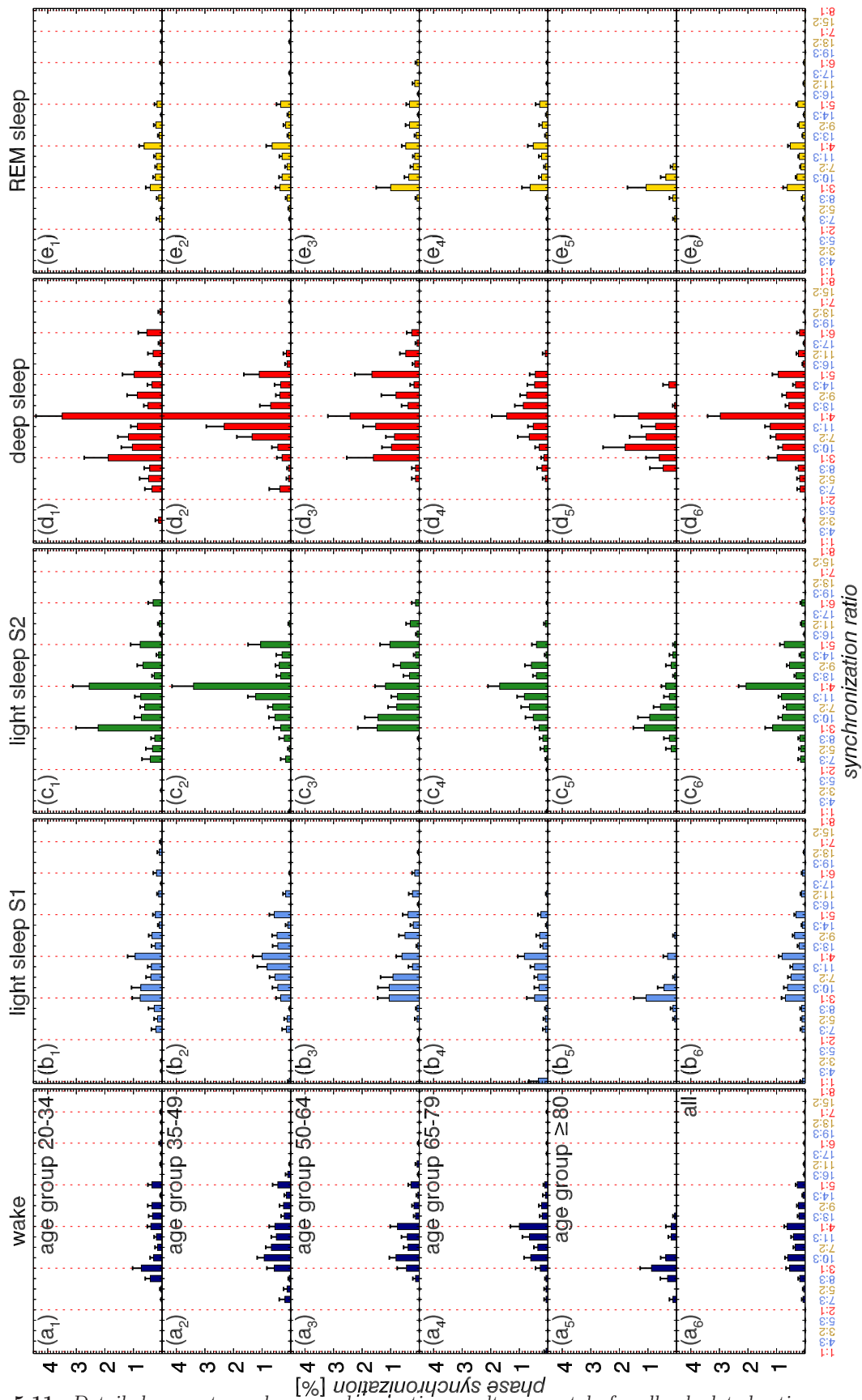


Figure 5.11.: Detailed percentage phase-synchronization results separately for all calculated ratios $n : m$ [X-axis], for different sleep stages [panel columns, same colors as in Fig. 5.10], and for all considered age groups [panel rows]: in years (a_1 - e_1) 20-34, (a_2 - e_2) 35-49, (a_3 - e_3) 50-64, (a_4 - e_4) 65-79, (a_5 - e_5) ≥ 80 , and (a_6 - e_6) 20-95 = all disease-free subjects. Ratios that contribute to $n : 1$ phase-synchronization in Figs. 5.10(a-e) are annotated in red, ratios $n : 2$ contributing to Fig. 5.10(f) in gold, and ratios $n : 3$ contributing to Fig. 5.10(g) in blue. Dotted red lines mark ratios $n : 1$ for orientation and error bars indicate standard errors. 4 : 1 synchronization in panel (d_2) is 5.075 ± 1.355 .

years and afterwards decreases, again. Such maximum at middle ages was also observed in α_1 as obtained by detrended fluctuation analysis [see Sect. 3.2.2]. It is known from other studies that sleep significantly changes, e.g., sleep fragmentation is altered, at ages around 50 years [ESPIRITU 2008] which might be related to but not completely explained by evening cortisol – a stress hormone – levels which were reported to suddenly and significantly increase at similar ages [VAN CAUTER *et al.* 2000].

Both, aging characteristics and magnitude of cardiorespiratory $n:1$ phase-synchronization during light sleep S1 is clearly different from findings during other non-REM sleep stages, i.e., light sleep S2 and deep sleep. This observation again justifies the separate consideration of both light sleep stages which took place across previous sections in this thesis and underlines the closeness of wake and light sleep S1. This also complies with the empirical observation that people who are aroused from light sleep S1 often claim never having slept.

Except for elderly during deep sleep [see discussion below] and wake all synchronization percentages $n:2$ and $n:3$ are in general significantly lower than corresponding values for $n:1$ synchronization in accordant sleep stages and age groups. However, results for $n:2$ phase synchronization are even notably lower than corresponding $n:3$ percentages suggesting a physiologically larger importance of $n:3$ synchronization.

Neglecting a few exceptions for young and elderly, previous results from $n:1$ synchronization including an even more apparent age-dependent alteration tendency are qualitatively retrieved: Roughly, an increase in coupling proportion during the first period of life (age ≤ 64 years) is followed by a decrease during the second half of life (age ≥ 65). Phase-synchronization percentages increase from REM sleep to intra-sleep wake, to light sleep stage 1, and to even more elevated values during light sleep S2, finally yielding deep sleep where the content of synchronized episodes is largest.

One especially pronounced exception appears in older subjects' (age groups 65 – 79 and ≥ 80) $n:3$ phase-synchronization percentage which is conspicuously larger than corresponding $n:1$ phase-synchronization proportions during deep sleep (during light sleep S2 only in oldest group) most pronounced during deep sleep suggesting a transition from $n:1$ phase synchronization in Young towards $n:3$ phase synchronization in Elderly. Nevertheless, it remains medically unclear whether a ratio of $n:1$ or $n:3$ is more advantageous for the cardio-respiratory system. Assuming being young implies presence of a better autonomous regulation clearly $n:1$ cardio-respiratory phase-synchronization is worthwhile. To check whether or not such transition from $n:1$ to $n:3$ synchronization occurs particularly during deep sleep Fig. 5.11 illustrates full phase-synchronization results for each considered ratio²¹ $n:m$ and separately for each sleep stage and age group.

Except for the oldest group [Figs. 5.11(a₅-e₅)] percentage of phase-synchronization exhibits a characteristic background distribution²² among ratios which is sometimes interrupted by strong occurrences of $n:1$, primarily $n:4$, coupling [marked by red dotted lines for clarity] poking out particularly during deep sleep [panels (d)] and light sleep S2 [panels (c)], but is otherwise, despite its overall magnitude [discussed earlier considering Fig. 5.10], more or less stable during all sleep stages. A similar background distribution was reported in unsynchronized surrogate data and is hence most likely random [Bartsch:2007].

The magnitude of $n:1$ synchronization clearly decreases with aging and ratio distributions appear most similar for age group 65–79 in Fig. 5.11(a₄-d₄) when compared between different sleep stages. This underlines the earlier claim of a reduction in sleep stage dependent cardio-respiratory coupling with age. However, the earlier speculated transition from $n:1$ to $n:3$ ratios during deep sleep is exclusively originated in a strong $10:3$ coupling appearing simultaneously with a reduced $3:1$ coupling in Fig. 5.10(d₅). They are likely related to individual fluctuations which are more

²¹In principle even more non-reducible ratios $n:m$ with $m > 3$ could be considered. The meaningfulness of an increased 'closeness' of ratios, however, is not only due to artifacts but also from a physiological point of view rather questionable.

²²Note, in Fig. 5.11 ratios appear correctly ordered but are not arranged according to their exact numerical value due to space limitations.

pronounced in elderly [error bars during deep sleep are largest²³]. A likely coincidental character of this finding is supported by a dominating 3 : 1 heartbeat-airflow phase synchronization across all other sleep stages in the same age group. Although, cardio-respiratory coupling during REM is weakest in general identified synchronous episodes are governed by $n : 1$ phase synchronization while other ratios are diminished. Hence, one cannot conclude a transition from $n : 1$ to $n : 3$ phase synchronization with normal aging.

Figure 5.10(h) finally integrates individual results from $n : 1$, $n : 2$, $n : 3$ cardiorespiratory phase-synchronization and is here considered to be a estimator for total cardiorespiratory phase-synchronization (other non-reducible ratios $n : m$ with $m > 3$ are neglected).

5.3. Cross-Modulation Analysis

So far I have presented phase-synchronization results from heartbeat and respiration during sleep. However, the most prominent signal in sleep research was not yet attended – the electroencephalogram (EEG). As introduced in Sect. 2.3 sleep stage classification in is mainly based on spectral components in EEG recordings. A comprehensive study on coupling between different components in human EEGs during sleep can further elucidate mechanisms of sleep control and sleep stage transitions, and is thus worth doing.

A traditional approach, aiming at a complete description of complex systems, is recording and analyzing multivariate data from (i) different spatial locations and/or (ii) containing different spectral components. Both types of data are provided by polysomnographic recordings which by default include multiple EEG leads from different spatial locations on the skull and whose power in characteristic frequency bands is used for sleep scoring [see Sect. 2.3]. For instance, the SIESTA database contains for each subject EEG signals recorded during two different nights from at least six different locations on the skull [Sect. 2.3]. Bipolar electrodes²⁴ were placed according to the 10-20 system [Fig. 2.8] at positions O1-M2 & O2-M1 (left & right occipital, i.e., back), C3-M2 & C4-M1 (left & right center), and Fp1-M2 & Fp2-M1 (left & right frontal pole). Following the classical approach and motivated by well established clinical sleep stage classification rules [RECHTSCHAFFEN AND KALES 1968; IBER *et al.* 2007] six physiologically relevant oscillatory components in the frequency range from 0.5Hz to 22Hz [see Tab. 5.2] are extracted from each EEG signal yielding in the case of SIESTA data altogether 36 different oscillatory signals.

Standard phase-synchronization analysis has recently become quite popular in brain wave studies [TASS *et al.* 1998; STAM 2005; NIKULIN AND BRISMAR 2006; WILL AND BERG 2007; KITAJO *et al.* 2007] with focuses on epilepsy [BIALONSKI AND LEHNERTZ 2006], migraine [ANGELINI *et al.* 2004], schizophrenia [BOB *et al.* 2008], as well as Parkinson's disease (PD) [TASS *et al.* 1998; JERBI *et al.* 2007] reporting differences in synchronization for different physiological states or pathologies. However, most studies deal with rather small databases ($n < 20$ subjects) and short recordings compared with polysomnographic data (duration approx. 7.8h) and investigate the coupling between components of similar frequencies. The coupling structure between components of different frequencies is hardly studied. Phase synchronization between different frequency components in the EEG cannot be calculated for arbitrary ratios $n : m$ but must in each case correspond to the considered frequency bands with respect to the locking condition in Eq. (5.9). For example, 1 : 1 synchronization is only meaningful for signals of the same frequency bands extracted from two different EEG leads (from different locations), while 2 : 1 phase-synchronization could yield useful information for an α - β coupling although the α frequency range is not exactly mapped to the β range by the factor of 2 [Tab. 5.2].

Another interesting type of coupling between two signals are auto modulations and cross modulations of their amplitudes and frequencies. I. e., changes in the amplitude (or, alternatively frequency) in the first signal could affect amplitude and/or frequency in the second signal and/or

²³Partly due to a reduced statistics during deep sleep in Elderly.

²⁴I denote an EEG signal as bipolar when it is measured between a point on the 'upper' skull and either one of the points A1, A2, M1, or M2. However, since auricular and mastoid electrodes are considered to be 'neutral' reference electrodes by some authors, one might consider pairs available in the SIESTA database as unipolar.

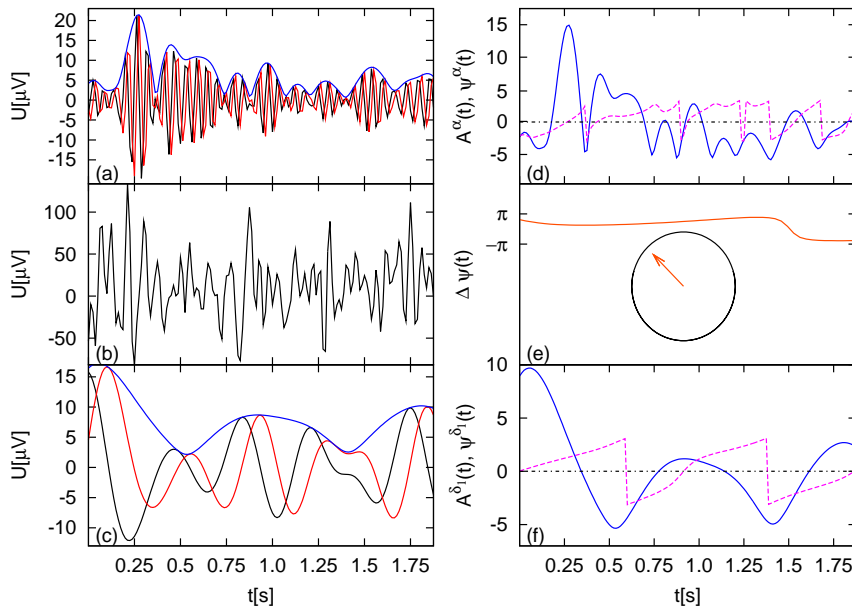


Figure 5.12.: Cross-modulation analysis in an EEG recording. The raw EEG (b) is decomposed into x_k^α [black in (a)] and $x_k^{\delta_1}$ [in (c)], $t_k = k \cdot 0.005s$ (sampling rate 200Hz). Instantaneous amplitudes A_k^α and $A_k^{\delta_1}$ [blue curves in (a,c)] are reconstructed using the Hilbert transformed signals \tilde{x}_k^α and $\tilde{x}_k^{\delta_1}$ [red]. Next, phases ψ_k^α and $\psi_k^{\delta_1}$ [purple in (d,f)] of mean-shifted amplitudes $A_k^{\delta_1} - \langle A_k^{\delta_1} \rangle$ and $A_k^\alpha - \langle A_k^\alpha \rangle$ [blue in (d,f)] are calculated. Finally, complex exponentials [inset in (e)] of the phase differences $\psi_k^\alpha - \psi_k^{\delta_1}$ [purple in (e)] are averaged over patches of 30 sec. yielding μ_ν .

band	freq. (Hz)	band	freq. (Hz)	band	freq. (Hz)
δ_1	0.5 – 1.99	θ	4 – 6.99	σ	11.5 – 15.99
δ_2	2 – 3.99	α	7 – 11.49	β	16 – 22

Table 5.2.: Frequency bands used for EEG analysis. Note that the δ band was divided into two new bands, δ_1 and δ_2 , in contrast to Tab. 2.1; the γ band is disregarded here.

vice versa.

To study the latter more sophisticated type of coupling we introduced *cross-modulation analysis* [explained in Sect. 5.3.1] and applied it to EEG data from 190 disease-free subjects from the SIESTA database. Results are discussed in Sect. 5.3.3 and were published in [GANS *et al.* 2009]. Recently, we further employed cross-modulation analysis to study effects of Parkinson’s disease on the coupling structure in sleep EEG, see Sect. 5.3.5 and [STUMPF *et al.* 2010].

5.3.1. Cross-Modulation Analysis Algorithm

The cross-modulation analysis method consists of four steps, where the first two steps are basically equivalent to studying phase synchronization in quasi-continuous signals. Although, the method can again in principle be employed for investigating signals of any source (prerequisites: narrow frequency band, oscillations around zero) it has, so far, only been employed in studying electro-encephalograms (EEGs) recorded during habitual sleep (SIESTA and DAPHNET data). Hence, I will illustrate the algorithm based on EEG signals and then present results which we partly published in [GANS *et al.* 2009; STUMPF *et al.* 2010]. Note that in the following the algorithm will be presented specifically for the SIESTA database and corresponding values for the DAPHNET database are noted in curly braces “{.}”.

Step 1:

Each EEG signal is decomposed into frequency components according to Tab. 5.2 employing the Fourier filtering technique [THEILER *et al.* 1992], i.e., (i) the signal is fast Fourier transformed (FFT) into the frequency domain where (ii) the transformed signal is bandpass frequency filtered keeping only Fourier coefficients of the desired band, and (iii) the inverse fast Fourier transform (FFT^{-1}) is applied to transform the bandpass filtered signal back into the time domain. This is illustrated in Fig. 5.12 where a raw EEG fragment is shown in Fig. 5.12(b) together with its α and δ_1 components in Figs. 5.12(a,c) [black curves]. Applying Fourier filtering to all six {three} synchronous EEG recordings yields ‘six EEG leads’ {‘three EEG leads’} \times ‘six frequency components’ equal 36 {18} time series, altogether. Note, quantities denoting different time series

of the same kind but from different raw signals are distinguished by superscripts j and l in the following.

Step 2:

Each of the 36 {18} time series x_k^j is complemented by its imaginary counterpart²⁵ \tilde{x}_k^j defined by a first Hilbert transform according to Eqs. (5.14) and (5.15) to obtain an analytical signal $x_k^j + i\tilde{x}_k^j = A_k^j \exp(i\varphi_k^j)$. Here, $k \in \mathbb{N}^+$ indexes discretized time $t \rightarrow t_k = k\Delta t$ with sampling Δt . Then instantaneous amplitudes A_k^j , instantaneous frequencies f_k^j , and instantaneous phases φ_k^j are defined following Eq. (5.17). For the raw EEG in Fig. 5.12(b) red curves in Figs. 5.12(a,c) illustrate \tilde{x}_k^α and $\tilde{x}_k^{\delta_1}$ while blue curves are corresponding instantaneous amplitude signals A_k^α and $A_k^{\delta_1}$.

Taking each unique pair of instantaneous phases $\{\varphi_k^j, \varphi_k^l\}$ one can study and quantify phase-synchronization properties by considering phase differences $\Delta\varphi_{n,m}^{j,l}(t_k) = n\varphi_k^j - m\varphi_k^l$ and calculating indexes such as $\gamma_{n,m}^{j,l} = |\langle i\Delta\varphi_{n,m}^{j,l} \rangle|$ or $\rho_{n,m}^{j,l}$ following Eqs. (5.23) and (5.22).

However, in cross-modulation analysis instantaneous phases of the EEGs are only required for the definition of instantaneous frequencies f_k^j [Eq. (5.17)] and are, thus, not further discussed here. Recall that a Hilbert transform requires two essential prerequisites in order to result in meaningful complements, amplitudes, and phases: (i) narrow-banded input signals, and (ii) signals oscillating around zero. The first property is ensured by the bandpass filtering in *Step 1*, and the latter by subtracting the signal's mean value. Further note that frequency signals f_k^j might be hampered by occasional artifacts (spikes) due to sudden phase jumps. For that reason, an additional filtering step has to be included where frequencies exceeding the designated frequency band [Step 1, Tab. 5.2] are replaced by a moving average, see Fig. 5.13. The moving average is calculated, i. g., by considering frequency adaptive windows of width $a \times 1/f_c$ where f_c denotes the center frequency of the frequency band and a (we use $a = 10$) is a parameter to adjust the averaging depending on the data.

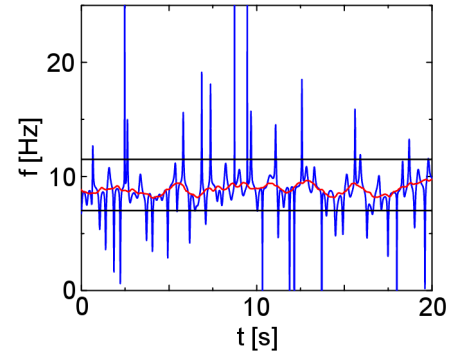


Figure 5.13.: Fragment of an instantaneous frequency signal obtained from human EEG after Fourier filtering adjusted to the alpha-frequency band. Note the frequent spikes in the original signal exceeding the band boundaries marked by solid horizontal lines. The associated moving average filtered frequency signal is shown in red. Figure adapted from [GANS et al. 2009].

Step 3:

In order to study the relationship of instantaneous amplitudes A_k^j and frequencies f_k^j from (i) different spatial locations and (ii) from different frequency components describing the complex brain system one can consider signals A_k^j and f_k^j as new input signals and employ a second Hilbert transform [Eq. (5.15)] to derive their corresponding instantaneous phases $\psi_k^{j'}$, where the index j' again denotes the signal number. One amplitude and one frequency signal are generated from each of the six {three} EEG recordings considering six frequency bands at a time. This leads to $2 \times 6 \times 6 = 72$ { $2 \times 3 \times 6 = 36$ } unique phase signals in total. Figures 5.12(d,f) illustrate fragments of instantaneous amplitude signals A_k^α and $A_k^{\delta_1}$ [blue] together with the corresponding phase signals ψ_k^α and $\psi_k^{\delta_1}$ [purple]. Based on the phase differences

$$\Delta\psi_{n,m}^{j,l}(t_k) = n\psi_k^j - m\psi_k^l \quad (5.27)$$

between each pair (j, l) of two signals [$\Delta\psi_{1,1}^{\alpha,\delta_1}(t_k)$, orange in Fig. 5.12(e)] a modulation index

²⁵In the following I drop the subscript H in $\tilde{x}_H^j(t_k) = \tilde{x}_k^j$.

$\mu_{\nu,n,m}^{j,l}$ is defined similarly to the synchronization index $\gamma_{n,m}^{j,l}$ and again obtained within predefined non-overlapping time windows ν of width $\Delta\tau$, e.g., $\Delta\tau = 30\text{s}$ [circle in Fig. 5.12(e); based on a longer fragment than the one shown, i.e., 30s].

$$\mu_{\nu,n,m}^{j,l} = \left\langle e^{i\Delta\psi_{n,m}^{j,l}(t_k)} \right\rangle, \quad (5.28)$$

where $t_k \in [t_1 + (\nu - 1)\Delta\tau, t_1 + \nu\Delta\tau]$, $\nu = 1, \dots, [N\Delta t/\Delta\tau]$. Note that in the definition of Eq. (5.27) the phase difference $\Delta\psi_{n,m}^{j,l}$ is not confined to the interval $[0, 2\pi)$. However, this is not problematic here because the complex exponential in Eq. (5.28) is a 2π periodic function.

Step 4:

Recall that phases ψ_k^j obtained by the second Hilbert transform employing an `atan2` operator have a range $(-\pi, +\pi]$. Our observations show that there are two typical modulations associated with: (i) phase differences $\Delta\psi_{n,m}^{j,l} \bmod 2\pi$ close to zero, i.e., both signals j and l 'behave alike' or *positively modulated*, and (ii) phase differences $\Delta\psi_{n,m}^{j,l} \bmod 2\pi$ close to a value of $\pm\pi$, i.e., both signals 'behave opposed' or *negatively modulated*. This motivates the definition of *positive modulations* $\mu_{+,n,m}^{j,l}$ and *negative modulations* $\mu_{-,n,m}^{j,l}$ according to

$$\mu_{+,n,m}^{j,l} = \frac{\sum_{\langle\Delta\Psi_{n,m}^{j,l}\rangle_{\nu \in (-\frac{\pi}{2}, \frac{\pi}{2})}} |\mu_{\nu,n,m}^{j,l}|}{[N\Delta t/\Delta\tau]} \quad \text{and} \quad \mu_{-,n,m}^{j,l} = \frac{\sum_{\langle\Delta\Psi_{n,m}^{j,l}\rangle_{\nu \notin (-\frac{\pi}{2}, \frac{\pi}{2})}} |\mu_{\nu,n,m}^{j,l}|}{[N\Delta t/\Delta\tau]}, \quad (5.29)$$

where $\langle\Delta\Psi_{n,m}^{j,l}\rangle_{\nu} = \arg(\mu_{\nu,n,m}^{j,l})$ denotes the expectation value of the cyclic phase difference $\Delta\Psi_{n,m}^{j,l} = \Delta\psi_{n,m}^{j,l} \bmod 2\pi$ within the time window ν or simply the argument of the modulation index. In practice the decision which $\mu_{\nu}^{j,l}$ belongs to which index in Eq. (5.29) can easily be made by evaluating $|\arg \mu_{\nu}^{j,l}|$ that is smaller $\pi/2$ for the (first) positively modulated case and larger (or equal) $\pi/2$ for the negatively modulated case²⁶. I have chosen the expectation value expression in Eq. (5.29) to make the reader aware of the fact that inside a window ν not all individual phase differences must lie in the same hemisphere ($(-\pi/2, \pi/2)$, $[\pi/2, -\pi/2 \hat{=} 3\pi/2]$). Further, note the normalization in Eq. (5.29) by the total number of windows ν instead of the number of windows contributing to the sums in order not to exaggerate modulation indexes which are only based on a few windows. For short time series or applications where a finer resolution is desired, windows ν can also be defined as overlapping windows in *Step 3*. This, however, requires a normalization by the correct total number of such windows in Eq. (5.29).

The application of the described algorithm yields $2 \times (72 \times 72)/2 = 5184$ $\{2 \times (36 \times 36)/2 = 1296\}$ unique modulation coefficients. Thus, for a given pair of signals (x^j, x^l) one can separately study positive and negative amplitude-amplitude and frequency-frequency auto-modulations as well as amplitude-frequency cross-modulations. The latter type can also be studied for a single signal. For instance, positive amplitude-amplitude modulation means that an increase in the amplitude of the first signal positively influences (increases) the amplitudes in the second signal and vice versa. Negative amplitude-frequency cross-modulation on the other hand would indicate that an enhanced frequency consequently causes reduced amplitudes. This is especially characteristic of $1/f$ noise where amplitudes are larger for smaller frequencies [see Sect. 5.3.4].

In contrast to our related publications [GANS *et al.* 2009; STUMPF *et al.* 2010] I have decided to present a generalized cross-modulation analysis that allows for studying higher order modulations in this thesis. This way I can motivate the next steps that I would like to take in the future. The algorithms as suggested in both papers can be retrieved by setting $n = m = 1$ in the above described (generalized) cross-modulation-analysis. In the following the published and due to page limitations only very few unpublished results [see Appendix] are presented and subscripts $n = m = 1$ are dropped.

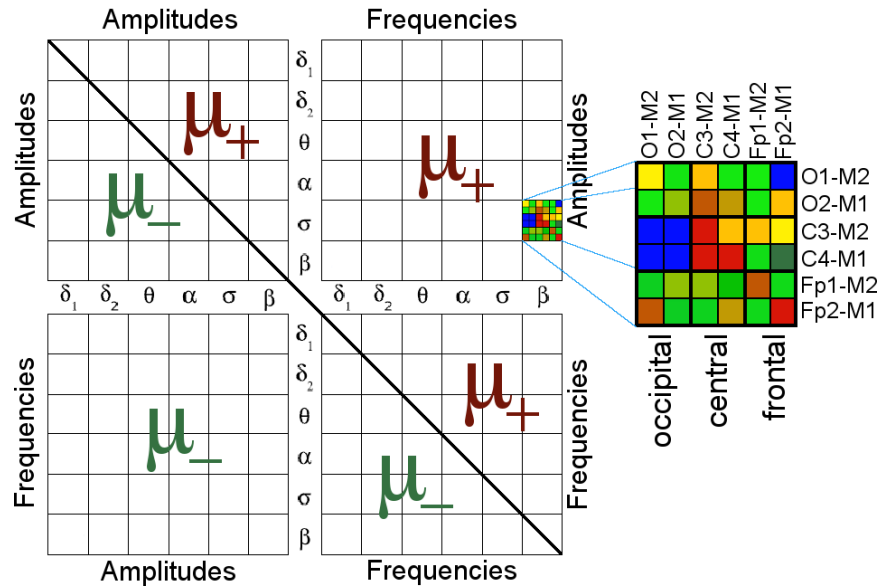


Figure 5.14.: Scheme how cross-modulation results are arranged throughout this chapter.

5.3.2. A Matrix Representation of Results

Even when setting $m = n = 1$ one obtains a large number of modulation coefficients ($N_c = 5184$) which are, hence, not easy to handle and interpret. To avoid confusion we suggested in our publication [GANS *et al.* 2009] a convenient way to visualize calculated positive and negative modulation coefficients in a matrix representation. I have illustrated the corresponding matrix scheme in Fig. 5.14: Modulation coefficients calculated following Eq. (5.29) are ordered according to: (i) frequency bands [from left to right and top to bottom $\delta_1, \delta_2, \theta, \alpha, \sigma, \beta$], (ii) signal combinations arranged in four sub-matrices amplitude-amplitude auto modulations [top left], frequency-amplitudes cross modulations [top right and lower left], and frequency-frequency auto modulations [lower right], (iii) positive direction [μ_+ , upper triangle] and negative direction [μ_- , lower triangle], and (iv) EEG leads in each cubicle of fixed frequency-band combinations. The order of the latter is from left to right and top to bottom: left and right occipital (back) EEG leads (O1-M2, O2-M1); left and right central EEG leads (C3-M2, C4-M1); and left and right frontal pole EEG leads (Fp1-M2, Fp2-M1) as depicted in the enlarged cubicle for positive $\sigma - \beta$ amplitude-frequency cross-modulation coefficients in Fig. 5.14. This scheme is employed to visualize cross- and auto-modulation results for sleep data from the SIESTA database.

5.3.3. Cross-Modulated Amplitudes and Frequencies During Disease-Free Sleep

Figure 5.15 shows average results from a cross-modulation analysis separately applied to EEG data from 190 healthy subjects in the SIESTA database during nocturnal wakefulness [Fig. 5.15(A)], light sleep S2 [Fig. 5.15(B)], deep sleep [Fig. 5.15(C)], and REM sleep [Fig. 5.15(D)]. Modulation coefficients are arranged according to Fig. 5.14, except for decreasing positive amplitude-amplitude modulations by a factor of 2 and increasing negative amplitude-amplitude modulations by a factor of 8 in panels (a) to enhance details. As can immediately be seen, certain features as for example traces of a diagonal in panels (b) are present across all sleep stages while others are only present during certain sleep stages [in Fig. 5.15 marked by red ellipses]. For a discussion on surrogate data to test whether such features are spurious or real see Sect. 5.3.4. Note that we checked that matrices remain practically the same when a second band-pass filter was employed before the second Hilbert transform to ensure narrow frequency bands. The reason is that instantaneous amplitude and frequency signals (A_k^j and f_k^j) already fluctuate within narrow bands after the first Hilbert transform. Before averaging over all 190 disease-free subjects qualitative stability of results was further checked (i) for single individuals [three examples are depicted in Appendix F.1], (ii) for three randomly chosen subsets comprising roughly 63 subjects each [results shown in

²⁶Whether an argument of exactly $\pi/2$, $-\pi/2$ belongs to either one of the modulation indexes is unimportant.

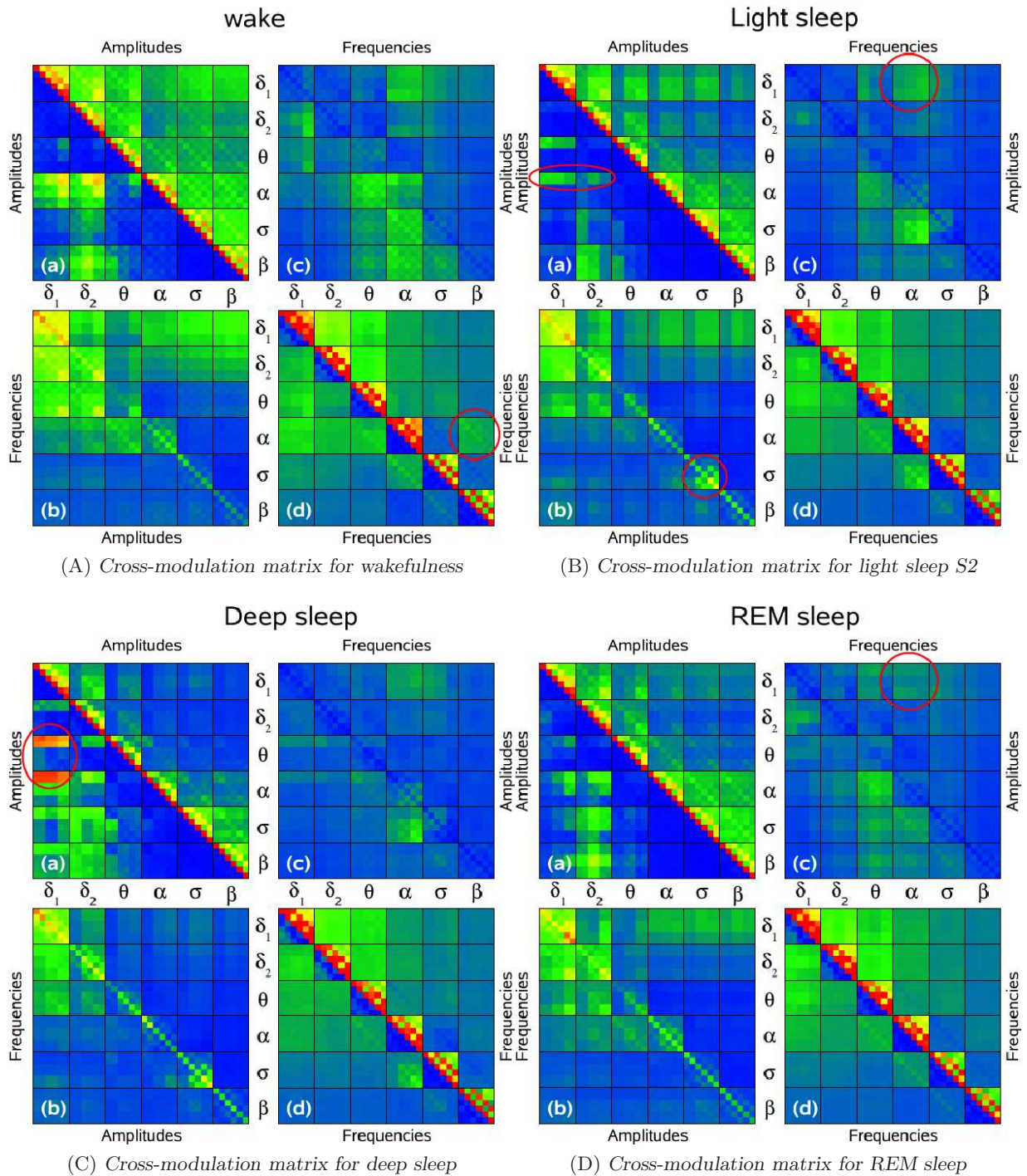


Figure 5.15.: Average cross-modulation results from 190 healthy subjects [SIESTA database] separately for (A) nocturnal wakefulness, (B) light sleep, (C) deep sleep, and (D) REM sleep. Matrices are arranged according to the scheme in Fig. 5.14 showing amplitude-amplitude auto modulations in panels (a), amplitude-frequency cross modulations in panels (b,c), and frequency-frequency auto modulations in panels (d). Modulation strength $|\mu_{\pm}|$ increases from blue to green, yellow, and red. Note: The color code is modified in panels (a) where values in the upper triangle ($\mu_+^{A^j A_k^l}$) are increased by a factor of 8 and values in the lower triangle ($\mu_+^{A_k^j A_k^l}$) are decreased by a factor of 2 to enhance details. Red ellipses mark typical features associated with the respective sleep stage. Figures adapted from supplements of our paper [GANS et al. 2009].

Appendix F.2], and (iii) for a linear decomposition of all six EEGs by independent component analysis in three random subjects [HYVÄRINEN et al. 2001; ZIEHE et al. 2004; MEINECKE et al. 2005].

Red main diagonals correspond to unit self-modulation coefficients, i.e., combining amplitude and frequency signals with themselves. The checkerboard structure around the self-modulation

coefficients which is especially pronounced for frequency-frequency auto modulations [Fig. 5.15 panels (d)] originates in enhanced interrelations when combining signals of the same frequency band from neighboring electrodes and the same hemisphere, i.e., left (right) occipital & left (right) central and left (right) central & left (right) frontal. Since EEG recordings represent integrals over action potentials from an extended region in the brain, they are spatially rather unlocalized and, thus, redundant information is expected to be obtained from neighboring EEG leads in the same hemisphere and for the same signal type. Secondary diagonals in Figs. 5.15(Ab,Bb,Cb,Db) are likely related to $1/f$ noise as is discussed in Sect. 5.3.4.

A prominent feature present during nocturnal wakefulness but not during sleep stages is a positive $f_k^\alpha f_k^\beta$ modulation [red circle in Fig. 5.15(Ad)] which is related but not identical with phase-synchronization between α and β brain waves [NIKULIN AND BRISMAR 2006] or their long-range temporal correlations [NIKULIN AND BRISMAR 2004] during wake. The main cause in my opinion is a fluctuating transition between being awake and conscious where β waves (focal waves) are especially present and falling asleep again where the brain descends from β to fast α and finally to a slow α towards increased θ and δ . During an arousal the α frequency has to increase since the subject reaches wakefulness and on the other hand as soon as the subject transits to a more conscious state high frequent β is established.

Traces of negative auto-modulation of α amplitude with δ amplitude are observed during all sleep stages and wakefulness, however, they are especially strong during deep sleep [Figure 5.15(Ca)] and enhanced during wake [Figure 5.15(Aa)] while at the lowest during REM sleep [Figure 5.15(Da)]. Hence, an increase in α amplitude is accompanied by a decrease in δ amplitude and vice versa. Prevalent α waves are the typical pattern of the wake state with closed eyes while δ waves are the main property of deep sleep. Consequently, sleep onset intrinsically results in a reduction in α activity and an incidental increase in δ amplitude that evolves via the light sleep stage towards deep sleep. REM sleep, on the other hand, is characterized by an overall reduced EEG amplitude, high varying frequencies, and an apparent mostly 'random' and 'chaotic' appearance compared with all other stages [cp. Sect. 2.3], maybe due to rapid eye movements. This explains its fainted $\alpha - \delta$ amplitude anti-modulation. The reason for corresponding modulation indexes being largest in occipital EEG leads is the generally larger α activity in the brain's rear parts.

Only throughout light sleep S2 and deep sleep (deeper non-REM sleep) a strong negative modulation of σ amplitudes with σ frequency [Figs. 5.15(Bb,Cb)] is prevalent and appears exclusively in central and frontal EEG leads. Aside such $A_k^\sigma f_k^\sigma$ anti-modulation one observes additional positive $f_k^\alpha A_k^\sigma$ cross-modulations [Figs. 5.15(Bc,Cc)] and negative $f_k^\alpha f_k^\sigma$ auto-modulations [Figs. 5.15(Bd,Cd)] which again are predominant in central- and frontal EEG leads compared with wakefulness and REM sleep where their values are weaker (particularly during REM sleep) and not concentrated in central- and frontal EEGs. σ waves are associated with sleep spindles [Sect. 2.3] which have a short duration of typically 2 to 4 seconds but can be as short as 0.5 seconds or as long as 10 seconds. Sleep spindles are predominantly found in frontal EEG leads (especially in young) and in central EEG leads during light sleep S2 but are also a typical pattern during deep sleep while almost absent in other sleep stages [OLBRICH AND ACHERMANN 2005]. This explains the prevailing observation of σ -related modulations during light sleep and deep sleep and especially in both central- and frontal leads [Figs. 5.15(B,C)]. Although, $A_k^\sigma f_k^\sigma$ anti-modulation complies with my own observation that sleep spindles of larger amplitude have smaller frequencies and vice versa I do not know about this being systematically checked in sleep research. Sleep spindles have been associated with electromagnetic stimulation (e. g., the use of cellular phones shortly before bedtime significantly increases the number of sleep spindles during the first 30min of non-REM sleep [HUBER *et al.* 2000]) and with cognitive function and performance (their number is decreased in mental retardation, see [SPINOSA AND GARZON 2007] and references therein). However, it remains open whether an increased σ activity has a positive effect on sleep quality and thus would be a desired effect. Both $f_k^\alpha A_k^\sigma$ modulation and $f_k^\alpha f_k^\sigma$ anti-modulation might be explained by the closeness of the two frequency bands. Since f_k^σ decreases when A_k^σ increases (anti-modulation) the frequency might migrate into the lower frequency band which is α and, thus, increase α frequency - A_k^σ increase causes f_k^α increase. On the other hand, an f_k^α increase

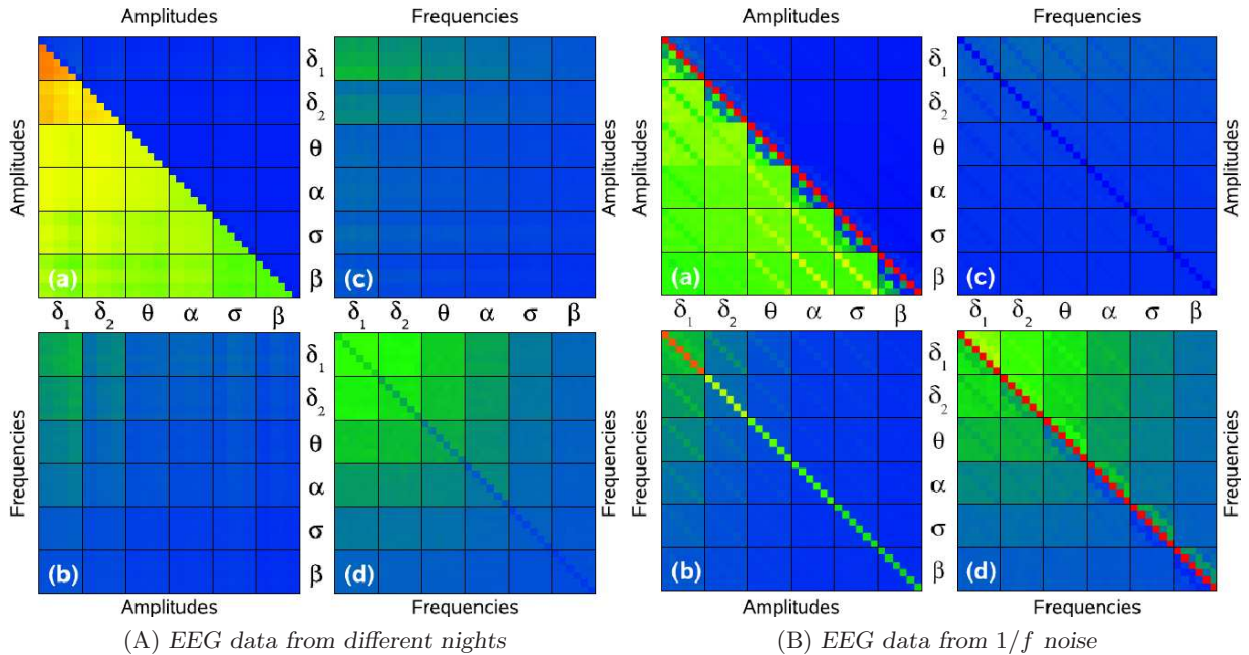


Figure 5.16.: Cross-correlation analysis results for surrogate data generated by (A) combining EEG data from different nights recorded in the same subject [for instance A_k^α from the first night is combined with f_k^α from the second night] and (B) $1/f$ -correlated random noise [$\beta = 1$]. In panels (a) the same value modification as in Fig. 5.15(a) was applied.

might fade to the σ band and reduce its frequency f_k^σ .

Except for frequency-frequency modulations inter-band coupling is generally attenuated throughout deep sleep compared with other sleep stages which might indicate a reduced cerebral control during deep sleep.

5.3.4. Surrogate Testing

Testing a method with surrogate or randomized data is the classical approach in time series analysis to check the significance of findings, i.e., identify real and spurious features in representations such as Fig. 5.15. Two easy ways to design surrogate data for cross-modulation analysis in brain wave recordings during sleep are (i) combining EEG data recorded in the same subjects but from different nights or (ii) feeding artificially generated time series of correlated $1/f$ noise into the cross-modulation analysis algorithm. The first approach is justified by the observation that brain recordings in the same subject but from different nights obey similar characteristic features. Modulation indexes are derived between each pair of amplitude and frequency signals recorded during two different nights. Corresponding cross-modulation results are depicted in Fig. 5.16(A). The second approach is motivated by the observation of long-term correlations and $1/f$ -noise in signals from many living systems and findings are illustrated in Fig. 5.16(B). In both figures differentiated modulation structure as in Fig. 5.15 is absent which implies discussed findings are unlikely²⁷ to be spurious. However, frequency-frequency modulations in the δ and θ bands [Figs. 5.16(Ad,Bd)] appear enhanced and, thus, findings in corresponding areas in Fig. 5.15 are likely spurious.

Another feature of Fig. 5.16(Bb) is the earlier mentioned characteristic secondary diagonal which links its concomitant appearance in Fig. 5.15 to $1/f$ noise. This makes sense when recalling that the power spectrum of $1/f$ noise decays as a power law with a spectral exponent $\beta = 1$ [Sect. 1.2] which means an increase in frequency is associated with a decrease in amplitude ($A \propto f^{-\beta/2}$).

Note also that the same enhancement by a factor of 8 in the anti-modulation triangle and the same reduction by a factor of 2 in the positive modulation triangle took place in Figs. 5.16(Aa,Ba). This

²⁷In a strict sense only the hypotheses of pure $1/f$ noise and 'random' can be discarded.

was originally done here to ensure the same rescaling as in Figs. 5.15(Aa,Ba,Ca,Da), however, it is subject to misinterpretation now. In reality both triangles corresponding to positive and negative modulation in panels (a) exhibit practically the same modulation values which would result in a similar picture as in panels (b). Discussed features in Figs. 5.15 are indeed enhanced compared with surrogate findings.

5.3.5. Cross-modulation in Parkinson's Disease

Besides recordings from disease-free subjects the SIESTA database contains polysomnographic recordings from Parkinson's disease (PD) patients which were gathered in the Barcelona and the Vienna laboratories [see also Sect. 2.3]. However, when studying the fluctuations I had to realized that disease classification in the SIESTA database could be questioned in several cases. In particular many PD patients simultaneously experience sleep apnea expressed in an apnea-hypopnea index (AHI) significantly larger than 10 per hour which might be related with their increase age. Especially in males, an age above 50 has been associated with an increased risk of sleep apnea disease. Thus, we decided to select only PD patients ($N_{PD} = 10$) with an AHI < 10/h from the SIESTA database and also selected age-matched disease-free subjects ($N_{df} = 10$) from the same labs. For simplicity and since we originally intended to compare our results to the results from the DAPHNET database [Sect. 2.3] not all six available electrodes were considered but only both central EEG leads C3-M1 & C4-M1 and the occipital lead O1-M2.

EEG recordings from patients and controls were analyzed by employing the cross-modulation analysis algorithm [Sect. 5.3.1] yielding cross-modulation indexes $\mu_+^{j,l}$ and $\mu_-^{j,l}$ (Steps 1-4) where 1 : 1 phase-synchronization indexes $\gamma_{1,1}^{j,l} = \gamma^{j,l}$ (Steps 1-2, and also setting $m = n = 1$; subscripts again dropped) were additionally derived. Note that for 1:1 phase-synchronization quantified by $\gamma^{j,l}$ only signals from the same frequency bands can be compared with each other, i.e., $j = l : j \in \{\beta, \sigma, \alpha, \theta, \delta_1, \delta_2\}$.

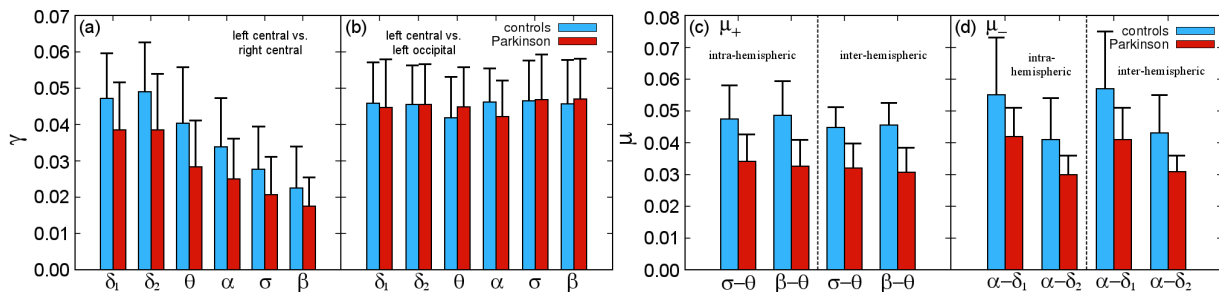


Figure 5.17.: Results from a comparative phase-synchronization analysis as well as from a cross-modulation analysis of 10 Parkinson's disease patients [in all panels red bars] versus 10 age-matched healthy controls [in all panels, blue bars]. (a,b) Whole night's average phase-synchronization indexes γ for each group and for all six frequency bands obtained from (a) central EEG leads from the left and right hemisphere (C4-M1 vs. C3-M2) and (b) central and occipital [back] EEG leads from the left hemisphere (C3-M2 vs. O1-M2). (c,d) Whole-night-averaged amplitude-frequency cross-modulation indexes; (c) μ_+ and (d) μ_- for the band combinations printed below the bars: $\sigma-\theta$, $\beta-\theta$ in (c) and $\alpha-\delta_1$, $\alpha-\delta_2$ in (d) for healthy subjects and Parkinson patients. Values in (c,d) are means of both intra-hemisphere combinations (C3-M2,C3-M2 and C4-M1,C4-M1) for the left four bars, and of both inter-hemisphere combinations (C3-M2,C4-M1 and C4-M1,C3-M2) for the four right bars. Standard deviations are indicated by error bars.

Figures 5.17(a,b) compare phase-synchronization results obtained from disease-free subjects [controls, light blue] with those from PD patients [red] where indexes $\gamma^{j,j}$ were separately calculated for pairs of signals from different locations on the skull and for all six frequency bands [see Tab. 5.2 for definition]. Phase-synchronization between central signals from the left and from the right hemisphere (C3-M2, C4-M1) is clearly reduced in PD patients compared with age-matched disease-free controls for all bands [Fig. 5.17(a)]. On the other hand, a comparison of phase synchronization indexes $\gamma^{j,j}$ obtained from pairs of signals recorded at left center position (C3-M2) and left occipital (left back) position (O1-M2), i.e., different anteriorposterior positions in the same hemisphere, yields no significant difference between controls and PD patients [Fig. 5.17(b)].

sleep stage	location	δ_1	δ_2	θ	α	σ	β
wake	left-right	0.74 † ○	0.73 † ‡	0.65 † ‡	0.76 ○	0.77 ○	0.7 ★ ‡
light	left-right	0.81	0.80 ★ ○	0.72 ★ ‡	0.77 ○	0.72 ★ ‡	0.82
deep	left-right	0.90	0.85	0.76 ‡	0.67 † ‡	0.75 ○	0.95
REM	left-right	0.78 † ‡	0.75 † ‡	0.68 † ‡	0.69 † ‡	0.76	0.8
whole night	left-right	0.82 ★ ○	0.78 ★ ‡	0.70 ★ ‡	0.74 ★ ‡	0.75	0.78
whole night	center-back	0.97	1.00	1.07	0.91	1.01	1.03

Table 5.3.: Ratios of 1:1 phase-synchronization indexes $\gamma^{j,j} : j \in \{\delta_1, \delta_2, \theta, \alpha, \sigma, \beta\}$ for PD patients and age-matched disease-free controls, $\gamma_{PD}^{j,j}/\gamma_{df}^{j,j}$, across different sleep stages and for different electrode locations. Significant differences between PD patients and controls are indicated by symbols, *t* test: $p < 0.01$ (†), $p < 0.05$ (★) and Wilcoxon test $p < 0.01$ (‡), $p < 0.05$ (○).

Besides, inter-hemispheric phase-synchronization decreases with increasing frequency (from δ_1 to β) while intra-hemispheric phase-synchronization is independent of frequency [cp. Figs. 5.17(a,b)]. In order to quantify and verify differences between both groups of subjects the ratio of the average phase-synchronization indexes, i. e., the values $\gamma_{\text{Parkinson}}/\gamma_{\text{healthy controls}}$, were studied separately for nocturnal wakefulness and different sleep stages (light sleep S2, deep sleep, and REM sleep) employing two different, significance tests – (i) a paired two-sided heteroscedastic Student’s-t test [Appendix D.1] and (ii) a Wilcoxon rank-order test²⁸ [see Appendix D.2]. Results are reported in Tab. 5.3 together with values for the whole nights averages. Symbols behind the numbers indicate significance for both statistical tests [see table caption]. The last row exemplarily reports non-significant intra-hemispheric results for comparison. We consider differences between the two groups as significant, if both tests indicate probabilities $p < 0.05$ for equality. Then we find a major reductions in PD phase-synchronization during REM sleep and during night-time wake. The absence of significance in both the σ and β band during REM sleep is substantiated by the earlier discussed property of σ waves predominantly occurring during light sleep 2 and deep sleep and β waves being associated with conscious task solving and focused thinking [see Sect. 5.3.3]. Similarly, a reduced (Student’s-t test) significance in the α band and σ band during nocturnal wakefulness can be explained by a reduced power of α and σ waves during wake – α waves indicate an increased drowsiness, sleep onset, and the transition to light sleep stages 1 & 2, and σ waves mainly occur during light sleep S2 and deep sleep. However, reductions in a few bands are weakly significant also during light sleep (non-REM S2 only) and for the whole night averages; the latter corresponding to the data also presented in Fig. 5.15(a). The only significant decrease during deep sleep (in the α band) seems not to be meaningful, since statistics is rather weak for deep sleep [see Fig. 2.9 for sleep stage distribution] All ratios in the last row of Tab. 5.3 corresponding to Fig. 5.17(b) fluctuate around one thus confirm no significant differences between both disease-free controls and PD patients.

Figures 5.17(c,d) show selected and averaged results, i.e., intra-hemispheric [left panel halves] and inter-hemispheric [right panel halves] positive cross modulations $\mu_+^{A^\sigma f^\theta}$ & $\mu_+^{A^\beta f^\theta}$ [Fig. 5.17(c)] and negative cross modulations $\mu_-^{A^\alpha f^{\delta_1}}$ & $\mu_-^{A^\alpha f^{\delta_2}}$ [Fig. 5.17(d)], from a cross-modulation analysis which yielded figures similar to Fig. 5.15 separately for PD patients and for disease-free controls [these figures can be found in Appendix F.3]. Note that the selected cross-modulation indexes show the most significant difference between disease-free controls and PD patients [dark red areas in Fig. 5.18; discussed later]. Depicted modulation indexes were averaged over similar EEG lead combinations after confirming the appropriateness of such averaging by an initial separate consideration. For instance, the values for the last two bars of the right half of Fig. 5.17(c) are defined by

$$\mu_+^{A^\beta f^\theta} = \frac{1}{2} \left(\mu_+^{A^\beta_{C3-M2}, f^\theta_{C4-M1}} + \mu_+^{A^\beta_{C4-M1}, f^\theta_{C3-M2}} \right). \quad (5.30)$$

²⁸The Student’s-t test is more common in physics, but becomes rather unreliable for a small number of considered data points (here $N_{df} = N_{PD} = 10$). The Wilcoxon rank-order test, on the other hand, is a standard significance test employed in medical applications and hence is more accepted there.

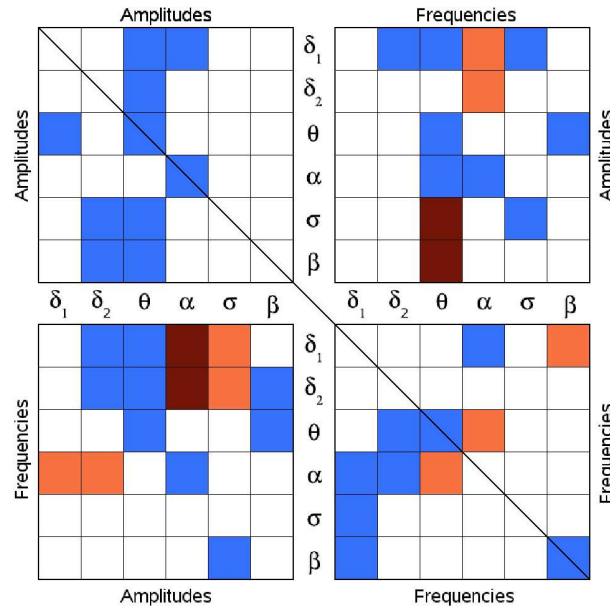


Figure 5.18.: Significance of differences in (cross)-modulation indices μ_+ (upper triangle) and μ_- (lower triangle) between PD patients and age-matched healthy controls as obtained from Student's t tests. Blue cubicles indicate probabilities $p < 0.05$, orange cubicles $p < 0.01$, and dark red cubicles $p < 0.001$ for equality of the cross-modulation indices in patients and controls. White cubicles indicate non-significant differences. The first row and column refer to amplitudes in the δ_1 band, the second to amplitudes in the δ_2 band, etc. The seventh row and column refer to frequencies in the δ_1 band, etc., so that all possible band combinations are represented. The results are simplified by harmonically averaging individual significance levels obtained for all nine studied electrode combinations based on the two central and one occipital EEG leads. The detailed results for the highly significant points ($p < 0.001$, dark red) are reported in Fig. 5.17.

In this more evolved type of analysis, differences between disease-free subjects and PD patients are also significant for signals recorded within the same brain hemisphere [left halves of Figs. 5.17(c,d)]. In addition, higher levels of significance are achieved for the comparison of the two groups than in the phase-synchronization results [Figs. 5.17(a,b)]. For both electrodes in the same brain hemisphere and electrodes in different hemispheres $\mu_+^{A^\sigma f^\theta}$, $\mu_+^{A^\beta f^\theta}$, $\mu_-^{A^\alpha f^{\delta_1}}$, and $\mu_-^{A^\alpha f^{\delta_2}}$ are significantly reduced in PD patients – a Student's- t test yields $p < 0.001$ for equivalence.

By cross-modulation-analysis of both whole-nights data (adaptation and recording night) averaged separately over PD patients and age-matched disease-free subjects a full significance matrix ordered similarly to the scheme in Fig. 5.14 – with only three EEG leads (C3-M2, C4-M1, and O1-M2) – can be derived employing a paired heteroscedastic Student's- t test. In order to simplify the altogether 1296 unique p values the nine individual significance values in each cubicle representing the same band combinations but different electrode combinations (and in particular those for intra- and inter-hemisphere effects) have been harmonically averaged. Results are depicted in Fig. 5.18, where the cubicle's color indicates the probability for an equivalence of modulation indexes from PD patients and age-matched disease-free subjects for the corresponding signal combination and in the corresponding frequency band [$p < 0.001$ dark red, $p < 0.01$ orange, < 0.05 blue; white cubicles indicate non-significant modulation]. Note, that some individual cross-modulation indexes in a cubicle might not be significantly different while the majority of the nine is. Note also that there is no significant increase of any average cross-modulation coefficient in PD patients. Figure 5.18 proves that significant decreases of cross-modulation indexes occur also for other band combinations in addition to those reported in detail in Figs. 5.17(c,d). We expect that some additional features could be quantified when significance matrices are separately calculated for individual sleep stages.

In addition to the here presented results we studied cross-modulations in EEG recordings from sleep apnea patients and healthy subjects of corresponding age (DAPHNET database). The full cross-modulation matrices can be found in Appendix F.4 separately for all sleep stages and nocturnal wakefulness and for apnea patients [Fig. F.5] and age-matched healthy subjects [Fig. F.6].

Although there are significant differences between healthy controls and apnea patients which exhibit larger cross-modulation coefficients in general, I will not further discuss these (preliminary) results. Note that results obtained from recordings of the SIESTA database cannot directly be compared with the ones obtained from the DAPHNET database because of a different experimental setup (recording devices and study protocol).

6. Summary

During my PhD thesis I have studied time series from physiological complex systems. The selection of databases presented in this thesis contains time series capturing the dynamics of both the cardiorespiratory system and the brain system.

Fluctuations

In Chapt. 3 I focused on studying fluctuations in physiological time series such as heartbeat and respiration. I have introduced the standard monofractal fluctuation analysis methods in Sect. 3.1. Further, I discussed in Appendix E.1 and illustrated in Appendix E.2 that a wavelet based fluctuation analysis can prove useful in studying large databases because it is characterized by less computational costs and provides equivalent detrending capabilities compared with detrended fluctuation analysis (DFA) which is the most established method today.

I have employed 2nd-order DFA to heartbeat and respiration from 180 healthy subjects and studied the effects of healthy aging on the scaling behavior in two different scales ranges. The short-term fluctuation exponent α_1 associated with parasympathetic autonomous control and sometimes employed to assess cardiac risk shows a strong age dependence during all sleep stages [Sect. 3.2.2]. Its value increases with disease-free aging for young towards intermediately aged subjects and then reduces again towards elderly. The long-term fluctuation exponent α_2 shows a similar qualitative behavior as the fluctuation exponent associated with respiration, i. e., it indicates uncorrelated signals during deep sleep and only weak correlations during light sleep. During nocturnal wakefulness and rapid-eye-movement sleep (REM) significant long-term correlations are found. While there is no age dependence in long-term scaling during light sleep and deep sleep there is a decrease in the fluctuation exponent upon aging during wake and respiratory REM. In heartbeat during REM I obtained an opposite behavior, i. e., an increase in α_2 upon aging.

In Sect. 3.3.4 I suggested a generalized binomial-multifractal model (GB-MFM) that allows for an independent adjustment of multifractality strength and monofractal correlation ($h(2)$). I comprehensively studied this model employing both the standard multifractal DFA (MF-DFA) and a newly suggested multifractal centered moving averaging analysis (MF-CMA). I think that the GB-MFM can be employed in time series for hypothesis testing against a model of certain multifractality and correlation. I have further discussed that any fluctuation function based method can trivially be generalized to a multifractal variant, this was shown in Appendix E.1 for wavelet fluctuation analysis.

Then I focused on studying spurious multifractality appearing in certain types of monofractal data, see Sect. 3.4. I motivated that weak multifractality with $\Delta h < 0.2$ can be obtained from purely monofractal data generated by Fourier filtering. In particular a block shuffling technique was suggested to selectively destroy correlations on small, large, or intermediate scales, see Sect. 3.3.6. Although, there were already attempts to study the statistics of ectopic beats this was never done for sleep data. It is known that the number of premature beats can be used as a predictor of total mortality. Hence, it is expected that other pathologies affect the statistics on ectopic beats as well. One could investigate properties such as return intervals of extrasystoles in diseased patients versus healthy controls.

Quasioscillations

In Chapt. 4 I have reviewed phase-rectified signal averaging (PRSA) and introduced deceleration capacity (DC) which was proven to be a better predictor of total mortality in post-infarction patients than the currently used gold standard left-ventricular ejection fraction (LVEF), see Sects. 4.1, 4.1.3. I have suggested improved anchor criteria and an inclusion of windows with missing data points as generally observed in large datasets. In order to study the daily rhythm in DC I have separated 24 hours ECG recordings from post-infarction patients into episodes of 3

hours duration [Sect. 4.1.7]. Knowledge of the daily rhythm is required for an improvement of risk classification thresholds and for a generalization from 24 hours recordings to short-term recordings of just a few hours or minutes. I obtained the intriguing result that there is a 24 hours cycle in DC. DC is lowest in the late morning which strongly correlates with the empirical observation that most deaths occur around 10am-11am. This finding supports the thesis of DC being a well performing predictor for total mortality. I further found that DC is systematically reduced in diabetes patients which complies with the general belief that diabetes increases cardiac risk.

I employed the PRSA method for the first time to polysomnographic recordings [Sect. 4.1.8] and studied the effects of Parkinson's disease, sleep apnea, depression, periodic leg movement, and anxiety on oscillations in heartbeat interval data [Sect. 4.1.9]. I reported notably differences for different sleep stages and diseases. Most prominent differences in sleep apnea subjects compared with healthy controls. There were no significant differences between recordings from different nights.

Finally, I studied the age dependence of DC in both post-infarction patients and healthy subjects during sleep [Sects. 4.1.6 and 4.1.10]. I obtained for both groups of subjects similar results indicating a linear reduction in DC upon aging. This finding, however, might be related to an in general higher cardiac risk in elderly. Moreover, DC seems to be reduced during REM sleep suggesting a higher risk during REM sleep compared with non-REM sleep. However, sleep itself is considered to be cardioprotective by most cardiologists.

In the second part of Chapt. 4 I generalized PRSA to a bivariate method and illustrated its potential use to study interrelated signals such as heartbeat and blood pressure [Sect. 4.2]. I hope in the future to systematically investigate the changes in heartbeat upon variations in blood pressure which are related to the baroreflex. We believe to exploit results from an bivariate analysis to additionally improve total mortality risk classification. I further suggest to systematically investigate the regulation between heartbeat, blood pressure, and respiration in a multivariate analysis in order to validate the respiratory gating theory. First results from 30min of simultaneously recorded heartbeat and blood pressure are promising. I believe that multivariate PRSA can also be employed to study data from various other sources in interdisciplinary research.

Synchronization

The first part of Chapt. 5 was dedicated to investigating the mutual coupling between heartbeat and respiration in terms of phase synchronization. Therefore, I suggested an automated method to characterize phase synchronograms which are usually studied by visually inspection in much smaller datasets separately for each subject, see Sect. 5.2. I employed automated synchronogram analysis to study aging effects upon cardiorespiratory phase synchronization across sleep stages in Sect. 5.2.6. While there are no significant aging effects during wakefulness, light sleep S1, and REM sleep $n : 1$ phase synchronization systematically reduces with healthy aging during light sleep S2 and deep sleep. Most total synchronization was found during deep sleep. In the second part of Chapt. 5 I introduced cross-modulation analysis to study cross modulations between amplitudes and frequencies in brain wave recordings. The advantage of cross-modulation analysis is that there is no limitation on which type of signals is studied compared to other synchronization methods that require fixed frequency ratios between the signals under investigation. I introduced cross-modulation analysis in a more general way in Sect. 5.3.1 compared with our papers because I would like to motivate future directions of research. I think higher order cross-modulation analysis, i. e. for parameters m and n in an analogous way as higher order phase synchronization was studied in Sect. 5.2.6. I am convinced that this can yield an improved understanding of complex systems. Moreover, I think it should be possible to implement a time delayed version of cross-modulation analysis which then facilitates studying the dynamics of modulations in a similar way as one studies the dynamics in time domain by cross-correlation analysis or BPRSA.

Furthermore, I would like to investigate the mutual synchronization in a multivariate analysis. The SIESTA database contains for each subject many more signals that were not systematically analysed yet. The results from such a study might be useful for implementing an automatic sleep stage detector.

A. Wiener-Khinchin Theorem

To see the equivalence of Eqs. (1.14) and (1.15) consider the separation $s = l - k$, and let g and h be some functions that map the index space ($k \in \mathbb{I} = \mathbb{N}$) to the real space ($g(k), h(k) \in \mathbb{R}$). Then the following expression which has the same structure as the double sum in Eq. (1.15) can be derived:

$$\begin{aligned}
\sum_{k,l=1}^N g(k)h(k + (l - k)) &= \underbrace{g(1)h(1 + (1 - 1)) + g(2)h(2 + (2 - 2)) + \dots + g(N)h(N + (N - N))}_{l=k} + \\
&\underbrace{g(1)h(1 + (2 - 1)) + \dots + g(N - 1)h((N - 1) + (N - (N - 1)))}_{s=l-k=+1} + \dots + \underbrace{g(1)h(1 + (N - 1))}_{s=l-k=N-1} + \\
&\underbrace{g(2)h(2 + (1 - 2)) + g(3)h(3 + (2 - 3)) + \dots + g(N)h(N + ((N - 1) - N))}_{s=l-k=-1} + \\
&\dots + \underbrace{g(N)h(N + (1 - N))}_{s=l-k=1-N}
\end{aligned}$$

$$\begin{aligned}
\sum_{k,l=1}^N g(k)h(k + (l - k)) &= \sum_{s=0}^{N-1} \sum_{k=1}^{N-s} g(k)h(k + s) + \sum_{s=1-N}^{-1} \sum_{k=|s|+1}^N g(k)h(k + s) \\
&= \sum_{s=0}^{N-1} \sum_{k=1}^{N-s} g(k)h(k + s) + \sum_{s=1-N}^{-1} \sum_{k=1}^{N-|s|} g(k + |s|)h(k + |s| + s)
\end{aligned}$$

Now, in the last double sum $s < 0$ yields $|s| + s = 0$. When $g = h$ the double sums can be unified and the sum over k equals the auto-covariance function [Eq. (1.9a) with $y = x$] times¹ N

$$\sum_{k,l=1}^N g(k)g(k + (l - k)) = \sum_{s=1-N}^{N-1} \frac{N}{N} \sum_{k=1}^{N-|s|} g(k)g(k + |s|) = N \sum_{s=1-N}^{N-1} \text{Cov}_{gg}(s) \quad (\text{A.1})$$

By combining Eqs. (1.15) and (A.1) one finally obtains the power spectrum as the Fourier transform of the auto-covariance function².

$$P(f) = \frac{1}{N} \sum_{s=1-N}^{N-1} \text{Cov}_{xx}(s) e^{-i\omega s} \quad (\text{A.2})$$

This property can rigorously be shown in the continuous case and is then known as the Wiener-Khinchin Theorem. Note that Eq. (A.2) is only in the limit $N \rightarrow \infty$ equivalent with the definition in Eq. (1.13).

¹For the unbiased version of Eq. (1.9a) the factor becomes $N - |s|$.

²Note: Indeed, I did not use Eq. (A.1), but instead the previous representation since $g(k) = x_k$ and $h(k + s) = x_{k+s} e^{-i\omega s}$. However, the sums can then be unified in the same way as shown yielding the auto-covariance function and a remaining $e^{-i\omega s}$ term.

B. Auto Correlation in AR(1) Time Series

Setting $p = 1$ and $a_0 = 1$ in the definition in Eq. (1.33) an AR(1) process follows

$$x_k = a_1 x_{k-1} + \varepsilon_k \quad , x_1 = \varepsilon_1, k = 2, \dots, N \quad (\text{B.1})$$

where $\{\varepsilon_k\}_{k=1, \dots, N}$ are drawn from a normalized normal distribution $\mathcal{N}(0, 1)$. Recursively inserting Eq. (B.1) in itself yields

$$\begin{aligned} x_k &= a_1 x_{k-1} + \varepsilon_k \\ &= a_1^2 x_{k-2} + \varepsilon_k + a_1 \varepsilon_{k-1} \\ &= a_1^3 x_{k-3} + \varepsilon_k + a_1 \varepsilon_{k-1} + a_1^2 \varepsilon_{k-2} \\ &\vdots \\ x_k &= \sum_{j=0}^{\infty} a_1^j \varepsilon_{k-j}. \end{aligned} \quad (\text{B.2})$$

Note that Eq. (B.2) represents an *infinite moving average process* ($MA(\infty)$) with the parameters $b_j = a_1^j$. MA(q) processes generally follow $x_k = \sum_{j=0}^q b_j \varepsilon_{k-j}$ with $b_0 = 1$. Obviously, Eq. (B.2) only converges for $|a_1| < 1$ which is satisfied in the example in Sect. 1.5.1 and Fig. 1.1 where $a_1 = 0.98$. AR(p) processes in general [Eq. (1.33)] can be expressed by a MA(∞) processes if the roots of their corresponding characteristic polynomial $1 - a_1 z - a_2 z^2 - \dots - a_p z^p = 0$ are outside the unit circle [SCHLITTEGEN AND STREITBERG 1999]. This condition can be obtained from rewriting the definition of an AR(p) process in Eq. (1.33) with the backshift operator $Bx_k = x_{k-1}$

$$\left(1 - \sum_{j=1}^p a_j B^j\right) x_k = \varepsilon_k. \quad (\text{B.3})$$

Because the noise $\{\varepsilon_k\}$ is stationary (here I set $\mu_\varepsilon = 0$, and $\text{Cov}_{\varepsilon\varepsilon}(\tilde{s}) = \sigma_\varepsilon^2 = \delta(\tilde{s})$ by definition), the AR(1) process being linear in ε is also stationary. For the expectation value of the AR(1) time series follows with $\langle \varepsilon_k \rangle = \mu_\varepsilon = 0$

$$\langle x_k \rangle = \langle a_1 x_{k-1} + \varepsilon_k \rangle = a_1 \langle x_{k-1} \rangle = \dots = 0 \quad (\text{B.4})$$

and for the variance considering Eq. (B.4) and using that $\{\varepsilon_k\}$ and $\{x_k\}$ are uncorrelated

$$\begin{aligned} \langle x_k^2 \rangle &= \langle a_1^2 x_{k-1}^2 \rangle + \langle \varepsilon_k^2 \rangle + \underbrace{\langle 2a_1 x_{k-1} \varepsilon_k \rangle}_{=0} \\ \sigma_x^2 &= \langle x_k \rangle^2 = \frac{\sigma_\varepsilon^2}{1 - a_1^2} \end{aligned} \quad (\text{B.5})$$

According to Eq. (1.10b) the auto-correlation function of an AR(1) process $\{x_k\}$ is then expressed by (without loss in generality $s > 0$)

$$\begin{aligned} C(s) = \text{Cor}_{xx}(s) &= \frac{1}{\sigma_x^2 N} \sum_{k=1}^{N-s} x_k x_{k+s} \stackrel{(\text{B.2})}{=} \frac{1}{\sigma_x^2 N} \sum_{k=1}^{N-s} \sum_{i=0}^{\infty} a_1^i \varepsilon_{k-i} \sum_{j=0}^{\infty} a_1^j \varepsilon_{k+s-j} \\ &= \frac{1}{\sigma_x^2} \sum_{i=0}^{\infty} \sum_{j=0}^{\infty} a_1^i a_1^j \frac{1}{N} \sum_{k=1}^{N-s} \varepsilon_{k-i} \varepsilon_{k+s-j} = \frac{1}{\sigma_x^2} \sum_{i=0}^{\infty} \sum_{j=0}^{\infty} a_1^i a_1^j \text{Cov}_{\varepsilon\varepsilon}(s+i-j) \end{aligned}$$

where from the vanishing auto-covariance function (and vanishing auto-correlation function) of white noise for all time lags different from zero ($\text{Cov}_{\varepsilon\varepsilon}(\tilde{s}) = \sigma_\varepsilon^2 = \delta(\tilde{s})$ with $\tilde{s} = s + i - j$) follows $j = s + i$, and hence, the auto-correlation function of the AR(1) process yields

$$C(s) = \frac{1}{\sigma_x^2} \sum_{i=0}^{\infty} a_1^{2i} a_1^s \sigma_\varepsilon^2 = a_1^s \quad (\text{B.6})$$

where I used the limit of the geometric series $\sum_{i=0}^{\infty} (a_1^2)^i = 1/(1 - a_1^2)$ and Eq. (B.5). To satisfy $C(s) = C(-s)$ Eq. (B.6) can be adapted to $C(s) = a_1^{|s|}$ for arbitrary time lags s . One might then define a characteristic decay time τ where $C(\tau) = 1/e$

$$\tau = -1/\ln a_1. \quad (\text{B.7})$$

C. Tile Patterns formed by Pentagons

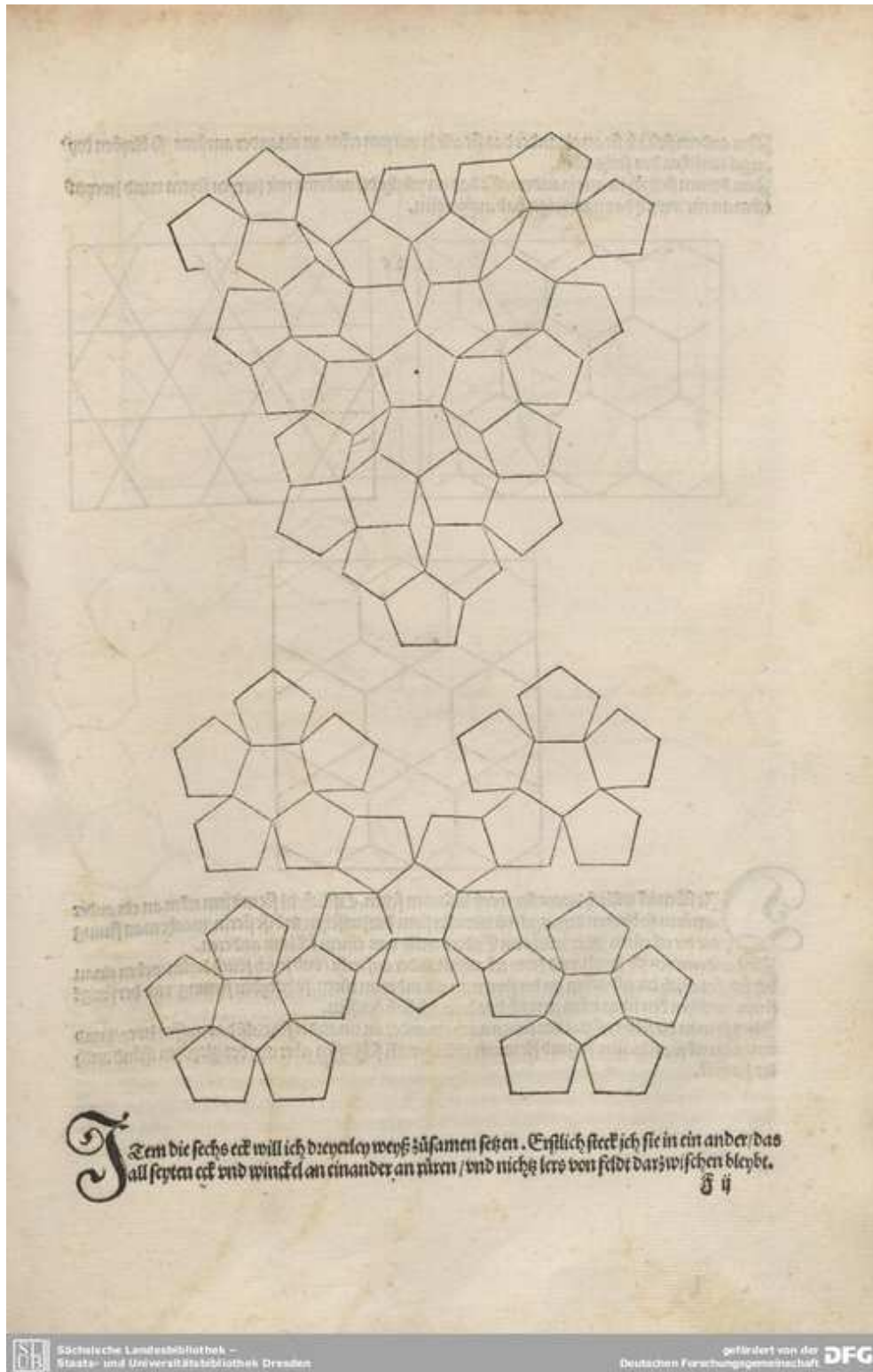


Figure C.1.: Tile of pentagons from page 67 of [DÜRER 1525] borrowed from Sächsische Landesbibliothek – Staats- und Universitätsbibliothek Dresden

D. Statistical Tests

D.1. Student's t-Test

A prominent test of statistical inference in medical time series analysis is the Student t-test for testing the null hypothesis of equal means against the hypothesis of different means.

Let in the following $\{x_k\}_{k=1,\dots,N_x}$ and $\{y_k\}_{k=1,\dots,N_y}$ denote two time series with estimators (indicated by 'hats', i.e. $\hat{\mu}$)

$$\hat{\mu}_x = \frac{1}{N_x} \sum_{k=1}^{N_x} x_k \quad \text{and} \quad \hat{\mu}_y = \frac{1}{N_y} \sum_{k=1}^{N_y} y_k \quad (\text{D.1})$$

for their true expectation values μ_x and μ_y . First consider only the signal $\{x_k\}$. In order to test the null hypothesis $\mu_x = \mu_0$ versus $\mu_x \neq \mu_0$ for a given mean value μ_0 a test statistic T is constructed following

$$T = \frac{\hat{\mu}_x - \mu_0}{\hat{s}_x} \sqrt{N_x} \quad (\text{D.2})$$

where

$$\hat{s}_x^2 = \frac{1}{N_x - 1} \sum_{k=1}^{N_x} (x_k - \hat{\mu}_x)^2 \quad (\text{D.3})$$

is an unbiased estimator for the variance, or the *sample variance*¹. T follows a Student's t distribution with $\nu = N - 1$ degrees of freedom. The t distribution is described by a probability density

$$p(\nu, t) = \frac{1}{\sqrt{\nu} B\left(\frac{1}{2}, \frac{\nu}{2}\right)} \left(1 + \frac{t^2}{\nu}\right)^{-\frac{\nu+1}{2}} = \frac{\Gamma\left(\frac{\nu+1}{2}\right)}{\sqrt{\pi\nu} \Gamma\left(\frac{\nu}{2}\right)} \left(1 + \frac{t^2}{\nu}\right)^{-\frac{\nu+1}{2}} \quad (\text{D.4})$$

where $B = \frac{\Gamma(a)\Gamma(b)}{\Gamma(a+b)}$ denotes the beta function and $\Gamma(z) = \int_0^\infty \xi^{z-1} e^{-\xi} d\xi$ is the gamma function. With increasing ν , i. e., increasing N and $\hat{s}_x^2 \rightarrow \sigma_x^2$, the t distribution approaches the normal distribution. The probability that a value t is found in the interval $t_1 < t < t_2$ is then given by

$$P(t_1 < t < t_2) = \int_{t_1}^{t_2} p(\nu, t) dt. \quad (\text{D.5})$$

The null hypothesis of μ_x being equal to μ_0 is rejected for a significance level α if the value T is outside the interval $(-t_{\nu, \alpha/2}, t_{\nu, 1-\alpha/2})$. While this example corresponds to a two-sided test, one could also test for the hypothesis that $\mu_x \leq \mu_0$ which is rejected for $T \geq t_{\nu, 1-\alpha}$ (one-sided test). For a given degree of freedom $\nu = N - 1$ and a given significance level α the values $t_{\nu, 1-\alpha}$ or $t_{\nu, 1-\alpha/2}$ can be found in tables². Statistical computer programs have the t -test already implemented.

Above described method can easily be adapted to test the hypothesis that $\mu_x = \mu_y$ versus $\mu_x \neq \mu_y$. Under the assumption $\sigma_x^2 = \sigma_y^2 = \sigma^2$ (*homoscedastic*) the T statistic in Eq. (D.2) becomes

$$T = \frac{\hat{\mu}_x - \hat{\mu}_y}{\sigma^2 \left(\frac{1}{N_x} + \frac{1}{N_y}\right)} = \sqrt{\frac{N_x N_y}{N_x + N_y}} \cdot \frac{\hat{\mu}_x - \hat{\mu}_y}{\hat{s}_{xy}} \quad (\text{D.6})$$

¹The variance of the population follows for a weakly stationary time series $\sigma_x^2 = 1/N_x \sum_{k=1}^{N_x} (x_k - \mu_x)^2$.

²Always check which version is given.

with the weighted average variance

$$\hat{s}_{xy}^2 = \frac{1}{N_x + N_y - 2} [(N_x - 1)\hat{s}_x^2 + (N_y - 1)\hat{s}_y^2] \quad (\text{D.7})$$

where \hat{s}_x^2 and \hat{s}_y^2 follow Eq. (D.3). When the variances σ_x^2 and σ_y^2 are not equal (*heteroscedastic*) one defines

$$T = \frac{\hat{\mu}_x - \hat{\mu}_y}{\sqrt{\frac{\hat{s}_x^2}{N_x} + \frac{\hat{s}_y^2}{N_y}}}. \quad (\text{D.8})$$

However, T is only approximately t distributed with a degree of freedom following

$$\nu = \frac{\left(\frac{\hat{s}_x^2}{N_x} + \frac{\hat{s}_y^2}{N_y}\right)^2}{\frac{1}{N_x - 1} \left(\frac{\hat{s}_x^2}{N_x}\right)^2 + \frac{1}{N_y - 1} \left(\frac{\hat{s}_y^2}{N_y}\right)^2}. \quad (\text{D.9})$$

In this thesis I consider a two-sided heteroscedastic Student's t -test and derive values by employing a software tool (ITT IDL).

D.2. Wilcoxon Rank Order Test and Mann-Whitney U Test

The Wilcoxon rank order test [WILCOXON 1945] is equivalent to the Mann-Whitney U test Mann and Whitney [MANN AND WHITNEY 1947].

Let $\{x_k\}_{k=1, \dots, N_x}$ and $\{y_k\}_{k=1, \dots, N_y}$ denote two time series with continuous distribution functions³ f_x and f_y . $\{x_k\}$ is called stochastically smaller than $\{y_k\}$ if $f_x(a) > f_y(a)$ for all a . The Wilcoxon-Mann-Whitney U statistics tests the hypothesis that $f_x = f_y$ against $\{x_k\}$ being stochastically smaller than $\{y_k\}$.

Test Algorithm:

Both time series are pooled and ordered by their rank without respecting their original set affiliation yielding $\{z_m\}_{m=1, \dots, N_x + N_y}$. For instance, in the case the ranking is performed according to the numerical values of $\{x_k\}$ and $\{y_k\}$ it is satisfied $z_1 < z_2 < \dots, z_{N_x + N_y}$. Note that ranking according to other properties might be applicable depending on the type of the observable. However, here I focus on ranking by value. Then the ranks (indexes m of $\{z_m\}$) corresponding to $\{x_k\}$ and $\{y_k\}$ are summed

$$R_x = \sum_{z_m \in \{x_k\}} m \quad \text{and} \quad R_y = \sum_{z_m \in \{y_k\}} m. \quad (\text{D.10})$$

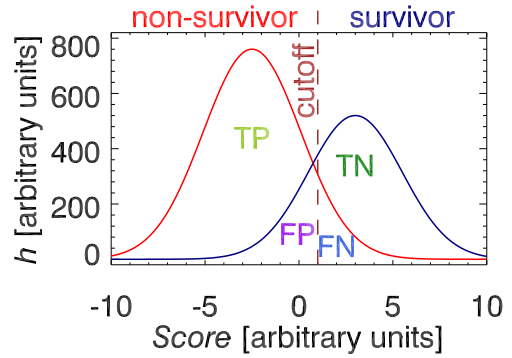
Note that $R_x + R_y = (N_x + N_y)(N_x + N_y + 1)/2$ being the sum of the first $N_x + N_y$ natural numbers. Then the U statistic is obtained for both subsets

$$U_x = N_x N_y + \frac{N_x(N_x + 1)}{2} - R_x \quad \text{and} \quad U_y = N_x N_y + \frac{N_y(N_y + 1)}{2} - R_y \quad (\text{D.11})$$

where $U_x + U_y = N_x N_y$. Note that non of the time series was preferentially selected over the other. Thus, both U_x and U_y are valid test statistics. However, in the application the smaller value $U_{\min} = \min\{U_x, U_y\}$ is preferred for statistical inference. For the U_{\min} statistics there exist tables [see, e. g. MANN AND WHITNEY 1947] where one can look up the probability that for a given pair (N_x, N_y) the value of U_{\min} is smaller than a fixed value U_* . As for the Student's t -test

³Cumulative probability density functions.

Figure D.1.: Example distribution of a score in a trial population (non-survivors [red] and survivors [blue]). The brown dashed line marks the cutoff value that is used for discrimination. Subjects with scores above the cutoff value are classified as survivors (negative outcome in a test for death) while individuals with a lower score are classified as non-survivor (positive test result). The true positive (TP) value denotes the number of individuals that are correctly classified as non-survivor; the true negative (TN) value indicates the number of correctly classified survivors; the false positive (FP) value corresponds to the number of patients classified as non-survivor but who indeed survived; the false negative (FN) value is the number of patients that are classified survivor but truly died.



these tables are implemented in statistical software tools. Further, it can be shown that for large time series the quantity

$$Z = \frac{U - N_x N_y}{\sqrt{\frac{N_x N_y (N_x + N_y + 1)}{12}}} \sim \mathcal{N}(0, 1) \quad (\text{D.12})$$

is approximately normal distributed with zero mean and unit variance. Equation (D.12) is more frequently employed compared with look-up tables for the U statistics.

D.3. P-Value

The P -value or p -value corresponding to a statistical test is a calculated (or estimated) probability for rejecting a null hypothesis, i. e. in the case of a Student's t -test for two different time series $\{x_k\}_{k=1, \dots, N_x}$ and $\{y_k\}_{k=1, \dots, N_y}$ the probability that both estimators for the expectation value $\hat{\mu}_x$ and $\hat{\mu}_y$ are equal. Note, although in medical applications a small p -value such as $p < 0.001$ is assumed to be an indication of, for instance, different mean values of two sample population [see e. g. Sects. 4.1.3 or 5.3.5] this assumption has no foundation in statistics. Null hypotheses can only be rejected, but a rejection does not imply a meaningful or important difference of the means. For the (plain) Mann-Whitney-U test the p -value is the probability that both distribution functions f_x and f_y are equal. In medical time series analysis three different significance levels are typically distinguished: (i) $p < 0.05$ (or $p < 0.03$) corresponding with *statistically significant*, (ii) $p < 0.01$ corresponding with *well significant*, and (iii) $p < 0.001$ *highly significant*. A p -value larger than 0.5 is associated with *not significant*. There is no consensus on the p -value used for distinguishing significant and not significant. Sometimes, one choses $p < 0.03$ rather than $p < 0.05$.

D.4. Receiver Operating Characteristics (ROC) Plots and Bootstrapping

ROC curves are generally used in medicine to quantify the diagnostic performance of a score [such as deceleration capacity (DC) in Chapt. 4] to discriminate different populations in an experiment, e. g., differentiate diseased patients from healthy controls. While the ROC methodology was originally developed in the context of radar experiments in the 1950s to tune radar devices to operate in an optimal condition, i. e., large number of correctly identified planes versus a small number of falsely identified objects, it is today well established in medical trials [METZ 1978; GRINER *et al.* 1981; ZWEIG AND CAMPBELL 1993]. For an illustration consider a medical trial such as the ISAR-I study [Sect. 2.4] where one obtains for each individual in the database some parameters (or scores⁴) one wishes to employ for distinguishing post-infarction patients that died within a follow up period⁵ of two years from those that survived. Such parameters are for instance

⁴With score I further denote both the parameter itself and its value.

⁵The time after an initial myocardial infarction that was recorded in the trial.

deceleration capacity (DC) or left ventricular ejection fraction (LVEF) [see Sect. 4.1.3]. Ideally, one then defines a threshold value (cutoff point) that discriminates both groups of patients (survivors and non-survivors). A score below the cutoff value might correspond to non-survivors and a score above the cutoff value might correspond to survivors. However, in general such a parameter will not perfectly discriminate both groups of patients, but rather some times falsely identify survivors as non-survivors and vice versa. Hence, the question arises for which cutoff value an optimal discrimination, e. g., a large number of truly classified survivors and non-survivors with only a few false classifications, is obtained. Figure D.1 illustrates a possible situation where the distributions of the scores for both subgroups overlap [non-survivors in red and survivors in blue]. A cutoff value is marked by a brown dashed line. In a test where one wants to identify non-survivors (positive outcome is a 'non-survivor' is found) the number of patients whose score is above the cutoff point and that are indeed survivors is called the *true negative value (TN)* [above cutoff and below blue curve in Fig. D.1], while falsely identified survivors correspond to the *false negative value (FN)* [above cutoff and below red curve in Fig. D.1]. On the other hand, the number of patients that exhibit scores below the cutoff point and are true non-survivors is denoted by the *true positive value (TP)* [below cutoff and below red curve in Fig. D.1], while the *false positive value (FP)* represents the patients that were classified as non-survivors but indeed did not die during the follow up time.

To judge the performance of the score and to decide which cutoff point is optimal one then defines the *sensitivity* or *true positive rate (TPR)* as the probability that a test result is positive for a non-survivor, and the *specificity* or *true negative rate (TNR)* as the probability that the result is negative for a survivor.

$$\text{Sensitivity} = 100\% \cdot \underbrace{\frac{TP}{TP + FN}}_{TPR} \quad \text{Specificity} = 100\% \cdot \underbrace{\frac{TN}{FP + TN}}_{TNR} \quad (\text{D.13})$$

Note that both sensitivity and specificity are usually given in percent while rates are between 0 and 1. For completeness I would like to mention that there are other quantities in use which are also based on on TP, FP, TN, FN . However, I do only use sensitivity and specificity in this thesis [see for instance Fig. 4.5(a)]. These quantities comprise the *positive likelihood ratio (PLR)* describing the ratio between the probability of a positive test result obtained for true non-survivors and the probability of a positive test result obtained for survivors. Analogously, the *negative likelihood ratio (NLR)* is the ratio of the probability that a negative result is given in the presence of a non-survivor and the probability that a negative result is given in the absence of a non-survivor (presence of a survivor).

$$PLR = \frac{TPR}{FPR} = \frac{\text{Sensitivity}}{1 - \text{Specificity}} \quad NLR = \frac{FNR}{TNR} = \frac{1 - \text{Sensitivity}}{\text{Specificity}} \quad (\text{D.14})$$

Moreover, the *positive predictive value (PPV)* is the probability that a positive test result is obtained for a non-survivor and the *negative predictive value (NPV)* is analogously the probability that a negative test result is obtained for a survivor.

$$PPV = \frac{TP}{TP + FP} \quad NPV = \frac{TN}{FN + TN} \quad (\text{D.15})$$

Finally, the *Receiver Operating Characteristics (ROC)* curve is traditionally obtained by plotting the *TPR* (or sensitivity) versus the *FPR* or $(100\% - \text{specificity})$ for many different cutoff values. However, in medical applications one often finds ROC curves being defined as specificity versus sensitivity, see Figs. 4.5(a) and D.2 for a few examples and consider the discussion on *bootstrapping* below. The diagonal in a ROC curve connecting 100% sensitivity at 0% specificity with 100% specificity at 0% sensitivity (in the traditional version $1 - \text{specificity}$) is associated with a random choice of survivors and non-survivors. Thus a score that performs better as a random classification yields a ROC curve above the diagonal. When the score yields a ROC curve completely below the diagonal, an inverted score has good performance with an ROC curve above the diagonal (either

the criteria above/below cutoff point have to be swapped or the score has to be negated). For perfect discrimination ($FN = FP = 0$) the ROC curve would pass the point 100% sensitivity and 100% specificity. Usually, the *area under the ROC curve* (AUC) is employed to compare the performance of different scores, i. e., the larger the value AUC the better the score⁶.

Note that in general the decision of a cutoff value is additionally linked to a cost function. A falsely identified non-survivor who receives an extended care might be 'cheaper' than a falsely identified survivor who dies due to omitted treatments. Moreover, ROC curves, i. e. AUC values, require a large enough number of elements in both subgroups. For instance in the case where only a few positive events (deaths) front many negative events (survivors) a good overall performance would be achieved by never triggering an alarm since catching the few positive events will likely correspond with an increase in false positive identified events.

Bootstrapping

Especially, in medical trials that did not include a very large number of individuals or in the case when the groups that one wishes to distinguish contain a very different number of individuals the ROC curves appear as a staircase since varying the cutoff value might not yield a change in TP , TN , FN , and FP and hence the corresponding point in the ROC curve does not change, either. To smoothen such ROC curves and to obtain statistical errors the *bootstrapping* methodology was established [EFRON 1979; MOISE *et al.* 1985; EFRON AND TIBSHIRANI 1993]. For a given set of data, i. e., pairs of score value and associated true outcome (dead or alive), many surrogate sets of the same number of elements are generated by randomly drawing elements from the original set by allowing repetitions. For each surrogate set a ROC curve is calculated, and finally, all ROC curves are averaged and properties as standard deviation and standard error can be obtained.

During the study of a different large database containing recordings from post-infarction patients and healthy subjects⁷ from observation the question arose whether the number of n consecutive increases in heartbeat intervals (RRI) in 24h ECG recordings could be used as a score for discriminating post-infarction survivors and non-survivors within a two years follow up. Figure D.2 reports ROC curves for related scores Sn where n denotes the number of consecutive increases in RRI. As can be seen a score based on the number of $n = 4$ consecutive RRI increases (deceleration of the heart) has an AUC of approximately 75% of the unit square. Although, this is a little less efficient than deceleration capacity (DC) defined via PRSA curves ($AUC = 77\%$ in the ISAR-I cohort), it is already significantly superior to the currently used gold standard 'left ventricular ejection fraction' ($AUC = 70\%$ in the ISAR-I cohort). Why four consecutive decelerations exhibit such good performance is at the moment physiologically not understood.

⁶Indeed this is a rough measure since for a certain application a particular point in a ROC curve might represent an optimized cutoff point. A score that performs best for the corresponding combination of specificity and sensitivity must not necessarily obey the largest overall AUC . This might in particular be the case if the distributions of the score are significantly different from normal distributions or for combined scores.

⁷Provided by Dr. Przemyslaw Guzik affiliated with Karol Marcinkowski University of Medical Science, Department of Cardiology and Intensive Therapy, Poznan, Poland.

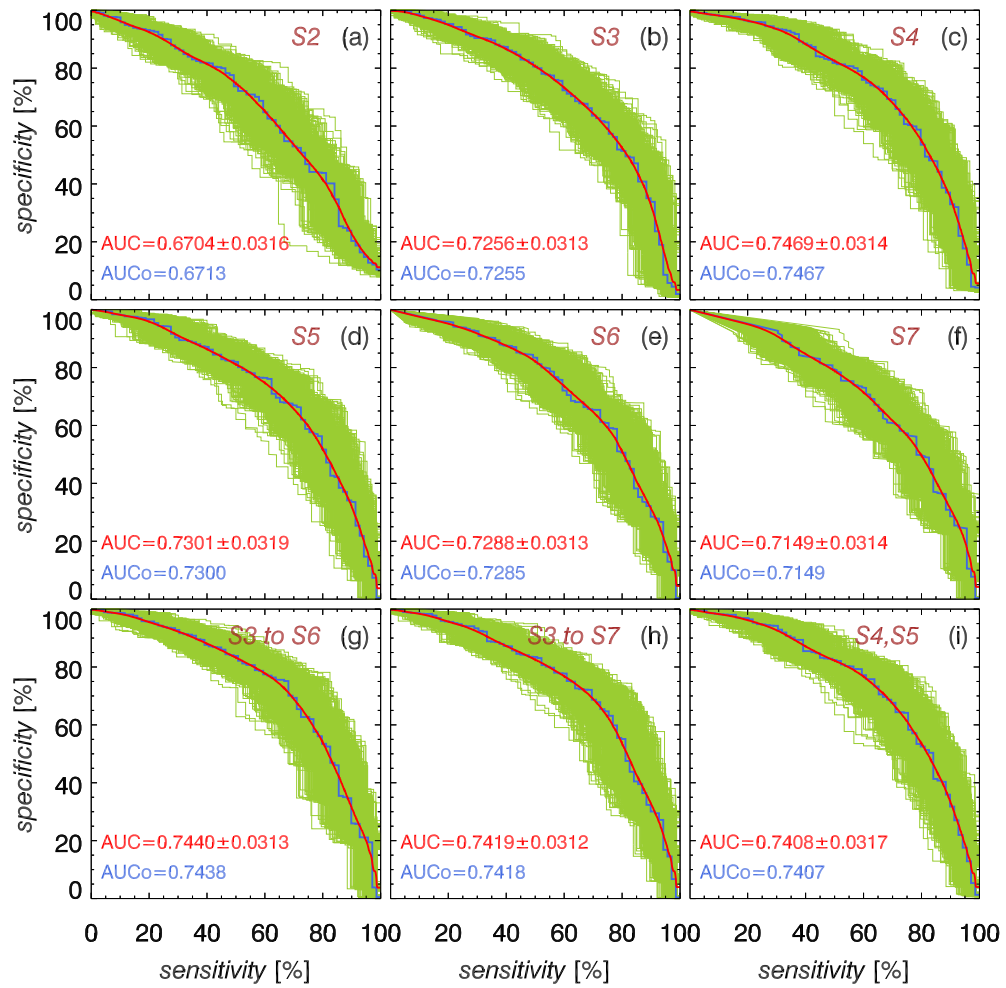


Figure D.2.: ROC curves obtained from 1455 post-infarction patients of the ISAR-I database for (a-f) single scores S_n , and (g-i) combined scores where n is the number of consecutive increases in beat-to-beat intervals. Red curves, corresponding AUC values, and standard deviations are obtained from $N = 1000$ surrogate datasets [light green ROC curves] obtained via the bootstrapping method. The blue curve and AUCo value correspond to the original dataset [no repetitions].

E. Further fluctuation analysis methods

E.1. Wavelet Based (Multifractal) Fluctuation Analysis

As already discussed in Sect. 3.1.4 certain wavelets, see also 1.3 for a discussion on wavelet transform, are orthogonal to certain characteristic features (such as polynomial trends) in the signal. Hence, wavelets can be utilized for a detrended fluctuation analysis. Particularly interesting are the Haar wavelet [Eq. (1.27a)] and Haar-wavelet-alike functions which are orthogonal to higher order polynomials. These functions can be defined as follows:

$$\Psi_{\text{Haar}}^{(0)}(t) = \begin{cases} 1 & : 0 \leq t < \frac{1}{2} \\ -1 & : \frac{1}{2} \leq t < 1 \\ 0 & : \text{else} \end{cases} \quad \Psi_{\text{Haar}}^{(2)}(t) = \begin{cases} -\frac{1}{3} & : 0 \leq t < \frac{1}{4} \\ 1 & : \frac{1}{4} \leq t < \frac{1}{2} \\ -1 & : \frac{1}{2} \leq t < \frac{3}{4} \\ \frac{1}{3} & : \frac{3}{4} \leq t < 1 \\ 0 & : \text{else} \end{cases} . \quad (\text{E.1})$$

$$\Psi_{\text{Haar}}^{(1)}(t) = \begin{cases} -\frac{1}{2} & : 0 \leq t < \frac{1}{3} \\ 1 & : \frac{1}{3} \leq t < \frac{2}{3} \\ -\frac{1}{2} & : \frac{2}{3} \leq t < 1 \\ 0 & : \text{else} \end{cases}$$

Note that only the function $\Psi_{\text{Haar}}^{(0)}$ represents a true wavelet function. The Haar wavelet has in principle no other orders than this first order which I will term in the following the *zeroth* order. The convenience of the later notation will allow a direct comparison with the DFA order and will become clear shortly, for a description of DFA consult Sect. 3.1.3. However, one can define Haar-wavelet-alike functions which are often considered as Haar wavelets of higher order, see e. g. [ROMAN *et al.* 2008], although such denotation is mathematically sloppy. In the following I will adopt this notation for simplification.

The beauty of Haar wavelets is that the convolution in a wavelet transform following Eq. (1.26b) reduces to simple n th-order differences of parts from the signal for a given scale s . For other mother wavelets the in the following described fluctuation analysis algorithm would become more complicated since the discretized integrals of Eqs. (1.26) have to be calculated. Moreover, the 'detrended features' are no longer polynomials.

The in the following introduced wavelet detrended fluctuation analysis method WL_n is a corrected version of the one introduced by Koscielny-Bunde [KOSCIELNY-BUNDE *et al.* 1998a,b]. In acknowledgement of the original research I here use the same acronym WL_n as was suggested by Koscielny-Bunde *et al.*. However, following the scheme of constructing acronyms that was used for DFA n and CMA a better suited abbreviation would be WDFAn where n is the detrending order. Currently, there might be no other fluctuation analysis method on the market that is defined in more different ways considering normalization and scaling, or denoted by different acronyms, e. g., WL, WTA, WTN, or FAHW.

Corrected WL_n

Let $\{x_k\}_{k=1,\dots,N}$ denote the time series on wishes to study. The WL_n algorithm consists also of four steps where *Step 2* is slightly modified compared with the DFA n methodology in Sect. 3.1.3.

Step 1:

The mean subtracted cumulative time series, the profile $\{Y_j\}_{j=1,\dots,N}$, is calculated according to Eq. (3.16). The subtraction of the mean is also not mandatory for WL_n due to the later detrending; see discussion concerning Eq. (3.16) in Sect. 3.1.3.

Step 2:

Having obtained the profile one again divides $\{Y_j\}$ into $2 \times [N/s]$ consecutive non-overlapping segments of length s , starting at the beginning and at the end of $\{Y_j\}$. In each segment $\nu, \nu = 0, \dots, 2[N/s] - 1$ the profile is averaged:

$$\mu_{\nu,s} = \frac{1}{s} \sum_{i=1}^s Y_{\nu s+i} \quad (\text{E.2a})$$

for the forward direction and $\nu = 0, \dots, [N/s] - 1$ and

$$\mu_{\nu,s} = \frac{1}{s} \sum_{i=1}^s Y(N - (\nu - [N/s] + 1)s + i) \quad (\text{E.2b})$$

for the backward direction and $\nu = [N/s], \dots, 2[N/s] - 1$, respectively. Note that one could speed up the calculation especially for small scales s by only deriving the cumulative profiles in Eqs. (E.2) and including the division by the scale s in a later step. Then only one division is required. However, the notation of means is more intuitive for illustration.

An n th-order Haar-wavelet in the definitions in Eqs. E.1 is orthogonal to polynomial trends of order n , i.e., the 0th order Haar-wavelet is orthogonal to constant trends, the 1st order Haar-wavelet to linear trends and so on.

One can then define a fluctuation function by considering the n -th order differences of the local means from the profile following Eqs. (E.2) in segments of scale s . These are related to a discrete convolution with dilated versions of the Haar wavelets in Eqs. E.1. The squared local WLn fluctuations in the window ν are then defined by

$$F_{WL0,\nu}^2(2s) = \left[\frac{1}{2} (\mu_{\nu,s} - \mu_{\nu+1,s}) \right]^2 \quad (\text{E.3a})$$

$$F_{WL1,\nu}^2(3s) = \left[\frac{1}{4} (\mu_{\nu,s} - 2\mu_{\nu+1,s} + \mu_{\nu+2,s}) \right]^2 \quad (\text{E.3b})$$

$$F_{WL2,\nu}^2(4s) = \left[\frac{1}{8} (\mu_{\nu,s} - 3\mu_{\nu+1,s} + 3\mu_{\nu+2,s} - \mu_{\nu+3,s}) \right]^2 \quad (\text{E.3c})$$

for $n = 0, 1, 2$. The normalization factors $1/2$, $1/4$, and $1/8$ descending from the number of contributing sums (μ_{\dots}) are not mandatory since we are interested in scaling rather than absolute values. However, including such a normalization eases a comparison between different detrending orders. Higher order detrending can be defined by employing higher order Haar-wavelet functions. Note that the detrending in Eqs. E.3 takes place **not** at a fixed scale s as in $DFAn$ [Sect. 3.1.3] and as claimed by Koscielny-Bunde *et al.* [KOSCIELNY-BUNDE *et al.* 1998a,b] but on a scale $(n+2)s$ where n is the detrending order. For instance, linear trends are removed from the profile in windows of $3s$ when employing $WL1$ but not within windows of scale s . To my knowledge there is no publication taking care of this issue. As a result differences between $DFAn$ and WLn were reported for the same detrending order. This is *not true!* A polynomial detrending of the same order should result in the same results for any detrending method unless something was implemented wrongly. For an illustration of the *true* equivalence of $DFAn$ and WLn consult Appendix E.2.

Step 3:

The WLn fluctuation functions are derived by averaging over all local fluctuations.

$$F_{WLn}((n+2)s) = \left[\frac{1}{2[N/s]} \sum_{\nu=0}^{2[N/s]-1} F_{WLn,\nu}^2((n+2)s) \right]^{1/2} \quad (\text{E.4})$$

Note that without cyclic continuation at the end of the profile the index ν cannot exactly take values up to $2\lfloor N/s \rfloor$ because the definitions in Eq. (E.3) require valid windows in the 'future' depending on the detrending order, e. g., at least two segments more are required for WL1 to obtain a valid $\mu_{\nu+2,s}$. I have chosen a sloppy definition in Eq. (E.4) to emphasize the similar structure as in Eq. (3.18) for DFA n . For a large number of windows there is no noticeable difference.

Step 4:

Finally, Eq. (E.4) is evaluated for many scales s and a scaling exponent $\alpha_{\text{WL}n}$ can be obtained in the case of power law fluctuations from linear fits to $F_{\text{WL}n}((n+2)s)$ in the double-logarithmic regime.

$$F_{\text{WL}n}((n+2)s) \sim s^{\alpha_{\text{WL}n}} \quad (\text{E.5})$$

Multifractal WL n

WL n can be generalized to a multifractal variant in a similar way as DFA n was generalized to MF-DFA n and CMA was generalized to MF-CMA by introducing higher moments q . Equation E.4 then becomes

$$F_{\text{MF-WL}n,q}((n+2)s) = \begin{cases} \left[\frac{1}{2\lfloor N/s \rfloor} \sum_{\nu=0}^{2\lfloor N/s \rfloor-1} [F_{\text{WL}n,\nu}^2((n+2)s)]^{q/2} \right]^{1/q} & : q \neq 0 \\ \exp \left[\frac{1}{4\lfloor N/s \rfloor} \sum_{\nu=0}^{2\lfloor N/s \rfloor-1} \ln F_{\text{WL}n,\nu}^2((n+2)s) \right] & : q = 0 \end{cases} \sim s^{h_{\text{WL}n}(q)}. \quad (\text{E.6})$$

where I was again a little sloppy in the sum, see discussion below Eq. (E.4).

E.2. Equivalence of DFA n and WL n

Maraun *et al.* discussed in their paper [MARAUN *et al.* 2004] shortcomings of DFA in the presence of short-range correlations. They studied a superposition of three AR(1) time series [Eq. (B.1)] characterized by three different characteristic decay times of the auto-correlation function, $\tau_1 = 3$, $\tau_2 = 21$, $\tau_3 = 500$. Indeed Maraun *et al.* defined three different parameters a_1 which can be translated into decay times following Eq. (B.7). Recall that AR(1) processes by definition are short-term correlated. The Maraun model is defined as

$$x_k = \sum_{i=1}^3 A_i y_{k,i} \quad \text{with} \quad y_{k,i} = a_{1,i} y_{k-1,i} + \varepsilon_{k,i} \quad (\text{E.7})$$

where the A_i are some weights to tune the influence if the i th AR(1) process and $a_{1,i} = \exp\{-1/\tau_i\}$. I follow the original model by setting $A_1 = 0.931$, $A_2 = 0.396$, and $A_3 = 0.098$ [MARAUN *et al.* 2004]. I generated $N_c = 1000$ different realizations of the Maraun model of $N = 10^6$ elements each and employed both DFA2 and WL2 to study correlations in the model. The associated averaged fluctuation function are depicted in Figs. E.1(a,b) [in (a) DFA2=black; in (b) WL2=red with uncorrected detrending scales and WL2=dark pink with corrected detrending scales]. Clearly, DFA2 shows spurious long-term correlated behavior. However, the oscillations in the fluctuation function already indicate that there is something wrong. While Maraun *et al.* blame DFA for falsely indication of long-range dependence, this inference is rather 'unfair'. Obviously, no method can identify short-range correlations that establish on larger scales than the investigated ones. When larger scales are considered in an analysis employing DFA (Maraun *et al.* study scales up to $s = 10^4$), uncorrelated behavior, expressed by a fluctuation exponent $\alpha_{\text{DFA}} = 0.5$, is clearly determined.

On the other hand, I discussed in the previous section [Appendix E.1] that detrending of WL n acts on larger scales while obtained results are indeed equivalent to results obtained from DFA n when

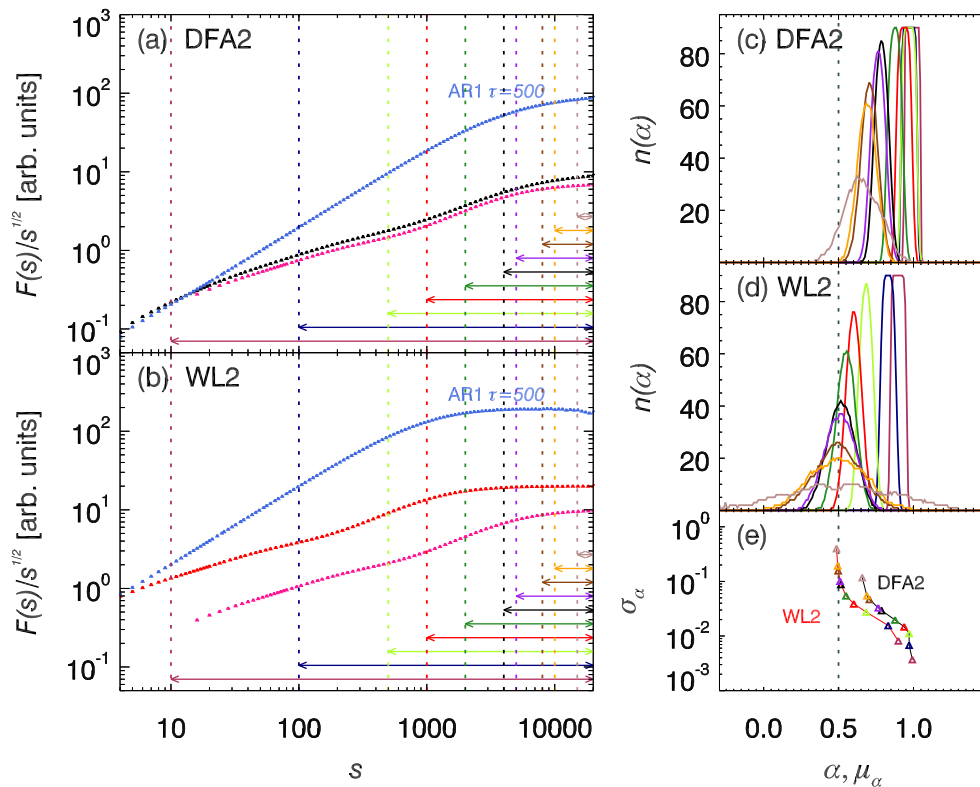


Figure E.1: Equivalence of WLn and DFA_n fluctuation analysis methods for $n = 2$ illustrated by employing the Maraun model of three superimposed AR1 processes [MARAUN et al. 2004, see discussion and]. Shown are averaged fluctuation functions of $N_c = 1000$ configurations obtained from employing (a) DFA2 and (b) WL2. (a,b) From top to bottom: fluctuation functions for a pure AR1 model [$\tau = 500$, $\alpha_1 = 0.998$, $N_1 = 10^5$; light blue], the Maraun model [$\tau_1 = 3$, $\tau_2 = 21$, $\tau_3 = 500$, $N_2 = 10^6$; black=DFA2, red=WL2], and results for the Maraun from WL2 after scale correction [dark pink; same curve in (a,b)]. Note that after scale correction results from WL2 and DFA2 are identical. There is no difference in detrending capabilities. (c,d) Histograms of fluctuation exponents obtained for the Maraun model and for different fit ranges as marked by arrows in the same colors in (a,b) [DFA2 (c); uncorrected WL2 (d)]. (e) Standard deviation versus mean value corresponding to results in (c,d) for WL2 [left curve] and DFA2 [right curve]. Symbols are shown in the same colors as before. Note that WL2 clearly indicates a transition to uncorrelated behavior while from DFA2 long-term correlations might be speculated.

a proper rescaling to equivalent detrending scales is performed. This equivalence is illustrated for the Maraun model in Fig. E.1(a) where I have plotted the original DFA2 fluctuation function [black] next to the rescaled WL2 fluctuation function [dark pink]. It is obvious that both are the same! Hence, both the fluctuation exponent α_{DFA} and the exponent α'_{WL} which is derived within the same fitting regime after rescaling are identical. Note that deriving differences (WLn) is computationally more efficient than obtaining polynomial fits (DFA_n). Therefore, WLn offers a better performance with the same detrending capabilities compared with DFA2. The only advantage of DFA_n is the possibility of deriving fluctuations independent of the detrending order for arbitrary scales $s \geq n + 2$ while WLn by definition can only yield fluctuation functions for scales that are integer multiples of otherwise arbitrary scales ($s' = (n + 2)s$).

Further note that the uncorrected WL2 fluctuation function already indicates short term correlations [flat region of red curve in Fig. E.1(b)] for the Maraun model. For comparison Figs. E.1(a,b) show results from a fluctuation analysis of a pure AR(1) time series with $\tau = 500$ for both methods [blue curves].

Figures E.1(c,d) show the distribution of individual scaling exponents α obtained from each of the $N_c = 1000$ datasets within different fitting regimes [indicated by colored arrows in (a,b)] employing DFA2 [(c)] and WL2 [(d)]. The distributions are broader for WL2 compared with DFA2 for the same regimes. However, the reason is the different true scale of WL2. Indeed, uncorrected scales in WL2 correspond to a true scale that is four times larger. In this region variations between realizations are much stronger due to reduced statistics (less summands $F_{WL2,\nu}^2$ contribute in Eq. (E.4)).

E.3. Multifractal Box Counting (MF-Box)

Let $\{x_k\}_{k=1,\dots,N}$ be a time series; then the multifractal box-counting technique for time series works as follows:

Step 1:

The profile $\{Y_k\}$ is calculated according to Eq. 3.7. Note that the mean is not subtracted in this version.

Step 2:

Analogously to other fluctuation analysis methods the profile is divided into $\nu = 0, \dots, [N/s] - 1$ segments of scale s . And the local fluctuations are obtained following

$$F_{\text{Box},\nu}(s) = \sum_{i=1}^s [Y((\nu+1)s+i) - Y(\nu s+i)]. \quad (\text{E.8})$$

Note that there is no square in this case.

Step 3:

The multifractal partition function is obtained by introducing higher moments q and summing all windows ν .

$$Z_{\text{MF-Box},q}(s) = \sum_{\nu=0}^{[N/s]-1} [F_{\text{Box},\nu}(s)]^q \quad (\text{E.9})$$

Note that in the partition function in Eq. (E.9) no window are obtained for starting the separation of the profile at the end. However, this is in principle also possible. However, the value of $Z_{\text{MF-Box},q}(s)$ then becomes approximately twice as large since in the box counting method there is no normalization by the number of windows.

Step 4:

From evaluating Eq. (E.9) for many scales s and for different moments q one can in the presence of power law correlations derive a scaling exponent from linear fits in the double-logarithmic regime.

$$Z_{\text{MF-Box},q}(s) \sim s^{\tau_{\text{MF-Box}}(q)} \quad (\text{E.10})$$

Note that MF-Box does not yield a scaling exponent $h(q)$. Since it is based on the partition function, the Rényi exponents $\tau(q)$ are directly obtained, see Sect. 3.3.3 for a relation between both types of exponents¹. In the classical approach the multifractality via segment counting method the summands $F_{\text{Box},\nu}(s)$ are substituted by the box probability² $p_{\nu,s}$. Therefore, one sometimes normalizes $\{x_k\}$ to ensure $\sum_{k=1}^N x_k = 1$, and thus, obtain probabilities. However, such normalization does not affect the scaling behaviour and is not required unless the value of the partition function is of interest.

Since Eq. (E.8) can in principle be zero or numerically identically to zero Eq. (E.9) might diverge for negative moments which is a limitation of MF-Box. One has to check for such summands. To overcome this problem wavelet transform modulus maxima (WTMM) was invented.

E.4. Wavelet Transform Modulus Maxima (WTMM)

The wavelet transform modulus maxima (WTMM) was originally introduced to incorporate detrending capabilities of wavelets in a generalized box counting method. Such detrending is particularly required for studying non-stationary data (with trends). In order to overcome problems with negative moments later a maximum operation was included in the definition of the partition function. For a comprehensive overview on WTMM see the original work [MUZY *et al.* 1991,

¹Sometimes time series are classified by a generalized entropy $D(q) = \tau(q)/\tau(q-1)$.

²Do not confuse this notation with the detrending polynomials in DFA n .

1994], an application to DNA sequences in [ARNEODO *et al.* 1995], or more recently [BUNDE *et al.* 2002; MEYERS 2009].

The WTTM method is performed in three steps:

Step 1:

Wavelet coefficients are obtained by the convolution of the signal $\{x_k\}$ with a mother wavelet $\Psi(t)$ for each pair of scale $s \in \mathbb{N}$ and time shift $k' \in \mathbb{N}$ according to

$$\text{WT}\{\{x_k\}\}_\Psi(s, k') = \frac{1}{s} \sum_{k=1}^N x_k \overline{\Psi}\left(\frac{k - k'}{s}\right) \quad (\text{E.11})$$

which $\overline{\Psi}$ denoting the complex conjugate of Ψ . Here I use the original normalization, $1/s$, as suggested by Muzy *et al.*. Note that everywhere else in this thesis I use a normalization $1/s^{1/2}$ as discussed in Sec. 1.3 below Eqs. 1.26. The requirements for the mother wavelet Ψ as discussed Sect. 1.3 remain valid. However, in order to achieve higher order detrending it is further required that higher moments vanish

$$\int_{-\infty}^{\infty} x^n \Psi(t) dt = 0. \quad (\text{E.12})$$

This is equivalent with the wavelet being orthogonal to higher order polynomial trends where n denotes the order of the trend. This requirement is satisfied for n th-order Gaussian derivatives $\Psi_{\text{DOG}n}$ whose first n moments according to Eq. (E.12) vanish, see Eq. (1.27b) for a definition of $\Psi_{\text{DOG}n}$.

Step 2:

Having calculated the wavelet transform following Eq. (E.11) one obtains from its modulus $|\text{WT}_\Psi(s, k')|$ the *wavelet skeleton*: (i) Local maxima are identified for fixed scales s , i. e., a maxima is found at position s, k' if $|\text{WT}_\Psi(s, k' - 1)| < |\text{WT}_\Psi(s, k')| \geq |\text{WT}_\Psi(s, k' + 1)|$ where the 'equal' case might be defined differently. (ii) Maxima lines are defined in the space-scale half-plane by starting at a maxima position at large scales [obtained in (i)] and following the nearest maxima down towards lower scales $s' < s$. It has been shown that at least one maxima line points to the position of every singularity in the original signal.

Step 3:

A multifractal partition function is then defined by

$$Z_{\text{WTMM},q}(s) = \sum_{l \in \mathfrak{L}(s)} \left(\sup_{\substack{(s', k') \in l \\ s' \leq s}} |\text{WT}_\Psi(s', k')| \right)^q, \quad \forall q \in \mathbb{R} \quad (\text{E.13})$$

where \mathfrak{L} denotes the set of all maxima lines obtained in *Step 2* and l is a particular maxima line evolving towards the smallest s' . The supremum was included in Eq. (E.13) to ensure a monotonous behavior of $Z_{\text{WTMM},q}(s)$. Practically, the supremum means that maxima values are moved upwards along the maxima line until the currently considered scale is reached.

F. Additional cross-modulation results

F.1. Cross-Modulation in Individuals

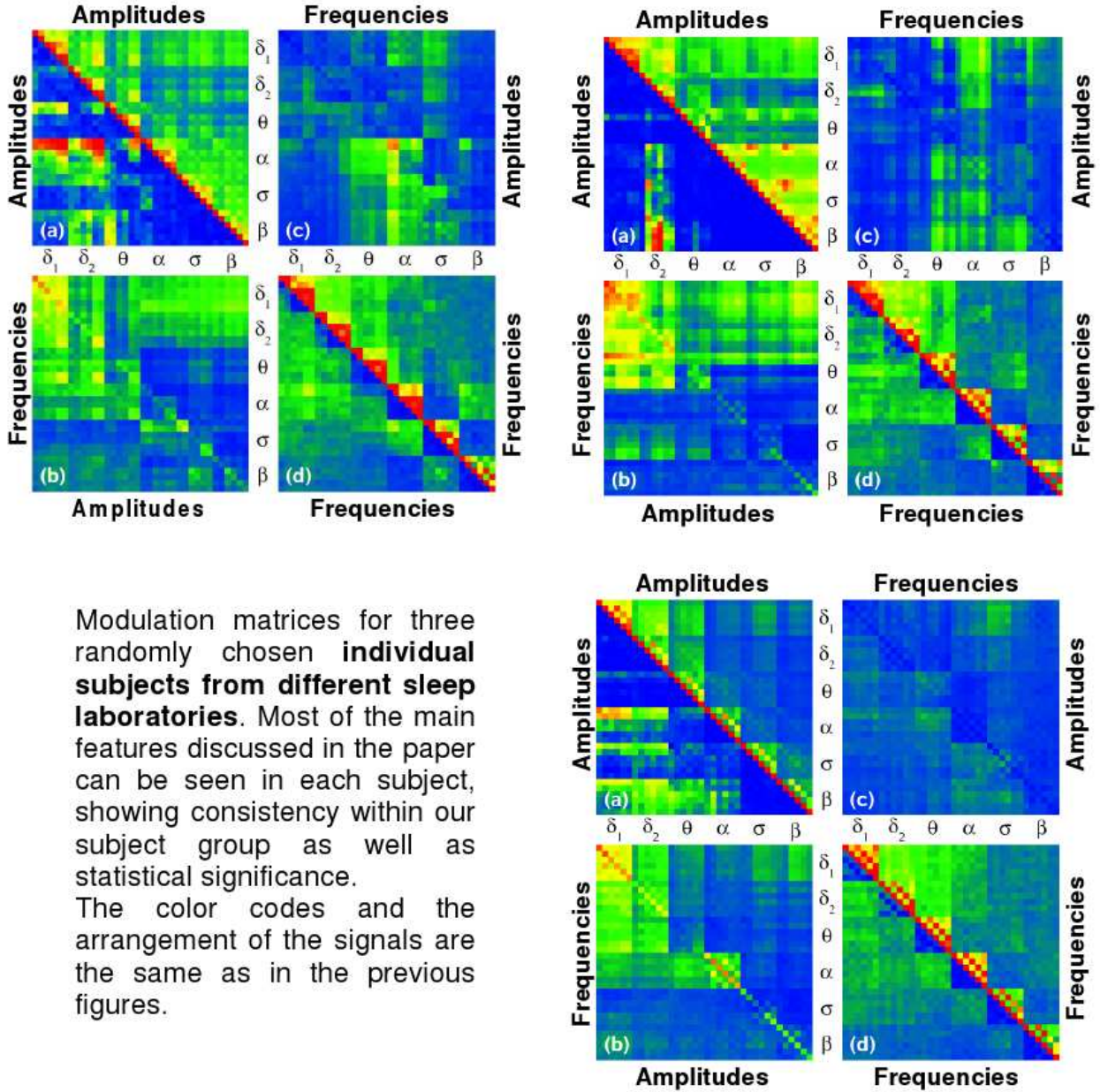


Figure F.1.: Cross-modulation matrices obtained from EEG recordings of three randomly chosen disease-free individuals from the SIESTA data base. The arrangement of frequency bands and of all six EEG leads complies the scheme in Fig. 5.14. Figure taken from supplemental material of our paper [GANS et al. 2009].

F.2. Cross-Modulation in Random Subgroups

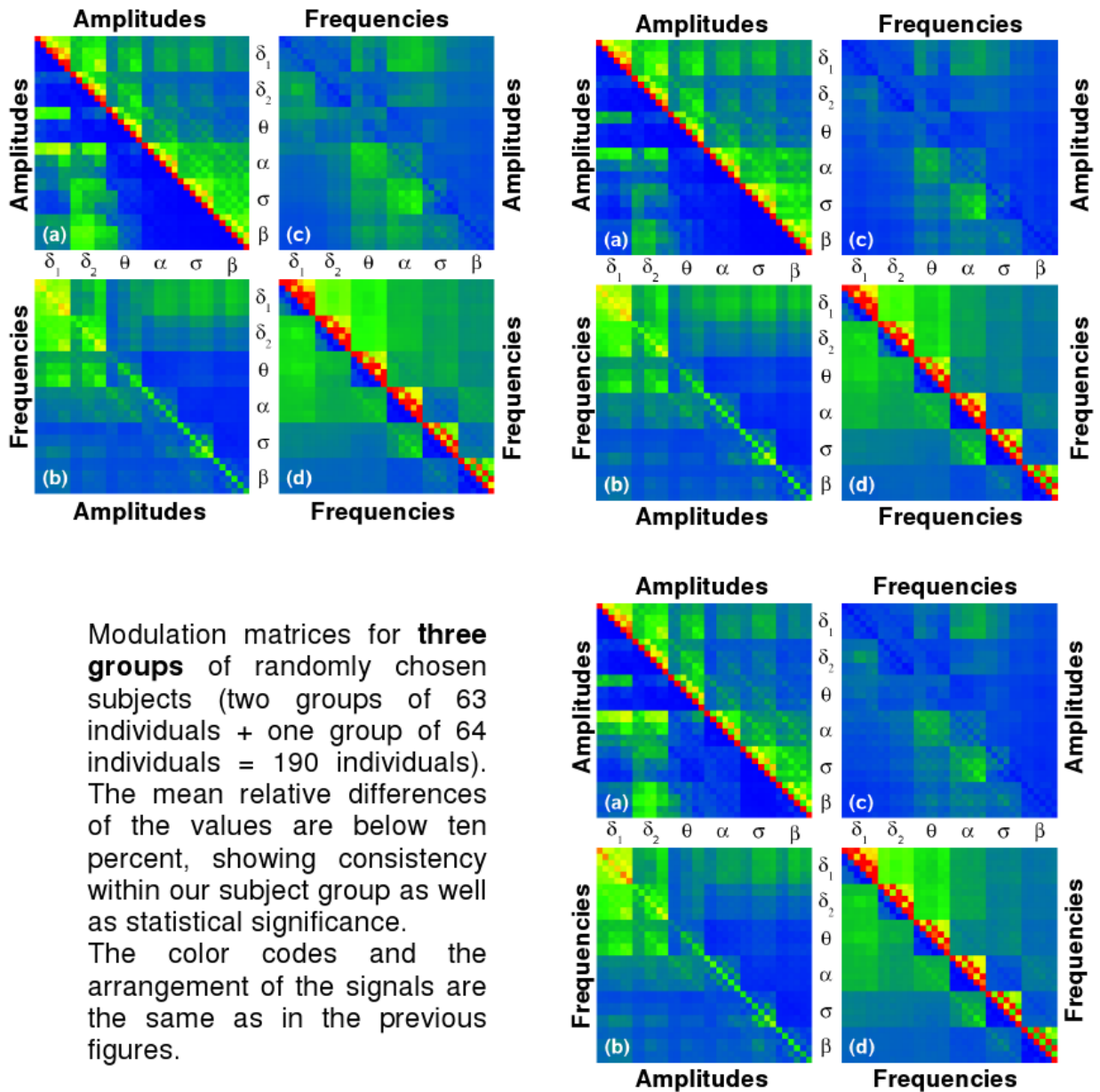


Figure F.2.: Averaged cross-modulation matrices of three subgroups that were generated by randomly subdividing all second nights recordings of disease-free individuals in the SIESTA database. The arrangement of frequency bands and of all six EEG leads complies the scheme in Fig. 5.14. Figure taken from supplemental material of our paper [GANS et al. 2009].

F.3. Cross-Modulation Matrices for Parkinson Patients and Age-Matched Disease-Free Controls

Parkinson Patients

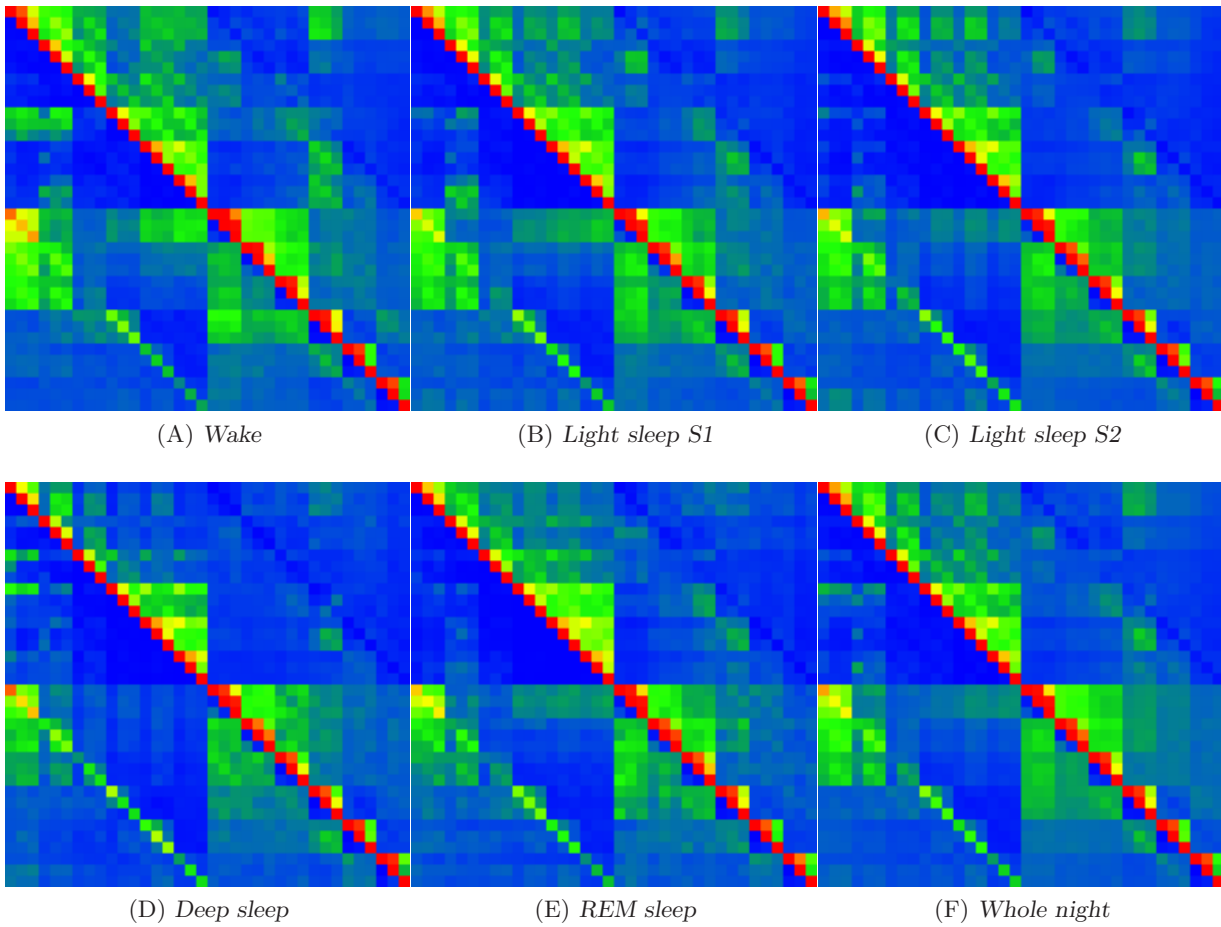


Figure F.3.: Averaged cross-modulation matrices of EEG recordings (adaption and recording night) from 10 Parkinson patients (20 datasets) taken from the SIESTA database. Frequency bands and modulation coefficients are ordered according to Fig. 5.14 only considering EEG recordings from both central leads C3-M1 and C4-M2, and from the occipital lead O1-M2 (same order as described in enlarged cubicle in Fig. 5.14).

Age-Matched Disease-Free Controls

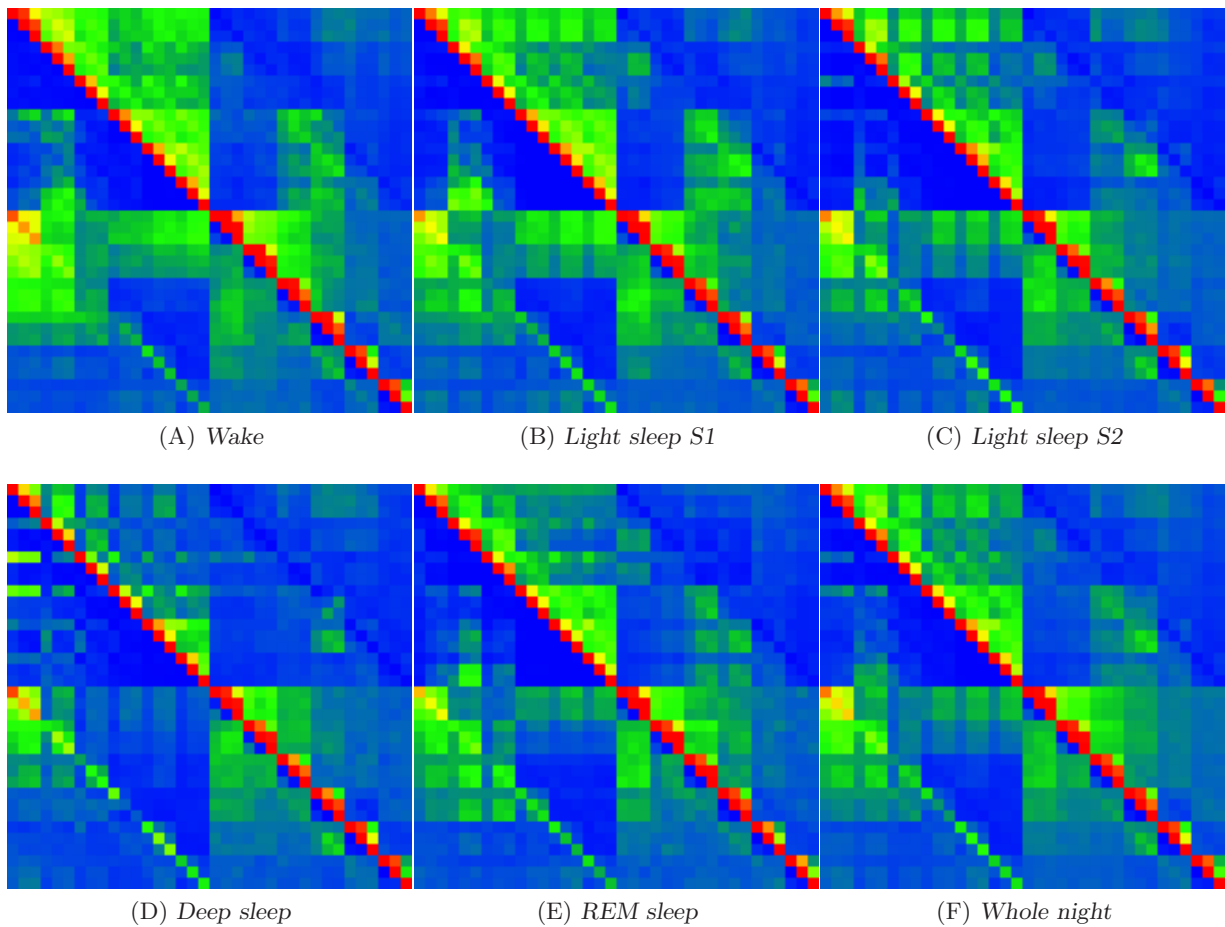


Figure F.4.: Averaged cross-modulation matrices of recordings (adaption and recording night) from 10 disease-free ('healthy') controls (20 datasets) taken from the SIESTA database. All subjects where age matched and laboratory matched with Parkinson patients considered in Fig. F.3. Frequency bands and modulation coefficients are ordered according to Fig. 5.14 only considering EEG recordings from both central leads C3-M1 and C4-M2, and from the occipital lead O1-M2 (same order as described in enlarged cubicle in Fig. 5.14).

F.4. Cross-Modulation Matrices for Sleep Apnea Patients and Age-Matched Disease-Free Controls

Sleep Apnea Patients

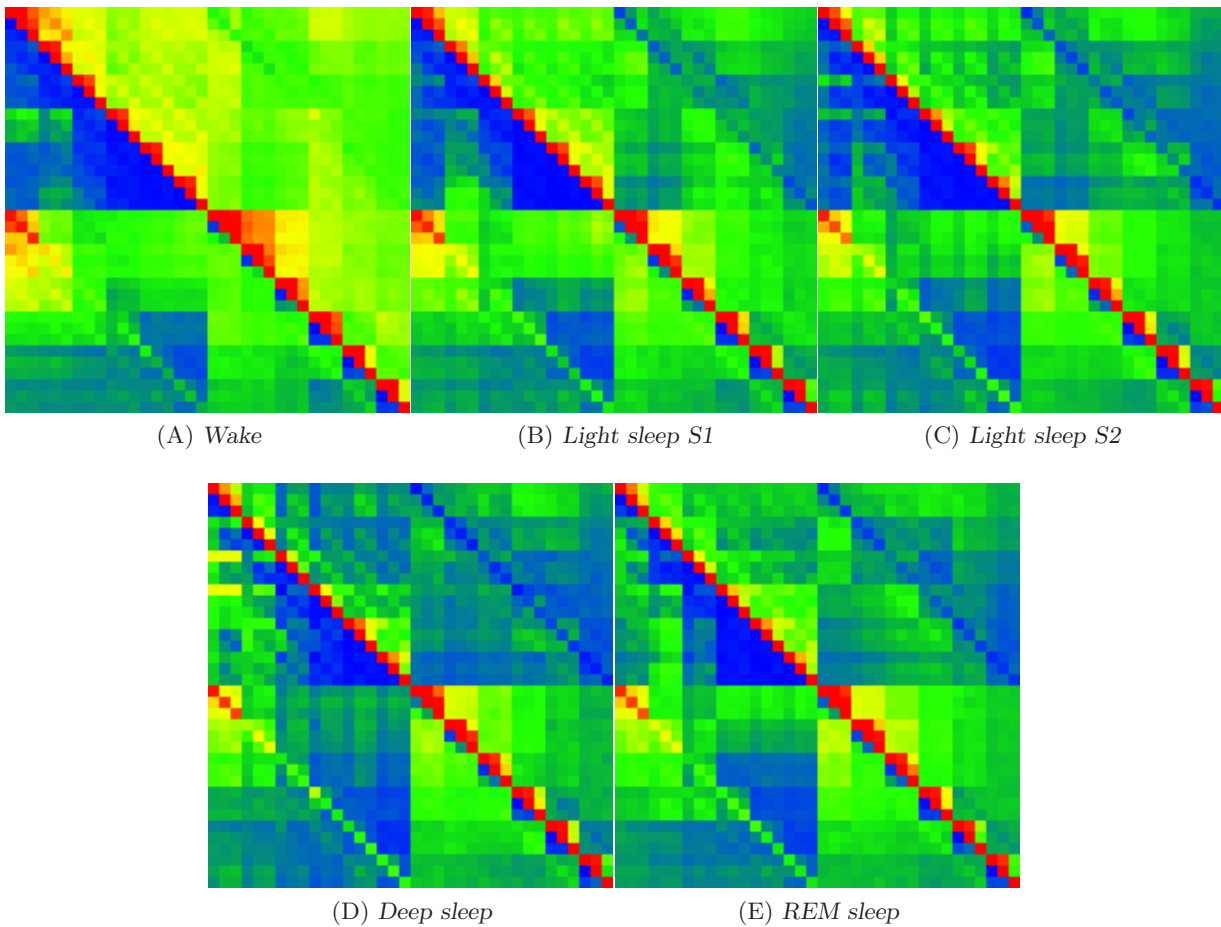


Figure F.5.: Averaged cross-modulation matrices of EEG recordings (adaption and recording night) from 47 sleep apnea patients (94 datasets) taken from the DAPHNET database. Frequency bands and modulation coefficients are ordered according to Fig. 5.14 only considering EEG recordings from both central leads C3-M1 and C4-M2, and from the occipital lead O1-M2 (same order as described in enlarged cubicle in Fig. 5.14).

Age-Matched Disease-Free Controls

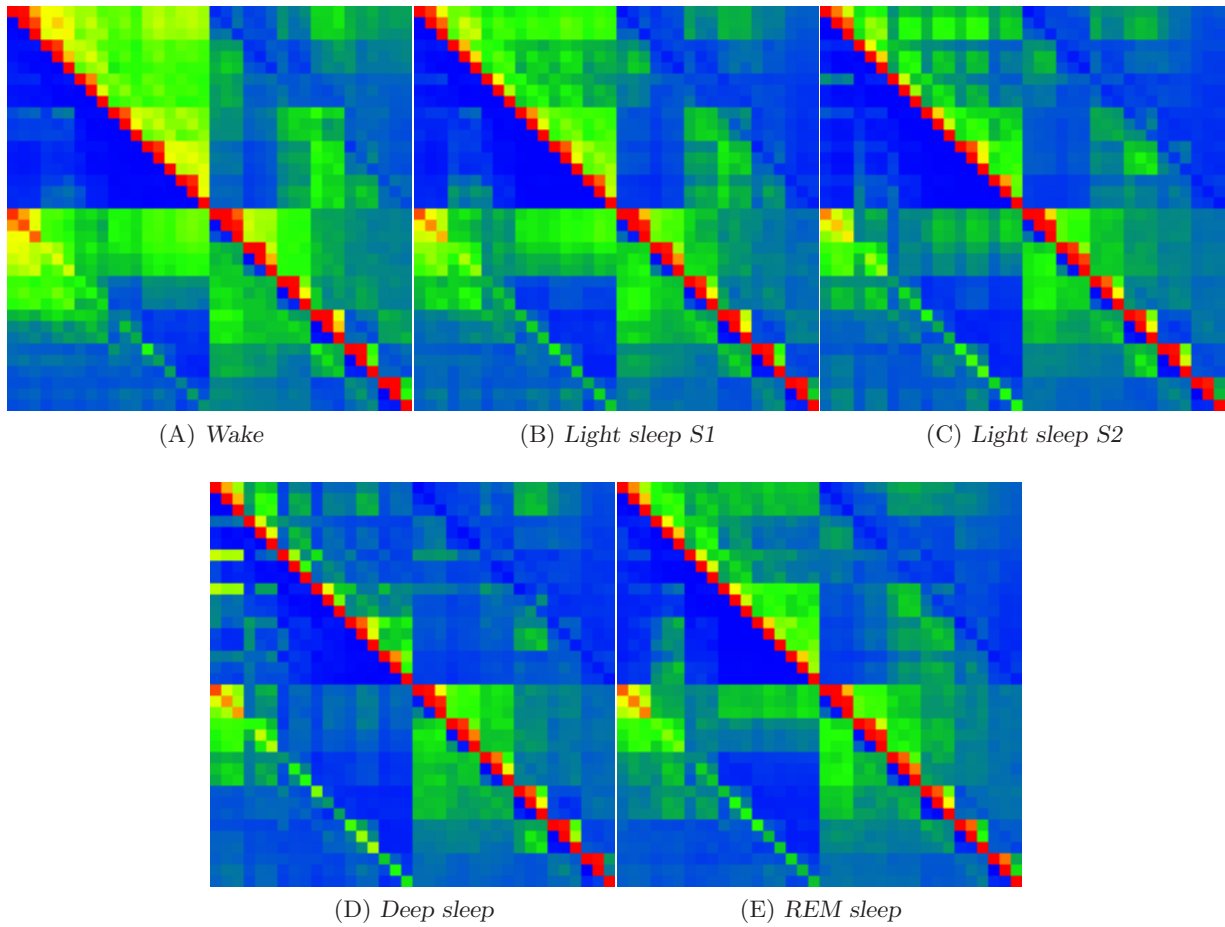


Figure F.6.: Averaged cross-modulation matrices of recordings (adaption and recording night) from 47 disease-free ('healthy') controls (94 datasets) taken from the DAPHNET database. All subjects were age matched with sleep apnea patients considered in Fig. F.5 and data was recorded in the same laboratory at Charité Berlin. Frequency bands and modulation coefficients are ordered according to Fig. 5.14 only considering EEG recordings from both central leads C3-M1 and C4-M2, and from the occipital lead O1-M2 (same order as described in enlarged cubicle in Fig. 5.14).

Bibliography

- ACHERMANN, P. *Oral communication at workshop on complex dynamics in large-scale interacting brain systems: Towards physical models of sleep and consciousness*. Dresden, 2009.
- AKSELROD, S., GORDON, D., UBEL, F. A., SHANNON, D. C., BARGER, A. C., and COHEN, R. J. *Power spectrum analysis of heart rate fluctuation: A quantitative probe of beat-to-beat cardiovascular control*. *Science*, 1981; **213**(4504):220–222.
- ALESSIO, E., CARBONE, A., CASTELLI, G., and FRAPPIETRO, V. *Second-order moving average and scaling of stochastic time series*. *Eur. Phys. J. B*, 2002; **27**:107–200.
- ALVAREZ-RAMIREZ, J., RODRIGUEZ, E., and ECHEVERRIA, J. C. *Detrending fluctuation analysis based on moving average filtering*. *Physica A*, 2005; **354**:199–219.
- ANGELINI, L., TOMMASO, M., GUIDO, M., HU, K., IVANOV, P., MARINAZZO, D., NARDULLI, G., NITTI, L., PELLICORO, M., PIERRO, C., and STRAMAGLIA, S. *Steady-state visual evoked potentials and phase synchronization in migraine patients*. *Phys. Rev. Lett.*, 2004; **93**(3).
- ANISHCHENKO, V., BALANOV, A., JANSON, N., IGOSHEVA, N., and BORDYUGOV, G. *Entrainment between heart rate and weak noninvasive forcing*. *Chaos*, 2000; **10**(10):2339–2348.
- ARNEODO, A., BACRY, E., GRAVES, P. V., and MUZY, J. F. *Characterizing Long-Range Correlations in DNA Sequences from Wavelet Analysis*. *Phys. Rev. Lett.*, 1995; **74**(16):3293–3296.
- ARRAULT, J., ARNEODO, A., DAVIS, A., and MARSHAK, A. *Wavelet based multifractal analysis of rough surfaces: Application to cloud models and satellite data*. *Phys. Rev. Lett.*, 1997; **79**:75.
- ASHKENAZY, Y., BAKER, D. R., GILDOR, H., and HAVLIN, S. *Nonlinearity and multifractality of climate change in the past 420,000 years*. *Geophys. Res. Lett.*, 2003; **30**:2146.
- BACRY, E., DELOUR, J., and MUZY, J. R. *Multifractal random walk*. *Phys. Rev. E*, 2001; **64**:026103.
- BARTHEL, P., SCHNEIDER, R., BAUER, A., ULM, K., SCHMITT, C., SCHÖMIG, A., and SCHMIDT, G. *Risk stratification after acute myocardial infarction by heart rate turbulence*. *Circulation*, 2003; **108**:1221.
- BARTSCH, R., KANTELHARDT, J. W., PENZEL, T., and HAVLIN, S. *Experimental evidence for phase synchronization transitions in the human cardiorespiratory system*. *Phys. Rev. Lett.*, 2007; **98**(5).
- BARTSCH, R., PLOTNIK, M., KANTELHARDT, J. W., HAVFIN, S., GILADI, N., and HAUSDORFF, J. M. *Fluctuation and synchronization of gait intervals and gait force profiles distinguish stages of Parkinson's disease*. *Physica A*, 2007; **383**(2):455–465.
- BASHAN, A., BARTSCH, R. P., KANTELHARDT, J. W., and HAVLIN, S. *Comparison of detrending methods for fluctuation analysis*. *Physica A*, 2008; **387**(21):5080–5090.
- BAUER, A., BARTHEL, P., MUELLER, A., KANTELHARDT, J., and SCHMIDT, G. *Bivariate phase-rectified signal averaging—a novel technique for cross-correlation analysis in noisy nonstationary signals*. *J. Electrocardiol.*, 2009; **42**(6):602–606.

- BAUER, A., KANTELHARDT, J. W., BARTHEL, P., SCHNEIDER, R., MÄKIKALLIO, T., ULM, K., HNATKOVA, K., SCHÖMIG, A., HUIKURI, H., BUNDE, A., MALIK, M., and SCHMIDT, G. *Deceleration capacity of heart rate as a predictor of mortality after myocardial infarction. Lancet*, 2006a; **367**:1674.
- BAUER, A., KANTELHARDT, J. W., BUNDE, A., BARTHEL, P., SCHNEIDER, R., MALIK, M., and SCHMIDT, G. *Phase-rectified signal averaging detects quasi-periodicities in non-stationary data. Physica A*, 2006b; **364**:423–434.
- BENLOUCIF, S., BURGESS, H. J., KLERMAN, E. B., LEWY, A. J., MIDDLETON, B., MURPHY, P. J., PARRY, B. L., and REVELL, V. L. *Measuring melatonin in humans. J. Clin. Sleep Med.*, 2008; **4**(1):66–69.
- BENZI, R., PALADIN, G., PARISI, G., and VULPIANI, A. *On the multifractal nature of fully-developed turbulence and chaotic systems. J. Phys. A*, 1984; **17**:3521.
- BERENDSE, H. W. and STAM, C. J. *Stage-dependent patterns of disturbed neural synchrony in parkinson's disease. Parkinsonism Relat. Disord.*, 2007; **13 Suppl 3**:440–445.
- BERNAOLA-GALVAN, P., IVANOV, P. C., AMARAL, L. A. N., and STANLEY, H. E. *Scale invariance in the nonstationarity of human heart rate. Phys. Rev. Lett.*, 2001; **87**(16):168105.
- BIALONSKI, S. and LEHNERTZ, K. *Identifying phase synchronization clusters in spatially extended dynamical systems. Phys. Rev. E*, 2006; **74**(5):051909.
- BIGGER, J., FLEISS, J., STEINMAN, R., ROLNITZKY, L., KLEIGER, R., and ROTTMAN, J. *Frequency-domain measures of heart period variability and mortality after myocardial-infarction. Circulation*, 1992; **85**(1):164–171.
- BOASHASH, B. *Estimating and interpreting the instantaneous frequency of a signal. 1. fundamentals. Proc. IEEE*, 1992; **80**(4):520–538.
- BOB, P., PALUS, M., SUSTA, M., and GLASLOVA, K. *EEG phase synchronization in patients with paranoid schizophrenia. Neurosci. Lett.*, 2008; **447**(1):73–77.
- BOGACHEV, M. I., EICHNER, J. F., and BUNDE, A. *The effects of multifractality on the statistics of return intervals. , 2008; 161*:181–193.
- BOX, G., JENKINS, G. M., and REINSEL, G. C. *Time Series Analysis: Forecasting and Control* (Prentice-Hall, NY, 1994), 3rd edition.
- BROCKWELL, P. and DAVIS, R. *Introduction to Time Series and Forecasting* (Springer, Berlin, 2003).
- BROWN, T., BEIGHTOL, L. A., KOH, J., and ECKBERG, D. *Important influence of respiration on human r-r interval power spectra is largely ignored. J. Appl. Physiol.*, 1993; **75**:2310.
- BUNDE, A. and HAVLIN, S. (eds.). *Fractals in Science* (Springer Berlin, 1994), 1st edition.
- BUNDE, A. and HAVLIN, S. (eds.). *Fractals and Disordered Systems* (Springer Berlin, 1996), 2nd edition.
- BUNDE, A., HAVLIN, S., KANTELHARDT, J., PENZEL, T., PETER, J., and VOIGT, K. *Correlated and uncorrelated regions in heart-rate fluctuations during sleep. Phys Rev Lett*, 2000; **85**:3736–3739.
- BUNDE, A., KROPP, J., and SCHELLNHUBER, H. J. (eds.). *Science of Disasters Climate Disruptions, Heart Attacks, and Market Crashes* (Springer, 2002).

- BUXTON, R. B. *Introduction to functional magnetic resonance imaging: principles and techniques* (Cambridge University Press, 2002).
- BUYSSE, D. J. *The International Classification of Sleep Disorders, Revised. Diagnostic and Coding Manual*. American Academy of Sleep Medicine, 1st edition, 2001.
- BUYSSE, D. J., REYNOLDS, C. H. F., MONKS, T. H., BERMAN, S., and KUPFER, D. J. *The pittsburgh sleep quality index: A new instrument for psychiatric practice and research. Psychiatry Research*, 1988; **28**:193–213.
- BUZSAKI, G. *Rhythms of the Brain* (Oxford University Press, 2006).
- CAIRNS, J. A., CONNOLLY, S. J., ROBERTS, R., and GENT, M. *Randomised trial of outcome after myocardial infarction in patients with frequent or repetitive ventricular premature depolarisations: Camiat. The Lancet*, 1997; **349**(9053):675 – 682.
- CARBONE, A., CASTELLI, G., and STANLEY, H. *Time-dependent Hurst exponent in financial time series. Physica A*, 2004a; **344**(1-2):267–271.
- CARBONE, A., CASTELLI, G., and STANLEY, H. E. *Analysis of clusters formed by the moving average of a long-range correlated time series. Phys. Rev. E*, 2004b; **69**(2):026105.
- CHEN, Z., HU, K., CARPENA, P., BERNAOLA-GALVAN, P., STANLEY, H. E., and IVANOV, P. C. *Effect of nonlinear filters on detrended fluctuation analysis. Phys. Rev. E*, 2005; **71**:011104.
- CHEN, Z., IVANOV, P. C., HU, K., and STANLEY, H. E. *Effect of nonstationarities on detrended fluctuation analysis. Phys. Rev. E*, 2002; **65**:041107.
- DANKER-HOPFE, H., SCHÄFER, M., DORN, H., ANDERER, P., SALETU, B. GRUBER, G., ZEITLHOFER, J., KUNZ, D., BARBANOJ, M., HIMANEN, S., KEMP, B., PENZEL, T., RÖSCHKE, J., and DORFFNER, G. *Percentile reference charts for selected sleep parameters for 20- 80-year old healthy subjects from the siesta database. Somnologie*, 2005; **9**:3–14.
- DESPOPOULOS, A. and SILBERNAGL, S. *Color Atlas of Physiology* (Thieme Stuttgart, New York, 2003), 5th edition.
- DING, L.-J., PENG, H., CAI, S.-M., and ZHOU, P.-L. *Multifractal analysis of human heartbeat in sleep. Chinese Phys. Lett.*, 2007; **24**(7):2149–2152.
- DORFFNER, G. *et al. Towards a new standard of modelling sleep based on polysomnograms: the siesta project. Proc, ECCN 98. Electroenceph. Clin. Neurophysiol.*, 1998; **106**:28.
- DÜRER, A. *Underweysung der Messung, mit dem Zirckel und Richtscheyt, in Linien, Ebenen unnd gantzen corporen* (SLUB Dresden, Digital Library, 1525).
- ECKBERG, D. L. *The human respiratory gate. J. Physiol.*, 2003; **548**(2):339–352.
- EFRON, B. *1977 rietz lecture - bootstrap methods - another look at the jackknife. Annals of Statistics*, 1979; **7**(1):1–26.
- EFRON, B. and TIBSHIRANI, R. J. *An Introduction to the Bootstrap* (Chapman & Hall, 1993).
- ERNST, J., LITVACK, D., LOZANO, D., CACIOPPO, J., and BERNTSON, G. *Impedance pneumography: Noise as signal in impedance cardiography. Psychophysiol.*, 1999; **36**(3):333–338.
- ESPIRITU, J. R. D. *Aging-related sleep changes. Clin. Geriatr. Med.*, 2008; **24**:1–14.
- FARGE, M. *Wavelet Transforms And Their Applications To Turbulence. Annu. Rev. Fluid Mech.*, 1992; **24**:395–457.
- FEDER, J. *Fractals* (Plenum Press, New York, 1988).

- FOLSTEIN, M. F., FOLSTEIN, S. E., and MCHUGH, P. R. *Mini mental state: A practical method for grading the cognitive state of patients for the clinician. J. Psychiatr. Res.*, 1975; **12**:189–198.
- FRIGO, M. *et al. Fastest fourier transform in the west (FFTW)*. www.fftw.org, 2003.
- GABOR, D. *Theory of communication. Radio Commun. Eng.*, 1946; **93**:429.
- GANS, F., SCHUMANN, A. Y., KANTELHARDT, J. W., PENZEL, T., and FIETZE, I. *Cross-modulated amplitudes and frequencies characterize interacting components in complex systems. Phys. Rev. Lett.*, 2009; **102**:098701.
- GILAD, O., SWENNE, C., TOLEDO, E., and AKSELROD, S. *Afferent somatosensory information as a possible cause of cardiac-locomotor coupling?* In: *Computers in Cardiology*, edited by A. Murray. European Soc. of Cardiology; Nat. Inst. of Health, USA (IEEE, Piscataway, NJ, USA, 2003), pages 797–800.
- GLASS, L. *Synchronization and rhythmic processes in physiology. Nature*, 2001; **410**(6825):277–284.
- GOLDBERGER, A. L., AMARAL, L. A. N., HAUSDORFF, J. M., IVANOV, P. C., PENG, C.-K., and STANLEY, H. E. *Fractal dynamics in physiology: Alterations with disease and aging. Proceedings of the National Academy of Sciences of the United States of America*, 2002; **99**(Suppl 1):2466–2472.
- GOLDBERGER, A. L., RIGNEY, D. R., and WEST, B. J. *Chaos and fractals in human physiology. Sci. Am.*, 1990; **262**(2):43–49.
- GOLDBERGER, J. J. *Sympathovagal balance: how should we measure it? Am J Physiol Heart Circ Physiol*, 1999; **276**(4):H1273–1280.
- GOUPILLAUD, P., GROSSMANN, A., and MORLET, J. *Cycle-octave and related transforms in seismic signal analysis. Geop exploration*, 1984; **23**(1):85–102.
- GOVINDAN, R. B. and KANTZ, H. *Long-term correlations and multifractality in surface wind speed. Europhys. Lett.*, 2004; **68**(2):184–190.
- GOWERS, S. W. R. *A Manual of Diseases of the Nervous System* (Blakiston Son & Co, Philadelphia, PA, 1893), 2nd edition.
- GREINER, M., EGGERS, H. C., and LIPA, P. *Analytic multivariate generating function for random multiplicative cascade processes. Phys. Rev. Lett.*, 1998; **80**:5333.
- GRINER, P., MAYEWSKI, R., MUSHLIN, A., and GREENLAND, P. *Selection and interpretation of diagnostic-tests and procedures - principles and applications. Annals of Internal Medicine*, 1981; **94**(4):553.
- GU, G. F. and ZHOU, W. X. *Detrended fluctuation analysis for fractals and multifractals in higher dimensions. Phys. Rev. E*, 2006; **74**:061104.
- HAAR, A. *On the theory of orthogonal function systems (First announcement). Mathematische Annalen*, 1910; **69**:331–371.
- HALSEY, T. C., JENSEN, M. H., KADANOFF, L. P., PROCACCIA, I., and SHRAIMAN, B. I. *Fractal measures and their singularities: The characterization of strange sets. Phys. Rev. A*, 1986; **33**(2):1141–1151.
- HAMANN, C., BARTSCH, R. P., SCHUMANN, A. Y., PENZEL, T., HAVLIN, S., and KANTELHARDT, J. W. *Automated synchrogram analysis applied to heartbeat and reconstructed respiration. Chaos*, 2009; **19**(1).

- HAYANO, J., YASUMA, F., OKADA, A., MUKAI, S., and FUJINAMI, T. *Respiratory Sinus Arrhythmia: A Phenomenon Improving Pulmonary Gas Exchange and Circulatory Efficiency. Circulation*, 1996; **94**(4):842–847.
- HENEGHAN, C. and MCDARBY, G. *Establishing the relation between detrended fluctuation analysis and power spectral density analysis for stochastic processes. Phys. Rev. E*, 2000; **62**(5):6103–6110.
- HIRSCH, J. A. and BISHOP, B. *Respiratory sinus arrhythmia in humans: how breathing pattern modulates heart rate. Am. J. Physiol.*, 1981; **241**:H620.
- HONERKAMP, J. *Stochastic Dynamical Systems. Concepts, Numerical Methods, Data Analysis* (VCH Publishers Inc., 1994).
- HOUTVEEN, J., GROOT, P., and DE GEUS, E. *Validation of the thoracic impedance derived respiratory signal using multilevel analysis. Int. J. Psychophysiol.*, 2006; **59**(2):97–106.
- HRV TASK FORCE. *Heart rate variability: standards of measurement, physiological interpretation, and clinical use. task force of the european society of cardiology and the north american society of pacing and electrophysiology. Circulation*, 1996; **93**(5):1043–1065.
- HU, K., IVANOV, P., CHEN, Z., CARPENA, P., and STANLEY, H. *Effect of trends on detrended fluctuation analysis. Phys. Rev. E*, 2001; **64**:011114.
- HUBER, R., GRAF, T., COTE, K., WITTMANN, L., GALLMANN, E., MATTER, D., SCHUDERER, J., KUSTER, N., BORBELY, A., and ACHERMANN, P. *Exposure to pulsed high-frequency electromagnetic field during waking affects human sleep EEG. Neuroreport*, 2000; **11**(15):3321–3325.
- HUIKURI, H. V., MÄKIKALLIO, T. H., PENG, C. K., GOLDBERGER, A. L., HINTZE, U., and MOLLER, M. *Fractal correlation properties of rr interval dynamics and mortality in patients with depressed left ventricular function after an acute myocardial infarction. Circulation*, 2000; **101**:47–53.
- HUIKURI, H. V., PERKIÖMÄKI, J. S., MAESTRI, R., and PINNA, G. D. *Clinical impact of evaluation of cardiovascular control by novel methods of heart rate dynamics. Phil. Trans. R. Soc. A*, 2009; **367**:1223–1238.
- HUNT, G. *Random Fourier Transforms. Trans. Amer. Math. Soc.*, 1951; **71**(JUL):38–69.
- HURST, H. *Long-term storage capacity of reservoirs. Trans. Americ. Soc. Civ. Eng.*, 1951; **116**:770–799.
- HUYGENS, C. *Horologium Oscillatorium* (Apud F. Muguet, Parisiis, 1673).
- HYVÄRINEN, A., KARHUNEN, J., and OJA, E. *Independent Component Analysis* (Wiley, New York, 2001).
- IBER, C., ANCOLI-ISRAEL, S., CHESSON JR., A. L., and QUAN, S. F. *The AASM Manual for the Scoring of Sleep and Associated Events. Rules, Terminology and Technical Specifications*. American Academy of Sleep Medicine, 1st edition, 2007.
- IVANOV, P., BUNDE, A., AMARAL, L., HAVLIN, S., FRITSCH-YELLE, J., BAEVSKY, R., STANLEY, H., and GOLDBERGER, A. *Sleep-wake differences in scaling behavior of the human heart-beat: Analysis of terrestrial and long-term space flight data. Europhys. Lett.*, 1999a; **48**(5):594–600.
- IVANOV, P. C., AMARAL, L. A. N., GOLDBERGER, A. L., HAVLIN, S., ROSENBLUM, M. G., STANLEY, H. E., and STRUZIK, Z. R. *From 1/f noise to multifractal cascades in heartbeat dynamics. Chaos*, 2001; **11**(3):641–652.

- IVANOV, P. C., AMARAL, L. A. N., GOLDBERGER, A. L., HAVLIN, S., ROSENBLUM, M. G., STRUZIK, Z. R., and STANLEY, H. E. *Multifractality in human heartbeat dynamics*. *Nature*, 1999b; **399**:461–465.
- IZHIKEVICH, E. M. and FITZHUGH, R. *FitzHugh-Nagumo model*. *Scholarpedia*, 2006; **1**(9):1349.
- JASPER, H. H. *et al.* *Report of the committee on methods of clinical examination in electroencephalography: 1957*. *Electroencephalography and Clin. Neurophysiol.*, 1958; **10**(2):370–375.
- JENKINS, G. M. and WATTS, D. G. *Spectral Analysis and Its Applications* (San Francisco: Holden-Day, 1969), 1st edition.
- JERBI, K., LACHAUX, J.-P., N'DIAYE, K., PANTAZIS, D., LEAHY, R. M., GARNERO, L., and BAILLET, S. *Coherent neural representation of hand speed in humans revealed by meg imaging*. *Proc. Nat. Acad. Sci. USA*, 2007; **104**(18):7676–7681.
- JOKINEN, V., TAPANAINEN, J. M., SEPPÄNEN, T., and HUIKURI, H. V. *Temporal changes and prognostic significance of measures of heart rate dynamics after acute myocardial infarction in the beta-blocking era*. *Am. J. Cardiol.*, 2003; **92**:907–912.
- JULIEN, C. *The enigma of mayer waves: Facts and models*. *Cardiovascular Research* **70**, 2006; **70**:12–21.
- KANTELHARDT, J., KOSCIELNY-BUNDE, E., REGO, H., HAVLIN, S., and BUNDE, A. *Detecting long-range correlations with detrended fluctuation analysis*. *Physica A*, 2001; **295**:441–454.
- KANTELHARDT, J., PENZEL, T., ROSTIG, S., BECKER, H., HAVLIN, S., and BUNDE, A. *Breathing during rem and non-rem sleep: correlated versus uncorrelated behaviour*. *Physica A*, 2003a; **319**:447–457.
- KANTELHARDT, J., ZSCHIEGNER, S., KOSCIELNY-BUNDE, E., HAVLIN, S., BUNDE, A., and STANLEY, H. *Multifractal detrended fluctuation analysis of nonstationary time series*. *Physica A*, 2002; **316**(1-4):87–114.
- KANTELHARDT, J. W., ASHKENAZY, Y., IVANOV, P. C., BUNDE, A., HAVLIN, S., PENZEL, T., PETER, J.-H., and STANLEY, H. E. *Characterization of sleep stages by correlations in the magnitude and sign of heartbeat increments*. *Phys. Rev. E*, 2002; **65**(5):051908.
- KANTELHARDT, J. W., BAUER, A., SCHUMANN, A. Y., BARTHEL, P., SCHNEIDER, R., MALIK, M., and SCHMIDT, G. *Phase-rectified signal averaging for the detection of quasi-periodicities and the prediction of cardiovascular risk*. *Chaos*, 2007; **17**(1):015112.
- KANTELHARDT, J. W., RYBSKI, D., ZSCHIEGNER, S. A., BRAUN, P., KOSCIELNY-BUNDE, E., LIVINA, V., HAVLIN, S., and BUNDE, A. *Multifractality of river runoff and precipitation: comparison of fluctuation analysis and wavelet methods*. *Physica A*, 2003b; **bf 330**:240.
- KANTZ, H. and SCHREIBER, T. *Nonlinear Time Series Analysis* (Cambridge University Press, 2004).
- KARASIK, R., SAPIR, N., ASHKENAZY, Y., IVANOV, P. C., DVIR, I., LAVIE, P., and HAVLIN, S. *Correlation differences in heartbeat fluctuations during rest and exercise*. *Phys. Rev. E*, 2002; **66**:052902.
- KESELBRENER, L. and AKSELROD, S. *Selective discrete fourier transform algorithm for time-frequency analysis: Method and application on simulated and cardiovascular signals*. *IEEE Trans. Biomed. Eng.*, 1996; **43**(8):789–802.
- KESTENER, P. and ARNEODO, A. *Generalizing the wavelet-based multifractal formalism to random vector fields: application to three-dimensional turbulence velocity and vorticity data*. *Phys. Rev. Lett.*, 2004; **93**:044501.

- KITAJO, K., DOESBURG, S. M., YAMANAKA, K., NOZAKI, D., WARD, L. M., and YAMAMOTO, Y. *Noise-induced large-scale phase synchronization of human-brain activity associated with behavioural stochastic resonance. Europhys. Lett.*, 2007; **80**(4).
- KLEIGER, R. E., MILLER, J., JR., J. B., and MOSS, A. J. *Decreased heart rate variability and its association with increased mortality after acute myocardial infarction. The American Journal of Cardiology*, 1987; **59**(4):256 – 262.
- KOBAYASHI, M. and MUSHA, T. *1/f fluctuation of heartbeat periods. IEEE Transactions on Biomedical Engineering*, 1982; **29**(6):456–457.
- KOHLER, B., HENNIG, C., and ORGLMEISTER, R. *The principles of software QRS detection. IEEE Eng. Med. Biol.*, 2002; **21**(1):42–57.
- KOSCIELNY-BUNDE, E., BUNDE, A., HAVLIN, S., ROMAN, H. E., GOLDRICH, Y., and SCHELLNHUBER, H.-J. *Indication of a universal persistence law governing atmospheric variability. Phys. Rev. Lett.*, 1998a; **81**(3):729–732.
- KOSCIELNY-BUNDE, E., ROMAN, H., BUNDE, A., HAVLIN, S., and SCHELLNHUBER, H. *Long-range power-law correlations in local daily temperature fluctuations. Philosoph. Magazin B Cond. Matt.*, 1998b; **77**(5):1331–1340.
- KRYGER, M. H., ROTH, T., and DEMENT, W. C. (eds.). *Principles and Practice of Sleep Medicine* (Elsevier, 2005), 4th edition.
- KURAMOTO, Y. *Chemical oscillations, waves, and turbulence* (Dover, 2003), 2nd edition.
- KUSUNOKI, Y., FUKUMOTO, M., and NAGASHIMA, T. *A statistical method of detecting synchronization for cardio-music synchrogram. IEICE Trans. Fund. Electr. Communic. Comp. Sci.*, 2003; **E86A**(9):2241–2247.
- LOTTRIC, M. B. and STEFANOVSKA, A. *Synchronization and modulation in the human cardiorespiratory system. Physica A*, 2000; **283**(3-4):451 – 461.
- LOWN, B. and VERRIER, R. L. *Neural activity and ventricular-fibrillation. New Engl. J. Med.*, 1976; **294**(21):1165–1170.
- LUCK, S. J. *An introduction to the event-related potential technique* (The MIT Press, 2005).
- MÄKIKALLIO, T. H., HOIBER, S., KOBER, L., TORP-PEDERSEN, C., PENG, C. K., GOLDBERGER, A. L., and HUIKURI, H. V. *Fractal analysis of heart rate dynamics as a predictor of mortality in patients with depressed left ventricular function after acute myocardial infarction. trace investigators. trandolapril cardiac evaluation. Am. J. Cardiol.*, 1999; **83**:836–839.
- MALMIVUO, J. and PLONSEY, R. *Bioelectromagnetism - Principles and Applications of Bioelectric and Biomagnetic Fields* (printed version: Oxford University Press, New York, 1995), open web book edition.
- MANDELBROT, B. B. *How long is the coast of britain? statistical self-similarity and fractional dimension. Science*, 1967; **156**(3775):636–638.
- MANDELBROT, B. B. *Les objets fractals, forme, hasard et dimension.* (Flammarion, Paris, 1975). English translation: *Fractals: Form, Chance and Dimension* (1977).
- MANDELBROT, B. B. *The Fractal Geometry of Nature* (W. H. Freeman & Co., 1982). Improved version of original publication: *Les objets fractals, forme, hasard et dimension* (1975); translation: *Fractals: Form, Chance and Dimension* (1977).
- MANDELBROT, B. B. and NESS, J. W. V. *Fractional brownian motions, fractional noises and applications. SIAM Review*, 1968; **10**(4):422–437.

- MANN, H. and WHITNEY, D. *On a test of whether one of 2 random variables is stochastically larger than the other. Annals of Mathematical Statistics*, 1947; **18**(1):50–60.
- MARAUN, D., RUST, H. W., and TIMMER, J. *Tempting long-memory – on the interpretation of dfa results. Nonlin. Proc. Geophys.*, 2004; **11**:495–503.
- MEINECKE, F., ZIEHE, A., KURTHS, J., and MULLER, K. *Measuring phase synchronization of superimposed signals. Phys. Rev. Lett.*, 2005; **94**(8).
- MEMBERS OF SIESTA EU PROJECT. *Protocol - recording of standardized all-night sleep records. Technical Report 2.0*, 1998.
- MENEVEAU, C. and SREENIVASAN, K. R. *Simple multifractal cascade model for fully-developed turbulence. Phys. Rev. Lett.*, 1987; **59**(1424).
- METZ, C. E. *Basic principles of roc analysis. Seminars in Nuclear Medicine*, 1978; **8**(4):283 – 298.
- MEYERS, R. A. (ed.). *Encyclopedia of Complexity and Systems Science* (Springer, 2009).
- MOISE, A., CLEMENT, B., DUCIMETIERE, P., and BOURASSA, M. *Comparison of receiver operating curves derived from the same population - a bootstrapping approach. Computers and Biomedical Research*, 1985; **18**(2):125–131.
- MULLER, J., LUDMER, P., WILlich, S., TOFLER, G., AYLMEER, G., KLANGOS, I., and STONE, P. *Circadian variation in the frequency of sudden cardiac death. Circulation*, 1987; **75**(1):131–138.
- MÜLLER-NORDHORN, J., ARNTZ, H. R., LÖWEL, H., and WILlich, S. N. *The epidemiology of sudden cardiac death. Herzschrittmachertherapie und Elektrophysiologie*, 2001; **12**(1):3–8.
- MUZY, J. F., BACRY, E., and ARNEODO, A. *Wavelets and Multifractal Formalism for Singular Signals - Application to Turbulence Data. Phys. Rev. Lett.*, 1991; **67**(25):3515–3518.
- MUZY, J. F., BACRY, E., and ARNEODO, A. *The Multifractal Formalism Revisited with Wavelets. Int. J. Bifurcat. Chaos*, 1994; **4**(2):245–302.
- NEIMAN, A., SCHIMANSKY-GEIER, L., CORNELL-BELL, A., and MOSS, F. *Noise-enhanced phase synchronization in excitable media. Phys. Rev. Lett.*, 1999; **83**(23):4896–4899.
- NIEUWBOER, A., VERCRUYSE, S., FEYS, P., LEVIN, O., SPILDOOREN, J., and SWINNEN, S. *Upper limb movement interruptions are correlated to freezing of gait in parkinson’s disease. Eur. J. Neurosci.*, 2009; **29**:1422–1430.
- NIKULIN, V. and BRISMAR, T. *Long-range temporal correlations in alpha and beta oscillations: effect of arousal level and test-retest reliability. Clinical Neurophysiology*, 2004; **115**(8):1896–1908.
- NIKULIN, V. and BRISMAR, T. *Phase synchronization between alpha and beta oscillations in the human electroencephalogram. Neuroscience*, 2006; **137**(2):647–657.
- OHLY, A. *EKG endlich verstdlich* (Urban Fisher Mnchen Jena, 2008).
- OLBRICH, E. and ACHERMANN, P. *Analysis of oscillatory patterns in the human sleep EEG using a novel detection algorithm. J. Sleep Res.*, 2005; **14**(4):337–346.
- OSWIECIMKA, P., KWAPIEN, J., and DROZDZ, S. *Multifractality in the stock market: price increments versus waiting times. Physica A*, 2005; **347**:626.
- OSWIECIMKA, P., KWAPIEN, J., and DROZDZ, S. *Wavelet versus detrended fluctuation analysis of multifractal structures. Phys. Rev. E*, 2006; **74**:016103.

- OTT, E. *Chaos in Dynamical Systems* (Cambridge University Press, 2002), 2nd edition.
- PALUŠ, M. *Detecting phase synchronization in noisy systems. Physics Letters A*, 1997; **235**(4):341–351.
- PARKINSON, J. *An Essay on the Shaking Palsy* (Whittingham and Rowland, London, 1817).
- PENG, C., BULDYREV, S., HAVLIN, S., SIMONS, M., STANLEY, H., and GOLDBERGER, A. *Mosaic organization of dna nucleotides. Phys Rev E*, 1994; **49**:1685–1689. First article on DFA.
- PENG, C. K., HAVLIN, S., STANLEY, H. E., and GOLDBERGER, A. L. *Quantification of scaling exponents and crossover phenomena in nonstationary heartbeat time series. Chaos*, 1995; **5**(1):82–87.
- PENTTILÄ, J., HELMINEN, A., JARTTI, T., KUUSELA, T., HUUKURI, H., TULPPO, M., COFFENG, R., and SCHEININ, H. *Time domain, geometrical and frequency domain analysis of cardiac vagal outflow: effects of various respiratory patterns. Clin. Physiol.*, 2001; **21**(3):365–376.
- PENZEL, T., KANTELHARDT, J., GROTE, L., PETER, J., and BUNDE, A. *Comparison of detrended fluctuation analysis and spectral analysis for heart rate variability in sleep and sleep apnea. IEEE Trans Biomed Eng*, 2003; **50**:1143–1151.
- PENZEL, T., LO, C. C., IVANOV, P. C., KESPER, K., BECKER, H. F., and VOGELMEIER, C. *Analysis of sleep fragmentation and sleep structure in patients with sleep apnea and normal volunteers. Proc. IEEE Eng. Med. Biol., 27th Annual Conference*, 2005; .
- PETERSON, B. M., WANDERS, I., HORNE, K., COLLIER, S., ALEXANDER, T., KASPI, S., and MAOZ, D. *On uncertainties in cross-correlation lags and the reality of wavelength-dependent continuum lags in active galactic nuclei. PASP*, 1998; **110**:660–670.
- PIKOVSKY, A. and ROSENBLUM, M. *Synchronization. Scholarpedia*, 2007; **2**(12):1459.
- PIKOVSKY, A., ROSENBLUM, M., and KURTHS, J. *A universal concept in nonlinear sciences* (Cambridge University Press, 2001).
- PLOTNIK, M., GILADI, N., BALASH, Y., PERETZ, C., and HAUSDORFF, J. M. *Is freezing of gait in parkinson's disease related to asymmetric motor function? Ann. Neurol.*, 2005; **57**:656–663.
- PLOTNIK, M., GILADI, N., and HAUSDORFF, J. M. *A new measure for quantifying the bilateral coordination of human gait: Effects of aging and parkinson's disease. Exp. Brain Res.*, 2007; **181**:561–570.
- PLOTNIK, M., GILADI, N., and HAUSDORFF, J. M. *Bilateral coordination of walking and freezing of gait in parkinson's disease. Eur. J. Neurosci.*, 2008; **27**:1999–2006.
- PLOTNIK, M., HERMAN, T., SHAVIV, E., BROZGOL, M., GILADI, N., and HAUSDORFF, J. M. *Impaired bilateral coordination of gait and upper extremity rhythmic movements in parkinson's disease: Association with freezing of gait. Mov. Disord.*, 2009; **24**:341.
- POLICH, J. (ed.). *Detection of Change: Event-related potentials and fMRI findings* (Kluwer Academic Publishers, 2003).
- PRESS, W. H., RYBICKI, G. B., and HEWITT, J. N. *The time delay of gravitational lens 0957+561. I. Methodology and analysis of optical photometric data. Astrophys. J.*, 1992; **385**:404–415.
- PRIESTL, M. *Nonlinear and Non-Stationary Time Series* (Academic Press, New York, 1988).

- PRIORI, S., ALIOT, E., BLOMSTROM-LUNDQVIST, C., BOSSAERT, L., BREITHARDT, G., BRUGADA, P., CAMM, A., CAPPATO, R., COBBE, S., DI MARIO, C., MARON, B., MCKENNA, W., PEDERSEN, A., RAVENS, U., SCHWARTZ, P., TRUSZ-GLUZA, M., VARDAS, P., WELLENS, H., and ZIPES, D. *Task force on sudden cardiac death of the european society of cardiology. Europ. Heart Journ.*, 2001; **22**(16):1374–1450.
- QUIAN QUIROGA, R., KRASKOV, A., KREUZ, T., and GRASSBERGER, P. *Performance of different synchronization measures in real data: A case study on electroencephalographic signals. Phys. Rev. E*, 2002; **65**(4):041903.
- QUIAN QUIROGA, R., REDDY, L., KREIMAN, G., KOCH, C., and FRIED, I. *Invariant visual representation by single neurons in the human brain. Nature*, 2005; **435**(7045):1102–1110.
- RANGARAJAN, G. and DING, M. *Integrated approach to the assessment of long range correlation in time series data. Phys. Rev. E*, 2000; **61**(5):4991–5001.
- RECHTSCHAFFEN, A. and KALES, A. *A manual of of standardized terminology, techniques, and scoring system for sleep stages of human subjects*. US Public Health Service, US Government Printing Office, 1968.
- RÉNYI, A. *On measures of entropy and information. Proc. Fourth Berkeley Symp. on Math. Statist. and Prob.*, 1961; **1**:547–561.
- ROMAN, H. E., CELI, A., and DE FILIPPI, G. *Fluctuation analysis of meteo-marine data.*, 2008; **161**:195–205.
- ROSENBLUM, M. G., TASS, P. A., and KURTHS, J. *Handbook of biological physics. Vol. 4, Neuroinformatics*, chapter Phase-Synchronization: Form theory to analysis (Elsevier, Amsterdam, 2001), pages 279–321.
- ROSTIG, S., KANTELHARDT, J. W., PENZEL, T., CASSEL, W., PETER, J. H., VOGELMEIER, C., BECKER, H. F., and JERRENTROP, A. *Nonrandom variability of respiration during sleep in healthy humans. Sleep*, 2005; **28**(4):411–417.
- ROTHLISBERGER, B., BADRA, L., HOAG, J., COOKE, W., KUUSELA, T., TAHVANAINEN, K., and ECKBERG, D. *Spontaneous ‘baroreflex sequences’ occur as deterministic functions of breathing phase. Clin. Physiol. Funct. Imaging*, 2003; **23**(6):307–313.
- RUST, H. W. *Detection of Long-Range Dependence - Applications in Climatology an Hydrology*. Ph.D. thesis, University of Potsdam, 2007.
- RYBSKI, D. and BUNDE, A. *On the detection of trends in long-term correlated records. Physica A*, 2009; **388**(8):1687–1695.
- SASSI, R., SIGNORINI, M. G., and CERUTTI, S. *Multifractality and heart rate variability. Chaos*, 2009; **19**(2).
- SCARGLE, J. D. *Studies in astronomical time series analysis iii. fourier transforms autocorrelation functions, and cross-correlation functions of unevenly spaced data. Astrophys. J.*, 1989; **343**:874–887.
- SCHÄFER, C., ROSENBLUM, M., KURTHS, J., and ABEL, H. *Heartbeat synchronized with ventilation. Nature*, 1998; **392**(6673):239–240.
- SCHÄFER, C., ROSENBLUM, M. G., ABEL, H.-H., and KURTHS, J. *Synchronization in the human respiratory system. Phys. Rev. E*, 1999; **60**(1):857–870.
- SCHLITGEN, R. and STREITBERG, B. H. J. *Zeitreihenanalyse* (R. Oldenburg Verlag München Wien, 1999), 8th edition.

- SCHMITT, D. T. and IVANOV, P. C. *Fractal scale-invariant and nonlinear properties of cardiac dynamics remain stable with advanced age: a new mechanistic picture of cardiac control in healthy elderly*. *Am. J. Physiol. Regul. Integr. Comp. Physiol.*, 2007; **293**:R1923–R1937.
- SCHMITT, D. T., STEIN, P. K., and IVANOV, P. C. *Stratification Pattern of Static and Scale-Invariant Dynamic Measures of Heartbeat Fluctuations Across Sleep Stages in Young and Elderly*. *IEEE Trans. Biomed. Eng.*, 2009; **56**(5):1564–1573.
- SCHNEIDER, R. *Opensource toolbox for handling cardiologic data, available on the internet www.librasch.org*. 2005.
- SCHREIBER, T. and SCHMITZ, A. *Improved surrogate data for nonlinearity tests*. *Phys. Rev. Lett.*, 1996; **77**(4):635–638.
- SCHUMANN, A. Y. *Waveletanalyse von Sedimentdaten unter Einbeziehung von Alters-Tiefen-Modellen*. Master's thesis, Department of Nonlinear Science, Potsdam University, 2004.
- SCHUMANN, A. Y., BARTSCH, R. P., PENZEL, T., IVANOV, P. C., and KANTELHARDT, J. W. *Normal aging effects on cardio-respiratory variability across sleep stages*. *Sleep*, 2010a; Submitted, two pos. reports received.
- SCHUMANN, A. Y., BAUER, A., PENZEL, T., SCHMIDT, G., and KANTELHARDT, J. W. *Cardiovascular oscillations and correlations during sleep*. *Proc. 5th Conference of the European Study Group on Cardiovascular Oscillations, Parma Italy*, 2008b; .
- SCHUMANN, A. Y. and KANTELHARDT, J. W. *Multifractal moving average analysis and test of multifractal model with tuned correlations*. *Physica A*, 2010b; Submitted, 5 pos. reports received.
- SCHUMANN, A. Y., KANTELHARDT, J. W., BAUER, A., and SCHMIDT, G. *Bivariate phase rectified signal averaging*. *Physica A*, 2008a; **387**(21):5091–5100.
- SHANNON, C. E. and WEAVER, W. *The mathematical theory of information* (University of Illinois Press, Urbana, IL, 1949).
- SPINOSA, M. J. and GARZON, E. *Sleep spindles: Validated concepts and breakthroughs*. *J. Epilepsy Clin. Neurophysiol.*, 2007; **13**(4):179–182.
- STAM, C. *Nonlinear dynamical analysis of EEG and MEG: Review of an emerging field*. *Clin. Neurophysiol.*, 2005; **116**(10):2266–2301.
- STEFANOVSKA, A., HAKEN, H., MCCCLINTOCK, P. V. E., HOŽIČ, M., BAJROVIĆ, F., and RIBARIČ, S. *Reversible transitions between synchronization states of the cardiorespiratory system*. *Phys. Rev. Lett.*, 2000; **85**(22):4831–4834.
- STROGATZ, S. and STEWART, I. *Coupled oscillators and biological synchronization*. *Scientific American*, 1993; **269**(6):102–109.
- STUMPF, K., SCHUMANN, A. Y., PLOTNIK, M., GANS, F., PENZEL, T., FIETZE, I., HAUSDORFF, J. M., and KANTELHARDT, J. W. *Effect of Parkinson's disease on brain-wave synchronization*. *Euro. Phys. Lett.*, 2010; **89**(4):48001.
- TAQUU, M. S., TEVEROVSKY, V., and WILLINGER, W. *Estimators for long-range dependence: An empirical study*. *Fractals*, 1995; **3**:785–798.
- TASS, P., ROSENBLUM, M. G., WEULE, J., KURTHS, J., PIKOVSKY, A., VOLKMANN, J., SCHNITZLER, A., and FREUND, H.-J. *Detection of $n : m$ phase locking from noisy data: Application to magnetoencephalography*. *Phys. Rev. Lett.*, 1998; **81**(15):3291–3294.

- THEILER, J., EUBANK, S., LONGTIN, A., GALDRIKIAN, B., and FARMER, J. D. *Testing for nonlinearity in time series: the method of surrogate data. Physica D: Nonlinear Phenomena*, 1992; **58**(1-4):77–94.
- TOLEDO, E., AKSELROD, S., PINHAS, I., and ARAVOT, D. *Does synchronization reflect a true interaction in the cardiorespiratory system? Med. Eng. Phys.*, 2002; **24**(1):45–52.
- TOLEDO, E., ROSENBLUM, M., KURTHS, J., and AKSELROD, S. *Cardiorespiratory synchronization: is it a real phenomenon? In: Computers in Cardiology 1999. Vol.26 (Cat. No.99CH37004)* (IEEE, Piscataway, NJ, USA, 1999), pages 237–40. *Computers in Cardiology 1999. Vol. 26*, 26–29 September 1999, Hannover, Germany.
- TURIEL, A., PEREZ-VICENTE, C. J., and GRAZZINI, J. *Numerical methods for the estimation of multifractal singularity spectra on sampled data: A comparative study. J. Comp. Phys.*, 2006; **216**:362.
- TYSON, J. *Biochemical oscillations, in: Computational Cell Biology: An Introductory Text on Computer Modeling in Molecular and Cell Biology* (Springer, New York, 2002).
- VALLADARES, E. M., ELJAMMAL, S. M., MOTIVALA, S., EHLERS, C. L., and IRWIN, M. R. *Sex differences in cardiac sympathovagal balance and vagal tone during nocturnal sleep. Sleep Medicine*, 2008; **9**:310–316.
- VAN CAUTER, E., LEPROULT, R., and PLAT, L. *Age-related changes in slow wave sleep and rem sleep and relationship with growth hormone and cortisol levels in healthy men. JAMA*, 2000; **284**:861–868.
- VANDEWALLE, N. and AUSLOOS, M. *Crossing of two mobile averages: A method for measuring the roughness exponent. Phys. Rev. E*, 1998; **58**:6832.
- VAROTSOS, P. A., SARLIS, N. V., and SKORDAS, E. S. *Attempt to distinguish electric signals of a dichotomous nature. Phys. Rev. E*, 2003; **68**:031106.
- VIO, R. and WAMSTEKER, W. *Limits of the cross-correlation function in the analysis of short time series. PASP*, 2001; **113**:86–97.
- VON KOCH, H. *On continuous curve without tangents, constructible from elementary geometry. Arkiv för Matematik, Astronomi och Fysik*, 1904; **1**:681–704. French title: Sur une courbe continue sans tangente, obtenue par une construction géométrique élémentaire.
- VON STORCH, H. and ZWIERS, F. *Statistical Analysis in Climate Research* (Cambridge University Press, 2001).
- WANG, F. Z., YAMASAKI, K., HAVLIN, S., and STANLEY, H. E. *Scaling and memory of intraday volatility return intervals in stock markets. Phys. Rev. E*, 2006; **73**:026117.
- WEHRLI, W. and LOOSLI-HERMES, J. (eds.). *Enzyklopädie elektrophysiologischer Untersuchungen* (Urban Fisher München Jena, 2003), 2nd edition.
- WELSH, W. *On the reliability of cross-correlation function lag determinations in active galactic nuclei. PASP*, 1999; **111**:1347–1366.
- WESSEL, N., DASH, S., KURTHS, J., BAUERNSCHMITT, R., and MALBERG, H. *Asymmetry of the acceleration and deceleration capacity of heart rate is strongly dependent on ventricular premature complexes. Biomed. Tech.*, 2007; **52**:264–266.
- WILCOXON, F. *Individual comparisons by ranking methods. Biometrics Bulletin*, 1945; **1**(6):80–83.
- WILL, U. and BERG, E. *Brain wave synchronization and entrainment to periodic acoustic stimuli. Neuroscience Letters*, 2007; **424**(1):55 – 60.

- WILSON, F. N., JOHNSTON, F. D., MACLEOD, A. G., and BARKER, P. S. *Electrocardiograms that represent the potential variations of a single electrode.* *Am. Heart J.*, 1934; **9**(4):447–458.
- WILSON, F. N., MACLEOD, A. G., and BARKER, P. S. *The potential variations produced by the heart beat at the apices of einthoven's triangle.* *Am. Heart J.*, 1931a; **7**(2):207–211.
- WILSON, F. N., MACLEOD, A. G., and BARKER, P. S. *The interpretation of the initial deflections of the ventricular complex of the electrocardiogram.* *Am. Heart J.*, 1931b; **6**(5):637–664.
- WILSON, F. N., MACLEOD, A. G., and BARKER, P. S. *The accuracy of einthoven's equation.* *Am. Heart J.*, 1931c; **7**(2):203–206.
- WINFREE, A. *Biological rhythms and behavior of populations of coupled oscillators.* *J. Theor. Biol.*, 1967; **16**(1):15.
- WINFREE, A. *The Geometry of Biological Time* (Springer, New York, 2001), 2nd edition.
- WU, M.-C. and HU, C.-K. *Empirical mode decomposition and synchrogram approach to cardiorespiratory synchronization.* *Phys. Rev. E*, 2006; **73**:051917.
- YANG, H. J., ZHAO, F. C., QI, L. Y., and HU, B. L. *Temporal series analysis approach to spectra of complex networks.* *Phys. Rev. E*, 2004; **69**:066104.
- YASUMA, F. and HAYANO, J.-I. *Respiratory sinus arrhythmia.* *Chest*, 2004; **125**(2):683–690.
- YOGEV, G., PLOTNIK, M., PERETZ, C., GILADI, N., and HAUSDORFF, J. M. *Gait asymmetry in patients with parkinson's disease and elderly fallers: when does the bilateral coordination of gait require attention?* *Exp. Brain Res.*, 2007; **177**:336–346.
- ZIEHE, A., LASKOV, P., NOLTE, G., and MULLER, K. *A fast algorithm for joint diagonalization with non-orthogonal transformations and its application to blind source separation.* *J. Machine Learning Res.*, 2004; **5**:777–800.
- ZSCHIEGNER, S. A. *An experimental R-peak detector based on wavelet transform.* unpublished, 2004.
- ZUNG, W. W. K. *Rating instrument for anxiety disorders.* *Psychosomatics*, 1971; **12**(6):371–379.
- ZUNG, W. W. K., RICHARDS, C. B., and SHORT, M. J. *Self-rating depression scale in an outpatient clinic - further validation of SDS.* *Archives of General Psychiatry*, 1965; **13**(6):508.
- ZWEIG, M. and CAMPBELL, G. *Receiver-operating characteristic (roc) plots - a fundamental evaluation tool in clinical medicine.* *Clinical Chemistry*, 1993; **39**(4):561–577.

G. Publications / Veröffentlichungen

1. K. Stumpf, A. Y. Schumann, M. Plotnik, F. Gans, T. Penzel, I. Fietze, J. M. Hausdorff, J. W. Kantelhardt, *Effect of Parkinson's Disease on Brain-Wave Synchronization*, (submitted to Europhys. Lett., Oct. 2009, 2 positive reports)
2. A. Y. Schumann, J. W. Kantelhardt, *Multifractal Moving Average Analysis and Test of Multifractal Model with Tuned Correlations*, (submitted to Physica A, Sept. 2009, 5 positive reports)
3. A. Y. Schumann, R. P. Bartsch, P. Ch. Ivanov, T. Penzel, and J. W. Kantelhardt, *Normal Aging Effects on Cardiorespiratory Variability Across Sleep Stages* (submitted to Sleep, Sept. 2009, 2 positive reports)
4. F. Gans, A. Y. Schumann, J.W. Kantelhardt, T. Penzel, and I. Fietze, *Cross-Modulated Amplitudes and Frequencies Characterize Interacting Components in Complex Systems*, Phys. Rev. Lett. **102**, 098701 (2009)
5. C. Hamann, R. P. Bartsch, A. Y. Schumann, T. Penzel, S. Havlin, and J. W. Kantelhardt, *Detection of Cardiorespiratory Synchronization Based on Reconstructed Respiration*, Chaos **19**(1),015106 (2009)
6. A. Y. Schumann, A. Bauer, T. Penzel, G. Schmidt, and J. W. Kantelhardt, *Cardiovascular Oscillations and Correlations During Sleep*, Proc. 5th Conference of the European Study Group on Cardiovascular Oscillations, Parma, Italy (2008).
7. A. Y. Schumann, J. W. Kantelhardt, A. Bauer, and G. Schmidt, *Bivariate Phase-Rectified Signal Averaging*, Physica A **387**, 5091 (2008).
8. J. W. Kantelhardt, A. Bauer, A. Y. Schumann, P. Barthel, R. Schneider, M. Malik, and G. Schmidt, *Phase-Rectified Signal Averaging for the Detection of quasi-periodicities and the Prediction of Cardiovascular Risk*, Chaos **17**, 015112 (2007).
9. A.Witt, A.Y. Schumann, *Holocene Climate Variability on Millennial Scales Recorded in Greenland Ice Cores*, Nonlinear Processes in Geophysics (2005) **12**: 1-8, SRef-ID: 1607-7946/npg/2005-12-1

H. Danksagung

Ganz besonders möchte ich mich bei Jan Kantelhardt für seine sehr gute Betreuung während meiner Promotion bedanken. Er hat mir häufig den nötigen Optimismus gegeben, wenn ich aufgrund einer Vielzahl von Artefakten und Fehlern in den Daten am Verzweifeln war. Das Arbeitsklima in Halle habe ich dabei als besonders inspirierend empfunden. Ich möchte mich weiterhin für die einzigartige Gelegenheit bedanken, zahlreiche internationale und nationale Konferenzen zu besuchen. Jan hat immer eine Möglichkeit zur Finanzierung von Dienstreisen oder moderner Rechentechnik gefunden. Ich habe mich stets in seiner Arbeitsgruppe sehr wohl gefühlt und hoffe, dass wir auch in Zukunft den Kontakt nicht verlieren werden und nicht nur begonnene Projekte zu Ende führen können, sondern auch neue beginnen werden.

Weiterhin möchte ich mich bei Lukas Jahnke bedanken, der mir in den letzten Jahren nicht nur die Zeit im Büro vertrieben hat, sondern auch ein guter Freund geworden ist. Insbesondere danke ich Dir, Lukas, für die aufbauenden Worte, wenn ich an mir selbst zweifelte. Ohne Dich wären die letzten Jahre sicherlich nur halb so angenehm gewesen.

Des weiteren gilt mein Dank Ronny Bartsch mit dem ich gemeinsam versucht habe, aus den oft problematischen Datensätzen gute Ergebnisse zu produzieren. Vielen Dank für die schöne Zeit in Israel. Ich hoffe, dass wir auch in Zukunft gemeinsame Projekte verwirklichen können.

Für die gute Unterstützung bei der EKG Peak-Detektion möchte ich mich bei unseren studentischen Hilfskräften Anne Mehnert, Regina Eichner, Inga Hettrich, und Ulrich Skrzypczak bedanken. Ohne Euch hätten wir noch immer nicht alle EKGs analysieren können.

Besonderer Dank gilt unserem ehemaligen Diplom-Studenten Fabian Gans und unserem ehemaligen Bachelor-Studenten Kilian Stumpf, die meine guten, aber auch die nicht erfolgreichen Ideen umgesetzt haben.

Vielen Dank Daniel Fulger für die angenehmen Gespräche über den Sinn von Wissenschaft.

Schließlich möchte ich mich bei der Europäischen Union bedanken für meine Finanzierung im Projekt DAPHNET in dessen Rahmen ich zahlreiche europäische und internationale Kollegen gefunden habe.

Auf jeden Fall möchte ich mich bei meiner Freundin Bettina bedanken, die es nie leicht mit mir hatte wenn ich wegen beruflichen Verpflichtungen Termine verschieben oder Urlaube absagen mußte. Danke, dass Du das durchgehalten hast! Zu großem Dank bin ich Dir auch verpflichtet für die Hoffnungen, die Du in mich gesetzt hast, wenn ich schon aufgeben wollte.

Affirmation / Eidesstattliche Erklärung

English

I herewith avow and confirm that this PhD thesis has been written only by the undersigned and without any assistance from third parties. Furthermore, I declare that no sources have been used in the preparation of this thesis other than those indicated in the thesis itself. This thesis, in same or similar form, has not been available to any audit authority yet.

Deutsch

Hiermit erkläre ich, dass ich die vorgelegte Dissertation selbstständig und ohne Hilfe Dritter angefertigt habe. Ich habe ferner keine anderen als die von mir angegebenen Quellen und Hilfsmittel zur Erstellung meiner Dissertation verwendet. Den verwendeten Quellen wörtlich oder inhaltlich entnommene Stellen sind als solche gekennzeichnet. Ich erkläre, die Angaben wahrheitsgemäß und in bestem Wissen gemacht zu haben und dass die wissenschaftliche Arbeit an keiner anderen wissenschaftlichen Einrichtung zur Erlangung eines akademischen Grades eingereicht wurde.

Aicko Yves Schumann
Halle/Saale, den 17. Januar 2010

Lebenslauf

Diplom Physiker
Aicko Yves Schumann
Rudolf-Haym Str. 5
06110 Halle/Saale

Persönliche Daten

Name: Aicko Yves Schumann
Geburtsdatum: 16. Juli 1977
Geburtsort: Potsdam (Deutschland)
Staatsangehörigkeit: Deutsch
Familienstand: Ledig

Ausbildung und wissenschaftlicher Werdegang

seit Februar 2010 Wissenschaftlicher Mitarbeiter
Complexity Science Group
University of Calgary, Canada

seit April 2005 Promotion zum Dr. rer. nat
am Lehrstuhl Computational Nanosciences,
Fachbereich Physik, Martin-Luther-Universität Halle-Wittenberg
Medizinische Zeitreihenanalyse
Thema: *Fluctuations and Synchronization in
Complex Physiological Systems*

2004 - 2005 Wissenschaftlicher Mitarbeiter am Max-Planck-Institut
für Kolloid und Grenzflächenforschung Golm
und am Institut für Mathematik der Universität Potsdam

2004 Wissenschaftlicher Mitarbeiter
Institute of Nonlinear Science
University of California San Diego

2003 bis 2004 Diplomarbeit: Nichtlineare Dynamik
Thema: *Waveletanalyse von Sedimentdaten
unter Einbeziehung von Alters-Tiefen Modellen*

1998 bis 2004 Studium der Physik an der Universität Potsdam
Abschluss: Diplom Physiker

1997 bis 1999 Studium der Geoökologie and der Universität Potsdam
Qualifikation zum Vordiplom

1997 Allgemeine Hochschulreife, Gymnasium Kleinmachnow

Aicko Yves Schumann
Halle/Saale, den 17. Januar 2010